Platinum group metals behaviour during iron precipitation and goethite seeding in nickel sulphate solution

by

Rj Coetzee

Thesis presented in partial fulfilment
of the requirements for the Degree

of

MASTER OF ENGINEERING
(Extractive Metallurgical Engineering)

in the Faculty of Engineering
at Stellenbosch University

Supervisor

Dr. C. Dorfling

Co-Supervisor

Prof. S.M. Bradshaw

MARCH 2016

Declaration

By submitting this thesis electronically, I declare that the entirety of the work contained therein is my own, original work, that I am the sole author thereof (save to the extent explicitly otherwise stated), that reproduction and publication thereof by Stellenbosch University will not infringe any third party rights and that I have not previously in its entirety or in part submitted it for obtaining any qualification.

Rj Coetzee March 2016

ABSTRACT

Platinum producers' base metal refineries leach converter matte to solubilise base metal sulphides and produce a platinum group metal residue. Nickel, cobalt and some of the iron present in the matte are solubilised during atmospheric sulphate leaching. The pregnant leach solution also contains dissolved other precious metals (OPMs, ruthenium, rhodium and iridium). The solution passes through holding tanks prior to being fed to heat exchangers and crystallisers for the production of nickel sulphate hexahydrate as by-product.

An iron sludge precipitates during long residence times in tanks and on contact with hot surfaces. This sludge entrains OPMs and could potentially be used as a mechanism for recovery of dissolved OPMs. The behaviour of OPMs needed to be established during impurity precipitation in the nickel sulphate solution. Goethite material was also seeded, as a means to provide a growth surface during precipitation.

The solution was heated to 70 °C or 90 °C and the pH was adjusted to pH 2.5 and pH 4.0, with caustic soda (NaOH). The total metal concentration was varied between the total metals of the first stage leach, 65 g/ℓ, and that of upgraded solution, 95 g/ℓ. Goethite seeding (10 g/ℓ, 50 g/ℓ and no seed) and iron valence (ferrous and ferric) were varied in six hour experiments.

It was found that the OPMs could be selectively precipitated via neutralisation, with pH and temperature being crucial factors. At pH 2.5, 89 % ruthenium and rhodium precipitated and 14 % iridium precipitated. All ruthenium and rhodium precipitated at pH 4.0 and iridium precipitation increased to 88 %. OPM precipitation was 34 % faster at high temperature experiments. The order of readability to precipitate was ruthenium, followed by rhodium and then iridium. OPM precipitation was also possible without iron in synthetic solutions.

Different iron oxide phases formed. Spherical, aggregated crystals between 50 nm – 100 nm in size were observed with elemental compositions agreeing well with that of synthetic ferrihydrate and schwertmannite. Sulphate inclusion was more prominent during the rapid precipitation in ferric runs. Ruthenium and rhodium were finely dispersed within the iron oxide precipitates of lower densities. Iridium precipitated in a clearly distinguishable phase consisting of iridium (50 – 80 wt.%), chloride and oxygen.

The observation of the acicular rod crystals that are associated with goethite, the absence of spherical crystals, the uniform density observed with back-scatter images and the observed increase of overall particle size strongly suggest that seeding did induce the targeted growth of goethite in nickel sulphate solution with ferric iron. Goethite seeding did not increase the rate of iron precipitation or OPM recovery.

Keywords:

Base metal refining, Platinum group metal recovery, Precipitation, Iron precipitation.

OPSOMMING

Platinum produseerders se basismetaal raffinaderye loog onedel metale vanuit omskakelaar mat, om sodoende ‘n platinum groep metaal residu te produseer. Nikkel, kobalt en yster word gedurdende atmosferiese sulfaat loging opgelos. Hierdie logingsoplossing bevat ook sogenaamde ander waardevolle metale, OPMe, wat rutenium, rodium en iridium insluit. Die logingsoplossing word in tenke gestoor en daarna gevoer na hitteruilers en kristalliseerders om nikkel heksahidraat kristalle as ‘n by-produk te produseer.

Yster presipiteer wat ‘n slyk newe-produk vorm gedurende die lang residensie tyd in tenke en ook wanneer die oplossing in kontak kom met warm oppervlaktes. OPMe word in hierdie slyk waargeneem en dus word die verwydering van slyk oorweeg as ‘n metode om OPMe te ontgin. Dit word verlang om vas te stel hoe OPMe optree gedurende yster presipitasie. Goethiet saad materiaal wat potensieel as ‘n middel kan optree om geordende kristal groei te bevorder, is ondersoek.

Die oplossing was verhit na 70 °C en 90 °C en the pH was aangepas met bytsoda (NaOH) na pH 2.5 en pH 4.0. Die totale metaal konsentrasie in die oplossing was gevarieer tussen die konsentrasie van tipiese logingsoplossings by 65 g/ℓ, sowel as die van opgegradeerde oplossing by 95 g/ℓ. Goethiet saad (10 g/ℓ, 50 g/ℓ en geen saad) en yster valensie (Fe(II) en Fe(III)) was ook gevarieer in ses uur experimentele lopies.

OPMe het selektief gepresipiteer as die logingsoplossing met ‘n neutralisasie middel behandel word. pH en temperatuur was die belangrikste faktore. 89 % rodium en ruthenium presipitasie en 14 % iridium presipitasie is waargeneem by pH 2.5. As die pH verhoog word na 4.0 sal alle rutenium en rodium presipiteer en 88 % iridium sal presipiteer. OPM presipitasie is 34 % vinniger by hoë temperatuur eksperimente. Rutenium het die maklikste gepresipiteer, gevolg deur rodium en laastens iridium. OPM presipitasie het ook plaasgevind in die afwesigheid van yster in oplossing.

Verskillende ysteroksied soliede fases het gevorm. Sferiese, aangepakte, 50 nm – 100 nm kristalle was waargeneem, wat ooreenstem met sintetiese weergawes van ferrihidraat en schwertmanniet. Sulfaat inkorporasie was meer prominent gedurende die spoedige presipitasie in Fe(III) lopies. Rutenium en rodium was fyn versprei in die ysteroksied fases. Iridium het as ‘n aparte solied gepresipiteer, wat primêr uit iridium (50 – 80 massa%), chloried en suurstof bestaan.

Resultate stel voor dat saad materiaal suksesvol geteikende presipitasie teweeg bring. Slegs langwerpige, silindriese goethiet kristalle en ‘n uniforme partikeldigtheid word

waargeneem. Die partikelgrootte het ook effektief gegroei. Die byvoeging van goethiet saad het alhoewel nie die tempo van yster presipitasie of OPM ontginning verhoog nie.

Sleutelwoorde:

Onedelmetaal raffinering, Platinum groep metaal ontginning, Presipitasie, Yster presipitasie.

ACKNOWLEDGEMENTS

I would like to acknowledge and sincerely thank the following people for their contributions towards this work:

Dr. Rian Bezuidenhout, who met my request to extend my undergraduate bursary with open arms and made my dream to do a masters come true.

Prof. Christie Dorfling, for his supervision, technical advice, patience and encouragement.

Mr. Marius de Beer, my manager and mentor for the past six years at Lonmin Plc, for his encouragement, insight, assistance and passion for the mining industry.

Prof. Steven Bradshaw, for his co-supervision and technical insight.

Ms. Hanlie Botha, for her technical assistance with ICP-OES, BET and PSD analysis. Her patience, technical advice and eagerness to help are greatly appreciated.

Mr. Nealle McCulloch, for valuable industry correspondence and assistance.

Ms. Petronel de Jager and Ms. Evelyne Rabolele of Lonmin Plc's Talent Department, for administrative support, active encouragement and their caring personalities.

Dr. Angelique Laurie, for her technical assistance during scanning electron microscopy work at Stellenbosch University's Central Analytical Facility.

Dr. Remi Bucher, for his technical assistance during X-ray diffraction analyses at iThemba LABS.

Stellenbosch University's technical and laboratory staff, notably Mr. Alvin Petersen and Mr. Jos Weerdenburg's help is appreciated.

Dr. Johann Steyl, for his technical advice.

Colleagues Willem Rossouw and Saviour Masambi, for their advice regarding experimental work.

Dr. Lidia Auret and Dr. Cara Schwarz, for the courses presented as part of the Master's program.

Ms. Francis Layman, for her swift and thorough administrative help.

Lonmin Plc base metal refinery laboratory staff, for their technical assistance and warm hearts.

Prof. Mike Nicoll, for the annual hydrometallurgy seminars at University of Cape Town and Prof. Jöchen Petersen, who funds these seminars annually.

My loving family and friends for their unwavering support.

Julia, for her support, encouragement and love.

Lonmin Plc, for extending my undergraduate bursary, enabling me to conduct Masters research. Their financial sponsorship is greatly appreciated.

TABLE OF CONTENTS

LIST OF TABLES

LIST OF FIGURES

NOMENCLATURE

Acronym	Definition
BET	Brunauer–Emmett–Teller theory
BFS	basic ferric sulphate
BIC	Bushveld Igneous Complex
BMR	Base Metals Refinery
BSE	Back-scattered electron
CAF	Stellenbosch University - Central Analytical Facility
EZ	Electrolytic Zinc
EDS	Energy-dispersive X-ray spectroscopy
FFE	Falling film evaporator column
ICP-OES	Inductively coupled plasma - optical emission spectrophotometer
OPM	Other Precious Metals, comprising of Rh, Ru and Ir.
PGM	Platinum Group Metals, comprising of Pt, Pd, Rh, Ru, Ir and Os.
PMR	Precious Metals Refinery
PSD	Particle size distribution
RO	Reverse osmosis
ROM	Run out mine
SE	Secondary electron
SEM	Scanning electron microscopy
UG 2	Upper Group chromitite layer, Seam 2
VM	Vieille Montagne
WPL	Western Platinum Ltd.
XRD	Powder X-ray diffraction
XRF	X-ray fluorescence spectrometry
NIST	American National Institute of Standards and Technology

CHAPTER 1 - INTRODUCTION

1.1. Background

South Africa contains the world's largest discovered deposits of platinum and the associated platinum group metals (PGMs). It was estimated in 2000 that approximately 80 % of the exploitable platinum group metal (PGM) reserves are found in South Africa (Rao & Reddi, 2000). In 2006, South Africa produced 57 % of the world's PGMs (Stilwell, 2008). In 2007, South Africa contributed to 77 % of the world's platinum production (Jollie, 2008). PGM-bearing ores are exploited from three reefs in South Africa, all found in the Bushveld Igneous Complex (BIC). They are the Merensky reef, the Upper Group chromitite layer, seam 2 reef (UG 2) and the Plat reef (Cramer, 2001).

Platinum group metals are either mined in underground shafts and open pit operations and follow a series of upgrading processes. Ore is subject to concentration by means of flotation, with the flotation concentrate treated pyrometallurgically, utilising smelting furnaces and converters. The base metal refineries (BMRs) operated by platinum producers entail the hydrometallurgical treatment of converter matte. The matte, containing primarily base metal sulphides and platinum group metals (PGMs), is treated to separate the PGMs from the base metals. Refined base metals are produced as by-products. The PGM residue is then further refined to pure metals at the precious metals refinery (PMR).

In the first step of the base metals refinery hydrometallurgical process, atmospheric leaching is employed to solubilise nickel and cobalt from the converter matte. Iron is also partially dissolved, while copper and other precious metals (OPMs, referring to rhodium, ruthenium and iridium) are precipitated from solution.

The nickel sulphate solution, obtained from atmospheric leaching, is subjected to evaporation by heat exchanging. Subsequent vacuum crystallisation produces nickel sulphate hexahydrate crystals. Sludge formation is observed within the heat exchangers and the holding tanks feeding the heat exchangers. The sludge fouls the heat exchanger pipes which can block these pipes. Fouling furthermore causes insufficient heat transfer between the heating medium and the nickel sulphate solution, which in turn results into insufficient evaporation. Vacuum crystallisation is retarded, which subsequently limits production throughput. Periodic shutdowns, required to descale the heat exchangers, also increase the total loss of time.

It is believed that the fouling is a result of precipitation of metal impurities in the stream. These impurities primarily include iron, cobalt, sodium, copper and arsenic, in order of abundance.

Sludge characterisation has revealed that iron is the most abundant impurity in the sludge. Iron is also the most abundant impurity in the nickel sulphate stream.

Other platinum metals are also lost to the nickel crystalliser section. Operating data shows that 3 % of iridium and 0.5 % of ruthenium in the base metal refinery feed reports to the nickel crystalliser section. Industry investigations detected OPMs in the fouling sludge; the recovery of OPMs from the nickel sulphate section by co-precipitation with the sludge could potentially be of economic benefit to the BMR.

1.2. Problem statement

Fouling in the heat exchangers needs to be minimised in order to allow more efficient operation of the nickel crystalliser section. Two approaches were considered: (a) the process conditions in the holding tanks need to be controlled to minimise sludge formation, or (b) if significant OPM recovery is possible, precipitation must be achieved in the holding tanks. The second approach may improve nickel sulphate crystal grades as a result of impurity precipitation. The nickel sulphate crystals are sold with higher levels of iron, sodium, arsenic and copper than for instance allowed by the British Standard BS 564 (1970) and the German Deutsches Institut Fur Normung E.V. standard DIN 50970 (1995).

1.3. Aims and objectives

A better understanding of the aqueous chemistry of impurities, as well as the effect of process variables on impurity precipitation was desired. A better understanding of the behaviour of other precious metals during impurity precipitation from a nickel sulphate stream was desired. Do the OPMs precipitate out as a co-precipitate product; is it structurally incorporated into the crystal lattice? Characterisation of the solid sludge was desired.

It was hypothesised that the observation of other precious metals in heat exchanger sludge was the result of cation substitution during iron precipitation with OPM cations. It was hypothesized that the addition of goethite seed material may act as a suitable growth site during the precipitation of iron from solution.

CHAPTER 2 - LITERATURE SURVEY

An overview of the platinum group metal extraction process is given in Section 2.1. A detailed description of the nickel crystalliser section at Western Platinum Ltd.'s base metal refinery is presented in Section 2.2. Fundamental platinum group metal chemistry, iron precipitation chemistry and arsenic precipitation chemistry are provided in Sections 2.3 – 2.5. Cation exchange and entrainment chemistry is presented in Section 2.6.

2.1. Platinum group metal extraction

Platinum group metal-rich ore, mined from Bushveld Igneous Complex's (BIC) reefs in South Africa, undergoes a series of upgrading processes to produce refined PGM's. The beneficiation process can be divided into four sections:

- Concentrator plant - Physical concentration
- Smelting complex - Pyrometallurgical concentration
- Base metals refinery - Hydrometallurgical upgrading
- Precious metals refinery - Individual refining of OPMs

The concentrator plants receive ore from the mining operations with platinum group metal grades in the range of 3 – 10 g PGMs per ton ore (Crundwell *et al.*, 2011). Western Platinum Ltd. (WPL) exploits the Merensky and UG 2 reefs in the BIC; the concentrate blend, consist of 75 % UG 2 ore concentrate and 25 % Merensky (Lonmin Plc, 2013).

Grinding, milling and classification are applied to liberate the platinum group metals from the gangue materials. The PGMs are mostly interlocked in the base metal sulphide mineral grains and gangue-mineral boundaries (Jones, 1999). Fine grinding is required to liberate the PGMs locked within the 15 µm (UG 2) and 45 µm (Merensky) grains (Jones, 1999). Subsequently flotation is used to concentrate the sulphide materials.

Western Platinum Ltd. (WPL) Smelter treats is the concentrate received from the company's seven concentrator plants. Conventionally, six-in-line furnaces were employed to smelt Merensky flotation concentrate, but the more-refractory, chromium (III) oxide rich UG 2 concentrate required smelting at higher power densities (Cramer, 2001; Nell, 2004). WPL Smelter currently utilises circular, AC, submerged arc furnaces. The furnace matte is then treated in Pierce Smith converters for iron and sulphur removal.

The converter matte is granulated and dispatched to WPL base metals refinery. Atmospheric sulphate leaching is followed by pressurized leaching, producing nickel sulphate crystals and

copper metal by-products. The residue, from the copper leaching autoclaves, is further upgraded, by means of caustic and formic batch leaching, to produce a high grade residue of 65 % PGM content.

The PGM-rich residue is dispatched to WPL precious metals refinery (PMR), for refining of individual PGMs. WPL PMR primarily rely on dissolution, precipitation and metal reduction chemistry to produce refined PGMs (Crundwell *et al.*, 2011).

2.2. Nickel crystalliser section process flow

An overall process description of the WPL base metals refinery is provided by Steenekamp & Dunn (1999). WPL BMR treats approximately 10000 tpa converter matte (Crundwell *et al.*, 2011). A process flow sheet of the overall process is provided in Figure 2-1 and a process flow sheet of the nickel crystalliser section is provided in Figure 2-2.

Converter matte enters a ball mill to produce a 75 µm pass size grind. The first stage leach section employs sulphuric acid and spent copper electrolyte, which is recycled from the copper electrowinning section, to leach nickel, cobalt and iron from converter matte. Copper and other precious metals are precipitated from the spent copper electrolyte solution. Five tanks are cascaded in series. The first three tanks are oxidised with oxygen in the decreasing ratio of 60:30:10. The last two tanks are not oxidised. Leaching commences at 80 °C to 90 °C.

Solid-liquid separation is done via a conventional thickener. A polyacrylamide flocculant is dosed to facilitate settling and to clarify the overflow. The separated, pregnant nickel sulphate solution undergoes two-stage filtration, to remove fines. Three pressure filter presses are installed in parallel. The filter presses' filtrate is fed to an ultrafine polishing filter, which is tailored to remove trace solids from electrolyte solutions up to 0.45 µm.

The nickel sulphate solution reports to two big holding tanks, 700-TK-020 (140 m^3) and 700-TK-090 (50 m^3). A plate heat exchanger and boil-off circuit at 700-TK-090 evaporates some water to concentrate the total metals content from < 120 g/ℓ to 150 – 170 g/ℓ. 700-TK-090's boil-off circuit is operated at 95 °C and the solution is exposed to the atmosphere.

A new nickel crystalliser section was commissioned in 2008 to increase crystalliser capacity. The new crystalliser section consists of a separate evaporator and crystalliser, to replace the previous draft tube crystallisers.

The falling film evaporator (FFE) column, which has a high heat exchanging surface area in the column's tubes, further concentrates the liquor to an SG of 1.55. The FFE column uses a mechanical vapour recompressing fan to remove the evaporated water.

The crystalliser is operated at 50 °C and vacuum pressure, in order to induce crystal formation. A purge stream from the crystalliser recycles back to the first stage leach. Classification cyclones are used to recycle undersize crystals. Centrifuges dewater the crystals to below 3 % moisture and a fluidized bed provides the final drying step for the process.

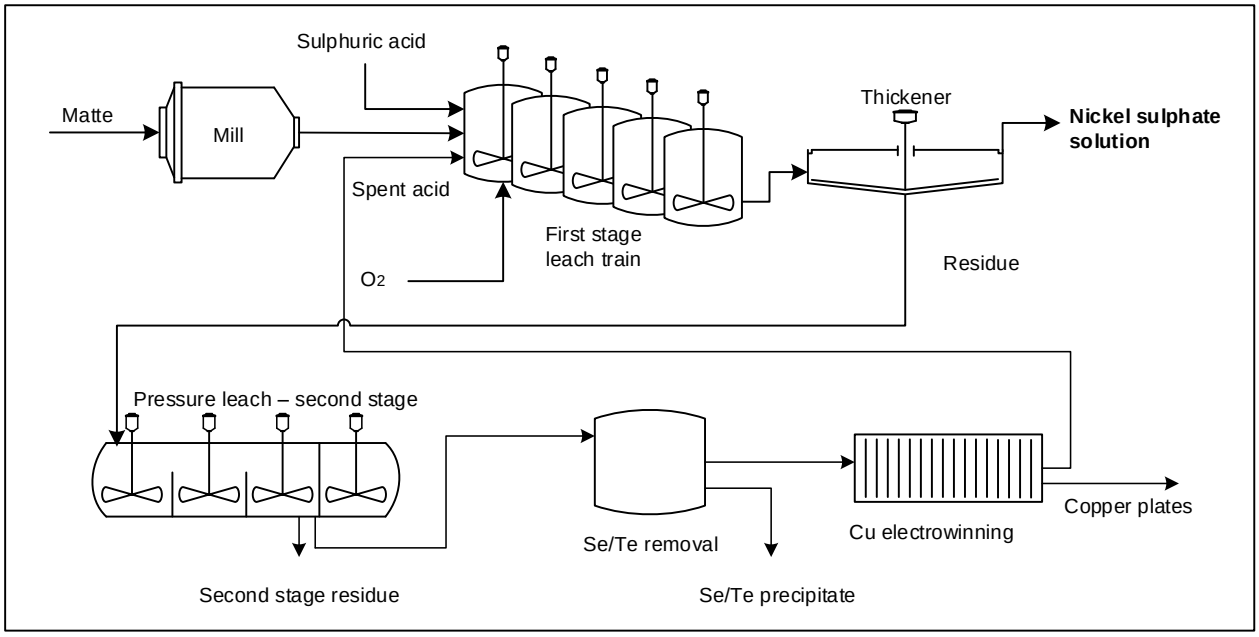

Figure 2-1: Western Platinum Ltd. base metal refinery flowsheet.

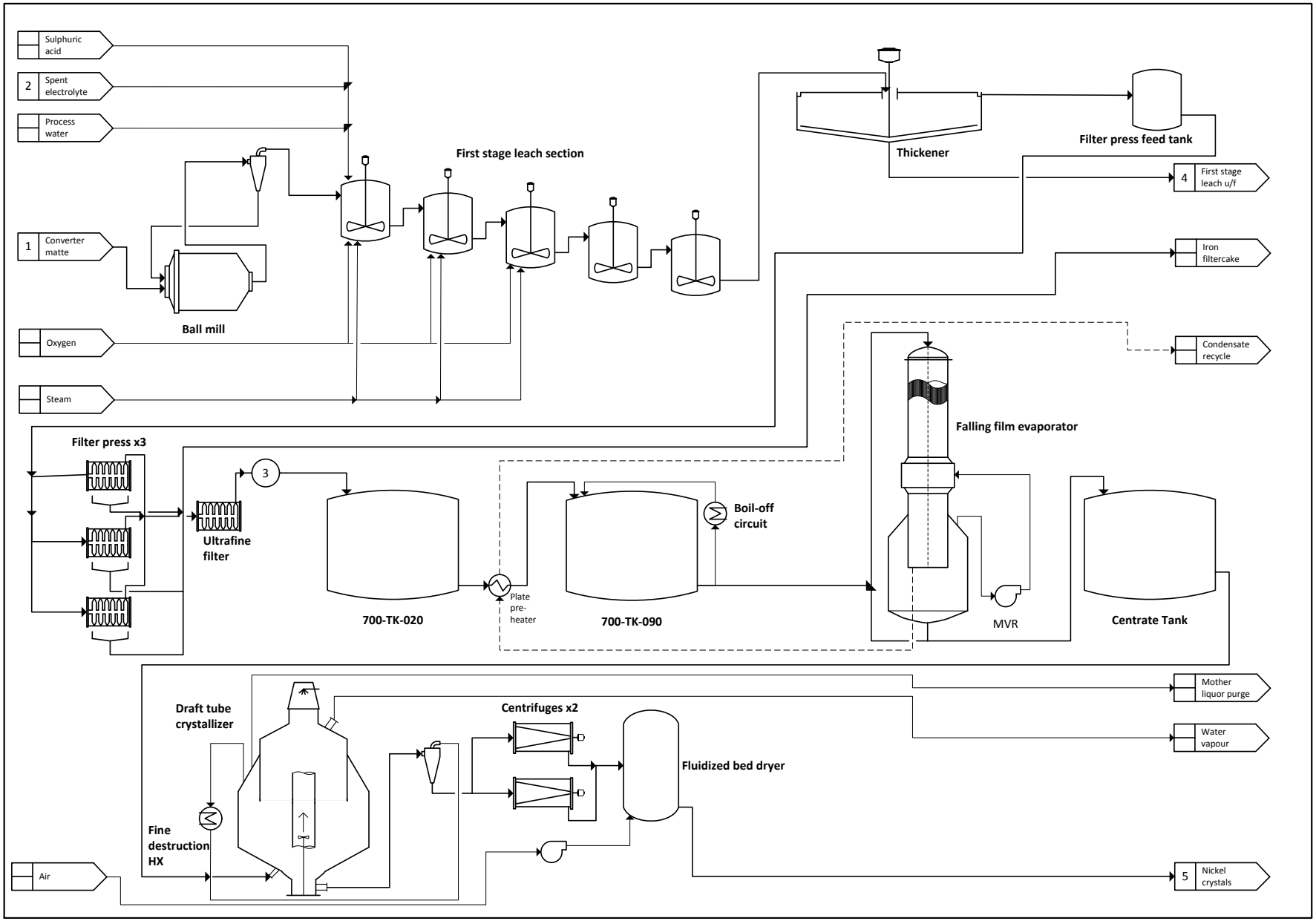

Figure 2-2: Western Platinum Ltd. base metal refinery – nickel section flow sheet.

Table 2-1 provides the elemental composition of the leach solution, compiled from industry data. The following impurities are detected in order decreasing concentration: iron, arsenic, copper, iridium, ruthenium and lead.

The iron in the converter matte was detected to be between 0.3 wt.% and 2.1 wt.% over the same period. The copper spent electrolyte stream contained an average of 0.5 g/ℓ Fe and 325 ppm As.

13.0 ppm other precious metals were detected in the liquor that varied between 4.4 ppm to 25.1 ppm over the time period. During the same time period, 6.8 ppm OPMs were detected in the nickel sulphate crystals.

Table 2-1: Average composition of the first stage leach over flow (o/f) from plant operations.

Name			**First stage leach over flow (o/f)**			
Phase			Liquid			
Specific gravity			1.38 - 1.42			
pH			2 - 3			
			Average	Var*	Min	Max
Base metals	**Ni**	[g/ℓ]	**103.1**	3 %	97.2	111.1
	Cu	[g/ℓ]	**0.050**	100 %	0.007	1.354
	Fe	[g/ℓ]	**2.067**	9 %	0.999	2.452
	Co	[g/ℓ]	**0.643**	6 %	0.541	0.716
PGE	**Pt**	[ppm]	Not detected (N/D)			
	Pd	[ppm]	N/D			
	Au	[ppm]	N/D			
	Rh	[ppm]	N/D			
	Ru	[ppm]	**4.6**	53 %	1.0	12.0
	Ir	[ppm]	**8.4**	31 %	2.4	14.9
	Total	[ppm]	**13.0**	36 %	4.4	25.1
Trace	**As**	[ppm]	**62.6**	30 %	9.6	149.8
	Pb	[ppm]	**0.003**	145 %	0.000	0.025
	Se	[ppm]	N/D			
	Te	[ppm]	N/D			

* - Standard deviation of data.

2.3. Platinum group metal chemistry

The platinum group metals show close similarities between physical and chemical properties and little difference between atomic sizes due to Lanthanide contraction (Renner, 2002). The PGMs occur in several oxidation states. The standard oxidation states of interest in aqueous solution are Pt: +2 and +4, Pd: +2, Ir: +3, Rh: +3, and +4, Os: +4 and Ru: +2, +3 and +4 (Renner, 2002)

(Seymour & O'Farrelly, 2006). The listed oxidation states for the other platinum metals, Ru, Rh and Ir, are coordinated in octahedral lattices (Baes & Mesmer, 1976; Seymour & O'Farrelly, 2006).

The platinum group metals are present two distinct euhedral phases in converter matte (Thyse, 2014). Platinum, palladium, rhodium and ruthenium are predominantly alloyed with nickel and copper in a Ni-Cu phase with varying nickel and copper content. Ruthenium, osmium, some iridium and platinum alloys within the heazlewoodite matrix as an Os-Ru predominant alloy.

Platinum group metals are resistant to concentrated sulphuric acid dissolution at 100 °C. Palladium dissolution at 1 $mg/cm^2.h$ and rhodium dissolution 0.1 $mg/cm^2.h$ is expected, whilst dissolution of other PGMs were insignificant (Renner, 2002). The base metals in PGM-base metal alloys would be dissolved during sulphuric acid leaching, producing noble-metal black, which has a higher tendency to be dissolved (Dorfling, 2011).

Other precious metal dissolution is observed in base metal pressure leaching (Dorfling, 2011). Dissolution of OPMs mostly occurred when copper leaching had been completed and the leaching temperature was identified as the most important variable for OPM dissolution (Dorfling, 2011).

Amphoteric elements, selenium and tellurium, are precipitated out of the pregnant copper sulphate solution with sulphurous acid. OPMs also partially precipitate, which require redissolution of the precipitated selenium and tellurium with caustic soda solution at 85 °C and 50 kPa. The precipitation step allows the dissolution of selenium and tellurium. The copper and OPMs in solution are recycled back into the process.

After the Se/Te precipitation, copper electrowinning takes place. No interference of OPMs are noted industrially.

The spent copper electrowinning solution, used for atmospheric leaching, contains appreciable amounts of other precious metals. The OPMs in spent solution is carried over from pressure leach solution. The precipitation of OPMs occurs during the first stage leaching of converter matte (Steenekamp & Dunn, 1999). The mechanism of OPM precipitation is not well understood, but is believed to follow the same trend as that of copper metathesis (van Schalkwyk, 2011).

Equation 2-1 presents the classical metathesis reaction between copper in solution and heazlewoodite, the predominant nickel sulphide mineral in converter matte. Equation 2-2 presents metathesis exchange with nickel in the alloy phase. Equation 2-3 presents the assumption of the metathesis of OPMs in sulphate media (Steenekamp & Dunn, 1999; van Schalkwyk et al., 2013).

$$Ni_3S_2 + 2Cu^{2+} \rightarrow Cu_2S + NiS + 2Ni^{2+}$$ Equation 2-1

$$Ni^0_{alloy} + CuSO_4 \rightarrow NiSO_4 + Cu^0_{alloy}$$ Equation 2-2

$$Ni^0_{alloy} + (Ru, Rh, Ir)SO_4 \rightarrow NiSO_4 + (Ru, Rh, Ir)^0_{alloy}$$ Equation 2-3

The iron endpoint of matte and oxidation has shown to impact the precipitation of copper and other precious metals (van Schalkwyk, 2011). van Schalkwyk's (2011) OPM precipitation data is presented in Table 2-2. Oxidised low iron end-point matte could effectively precipitate all OPMs during nickel leaching.

All other precious metals were precipitated during the oxidative leaching of low iron end-point matte. 70 % of rhodium and less than half the iridium and ruthenium were precipitated in 1) non-oxidative leaching of low iron matte and 2) oxidative leaching of high iron matte. Rhodium is observed to precipitate more readily than iridium and ruthenium. Industry data, presented in Table 2-1, correlate well with van Schalkwyk's (2011) data: 8.4 mg/ℓ iridium and 4.8 mg/ℓ ruthenium is present in the first stage overflow, with little to no rhodium.

Table 2-2: OPM precipitation during first stage leach (van Schalkwyk, 2011).

	0.83 % Fe matte, no oxygen	**5.17 % Fe matte, oxygen**	**0.53 % Fe matte, oxygen**
Ir	38%	56%	92%
Ru	48%	40%	100%
Rh	70%	70%	93%

Various binary halide compounds of the other platinum metals exist, of which chloride compounds are of interest in this work. The trichloride compounds, i.e., $RuCl_3$, $RhCl_3$ and $IrCl_3$ exist in insoluble anhydrous, in α- and β-form, as well as soluble hydrous forms. The soluble hydrous trichloride salts are among the preferred salts for chemical synthesis and are commercially available. Other binary halides include $RuCl_2$, $RuCl_4$ and $IrCl_4$.

Renner (2002) lists the synthesis routes of soluble other platinum metal chlorides. Soluble ruthenium chloride consists of $RuCl_3.xH_2O$ and $Ru(OH)Cl_3$. It is produced by reacting RuO_4 with hydrochloric acid and then evaporating the solution. Soluble rhodium chloride, $RhCl_3.2.5H_2O$, is obtained by evaporating a solution of $H_3[RhCl_6]$ (hexachloro-rhodium) in hydrochloric acid. The synthesis procedure of soluble iridium chloride: $IrCl_3.xH2O$ is not available.

Binary oxide compounds of other platinum metals include RuO_2. Rhodium oxides and hydroxide RhO_2, Rh_2O_3 and $Rh(OH)_3$ have been reported. It is believed that $Rh(OH)_3$ may be a hydrated

form of Rh_2O_3. Iridium oxides IrO_2, Ir_2O_3 and hydroxides: $Ir(OH)_3$ and $Ir(OH)_4$ has been reported. Rhodium and iridium are the first heavy transition elements that do not form oxo-anion complexes (Greenwood & Earnshaw, 1995).

Soluble rhodium sulphate, $Rh_2(SO_4)_3xH_2O$, is utilised for the electro winning of rhodium. Two forms, a yellow form that likely contains hexaaqua rhodium and a red form, which contains coordinated sulphate, has been distinguished (Seymour & O'Farrelly, 2006). Iridium and ruthenium have no reported sulphate complexes. Synthesis of rhodium sulphate is achieved via dissolution of $Rh(OH)_3.xH_2O$ in sulphuric acid (Renner, 2002). Chloride is known to be a much stronger ligand for Rh(III) than water or sulphate (Pletcher & Urbina, 1997b). It is believed that the hydroxide ion is a strong a ligand as chloride (Pletcher & Urbina, 1997b).

Four different rhodium sulphate solutions were prepared by Pletcher and Urbina (1997b), from golden-yellow rhodium hydroxide, rhodium sulphate, rhodium sulphate electroplating solution and a 20-year old industrial rhodium sulphate solution. The pH was adjusted to pH = 3.3 via sodium hydroxide and it was noted that no precipitates formed, even over several months' standing time. The NMR spectra reported implies the presence of various rhodium sulphate complexes (Pletcher & Urbina, 1997b).

The hexaaqua complexes of Ru(II), Ru(III), Rh(III) and Ir(III) are known to exist in solution, as well as selenides, tellurides (only Ir and Ru reported), and arsenides.

The complexation of other precious metals with chloride is well understood and is the most comprehensive source of aqueous OPM information. The discussion thereof might aid the interpretation of OPMs in sulphate solution.

The investigation of the replacement of a water molecule with a chloride ion on $Rh(H_2O)_6^{3+}$, $RhCl_4(H_2O)_2^-$ and $RhCl_5H_2O^{2-}$, the rate of reaction was wholly dependent on the amount of chloride ions coordinated. The estimated half-time would range from several months for $Rh(H_2O)_6^{3+}$ (k_{01}) to a few minutes for $RhCl_5H_2O^{2-}$ (k_{56}) at 25 °C (Baes & Mesmer, 1976).

A comprehensive mechanism and review of data for the anation and aquation of rhodium in chloride media is presented by Palmer and Harris (1975). Anation is the rate of replacement of an inner-sphere coordinated water molecule with a ligand, and aquation is the rate of displacement of a ligand with water in the inner coordination sphere. Figure 2-3 lists this reaction pathway with kinetic rate constants given for rhodium.

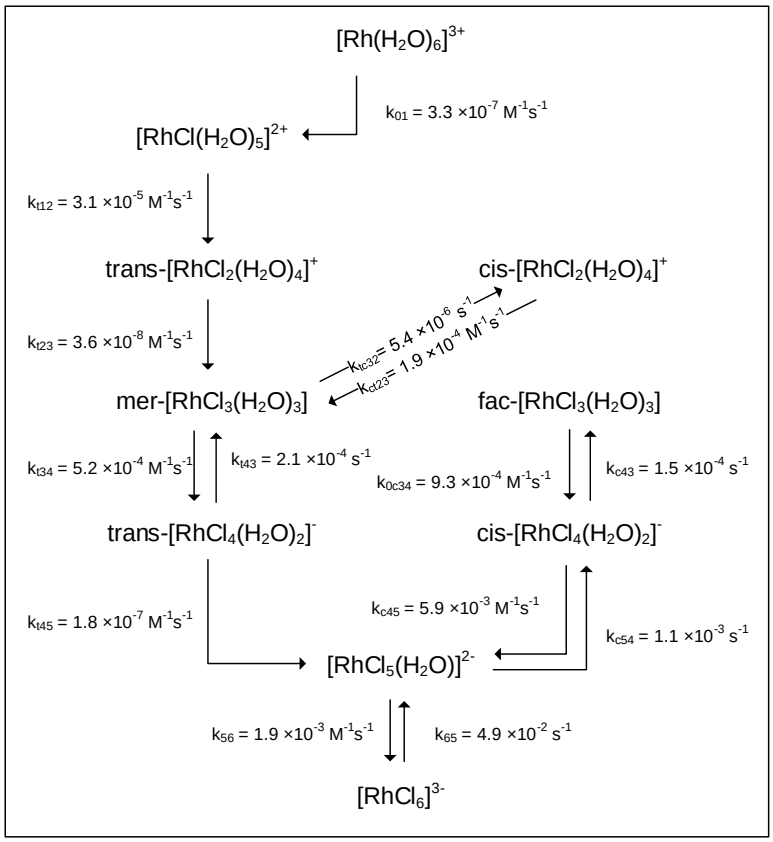

Figure 2-3: Reaction pathway and corresponding kinetics of hexaaqua Rh(III) to $[Rh(III)Cl_6]^{3-}$ with intermediate complexes at 50 °C. Diagram redrawn and data obtained from Palmer and Harris (1975).

Equations 2-1 to 2-4 present the rate equation interpretation for the anation of $RhCl_6^{3-}$ to aid the interpretation of rate constants. The kinetic rate constant subscript notation indicates the movement of chloride ions, e.g. k_{65} would be the rate constant for the aquation of $RhCl_6^{3-}$. The equilibrium constant for this reaction is given in Equation 2-5, with a_i the activity of each species. All anation reactions listed are first order with respect to the rhodium-chloro complex and aquation reactions are first order with respect to both the rhodium-chloro complex and the chloride concentration.

$$RhCl_6^{3-} + H_2O \overset{k_{65}}{\leftrightarrow} [RhCl_5H_2O]^{2-} + Cl^- \qquad \text{Equation 2-4}$$

$$K_6 = \frac{a_{RhCl_6^{3-}}}{a_{RhCl_5(H_2O)^{2-}} \cdot a_{Cl^-}} \qquad \text{Equation 2-5}$$

$$\frac{-d[RhCl_6^{3-}]}{dt} = k_{65}[RhCl_6^{3-}] \qquad \text{Equation 2-6}$$

$$\frac{d[RhCl_6^{3-}]}{dt} = k_{56}[RhCl_5H_2O^{2-}] \cdot [Cl^-] \qquad \text{Equation 2-7}$$

An illustration of same side (cis) and across (trans) ligand arrangements for ML_2 and ML_3 ligand substitution is presented in Figure 2-4. The constructed reaction pathway obeys the structural trans effect. Labialisation of the chloride ligands occur trans to another chloride in the octahedral arrangement. $[RhCl_5(H_2O)]^{2-}$ selectively undergoes trans labialisation to produce cis-$[RhCl_4(H_2O)_2]^-$, which in turn undergoes further trans labialisation to form fac-$[RhCl_3(H_2O)_3]$. fac-$[RhCl_3(H_2O)_3]$ does not undergo further labialisation and is considered very stable (Palmer & Harris, 1975).

The chloride ligand trans effect also governs the anation from hexaaqua rhodium. The rate of first anation is very slow, while second anation is comparatively faster. Further labialisation to mer-$[RhCl_3(H_2O)_3]$ is very slow, hindered by the trans effect.

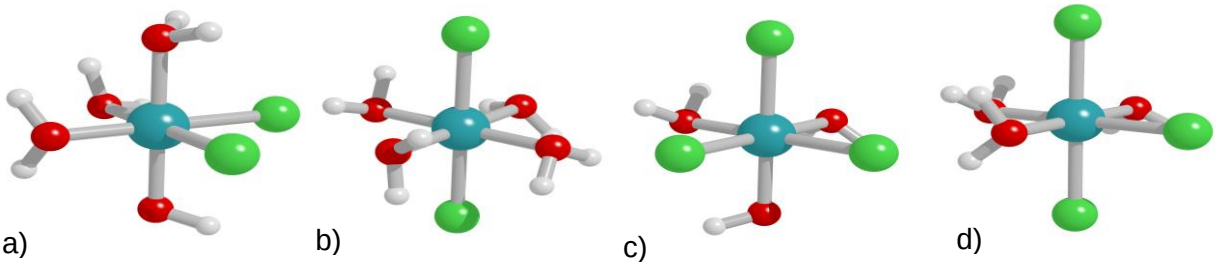

Figure 2-4: Isomer configurations of a) cis-ML_2, b) trans-ML_2, c) fac-ML_3 and d) mer-ML_3. Redrawn from Viljoen (2003).

The mer-$[RhCl_3(H_2O)_3]$ compound, can only undergo aquation of a chloride across an existing chloride ion and hence the formation of cis-$[RhCl_2(H_2O)_4]^+$ is favoured above that of trans-$[RhCl_2(H_2O)_4]^+$.

The reaction pathway of ruthenium is presented in Figure 2-5 at 25 °C. The ruthenium reaction pathway reveals that ruthenium does not adhere as strongly as rhodium to the trans effect. The reaction rates of ruthenium anation were correspondingly higher than rates of rhodium anation, even at lower temperature. The exception was the anation and aquation rate between cis-$[MCl_2(H_2O)_4]^+$ and mer-$[MCl_3(H_2O)_3]$ (M = Ru or Rh). mer-$[RuCl_3(H_2O)_3]$ could also aquate to trans-$[RuCl_2(H_2O)_4]^+$ and an equilibrium between mer-$[RuCl_3(H_2O)_3]$ and fac-$[RuCl_3(H_2O)_3]$ is observed.

Ruthenium's anation and aquation rates are generally faster than rhodium's anation and aquation rates, even at the lower temperature observed.

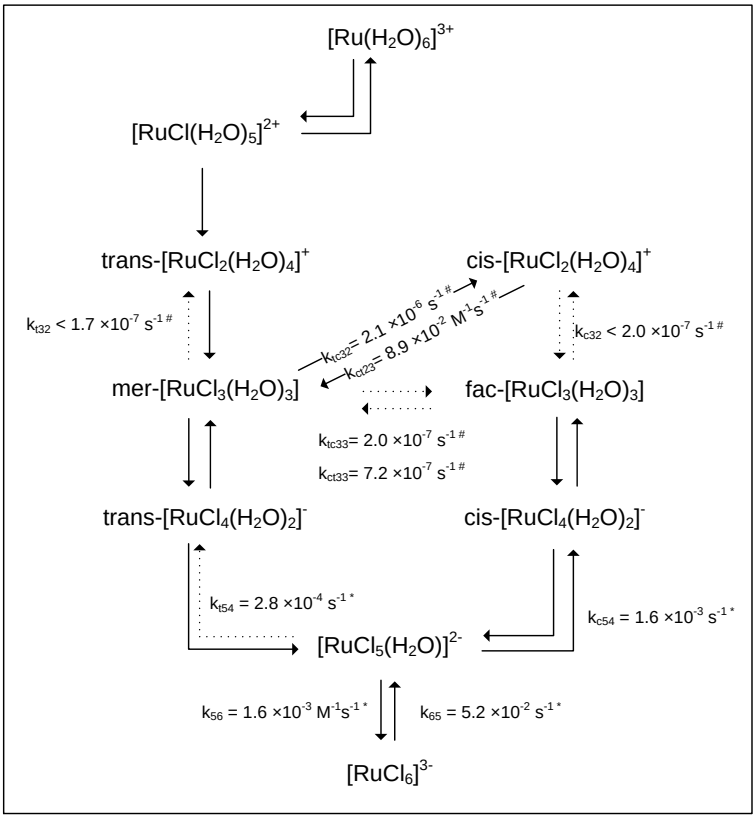

Figure 2-5: Reaction pathway and corresponding kinetics of hexaaqua Ru(III) to $[Ru(III)Cl_6]^{3-}$ with intermediate complexes at 25 °C. Diagram redrawn from Viljoen (2003) and data used: * - Viljoen (2003) and # - Connick and Fine (1960).

The reaction pathway for iridium-chloro complexation is provided in Figure 2-6. Poulsen & Garner's (1962) data could not be extrapolated and is presented at 15 °C. Other data is presented at 50 °C.

It is apparent that the rates of anation and aquation of iridium are several orders of magnitude smaller than the comparative rates of rhodium. The iridium complexes are very stable and anation and aquation rates are the slowest.

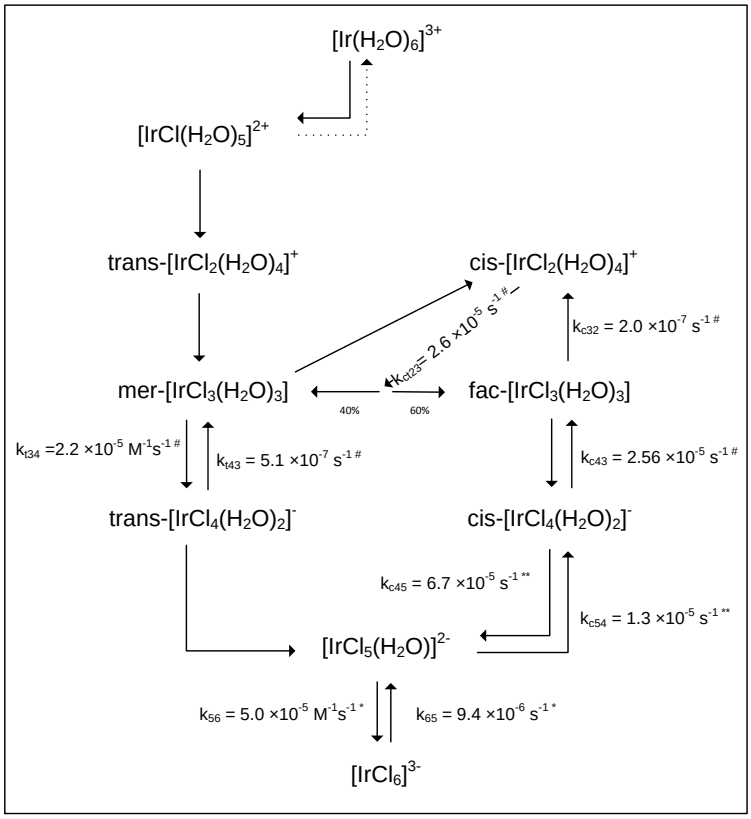

Figure 2-6: Reaction pathway and corresponding kinetics of hexaaqua Ir(III) to $[Ir(III)Cl_6]^{3-}$ with intermediate complexes. * - Poulsen and Garner (1962) at 15 °C, ** - Chang and Garner (1965) at 50 °C, #- El-Awady *et al.* (1967) at 50 °C.

An equilibrium distribution graph of ruthenium aqua-chloro complexes, as a function of the chloride content in solution, is given in Figure 2-7. 35 % $[RuCl(H_2O)_5]^{2+}$, 57 % $[RuCl_2(H_2O)_4]^{+}$ and 7 % $[RuCl_3(H_2O)_3]$ is predicted in 0.05 M Cl solution. The predominance of $[RuCl(H_2O)_5]$ would likely increase in solutions containing less than 0.05 M Cl solution.

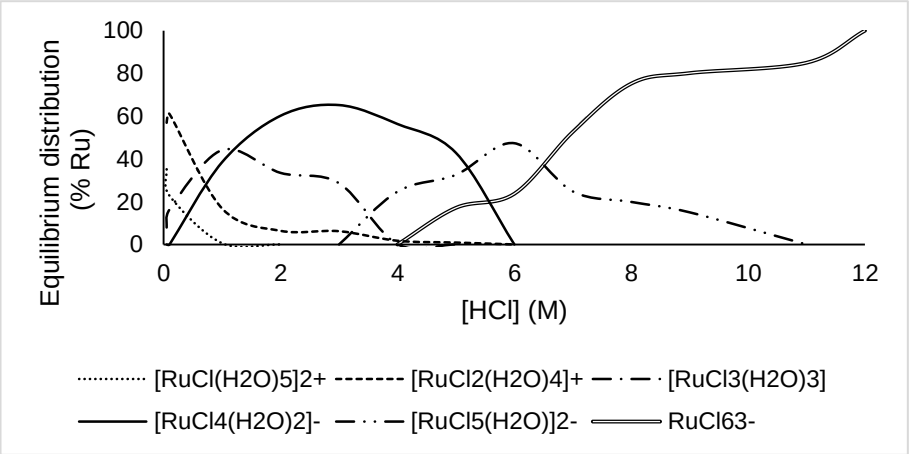

Figure 2-7: Equilibrium distribution diagram of ruthenium aqua-chloro complexes as a function of [HCl]. Redrawn from Connick and Fine (1960).

No information is present for the hydrolysis equilibria of Ru(II). The solubility of hydrated ruthenium oxide, $RuO_2.xH_2O$, is given as proportional to the square of the hydrogen ion between pH 1 to pH 3 (Baes & Mesmer, 1976). The hydrolysed species $[Ru(OH)_3]_x^{x+}$ is predicted from Ru(IV) solutions between pH 2 to pH 4 (Baes & Mesmer, 1976).

Hydrolysis reactions producing mononuclear compounds occur rapidly, and slow formation of polynuclear species can be expected for other platinum metals (Baes & Mesmer, 1976).

The formation of $RhOH^{2+}$ was studied by making rapid NaOH titrations at 25 °C (Equation 2-8) and a solubility product for $Rh(OH)_3$ of -33 was obtained, presented in Equation 2-9 (Forrester & Ayres, 1963). A value of – 37 is calculated from the free energies of Rh_2O_3 and Rh(III) presented in Goldberg and Hepler (1968).

$Rh^{3+} + H_2O \leftrightarrow RhOH^{2+} + H^+$; Log K = -3.4 Equation 2-8

$Rh(OH)_3 \leftrightarrow Rh^{3+} + 3OH^-$; Log K_{sp} = -33 Equation 2-9

The solubility of precipitated $Rh(OH)_3$ has in turn been determined in 1 – 7 M NaOH at 25 °C, as presented in Equation 2-10 (Ivanov-Emin, *et al.,* 1971).

$Rh(OH)_3 + OH^- \leftrightarrow Rh(OH)_4^-$; Log K = -3.9 Equation 2-10

No hydrolysis data for iridium was present in literature. Reviewers Baes and Messmer (1976) predict behaviour approximating that observed for Rh(III).

2.4. Iron precipitation

The fundamental chemistry of iron precipitation in hydrometallurgical processes is covered in three sub-sections. A generalised reaction mechanism for the precipitation of iron as a whole process is given by Grundl and Delwiche (1993).

$$Fe^{2+} \xrightarrow{Oxidation} Fe^{3+} \xrightarrow{Hydrolysis} Fe(OH)_n^{3-n} \xrightarrow{Precipitation} amorphous\ crystallites \xrightarrow{Aging} crystalline\ phase$$

First the oxidation of ferrous to ferric iron is discussed. Next the complexation and precipitation chemistry of iron with relevant precipitation mechanisms are discussed. Precipitation is essentially reactive crystallisation and the principles of nucleation and growth are particularly important to understand the variables that affect crystalline solid formation.

2.4.1. Ferrous oxidation

The reaction path for the oxidation of ferrous iron can be presented by the following set of equations (Dreisinger & Peters, 1989). First oxygen in the gas phase needs to diffuse over the gas-liquid interface according to Equation 2-11. Thereafter oxygen reacts with ferrous iron to oxidise it to the ferric state, which can be expressed as the overall equation as given in Equation 2-12. It has been established that the chemical reaction shown in Equation 2-12 is the rate determining step below temperatures of 150 °C (Singer & Stumm, 1970; Lowson, 1982; Nicol, 2006). A more comprehensive mechanism for ferrous oxidation was deducted for further reference by Colborn and Nicol (1973).

$$O_2(g) \rightarrow O_2(aq) \qquad \text{Equation 2-11}$$

$$4Fe^{2+} + O_2(aq) + 4H^+ \rightarrow 4Fe^{3+} + 2H_2O \qquad \text{Equation 2-12}$$

Several factors can influence the rate of ferrous oxidation. These factors include the ferrous iron concentration, oxygen partial pressure, temperature, pH, the presence of ligands and the presence of catalysts (Lowson, 1982).

The rate of iron oxidation can be presented by Equation 2-13 (Lowson, 1982). This rate equation depicts a dependency to the order α with respect to the ferrous iron concentration and a first order dependency on the partial pressure of oxygen, with α generally equalling 2 in highly acidic (0 < pH < 2) sulphuric acid solutions and 1 in less acidic to neutral solutions (3 < pH < 7). The ferric ion concentration generally does not inhibit the rate of oxidation (Lowson, 1982).

$$-\frac{d[Fe^{2+}]}{dt} = k[Fe^{2+}]^{\alpha} p_{O_2} \qquad \text{Equation 2-13}$$

Some researchers added additional concentration dependencies to account for the pH and anions present, as shown in Equation 2-14. A hydrogen ion dependency in highly acidic solutions and a hydroxide ion dependency in less acidic to neutral solutions yielded adequate experimental fits. Huffman and Davidson (1956) observed an increased reaction rate with the increase of solution pH.

$$-\frac{d[Fe^{2+}]}{dt} = k[Fe^{2+}]^{\alpha} pH^{\beta} p_{O_2} \qquad \text{Equation 2-14}$$

The pH-term in Equation 2-14 is used to represent a broad range of empirically fitted rate terms, such as the concentration of hydrogen or hydroxide ions or the concentration of the particular anion HCl, $H_4P_2O_7$, H_3PO_4 or H_2SO_4.

Three temperature regions of interest can be defined: a low temperature region between 20 °C to 50 °C and medium temperature region between 70 °C to 100 °C and a high temperature region: >

100 °C at elevated pressure oxidation. The oxidation of ferrous is typically very slow in the low temperature region and when the solution pH is below 2 (Lowson, 1982).

When elevated pressure, i.e. increased oxygen concentration, and temperature (> 100 °C) are employed, the reaction order of [Fe^{2+}] changes, the reaction rate drastically improves and both first and second order according to Equation 2-15. This rate equation was first proposed by Huffman and Davidson (1956).

$$-\frac{d[Fe^{2+}]}{dt} = k_1[Fe^{2+}]^2 p_{O_2} + k_2[Fe^{2+}]p_{O_2} \qquad \text{Equation 2-15}$$

In this highly acidic region, pH and acid dependence was not noted as significant. Mathews and Robins (1972) noted a slight decrease in reaction rate at lower acidities from pH 2 to pH 0.5 and denoted the order to hydrogen as $[H^+]^{-0.25}$.

In the less acidic pH region, the pH's effect on the rate becomes more pronounced. Considering sulphate acid mine drainage between pH 3 and pH 7, Nikishova *et al.* (1974) and Lowson (1982) along presents the following rate equation (Equation 2-16) being first order with respect to ferrous and oxygen, with dependency on the hydroxyl concentration. At pH > 5, the pH dependence was noted to be even higher with an order of -2 (Singer & Stumm, 1970).

$$-\frac{d[Fe^{2+}]}{dt} = k_1[Fe^{2+}]p_{O_2}[OH^-] = \frac{k_1 K_W[Fe^{2+}]p_{O_2}}{[H^+]} \qquad \text{Equation 2-16}$$

Of the possible catalysts for ferrous oxidation, the cuprous ion has the most prominent effect (Huffman & Davidson, 1956). Lowson (1982) lists reported effects of other possible catalysts, of which other elements present in the solution in question, notably, nickel, cobalt, sodium and arsenic, is orders smaller than the effect of the cupric ion and was therefore not taken into consideration. The occurrence of iron oxidation catalysis by means of cuprous ions can be described by Equation 2-17 and Equation 2-18 (Dreisinger & Peters, 1989).

$$Cu^{2+} + Fe^{2+} \leftrightarrow Cu^{+} + Fe^{3+} \qquad \text{Equation 2-17}$$

$$Cu^{+} + O_2 + H^{+} \leftrightarrow Cu^{2+} + HO_2 \qquad \text{Equation 2-18}$$

Depending on the various influencing conditions, several reaction orders and rate equations are presented in the open literature (Lowson, 1982; Dreisinger & Peters, 1989). Of all the possible literature sources, McKay's (1952) experimental conditions are in excellent agreement with the current study's conditions, with the exception that the pH environment is lower than the current study. McKay (1952) proposed the rate equation in Equation 2-19.

$$-\frac{d[Fe^{2+}]}{dt} = k_1[Fe^{2+}]^2 p_{O_2} + k_2[Fe^{2+}]^2 p_{O_2}[Cu^{2+}]^{0.5} \qquad \text{Equation 2-19}$$

The partial pressure of the vapours, formed from solution at elevated temperatures, needs to be accounted for. Rönnholm *et al.* (2001) proposed Equation 2-20 to account for the solution vapours.

$$p_{O_2} = P_{system} - \delta P_{H_2O}^{vap} \qquad \text{Equation 2-20}$$

P_{system} presents the system pressure, δ and empirical correction factor and $P_{H_2O}^{vap}$ the vapour pressure of water at the desired temperature. The correction factor δ is based on the weight fraction of sulphuric acid in the solution, from data presented by Sippola (1992), and can be expressed with Equation 2-21.

$$\delta = 1 + b_1 x_{H_2SO_4} + b_2 x_{H_2SO_4}^2 \qquad \text{Equation 2-21}$$

The solubility of oxygen in water can be expressed with Henry's Law in Equation 2-22 (Koretsky, 2004).

$$H_{O_2} = \frac{p_{O_2}}{M_{O_2}} \qquad \text{Equation 2-22}$$

H_i^T presents the Henry's Law constant of at temperature T, p_i the partial pressure and M_i = molarity of species i.

The most recent Henry's Law data for oxygen equals 0.0013 mol/kg.bar at 25 °C. $\frac{d\ lnH_i}{d\frac{1}{T}}$ is equal to 1500 K (NIST, 2011). The Henry's law constant can be temperature extrapolated with Equation 2-23 (NIST, 2011).

$$H_i^{T_2} = H_i^{298.15\ K} \exp\left(\frac{d\ lnH_i}{d\frac{1}{T}} \cdot \left(\frac{1}{T_2} - \frac{1}{298.15\ K}\right)\right) \qquad \text{Equation 2-23}$$

The theoretical solubility of oxygen in water was calculated for the nickel sulphate solution. The solubility, as a function of temperature, is provided in Figure 2-8. The oxygen solubility is progressively lower at elevated temperatures.

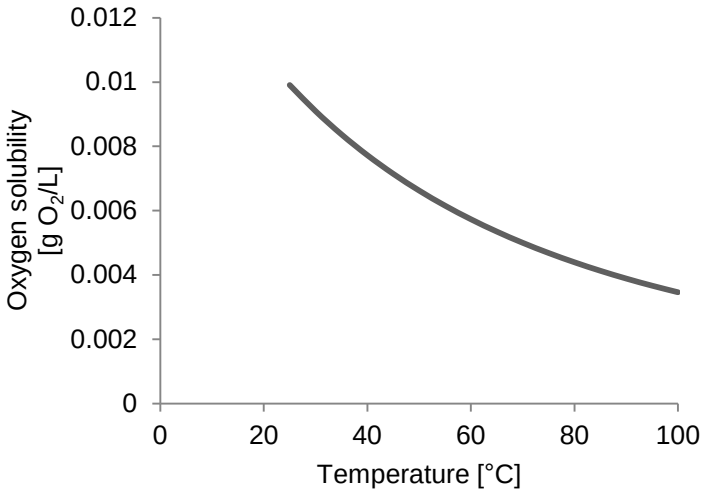

Figure 2-8: Oxygen solubility with nickel sulphate solution as a function of temperature.

2.4.2. Precipitation chemistry

The mechanism of ferric hydroxide and oxide iron precipitation is the result of the complexation of the ferric ion with hydroxide (OH^-) ligands in the acidic media (Faramanz *et al.,* 2005). The ligands occurring in the base metal solution include sulphate (SO_4^{2-}) and hydroxide (OH^-) species. The complexation of the hydroxide ligand will be discussed, followed by the complexation of the sulphate ion.

An ion predominance diagram of the iron-water system is provided in Figure 2-9. The two valence states are predominant, with their hydrolysed complexes predominant at specific EpH regions. The comparison of multiple species' hydrolysing boundaries is provided in Figure 2-10. Ferric is susceptible to hydrolysis above pH 2 and for ferrous above pH 6, depending on the metal concentration.

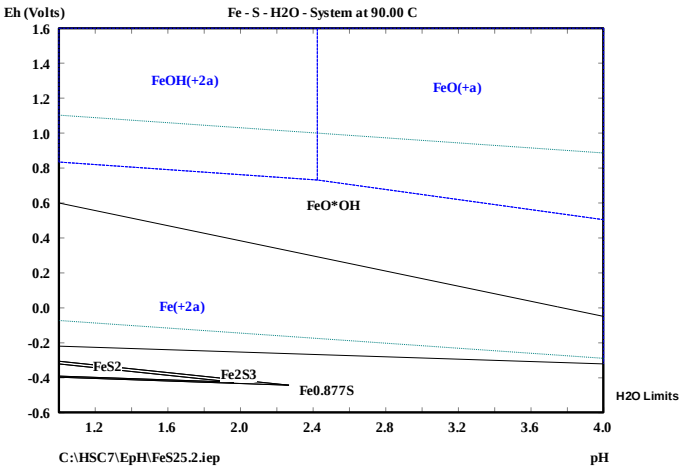

Figure 2-9: EpH and ion predominance diagram for the Fe-H_2O system at 90 °C. Drawn with HSC Chemistry

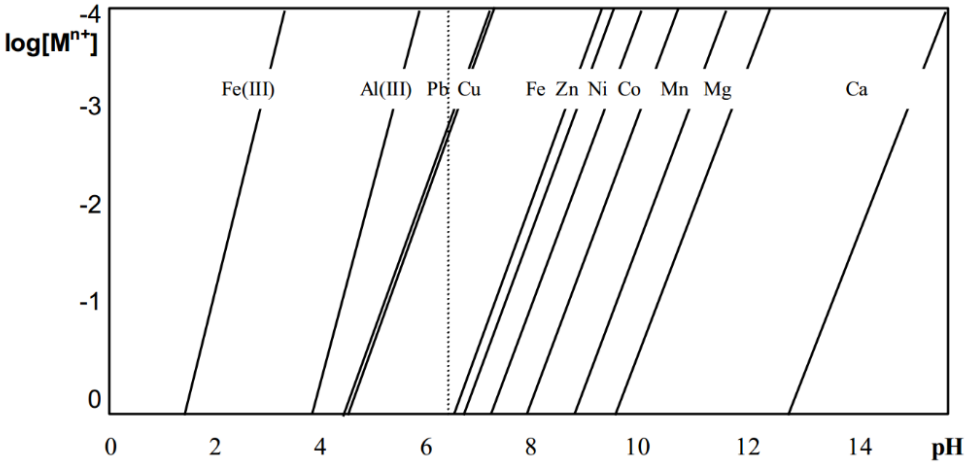

Figure 2-10: Solubility diagram of metal ion concentration over pH (Nicol, 2006).

In the aqueous solution, ferric exists in an aqua metal complex in octahedral configuration, which can be denoted as $[Fe(OH_2)_6{}^{3+}]$. Hydrolysis reactions, i.e. the ionisation of one adjacent water molecule, proceeds according to Equation 2-24 to Equation 2-26 (Nicol, 2006). The net reaction is provided in Equation 2-27.

$Fe(OH_2)_6{}^{3+} \leftrightarrow Fe(OH_2)_5(OH)^{2+} + H^+$, log K = 11.81 Equation 2-24

$Fe(OH_2)_5(OH)^{2+} \leftrightarrow Fe(OH_2)_4(OH)_2{}^{+} + H^+$, log K = 22.32 Equation 2-25

$Fe(OH_2)_4(OH)^{2+} \leftrightarrow Fe(OH_2)_3(OH)_3{}^{0} + H^+$, log K = 30 Equation 2-26

$\therefore\ Fe(OH_2)_6{}^{3+} \leftrightarrow Fe(OH_2)_3(OH)_3{}^{0} + 3H^+$ Equation 2-27

Dutrizac (1980) noted that dimerisation is predominant in more concentrated solutions ($[Fe^{3+}] > 10^{-3}$ M). Dimerisation is followed by olation, which entails the displacement of water molecules from adjacent hydroxyl complexes. The dimerisation reaction is provided in Equation 2-28 (Helm & Merbach, 2005). A proposed dimer is pictured in Figure 2-11.

$2Fe(OH_2)_6{}^{3+} \rightarrow (H_2O)_4Fe(OH)_2Fe(OH_2)_4^{4+} + 2H^+ + 2H_2O$ Equation 2-28

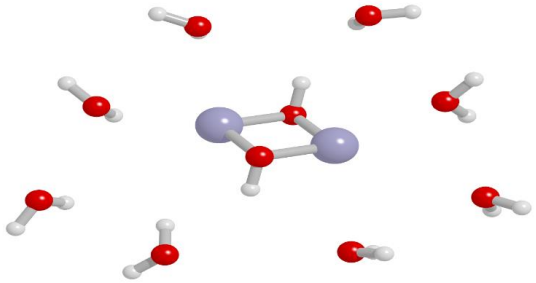

Figure 2-11: Ferric dimer linked by hydroxyl bridges, in aqueous solution (with • - Fe; • - O & • - H) (redrawn from Dutrizac (1980)).

The metastable hydroxyl-complex product of Equation 2-28 undergoes polymerisation, possibly by the displacement and ionisation of adjacent water molecules with other ferric monomers and oligomers to form longer iron-hydroxyl compounds, as illustrated in Figure 2-12.

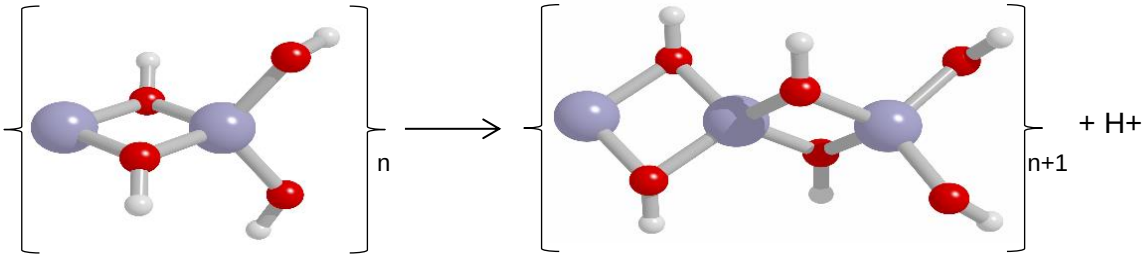

Figure 2-12: Simplified linear polymerisation of iron-hydroxyl complexes (redrawn from Dutrizac (1980)).

These polymers can incorporate other ligands into the structure, such as sulphate ions (Dutrizac, 1980). As the pH of the solution is increased, the higher presence of OH^- ions would favour further growth. It could even allow further hydroxyl-bridging between polymer strands. Inter-polymer hydroxyl bridging is illustrated in Figure 2-13.

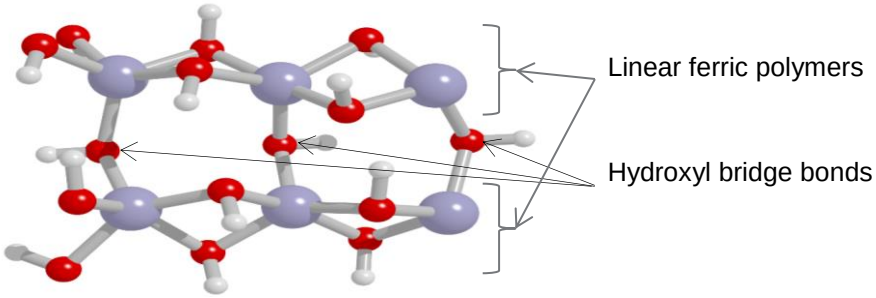

Figure 2-13: Hydroxyl bonding between linear polymers in a state of increased pH (redrawn from Dutrizac (1980)).

When insufficient OH^- ions are present in the solution, the linear polymers are increasingly bound with oxo-bridges, a process termed oxolation. A typical result of a polymer with both hydroxyl and oxo-bridges is shown in

Figure 2-14.

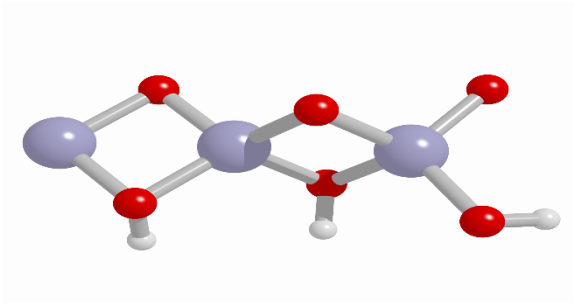

Figure 2-14: Oxolated polymer stand (redrawn from Dutrizac (1980)).

These polymer intermediate products discussed above are believed to be the precursors of iron hydroxide oxide solids.

The iron system in the presence of sulphate ions will now be discussed. Ferric–sulphate complexes are formed according to Equation 2-29 and Equation 2-30 (Cornell & Schwertmann, 2003).

$Fe^{3+} + SO_4^{-2} \leftrightarrow Fe(SO_4)^+$, log K = 4.04 Equation 2-29

$Fe(SO_4)^+ + SO_4^{-2} \leftrightarrow Fe(SO_4)_2^-$, log K = 5.38 Equation 2-30

Jiang and Lawson (2006) developed a mechanism for iron sulphate precipitation in the pH range of pH 1.5 to pH 2.2, temperature between 80 °C to 95 °C and at atmospheric pressure. The iron sulphate complexes in Equation 2-29 and Equation 2-30, would slowly form ferric sulphate intermediate products. $Fe(OH)SO_4$ or the evolved complex, $(Fe(OH)_2)_2SO_4$, is believed to be the precursor sulphate precipitation complexes. These complexes are formed according to Equation 2-31 and Equation 2-32.

$Fe(SO_4)(OH_2)_5^+ \leftrightarrow Fe(OH)SO_4(OH_2)_4^0 + H^+$ Equation 2-31

$2Fe(OH)SO_4(OH_2)_4^0 \leftrightarrow (Fe(OH)_2)_2SO_4^0 + SO_4^{2-} + 2H^+ + 6H_2O$ Equation 2-32

Jiang and Lawson (2006) denote that sulphate addition to ferric hydroxide complexes, an opposing mechanism, is probable. Ferric sulphate precipitation might be the result of ferric hydroxide complex formation with the increased substitution of sulphate ligands due to a lower pH and a higher SO_4^{2-} concentration.

Dimerisation and polymerisation of the basic ferric sulphate complexes can occur similar to presented above. Jiang and Lawson (2006) describes the intermediate complexes $Fe(OH)SO_4$ and $(Fe(OH)_2)_2SO_4$ as the unit complexes that reacts with available known alkali metals and other cations (M^+): Ag^+, H_3O^+, K^+, Na^+, NH_4^+ and $0.5Pb^{2+}$ to form synthetic jarosite according to Equation 2-33.

$$3(Fe(OH)_2)_2SO_4^0 + 2M^+ + SO_4^{2-} \leftrightarrow 2M(Fe(OH)_2)_3(SO_4)_2 \qquad \text{Equation 2-33}$$

Pre-cursor complexes and intermediate reaction routes to solid iron precipitates have been presented. The type of precipitate that forms depend on the conditions the solution is exposed to. The addition of excess base to a ferric system would lead to rapid growth of ionic complexes with insufficient time to spatially order the ions into a homogeneous crystal structure.

Thermodynamically stable iron solids are desired from precipitation systems. Several polymorphs of ferric hydroxide and oxide precipitates exist (Cornell & Schwertmann, 2003). The five natural polymorphs of iron hydroxide (FeOOH) include: goethite (α-FeOOH), akaganéite (β-FeOOH), lepidocrocite (γ-FeOOH), δ-FeOOH and feroxyhyte (δ'-FeOOH). Four iron oxide (Fe_2O_3) polymorphs also exist naturally: hematite (α-Fe_2O_3), β-Fe_2O_3, maghemite (γ-Fe_2O_3) and ε-Fe_2O_3. Goethite and hematite are the thermodynamically most stable species in their respective categories and commercial processes are based on the desired formation of these species. Jarosite is the thermodynamically stable iron sulphate precipitation product. The mineral names given throughout this text are used to refer to synthetic solid compounds with the same characteristics of the naturally occurring minerals, as is common metallurgical practice.

The three predominant commercial iron precipitation processes are the goethite, hematite and jarosite processes, which is summarised in Table 2-3 (Gupta & Mukherjee, 1990; Mazeina *et al.,* 2006).

Table 2-3: Commercial iron removal process comparison (Gupta & Mukherjee, 1990; Mazeina *et al.,* 2006).

	Goethite	**Jarosite**	**Hematite**
pH	2 – 3.5	< 1.5	> 1, up to 2 % H_2SO_4
Temperature [°C]	70 – 90	90 – 100	200
Anion	Any	SO_4^{2-} only	SO_4^{2-} only
Cation requirement	none	K^+, Na^+ or NH_4^+	none
Compound formed	α-FeOOH; β-FeOOH and Fe_2O_3	$MFe_3(SO_4)_2(OH)_6$	Fe_2O_3
Cationic impurities	Medium	Low	Low
Anionic impurities	Medium	High	Medium
Filterability	Good	Very good	Very good
Residual iron in solution [g/ℓ]	< 0.05	1 – 5	3
Relative capital cost	High	Low	Highest

During rapid hydrolysis, amorphous iron gels form. Cornell and Schwertmann (2003) term this product ferrihydrite. However if slow hydrolysis at elevated temperature occurs, also termed forced hydrolysis, akaganéite or the sulphate derivative, schwertmannite ($Fe_8O_8(OH)_x(SO_4)_y$) would form (Cornell & Schwertmann, 2003). These gels are undesired in precipitation processes due to its low filterability and the increased entrainment of metals (Gupta & Mukherjee, 1990).

2.4.3. Nucleation and growth

This section reviews the fundamentals of chemical precipitation. The work presented is based on monographs by Nielsen (1964) and Walton (1967), the recent review of Dirksen and Ring (1991), as well as Droppert's (1996) application thereof for atmospheric crystalline scorodite precipitation.

Precipitation is essentially reactive crystallisation, which relies on the reaction of two or more species in the aqueous phase to produce an insoluble product.

The driving force or energy barrier to the formation of stable nuclei is supersaturation. Two regions of supersaturation can be distinguished, the meta-stable region and the labile region. In the labile (unstable) region the degree of supersaturation is high enough to induce solid particle nucleation. The meta-stable region is at a state of lower supersaturation where spontaneous nucleation is no longer possible, but the growth of available solid particles may occur.

The effect of temperature on the solubility of the solid precipitate is an important factor. In most cases, the solubility of solid decreases with temperature. Evaporation is commonly employed to supersaturate the solution, prior to cooling. Only evaporation is employed in the case where solubility is not strongly affected by temperature. Heating is employed in the rare case of decreased solubility with temperature elevation. Elevated pressure may also be used to induce supersaturation. Other factors also affect precipitation reaction kinetics.

The Gibbs free energy of the aqueous to crystal phase transition can be expressed by Equation 2-34 (Pamplin, 1975; Dirksen & Ring, 1991).

$$\Delta G = \mu_i^{crystal} - \mu_i^{aq} \qquad \text{Equation 2-34}$$

μ_i^{α} is the chemical potential for species i, phase α.

The chemical potential of the crystal needs to be smaller than the chemical potential in the aqueous solution; in order for the phase transition to occur spontaneously. The Gibbs free energy, as a function of activity and its relation to saturation, is expressed with Equation 2-35 (Dirksen & Ring, 1991).

$$\Delta G = -RTln\left(\frac{a}{a_0}\right), with\ \frac{a}{a_0} = \frac{C}{C_{eq}} = S \qquad \text{Equation 2-35}$$

a is the activity of the solute species, a_0 is the activity of pure solute in equilibrium with a crystallised solid, C is the concentration of solute, C_{eq} is the equilibrium concentration of solute at T_{system} and P_{system} and S is the degree of saturation.

The solubility product (K_{sp}) of Equation 2-36 is given in Equation 2-37 when the system is in equilibrium. The ion activity product (IAP) is given in Equation 2-38 and the degree of saturation can be expressed in Equation 2-39. When S > 1, the solution is supersaturated.

$$A(aq)^+ + B(aq)^- \rightarrow AB(s) \qquad \text{Equation 2-36}$$

$$\mathrm{K}_{sp} = \left[A_{aq}^+\right]\left[B_{aq}^-\right] \qquad \text{Equation 2-37}$$

$$\mathrm{IAP} = \left[A_{aq}^+\right]\left[B_{aq}^-\right] \qquad \text{Equation 2-38}$$

$$\mathrm{S} = \frac{IAP}{K_{sp}} \qquad \text{Equation 2-39}$$

2.4.3.1. Nucleation

More than one theory has been developed to describe homogeneous nucleation. The nature of the clusters formed prior to precipitation is the basis of the validity for a particular model. The classical model describes a cluster which is predominantly formed by ionic interaction forces and is essentially a small “building block” or unit cell of the target nuclei. The other extreme, where ionic interactions are weak and the agglomeration of a cluster takes place as it occurs in the solution, can be described by non-classical models.

The classical model will best describe a unit cell of similar morphology of the end crystalline precipitate structure, while non-classical models might be better suited for an amorphous nucleation route. The classical model will be discussed, since crystalline nucleation is desired. For further reference to non-classical models, please refer to Walton (1967).

At a supersaturated state, the molecules of the solute associates with each other and form solute clusters termed embryos. These embryos, typically in the size range of ten to 10 000 molecules, continuously form and disperse. As the degree of supersaturation increases, the size of the embryos increases, up to the point where the critical embryo size of r^* for the particular system is reached. Upon reaching the supersaturated state at which r^* is overcome, a reduction in the systems Gibbs free energy is observed, resulting in the formation of a stable nuclei species in the solid phase.

The Gibbs free energy of the formed embryo is the difference between the Gibbs free energy due to interactions in the crystal lattice, termed the volume energy, and the Gibbs free energy caused

by the formation of new surface interfaces, termed the surface energy (Walton, 1967). The expression is given in

Equation 2-40 (Dirksen & Ring, 1991) and the behaviour of these free energies with increasing nuclei radii is given in Figure 2-15. The spontaneous nucleation of a crystal from aqueous solution is termed primary homogeneous nucleation.

$$\Delta G_{embryo,homo} = (\Delta G_{surface} + \Delta G_{volume}) = -\frac{V_{unit\ cell}}{v_{embryo}} k_b T ln(S) + \gamma_{CL}\, A_{unit\ cell} \qquad \text{Equation 2-40}$$

$V_{unit\ cell}$ and $A_{unit\ cell}$ are the volume and surface area of a unit cell, respectively. v_{embryo} is the molecular volume of the stable embryo, k_B is the Boltzmann constant = 1.38 x 10^{-23} m^2 kg s^{-2} K^{-1} and γ_{CL} is the free (interfacial) energy between crystal and solution per unit surface area.

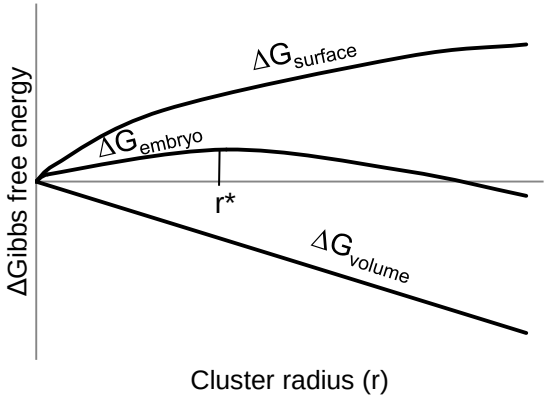

Figure 2-15: Gibbs free energy behaviour at S > 1 for primary homogeneous nucleation (redrawn from Dirksen & Ring (1991)).

The critical size is often as large as the unit crystal lattice of the solid phase and the relation between the degrees of supersaturation to the nuclei size radius is provided in Figure 2-16, indicating that a higher degree of supersaturation would induce smaller nuclei being formed. If the nucleus size decreases below that of a unit cell of the crystal, the risk of amorphous crystal growth increases, since the “blueprint” of the crystal is not clearly defined in the incomplete but stable unit cell. S^*_{homo} is the minimum critical supersaturation for homogeneous growth.

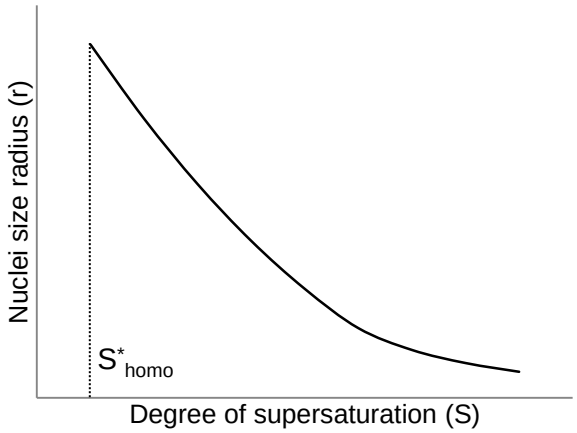

Figure 2-16: Nuclei size as a function of the degree of supersaturation (redrawn from Dirksen & Ring (1991)).

Primary homogeneous growth is the ideal form of nucleation of a crystalline solid. However, the effect foreign material has on precipitation is not addressed. In the presence of a foreign surface, such as reactor vessel walls, impellers and solid impurities within solution, primary heterogeneous nucleation can occur. The foreign material has a comparatively lower surface free energy to be overcome and therefore heterogeneous nucleation resultantly occurs at lower degrees of supersaturation.

The effectiveness of impurity particles differs and, once again, several theories are available to address the phenomenon. The Gibbs free energy of the heterogeneous embryo can be presented by Equation 2-41, as originally formulated by Turnbull and Vonnegut (1952), but adapted to be applied for any unit cell shape according to Dirksen's (1991) formulation. The unknowns, χ, γ_{CS} and γ_{SL}, and the complexities they entail would make this equation difficult to solve.

$$\Delta G_{embryo,hetero} = -\frac{V_{unit\ cell}}{v_{embryo}}(k_b T ln(S) + \chi) + (\gamma_{CL} + \gamma_{CS} - \gamma_{SL})\, A_{unit\ cell} \qquad \text{Equation 2-41}$$

χ presents the misfit of nucleus to substrate, γ_{CS} is the interfacial energy between crystal and (foreign) substrate per unit surface area and γ_{SL} is the interfacial energy between substrate and solution per unit surface area.

The early monographs studied by Nielsen (1964) and Walton (1967) gave no mention to secondary nucleation types. A more recent review (Dirksen & Ring, 1991) discusses secondary nucleation.

Secondary nucleation addresses the nucleation catalysed by already-present crystal structures of the same structural crystal form as the target precipitate. True secondary nucleation occurs

when the degree of supersaturation is higher than the critical supersaturation for a particular regime. In this case the already formed crystals would act as surfaces for the solution to nucleate upon, closely resembling and also difficult to distinguish from particle growth, which will be discussed later. Apparent secondary nucleation is a special case dealing with the physical handling of seed material, when small fragments of the seed is washed from the seed particle, which in turn acts as a lower-energy zone for subsequent nucleation. In both these types of secondary nucleation, the supersaturation is decreased after some time, but the initial critical boundary is not moved.

Contact secondary nucleation, the third type of secondary nucleation, in contrast occurs when external factors influence a meta-stable embryo, in order to form precipitates. A highly relevant example of such external factors is fluid transfer mechanics inside a vessel. When a growing particle comes into contact with external surfaces such as the walls of a reactor due to agitation, the embryo may be “plastered” onto the reactor wall. This subsequent build-up is expected to be the main factor behind industrial scaling of process units (Dirksen & Ring, 1991). Contact nucleation, due to the forced contact of the embryo with a foreign surface, further decreases the degree of supersaturation required and as can be envisioned, is a phenomenon observed at industrial scale. Fouling can theoretically occur in slightly supersaturated solutions, which would not nucleate spontaneously or in the presence of foreign material. Figure 2-17 indicates the relation between the different types of nucleation and their area of occurrence of each regime.

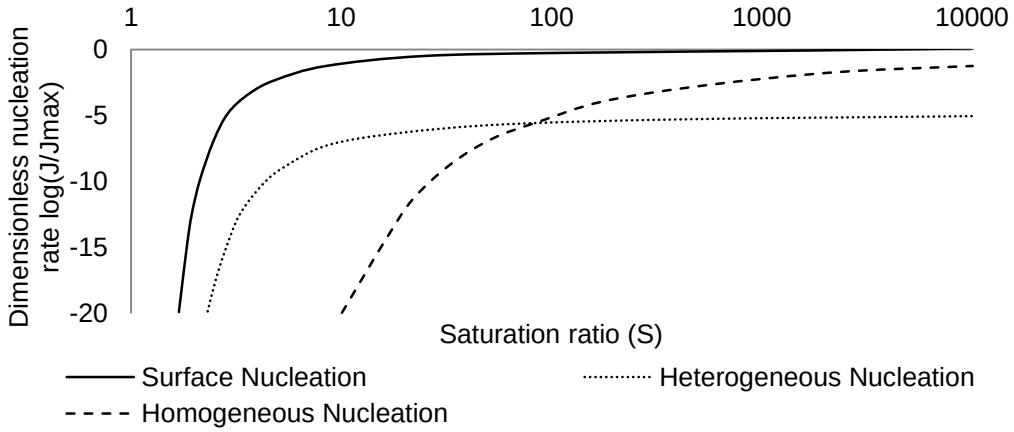

Figure 2-17: A generalised nucleation rate over the degree of supersaturation diagram (redrawn from Dirksen & Ring (1991)).

Figure 2-18 provides a graphical summary of each nucleation regime. Primary homogeneous nucleation is spontaneous from solution, provided a high enough degree of supersaturation is achieved. At high supersaturation, the stable precipitate unit cells become increasingly smaller, which might induce amorphous phase formation. Heterogeneous nucleation occurs in the inevitable presence of solid impurities at lower states of supersaturation and the crystal structure

might be distorted by the impurity substrates. Secondary contact nucleation occurs due to external effects onto the embryos-in-growth, which is also commonly believed to be a source of fouling in industrial situations.

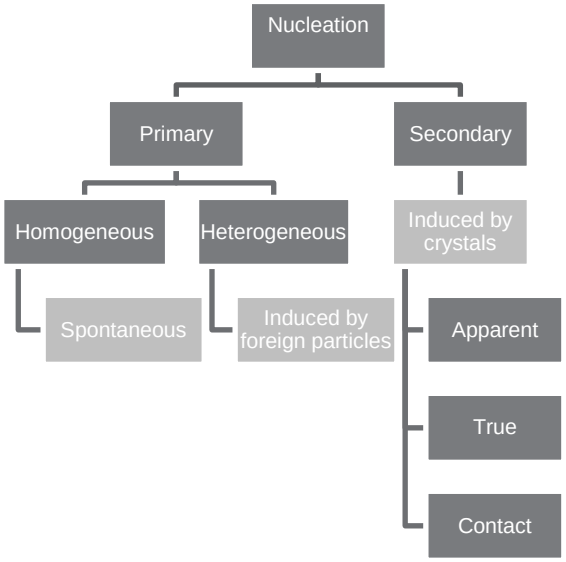

Figure 2-18: A summary of the different nucleation regimes.

The theory provided above considers a system where only one target solid species is precipitated, but in reality, especially the iron oxide system, multiple solid species can precipitate. Ostwald's step rule stipulates that the least stable (insoluble) species tend to form first and in this case, this is true for the less soluble, amorphous ferric hydroxide gels (Cornell & Schwertmann, 2003). The less stable species, given time, would morph into more stable species. The eventual transformation to goethite was noted during 54 day aging of iron residues containing ferrihydrite (Bazilevskaya *et al.,* 2012).

Hydrolysed iron polymers in aqueous phase are generally accepted to be the precursor of the colloidal (between 1 nm and 10 µm) unit cells of the solid precipitate (Dutrizac, 1980; Grundl & Delwiche, 1993; Rose & Waite, 2007). Several amorphous iron precipitate products were observed, for instance in neutralised nitric acid (Murphy *et al.,* 1976) and in acid mine drainage (Knight & Sylva, 1975). In less acidic, pH > 3 solutions, amorphous iron precipitation is expected due to the fractal nature of the precursor polymers (Rose & Waite, 2007). The fractal polymer growth is in turn induced by a higher OH^- to Fe^{3+} ratio in acidic media.

2.4.3.2. Growth

It is important to characterise the fundamental difference between crystal growth and heterogeneous and secondary nucleation. While nucleation is essentially controlled by the degree of supersaturation of the solute particles, which has a distinct starting saturation to

overcome, growth can occur at lower degrees of supersaturation states (Walton, 1967). The solvated ions or molecules can be directly incorporated into the present growth medium without the need to achieve a critical embryo radius. In order to clarify this phenomenon, further investigation of the mechanism of growth is required.

Epitaxial crystal growth of a crystal comprises of the following steps (Walton, 1967; Cornell & Schwertmann, 2003): First the solvated ions or molecules need to undergo bulk transport to the crystal surface. Thereafter adsorption onto the crystal surface–liquid interface and the subsequent diffusion over the surface needs to occur. The ions or molecules then undergo attachment onto an active growth site where it undergoes rearrangement for incorporation into the crystal surface. The rearrangement can be a result of reactions such as dehydration and dehydroxylation (Cornell & Schwertmann, 2003). Lastly solvents may be released via counter diffusion.

The mechanism is illustrated for a ferric monomer and its incorporation into a goethite crystal structure in Figure 2-19, indicating the steps: a) bulk transport and adsorption, b) diffusion to a step site, c) diffusion to a kink site and subsequent incorporation into the crystal and d) as a result of surface reaction, the release of solvents.

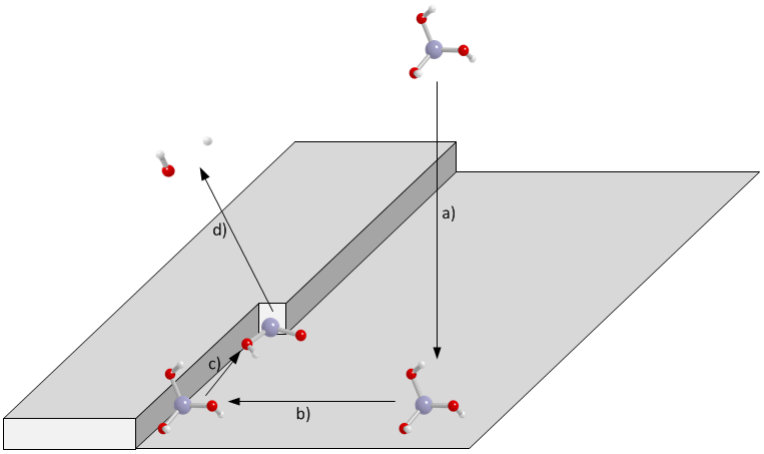

Figure 2-19: Proposed epitaxial growth mechanism for a ferric monomer onto goethite growth surface.

In order for epitaxial crystal growth to occur, dislocation sites are required. Solvated ions or molecules attach to “step”-sites, whereby two bonds are possible with the crystal surface (Dirksen & Ring, 1991). Diffusion over the step site to “kink”-sites, where three bonds are possible, leads to incorporation into the crystal. Dislocations can either originate from screw or step dislocations (not to be confused with step-sites) which is illustrated in Figure 2-20. In the presence of a “step”, i.e. an outer surface nucleus, sequential step growth would occur until a surface layer is completed and a new step would need to be nucleated in order for growth to continue. In the event of a crystal defect, of which many causes are possible, a screw dislocation would lead to a

winding, spiral growth regime. No further active sites are required in the event of screw dislocation growth, which could theoretically continue until growth media is depleted.

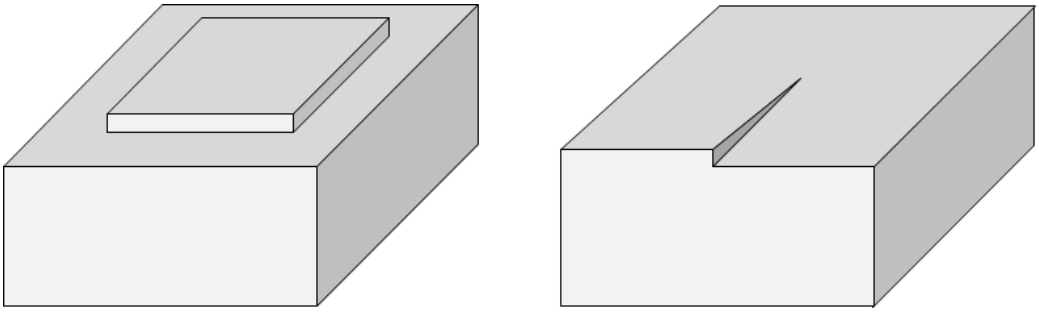

Figure 2-20: Step (left) and screw (right) dislocation crystal growth mechanisms for a cubic crystal (redrawn from Walton (1967)).

The growth mechanism would ultimately determine the morphology of the final crystal. Growth at relatively low supersaturation from a pure solution is expected to yield well-formed crystals (Dirksen & Ring, 1991). Although the growth rate is not limited to a critical supersaturation, it is still affected by supersaturation. Specific target crystals do not have distinct growth mechanisms, entailing that several mechanisms can yield the same crystal, making the quantification of a particular study hard to base on prior work. Bazilevskaya *et al*. (2012) observed the formation of two distinctly different goethite crystals in the same subsystem. Polymorphs were formed during crystal aging: one polymorph was needle shaped and the other had thick, cylindrical rods. Impurities have a significant effect on crystal growth.

With the complex factors aside, the epitaxial growth rate can be approximated to be linear with time at fixed super saturation (Walton, 1967). Growth of crystal particles may be controlled by mass transport limitations, for instance under low agitation rate conditions (Elwell & Scheel, 2011).

The introduction of seed material leads to no requirements for nucleation to occur, effectively lowering the required process conditions required to precipitate a particular solid. Dutrizac (1996) conducted batch work to clarify the effect of seed on jarosite precipitation. The amount of iron precipitation achieved within a fixed time is increased with increasing seed addition and the presence of seed material diminished the nucleation dead-time associated with jarosite precipitation. 78 % iron precipitated at the ratio of seed to initial iron of 0.3 and at typical commercial operating conditions (T = 98 °C, pH 1.5, 0.3 M Fe^{3+} & 500 min^{-1} agitation). Iron precipitation increased progressively to obtain a maximum of 96 % iron precipitation at the ratio of seed to initial iron of 6.0.

Crystal growth can also occur due to agglomeration (Droppert, 1996). Several configurations of agglomeration can occur. For instance seed material can agglomerate, as well as partial growth

embryos can agglomerate with each other and seeds. The different iron hydroxide intermediate steps, listed in Section 2.4.2, may be considered partial growth embryo's which can precipitate in a system of increased agglomeration.

2.4.4. Commercial Iron removal processes

2.4.4.1. Goethite process

Two variants of the goethite process were developed to facilitate iron removal in the zinc electrolyte industry. These variants were developed by Electrolytic Zinc Co., Australia (E.Z. Goethite process) (Patent No. AUS 424,095, 1970) and Vielle Montague S.A., Belgium (V.M. Goethite process) (André & Masson, 1973). The aforementioned processes rely on the state of iron in solution, be it in the ferrous or ferric oxidation states. In the E.Z. goethite process, ferric is continuously added to maintain the iron concentration at < 1 g $[Fe^{3+}]/\ell$. The V.M. process oxidizes ferrous at a controlled rate, which is precipitated thereafter. Reduction of ferric is required prior to the V.M. process, should iron concentration be too high. The overall reaction for goethite precipitation is given in Equation 2-42.

$$Fe_2(SO_4)_3 + 4H_2O \rightarrow 2FeO(OH) + 3H_2SO_4(aq) \qquad \text{Equation 2-42}$$

Both processes operate in a pH region of pH 2.0 to pH 3.5 and at a temperature range between 70 °C and 90 °C (Gupta & Mukherjee, 1990). Since the governing reaction relies on ferrous to ferric oxidation and forms free sulphuric acid, an oxidant and continuous pH neutralisation is required. Air is commonly used as the oxidant in the industry.

Davey and Scott (1976) independently reviewed the two aforementioned processes based on anion and cation contamination from synthetic solution containing 30 g/ℓ Fe and 15 g/ℓ cation, which the cations nickel, copper, cobalt, zinc and manganese investigated. Table 2-4 shows the iron removed utilising the two processes at pH 2.0 and pH 3.5. Overall better precipitation is achieved at a higher pH. V.M.'s iron removal is superior. A known disadvantage of the goethite process is the loss of valuable metals with the iron precipitate (Gupta & Mukherjee, 1990). Table 2-5 provides the extent of sorption of particular metals onto the iron precipitate for both processes and at pH 2.0 and pH 3.5. The E.Z. process co-precipitated the least amount of nickel and cobalt at pH 3.5, while the V.M. process co-precipitated its minimum nickel and cobalt at pH 2.0.

Table 2-4: Residual iron content [g/ℓ] after goethite precipitation according to the E.Z. and V.M. processes at 85 °C (Davey & Scott, 1976).

Process	pH	
	2.0	3.5
V.M.	< 0.02	0.0001
E.Z	0.2-1.1	0.1-0.4

Table 2-5: The sorption of cations onto the iron precipitate during the E.Z. and V.M. processes at 85 °C (Davey & Scott, 1976).

Procedure	pH	Ni %	Co %	Cu %
V.M.	2.0	0.3	0.37	5.8
V.M.	3.5	1.7	-	22
E.Z	2.0	0.25	0.1	0.5
E.Z	3.5	0.15	-	~ 20

2.4.4.2. Hematite process

The hematite process utilizes a high temperature of 200 °C and pressurized autoclaves to oxidize and convert iron to hematite. Equation 2-43 presents the overall hematite precipitation reaction.

$$Fe_2(SO_4)_3(aq) + 3H_2O \rightarrow Fe_2O_3(s) + 3H_2SO_4(aq) \qquad \text{Equation 2-43}$$

The solid product is a good source of iron with fewer impurities, but the unwanted formation of basic ferric sulphate becomes a risk when the sulphate levels are too high. The hematite process is a preferred iron removal method in the gold industry, due to the non-porous nature of the precipitate formed (Fleming, 2009). The precipitate does not absorb any gold.

2.4.4.3. Jarosite process

The jarosite process precipitates iron in an acidic environment (pH < 1.5) at either atmospheric pressure and temperatures from 90 °C to 95 °C, or at pressurized conditions and elevated temperatures between 100 °C to 180 °C. Equation 2-44 provides the overall reaction for jarosite precipitation.

$$3Fe_2(SO_4)_3 + 2NaOH + 10H_2O \rightarrow \qquad \text{Equation 2-44}$$

$$2NaFe_3(SO_4)_3OH_6(s) + 5H_2SO_4(aq)$$

Jarosite formation does occur at atmospheric conditions and room temperature, but is very slow with residence times up to 6 months (Gupta & Mukherjee, 1990). A high initial acid concentration

lowers the eventual iron precipitation. Seeding is a very important parameter in the jarosite process, with initial seed content linearly correlating to the rate of formation. Recycling of large seed particles is recommended to obtain an easily filterable jarosite precipitate. Seeding also extents the temperature and pH ranges in which jarosite precipitation would occur (Dutrizac, 1996).

A big advantage of jarosite processes is less entrainment of nickel and cobalt into the iron residues. Potassium jarosite residues contain approximately 1 % nickel and cobalt, while sodium and ammonium jarosite residues only entrain 0.4 % nickel and cobalt (Dutrizac & Chen, 2004).

2.4.5. Factors influencing iron precipitation

2.4.5.1. pH

The iron formation reactions produce free acid with the main reactions and therefore a neutralisation agent is required to maintain the pH. Current considerations of neutralising agents include NaOH, NH_4OH, $Ni(OH)_2$ and CaO. It is important to specify a neutralising agent that would not cause downstream contamination of the nickel sulphate crystals. In the case of contamination, the removal thereof to trace quantities should be achieved downstream of the iron removal step.

Davey & Scott (1976) used MgO to neutralise test work of the two original goethite processes, due to reported problems of jarosite precipitation when using alkali-hydroxide bases.

2.4.5.2. Residence time

Zinck (1993) reports that the iron hydrolysis equilibrium was reached within an hour at pH 3.0, 50 °C and with gradual NaOH addition to ferric solution. Davey & Scott (1976) reported that the iron equilibrium was reached within 3 h to 3.5 h at pH 3.0 and 85 °C.

The residence time in industry holding tanks can vary from 9 h – 15 h, as calculated from operational data. A residence time of 6 h is proposed for this study. It would be sufficient to obtain iron hydrolysis equilibrium.

2.4.5.3. Temperature

The goethite, jarosite and hematite processes operate at 70 °C to 90 °C, 100 °C and 200 °C, respectively (Gupta & Mukherjee, 1990).

It is not desirable to implement temperature changes in the plant. The process units involved are used to concentrate the nickel sulphate solution by means of evaporation of water from the solution.

The effect of temperature on iron precipitation in the range of interest might be very small. The effect of temperature over the range of 20 °C to 80 °C on an iron precipitation process coupled with acid mine drainage was investigated by Zinck (1993). The residual ferric content exponentially decreased from 15 mg/ℓ to 2 mg/ℓ at 60 °C. The residual iron content didn't drop lower than 2 mg/ℓ between 60 °C to 80 °C.

During jarosite precipitation, Jiang and Lawson (2006) reported insignificant spectral changes between solids synthesized at 80 °C and 95 °C.

2.4.5.4. Degree of agitation

Agitation has an effect on the nucleation and growth of precipitates. Slower agitation generally leads to larger precipitated solids (Bryson & Te Riele, 1987). During jarosite precipitation, agitation is required to suspend seeds, but the rate of agitation did not have an influence on precipitation rates (Dutrizac, 1996).

The holding tanks at WPL aren't agitated, yet 700-TK-090's recycle boil-off circuit would induce some agitation in the tank due to circulation.

2.4.5.5. Neutralising agent choice

Zinck (1993) reported that NaOH usage didn't cause any detectable natrojarosite precipitation; when used as a neutralising agent in acid mine drainage experiments.

The choice of a neutralising agent must not cause any contamination of the down-stream processes or induce any side reactions. The presence of alkali cations Na^+ and NH_4^+ might cause unwanted jarosite precipitation side reactions at process conditions. Noguira *et al.* (2009) also reported the formation of unwanted nickel amine precipitates using ammonia as a neutralising agent. Calcium additions formed insoluble calcium sulphate during neutralisation (Davey & Scott, 1976).

2.4.5.6. Oxidation

Agatzini *et al.* (1986) studied goethite precipitation from a synthetic solution containing 5 g/ℓ ferrous. Rapid ferrous to ferric oxidation by means of peroxide (H_2O_2) as oxidant led to > 99 wt.% removal at pH 3 and 90 °C. This was achieved in between 1.7 min to 20 min, depending on the

rate of peroxide addition. Residual iron content, at optimal conditions, was between 0.02 g/ℓ to 0.04 g/ℓ.

2.5. Arsenic precipitation

Arsenic is present in the nickel sulphate stream as an impurity. Arsenic is solubilized from the converter matte during the atmospheric and pressurised leaching stages. Arsenopyrite (FeAsS), present in converter matte, is oxidised by Equation 2-45 to produce the soluble arsenic complexes arsenic acid (H_3AsO_4) and arsenate ($HAsO_2$) (Fleming, 2009).

$$4FeAsS(s) + 2H_2O + 2H_2SO_4(aq) + 13 \leftrightarrow 2Fe_2(SO_4)_3(aq) + 2H_3As^{5+}O_4(aq) + 2HAs^{3+}O_2(aq) \quad \text{Equation 2-45}$$

The oxidation of As^{3+} (arsenous) to As^{5+} (arsenate) is normally done at elevated temperatures, in neutral to alkaline pH environments and in the presence of air or oxygen (Emett & Khoe, 1994). In acidic, sulphate solutions, strong oxidants are required for arsenic oxidation. Ferric ions are not strong enough to oxidise arsenous at 95 °C (Droppert, 1996). Arsenic complexes in hydrometallurgical solutions are detected as As^{5+}-complexes, suggesting that oxidation does occur in acidic systems (Jia & Demopoulos, 2008; Fleming, 2009).

An EpH diagram for the As-S-H_2O system, Figure 2-21, indicates the predominance of arsenic acid at pH < 2.5 and arsenate at pH > 2.5.

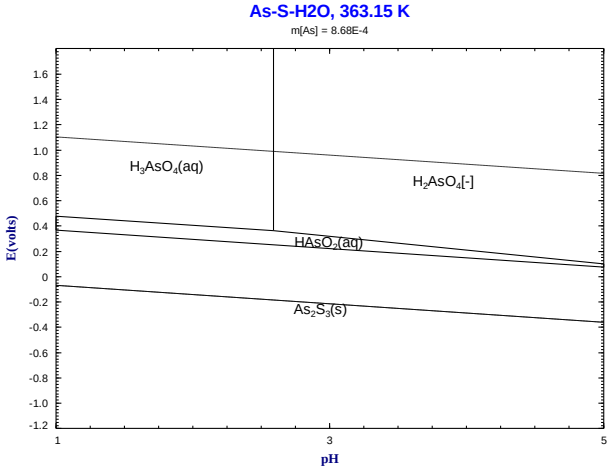

Figure 2-21: EpH diagram for As-S-H_2O at 90 °C, [As] =8.7x10^{-4} mol/kg. Drawn with Fact-Sage.

Arsenic would co-precipitate in an iron-precipitation circuit and be incorporated in the iron precipitate. Arsenate ions (AsO_4^{3-}) are reported to bond stronger to iron precipitates than sulphate ions (SO_4^{2-}) (Kendall, Madden, Madden, & Hu, 2013). Various Fe-As solid phases have

been reported, which highly depends on the Fe:As ratio. Relevant published literature with Fe-As systems, gold refractory leaching and in AMD, investigated Fe:As ratios in the vicinity of 1:1 to 11:1 (Dutrizac & Jambor, 2007; Pantuzzo *et al.,* 2008).

This work has a much higher Fe:As ratio of 38:1. Plasket and Dunn (1986) reports that arsenic could be reduced to below 1 ppm at a Fe:As ratio above 12:1; during neutralisation to pH 5.5 and at 12 h reaction times.

The formation of ferric arsenate in sulphate liquor is classically described by Equation 2-46 (Au-Yueng & Bolton, 1986).

$$3Fe_2(SO_4)_3(aq) + 2H_3AsO_4(aq) \rightarrow 2FeAsO_4(s) + 3H_2SO_4(aq) \qquad \text{Equation 2-46}$$

Scorodite, a crystalline version of ferric arsenate, is an attractive arsenic carrier mineral from an environmental perspective, due to its stability in dumping sites (Le Berre *et al.,* 2008). The formation of scorodite is governed by two equilibrium equations (Droppert, 1996). At a pH lower than 2, ferric and arsenic reacts to form crystalline scorodite ($FeAsO_4.2H_2O$) via Equation 2-47.

$$Fe_2(SO_4)_3(aq) + 2H_3AsO_4(aq) + 4H_2O \leftrightarrow 2FeAsO_4 \cdot 2H_2O(s) + 3H_2SO_4(aq) \qquad \text{Equation 2-47}$$

Between pH 2 and pH 6, equilibrium between scorodite and goethite is reached, which dissolves arsenic via Equation 2-48.

$$FeAsO_4 \cdot 2H_2O(s) \leftrightarrow Fe^{3+} + H_2AsO_4^- + FeOOH(s) \qquad \text{Equation 2-48}$$

2.6. Entrainment of cations into iron precipitate

Two factors play a role in the substitution of a foreign cation into a crystal structure namely the ion valence state and the ionic radius similarity between the foreign cation and the host cation (Goldschmidt, 1937). The relevant foreign cations present in the nickel sulphate solution that could possibly be included in goethite's octahedral crystal lattice are provided by Cornell and Schwertmann (2003). Table 2-6 provides the ionic radius length when the ion is coordinated in an octahedral lattice; along with the maximum predicted cation substitution of these particular cations.

Nickel, known to be scavenged in industrial iron precipitation operations, is detected to be an eligible cation substitute for goethite, akaganéite and hematite. Cobalt and lead substitution is also expected in goethite.

Table 2-6: The ionic radius and the maximum detected substitution of cations onto goethite

Cation	**Ionic Radius*** [nm]	**Maximum substitution#** [mol M/(mol Fe + mol M)]
Fe^{3+}	0.0645	-
Ni^{2+}	0.0690	0.06
Co^{3+}	0.0545	0.10
Cu^{2+}	0.0730	0.05
Pb^{4+}	0.0775	0.02
Rh^{3+}	0.0665	-
Ru^{3+}	0.0680	-
Ir^{2+}	0.0680	-

* - Source (Shannon, 1976) and references therein; # - Source (Cornell & Schwertmann, 2003).

The ionic radius and maximum observed substitution onto goethite are presented for ions of interest in Table 2-6. Singh *et al.* (2002) observed up to 5 mol% Ni^{2+} was substitutable onto goethite, which corresponds well with the 6 mol% substitution reported above. It is believed that in order to achieve charge neutrality, an OH^- ion is replaced with O^{2-} when Ni^{2+} is substituted with Fe^{3+} (Carvalho-e-Silva *et al.,* 2003). Co^{3+}, which has the same valence state as ferric, has the highest mol% inclusion. Figure 2-22 was constructed with the available data presented in Table 2-6. A correlation can be seen between the ionic radius (relative to ferric) and the maximum substitution for that cation, suggesting that the smaller the relative ionic radius, the higher the maximum substitution of the ion. Cobalt's maximum substitution potential is higher due to its similar valence with ferric.

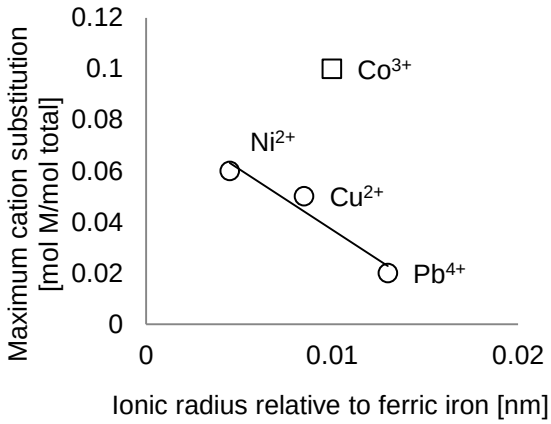

Figure 2-22: Comparison between the maximum cation substitution of a metal ion and its ionic radius relative to ferric.

It can be anticipated that other platinum metals, which are in the same valence state as ferric in solution and secondly have ionic radii closely resembling ferric, might be cation substituted into solid iron precipitates' crystal lattices.

The results of the above calculations are presented in Table 2-7. The maximum substitution of OPMs are several orders of magnitude higher than the quantity of OPMs present. All OPMs may potentially be cation substituted onto the goethite crystal lattice.

Table 2-7: Calculations for single cation substitution onto iron residue.

Ion	Relative ionic radius	Predicted maximum substitution	Mol metal substitutable	Max weight metal substitutable	Metals in solution	% metal substitutable
	[nm]	[mol M/mol M+Fe]	[mol]	[ppm]	[ppm]	[%]
Rh^{3+}	0.002	0.19	1.0E-02	1050	10	100%
Ru^{3+}	0.0035	0.18	9.7E-03	983	10	100%
Ir^{2+}	0.0035	0.07	3.3E-03	627	10	100%

Table 2-8 presents cation substitution calculations for the base metals. It predicts complete removal of copper ions with the residue, as well as the significant removal of half of the cobalt. Nickel removal of 0.2 % is predicted, which is considered lower than industry observations.

Table 2-8: Base metal cation substitution onto iron residue.

Ion	Maximum substitution	Mol metal substitutable	Molar weight	Max weight metal substitutable	Metals in solution	% metal substitutable
	[mol M/mol Total]	[mol M]	[g/mol]	[g]	[g]	[%]
Ni^{2+}	0.06	2.9E-03	58.69	0.17	103.1	0.2%
Cu^{2+}	0.05	2.4E-03	63.55	0.15	0.01	100%
Co^{3+}	0.10	5.0E-03	58.93	0.29	0.6	49%

Nickel and cobalt would hydrolyse and precipitate above pH 7.2 and pH 9.2, respectively (Nicol, 2006). Local basic "hot spots" may form in the case of insufficient mixing when a strong base, such as NaOH, is added. These hot spots may cause areas with high enough pH zones to hydrolyse and precipitate nickel and cobalt.

Amorphous iron precipitate, which is gel-like with known filterability problems, would also entrain some of the mother solution (Wang, 2012).

A correlation between nickel entrainment and pH is observed, whereas lower entrainment would occur at a lower solution pH. More nickel entrainment was observed in solutions with more iron. Iron removal test work from lateritic nickel resources, with 22.2:1 Ni:Fe content, reported 4.1 %

nickel entrainment between pH 2.5 and pH 3.0. This value rose to 15.9 % between pH 3.0 to pH 4.0 (Chang *et al.,* 2009).

Nickel entrainment is much lower at the lower pH range the jarosite process operates at. With the jarosite process, Dutrizac and Chen (2004) observed 0.4 % of both nickel and cobalt entrainment at a Fe:Ni ratio of 1:4 and Fe:Co ratio of 1:5. The experiments were conducted at 160 °C and at pH 1.6. The base metals were structurally incorporated into the jarosite structure.

The contamination of zinc onto goethite was shown to be proportional to the concentration of initial zinc in solution (Bryson & Te Riele, 1987). Nickel losses in the range of 3.5 % to 5.5 %, depending on the rate of oxidation was observed by Agatzini *et al.* (1986).

Impala Platinum BMR initially employed a goethite type process to remove iron and arsenic by raising the pH to pH 5.5 with aqueous ammonia and oxidisation with air (Plasket & Dunn, 1986). Nickel and cobalt were partially hydrolysed according to Equation 2-49.

$$MSO_4 + 2NH_4OH \rightarrow M(OH)_2 + (NH_4)_2SO_4$$ Equation 2-49

With M = Ni or Co. Base metal losses as high as 6 % were recorded and a three stage leaching circuit was required to recover nickel and cobalt from the precipitate.

CHAPTER 3 - THERMODYNAMIC INVESTIGATION

Pourbaix (EpH) diagrams are utilised to graphically display the thermodynamically predominant aqueous solution ions as a function of the solution's pH and electrochemical potential. HSC Chemistry 7.1, developed by Outotec, was employed to construct EpH diagrams at the conditions of this study. This study was primarily concerned with the precipitation of metals from solution. Likely species were hand-picked from the lists generated by commercial software, based on the probable interactions between ligands and metals. For example the precipitation of Fe_xS_y compounds are impossible since no elemental sulphur is present in the system. The usage of sulphur in EpH diagrams were primarily concerned with sulphate's complexation with metal ions.

The molality of each metal is given in Table 3-1, as calculated from operational data given in Table 2-1. All EpH diagrams in this section were constructed with 65 g/ℓ total metals solution, unless otherwise annotated. The concentrated 95 g/ℓ solution and original high nickel content solution (100 g/ℓ) were also investigated. The high nickel content solution has an identical composition to the 62.5 g/ℓ solution, only with higher nickel content. The total sulphur content was not known and needed to be estimated. Sulphate-containing salts (e.g. $NiSO_4.6H_2O$) were used in experiments to make up synthetic solution, listed in Table 4-2. The quantity of sulphate ions due to metal addition was calculated using stoichiometry. Typical residual free acid present after first stage leach operations of 1 g/ℓ was added to the calculated sulphate quantity (Bryson *et al.,* 2008).

Table 3-1: Molality for the first stage leach over flow liquor.

Metal	**100 g/ℓ solution** mol/kg	**62.5 g/ℓ solution** mol/kg	**95 g/ℓ solution** mol/kg
Ni	1.70	1.06	1.52
Cu	7.87E-04	7.87E-04	1.12E-03
S	1.85	1.18	2.70
Fe	4.48E-02	4.48E-02	6.40E-02
Co	1.10E-02	1.10E-02	1.58E-02
Ru	9.89E-05	9.89E-05	1.45E-04
Rh	9.72E-05	9.72E-05	1.42E-04
Ir	5.20E-05	5.20E-05	7.60E-05
As	8.41E-04	8.41E-04	1.24E-03
Pb	1.45E-08	1.45E-08	2.12E-08
Na	3.26E-02	3.26E-02	4.77E-02
Cl	2.54E-03	2.54E-03	3.71E-3

The following conditions were investigated:

- Temperature: 25 °C, 50 °C, 70 °C and 90 °C.

- pH: 1.0 to 4.0.
- E(V): -0.6 V to 1.6 V
- Total metals concentration: 65 g/ℓ, 95 g/ℓ and high nickel 100 g/ℓ solutions.

3.1. The Fe-As-Cu-S-H_2O system

The Fe-As-S-H_2O EpH diagrams were constructed for the temperature range of investigation and are collectively shown in Figure 3-1. Diagrams generated correlate well with published data of the Fe-S-H_2O system (Burkin, 2001). The goethite (FeOOH) thermodynamic stability region overarches the ferrous predominance region, as can be seen with the blue dotted lines in Figure 3-1 a) to d).

The thermodynamic stability region area of goethite increases with temperature. Goethite would be thermodynamically stable at a lower solution electrochemical potential at increasingly higher temperature from 25 °C to 90 °C.

The ion predominance stability regions of hydrolysed iron complexes increase with increasing temperature. The decrease in ferric ion predominance area is observed between 25 °C to 90 °C, as the first hydrolysed complex, $Fe(OH)^{2+}$, increases in predominance at lower pH with increased temperature. The dehydrated complex of the first hydrolysis complex, FeO^{+}, predominance also increases to the lower pH region with increased temperature.

The observations suggest that the predominant precipitate to be formed would be an iron hydroxide species: either goethite or meta-stable variants thereof. Hydrolysed iron complexes are predominant over iron-sulphate complexes (e.g. $FeSO_4^{+}$). No iron sulphate precipitates, i.e. jarosite or basic ferric sulphate type compounds, were thermodynamically stable. Arslan and Arslan (2003) noted a K-Jarosite region that was thermodynamically more stable than goethite at [Fe] = 1 mol/kg, [S] = 1 mol/kg and [K] = 0.1 mol/kg. At the significantly higher iron and alkali-ion concentration (compared to sodium in this study) the jarosite compound was thermodynamically stable at $0 < pH < 2$ and $0.7\ V < Eh < 1.2\ V$.

Arsenate complex ($(AsO_4)^{3-}$) co-precipitation with iron species would occur. No scorodite thermodynamic stability is observed, but the ferrous arsenate: ($Fe_3(AsO_4)_2$) becomes increasingly thermodynamically stable, with a larger area, at increasing temperature. Ferrous complexes with arsenate needs not to be oxidised to precipitate. At much lower total iron and arsenic content, Zhu & Merkel (2001) observed scorodite thermodynamic stability (over Goethite) between $3.5 < pH < 5$ and $0.5\ V < Eh < 1.0\ V$ at [Fe] = [As] = 10^{-6} mol/kg and ferrous arsenate stability at pH 7.0 onwards.

Notably hematite (Fe_2O_3) was removed from the species list: Hematite is only expected to form at higher temperatures under pressurized conditions (Gupta & Mukherjee, 1990). When goethite was also removed from calculations, $Fe(OH)_3$ was the thermodynamically stable solid presented in place of goethite.

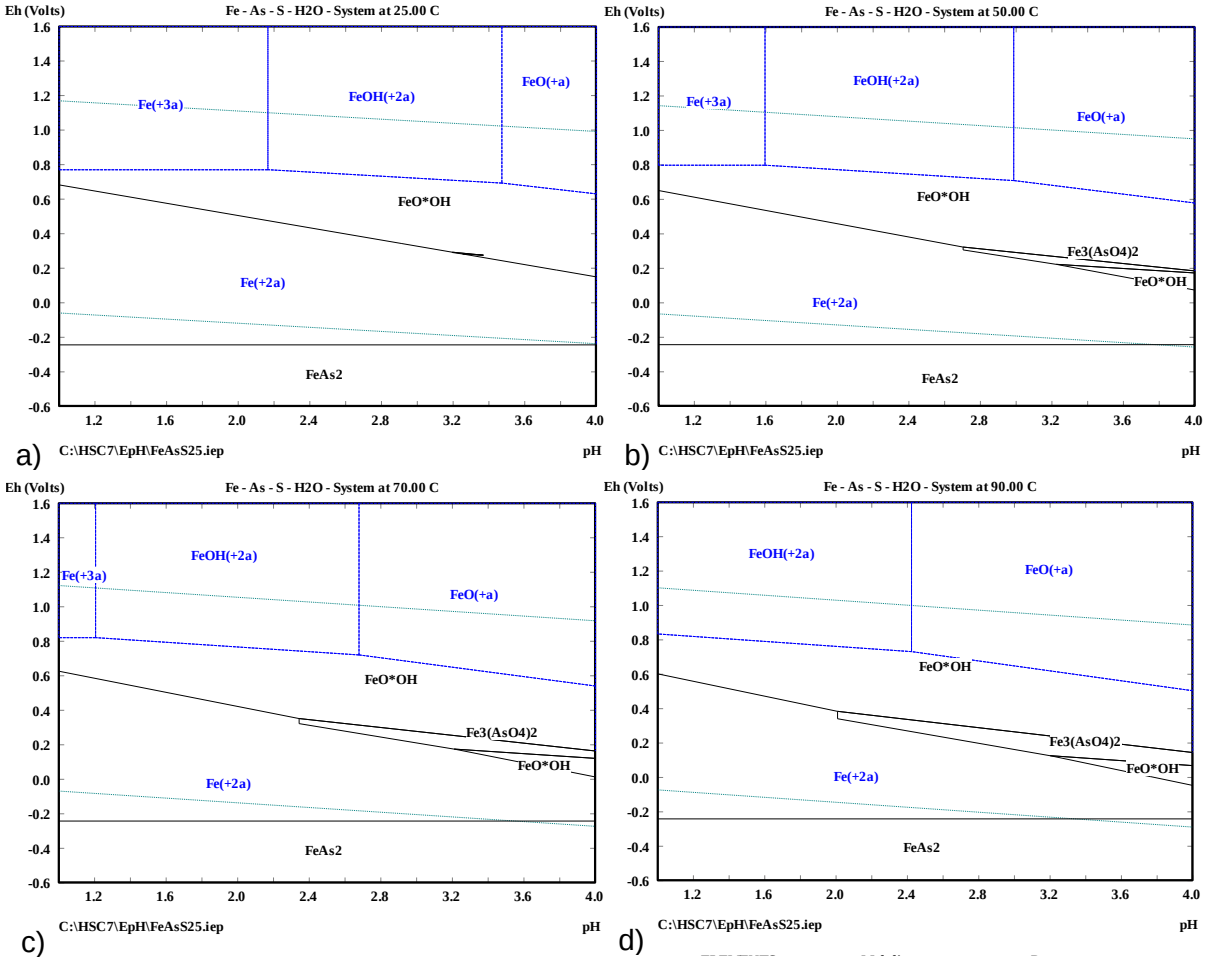

Figure 3-1: EpH diagrams for the Fe-S-H_2O system for a) 25 °C, b) 50 °C, c) 70 °C and d) 90 °C. 65 g/L: [Fe] = 4.48x10^{-2} mol/kg and [S] = 1.18 mol/kg. Predominant ions are shown with blue lines and the stability region for water with cyan lines.

The investigation area above was insensitive to total metals concentration increases. No difference in stability regions or ion predominance regions were observed when increasing the total metals concentration from 65 g/ℓ to 95 g/ℓ and comparing to the high nickel 100 g/ℓ solution.

Arsenic and copper have also been modelled to establish its possible precipitation and to identify the complexes involved. The As-S-H_2O system's EpH diagrams are presented in Figure 3-2 for variable temperature. No solid species are thermodynamically stable, except Arsenous oxide (As_2O_3). Two predominant complexes are observed, the arsenous acid $H_2AsO_3^-$ or $AsO(OH_2)^-$ and arsenic acid $H_2AsO_4^-$ or $AsO_2(OH)_2^-$. Complex stability is unaffected by temperature changes

(for all four temperatures investigated, 50 °C and 70 °C are not shown). Arsenic acid leads to the formation of arsenate complexes in the presence of metal ions, similar to the observations with ferrous above.

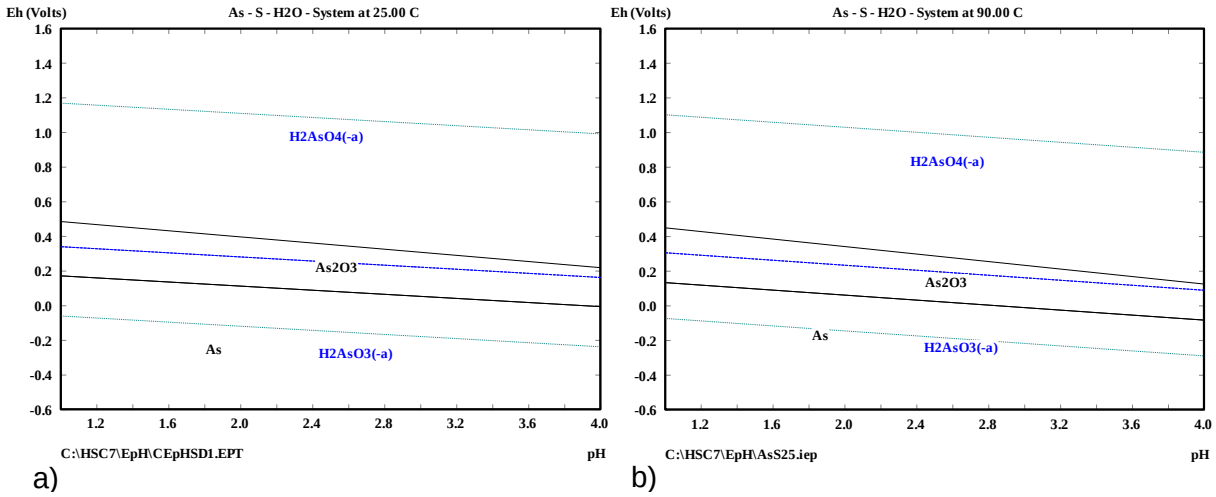

Figure 3-2: EpH diagrams for the As-S-H_2O system at a) 25 °C and b) 90 °C with [As] = $8.41x10^{-4}$ mol/kg.

EpH diagrams for the Cu-S-H_2O system are presented in Figure 3-3. The cuprous-cupric ion pair can act as an oxidising catalyst and the slight upward predominance shift detected, at 0.05 V with temperature increase, may impact its catalytic potential. Current understanding of OPMs in sulphate systems speculate that OPMs and copper behave similarly in the aqueous solution, therefore the behaviour of copper might imply similar behaviour with OPMs. Potential copper hydrolysis produced $Cu(OH)_2$ at pH 4.0 and 90 °C. Copper hydrolysis was not observed at 50 °C or 70 °C.

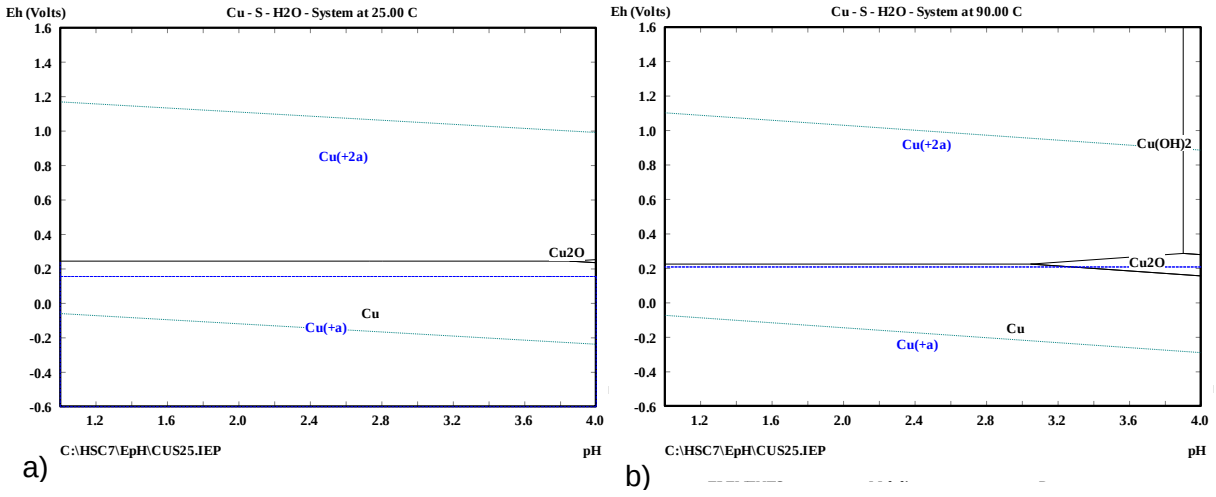

Figure 3-3: EpH diagrams for the Cu-S-H_2O system at a) 25 °C and b) 90 °C with [Cu] = $7.87x10^{-4}$ mol/kg.

3.2. The multi-element system

An extended model of the above evaluated the existence of other thermodynamically stable solids in the presence of the other elements: arsenic, copper, nickel, cobalt and sodium; using HSC Chemistry's EpH module with multiple elements selected.

Arsenate and arsenite complexes were thermodynamically stable at variable conditions of nickel, cobalt, copper and sodium. Figure 3-4 presents the mentioned arsenate and arsenite complexes for a) nickel, b) cobalt, c) copper and d) sodium. Cobalt, copper and sodium arsenite complexes are thermodynamically stable at the operating pH investigated. Nickel and cobalt arsenate are also stable. Copper arsenate is observed at pH 4.0.

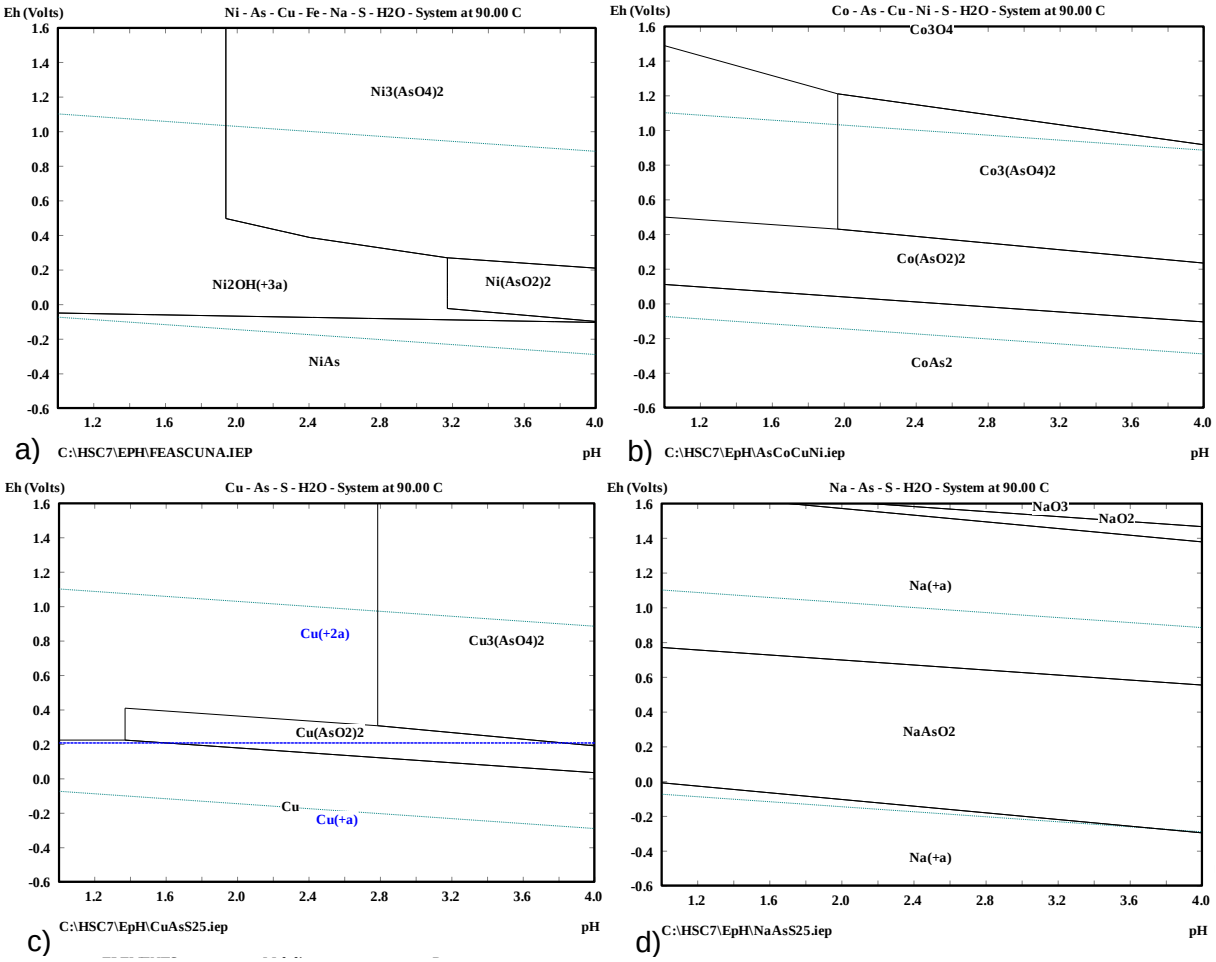

Figure 3-4: EpH diagrams of metals in the multi-element system at 90 °C. a) Ni, b) Co, c) Cu and d) Na.

The arsenic concentration is significantly lower than the concentration of base metals and iron. Although various metals indicated its thermodynamic stability as arsenite and arsenate complexes, the selectivity of arsenic is given in Figure 3-5. Cobalt is the favoured element at relevant conditions and therefore its complexes with arsenic are predicted above the complexes of other metals, including iron, in this system.

Figure 3-5 also shows the impact of increasing metals concentration from 65 g/ℓ to 95 g/ℓ: Copper and cobalt arsenate are more predominant at a lower pH as the metals concentration is increased. Similar temperature investigation revealed that if the temperature is increased from 25 °C to 50 °C, to 70 °C and to 90 °C, cobalt arsenate is the stable compound from pH 3.1, pH 2.6, pH 2.3 and pH 2.0, respectively. An increased temperature would favour the formation of cobalt arsenate.

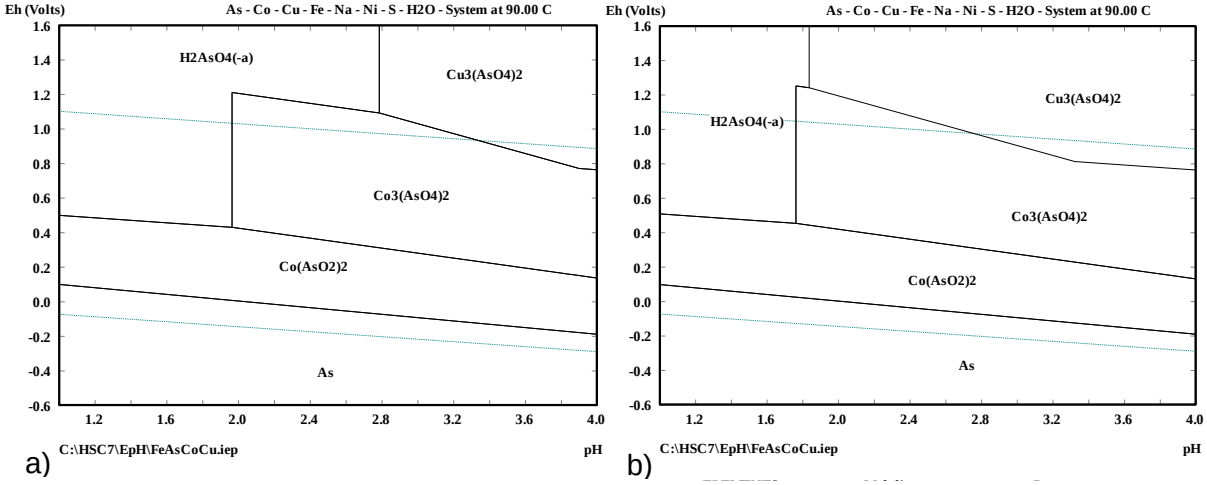

Figure 3-5: EpH diagrams of As predominance in the multi-element system at 90 °C. a) 65 g/ℓ and b) 95 g/ℓ total metal concentration.

3.3. OPM thermodynamic modelling

The other precious metals were thermodynamically modelled within the multi-element system. Figure 3-6 presents the resulting diagrams. HSC Chemistry has limited data on the OPMs and cannot predict predominant phases in the sulphate system. Only solid phases are predicted: OPM oxides are thermodynamically stable within the water stability region. When including the amount of chlorine added with the soluble OPM salts, Iridium chloride complexes: $IrCl_6^{2-}$ and $IrCl_6^{3-}$ are observed. No rhodium and ruthenium complexes were detected when modelling with Cl. Industrially chlorine is present in the water source.

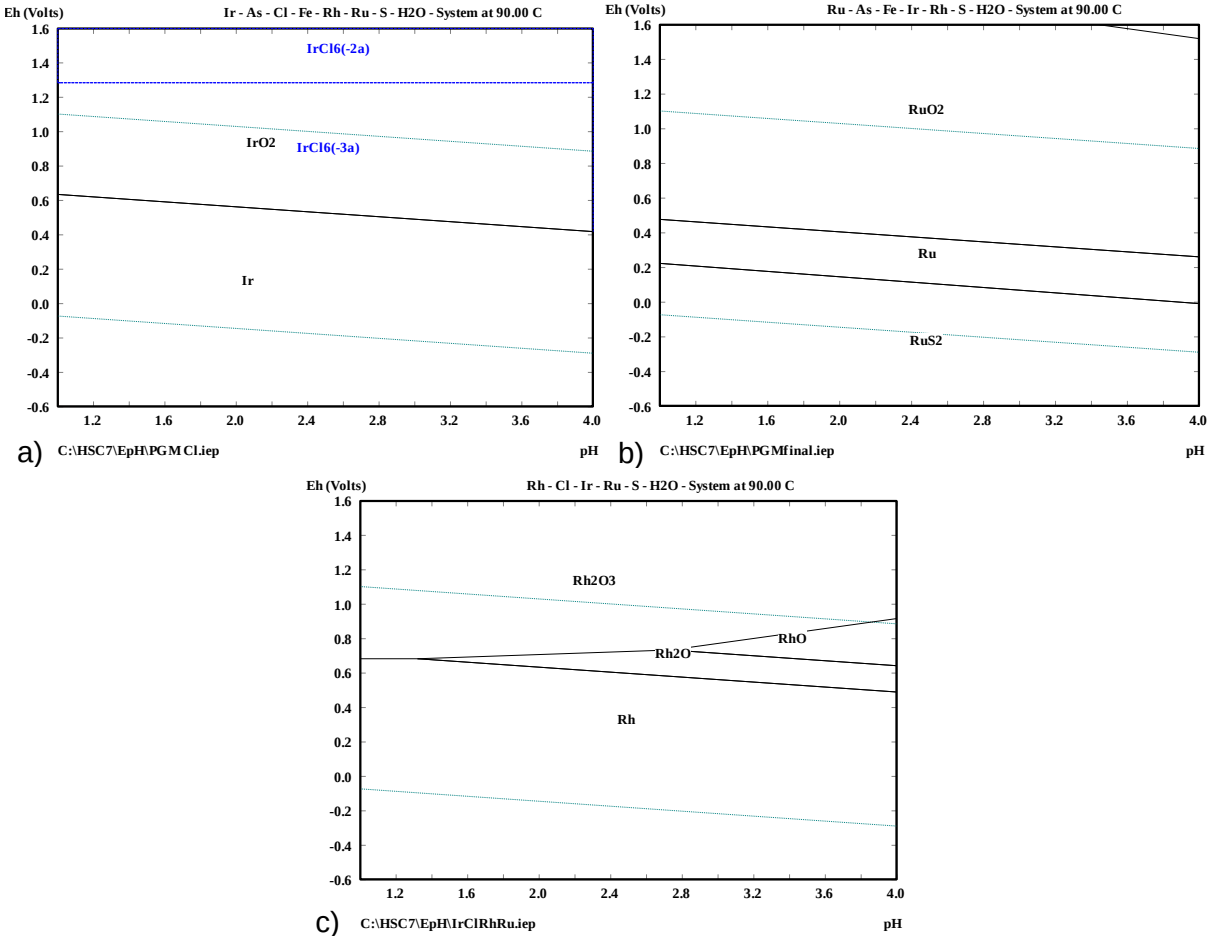

Figure 3-6: EpH diagrams for a) Ir, b) Ru and c) Rh in the multi-element system at 90 °C.

Modelling with all the elements in the multi-element system was done. No new complexes in the presence of base metals, arsenic or sodium were observed. No correlation could be observed between copper and OPMs' EpH diagrams. Fact-Sage 6.2 was also employed to construct EpH diagrams of the OPMs. The standard database, as well as SGnobl and FSnobl databases, were used. The additional databases contain additional data for precious and noble metals. No diagrams could be constructed for iridium or rhodium, whilst the ruthenium diagram consisted of RuO_4 in the range of investigation. RuO_4 synthesis, described by Pley and Wickleder (2005), requires strong oxidation ($KMnO_4$ used) unlikely to be present in this system and it is therefore unlikely.

Takeno (2005) reported EpH diagrams of ruthenium and rhodium at 25 °C with [M] = 10^{-10} mol/kg. The data suggests that ruthenium is stable as Ru^{3+} below pH 2 and $Ru(OH)^{2+}$ above pH 2 within the water stability region. In the upper water stability region, $Ru(OH)_2^{2+}$ is stable at pH < 2 and solid RuO_2 is stable at pH > 2.

Rhodium is shown to be stable as Rh^{2+} in solution from 0 < pH < 4 within the water stability region higher than Eh = 0.3 V. RhO^{+} is progressively more stable at the upper boundary of water stability region; at pH > 3.0.

Other precious metal predominant ions could not be fully established using EpH diagrams.

3.4. Ionic strength evaluation

The variation of total metals concentration would invariably lead to differences in the ionic strength of the solutions. The ionic strength would increase, also increasing the saturation index of certain metal ions in solution, making it more probable for them to precipitate. Thermodynamic modelling aided in the evaluation of the effect of varying total metals concentrations and concluded that no significant differences were observable for the mayor elements in solution. No significant differences in thermodynamic stability regions were observed and it is concluded that the total metals concentration solutions would not necessarily lead to more readable precipitation.

CHAPTER 4 - EXPERIMENTAL

4.1. Materials

Industry solutions were obtained whilst the plant was operational. Samples were taken at the sample port of the ultrafine filter (refer to Figure 2-2). A sample was taken during morning shift, filtered with 0.45 µm filters and heated up to the desired temperature for the commencement of experiments.

An additional aged industry solution sample was taken from the sampling port on outward pipe of 700-TK-020, after the solution stood in the tank for 21 days.

The composition of the synthetic nickel sulphate solutions are given in Table 4-1. The synthetic solution synthesized to the metals concentration of the industry solution, as provided in Table 2-1. 10 mg/ℓ of each OPM was used for the synthetic solutions, which is slightly higher than observed industrially. This was mainly done to improve the observation of OPM behaviour, as well as to be able to objectively compare the individual OPMs' behaviours. Preparatory experimental runs contained 100 g/ℓ Ni instead of 62.5 g/ℓ Ni. The reduction of the total metals concentration is discussed in Appendix B.

Table 4-1: The synthetic solution compositions.

	Total metals	Ni	Co	Fe	Cu	As	Rh	Ru	Ir
		g/ℓ	mg/ℓ	mg/ℓ	mg/ℓ	mg/ℓ	mg/ℓ	mg/ℓ	mg/ℓ
Synthetic solution	65	62.5	650	2500	50	65	10	10	10
	95	89.3	930	3570	70	93	14	14	14

Analytical reagent quality metal salts were used. Most salts were acquired from Kimix SA and Sigma Aldrich. Metal salt information is provided in Table 4-2.

Table 4-2: Metal salts used for synthesis.

Metal	Source	Grade	Purity
Ni	$NiSO_4.6H_2O$	Analytical Reagent	99 %
Cu	$CuSO_4.5H_2O$	Analytical Reagent	98.5 %
Fe^{2+}	$FeSO_4.7H_2O$	Analytical Reagent	98 %
Fe^{3+}	$Fe_2(SO_4)_3.xH_2O$	Technical grade	97 %
Co	$CoSO_4.7H_2O$	Analytical Reagent	99 %
Rh	$RhCl_3.xH_2O$	No specification	38-40 % Rh
Ru	$RuCl_3.xH_2O$	Reagent plus	38-42 % Ru
Ir	$IrCl_3.xH_2O$	Reagent grade	Not given
As	As_2O_3	Analytical Reagent	> 99.8 %
Na	NaOH	Analytical Reagent	> 99 %

Goethite and hematite seed material were obtained from Sigma Aldrich. The specifications are provided in Table 4-3. . Hematite as supplied by Sigma Aldrich: “Iron (III) oxide, < 5 µm, ≥ 99%” has been previously used as iron precipitation seed material (Webster *et al.,* 2011).

Table 4-3: Seed material specifications.

Mineral	**Structure**	**Supplier specifications**	
		Purity	**Particle size**
Goethite	α-FeOOH	30 – 63 % Fe	not given
Hematite	α-Fe_2O_3	≥ 99 % Hematite	< 5 µm

The method of synthesis developed is given for 500 mℓ solution. 300 mℓ reverse osmosis (RO) water was poured into a slow-stirring beaker. NaOH was added to raise the pH, in order to dissolve arsenic. Arsenic was then added in the form of arsenic oxide, As_2O_3 and a waiting time of approximately 15 min was sufficient for dissolution. Sulphuric acid was used to lower the pH to 3.0. Nickel, cobalt, copper and the OPM salts could then be added without risk of hydrolysis of the particular metals. The OPMs readily dissolved, iridium had a dark brown colour. The solution was then diluted closer to 500 mℓ and further acidified to pH 1.7 prior to iron addition. The solution was stirred for a few hours, if not left overnight, to dissolve all the metals. The solution was transferred to a graduated cylinder and the required make up water to yield 500 mℓ was added.

The mass salt required to add the metal quantity desired is given in Equation 4-1.

$$wt_{salt} = wt_{metal} \frac{M_{salt}}{M_{metal}} \div purity \qquad \text{Equation 4-1}$$

wt_{salt} is the calculated amount of salt required (g), wt_{metal} the desired amount of metal in solution (g), M_x the molecular weight (g/mol) of salt and metal and purity the fraction purity listed by the manufacturer of the salt.

The measured oxidation-reduction potential (ORP) of 366 mV for industry solution and 354 mV for synthesized solutions were in perfect agreement, as given at 90 °C. The stability of ORP observed over time in the industry experimental and the close agreement with ORP of the synthesized solution enables effective comparison between the thermodynamic model and the experimental results, particularly for work done after the preparatory experimental, in the absence of peroxide addition. ORP was measured with a standard Pt – Ag/AgCl probe, of which calculation of Eh = ORP + 200 mV.

4.2. Experimental equipment

The industry experimental setup is given in Figure 4-1. The setup consisted of 500 mℓ reaction vessels with side sampling ports. FMH hotplates with magnetic stirrers and Liebig condensers were used.

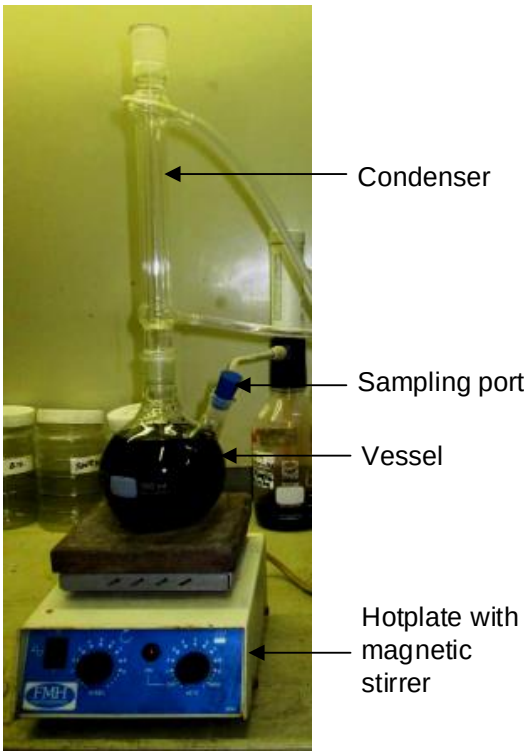

Figure 4-1: Industry experimental setup.

Two identical 105 mm diameter, 1.6 ℓ glass vessels with a multi-port hood, manufactured by Glaschem (Pty) Ltd., were used for all the synthetic experimental work. Four-finned, epoxy-coated baffles, coated by Plastisan (Pty) Ltd., were used in order to prevent vortex formation. The experimental solution occupied 500 mℓ of the vessel. The synthetic experimental setup is pictured in Figure 4-2.

LAB-smart MS-H-Pro+ hotplates with magnetic stirrers were used to heat up and stir the solution; a Pt-100 temperature probe provided the input to the hotplate feedback temperature controller, which controlled the solution temperature to within 2 °C of the set point. Agitation was set to 600 rpm throughout all experiments.

The pH probe was connected to a Eutech Alpha pH 560 pH controller to enable continuous pH monitoring. The pH probe had an operational temperature range of 0 °C to 130 °C, pH range from pH 0 to pH 14 and could compensate for electrical interference. A Liebig condenser was used to reflux and prevent boil-off of experiment solution. The condenser was coupled to an ice-cooled bucket. Two identical setups were used.

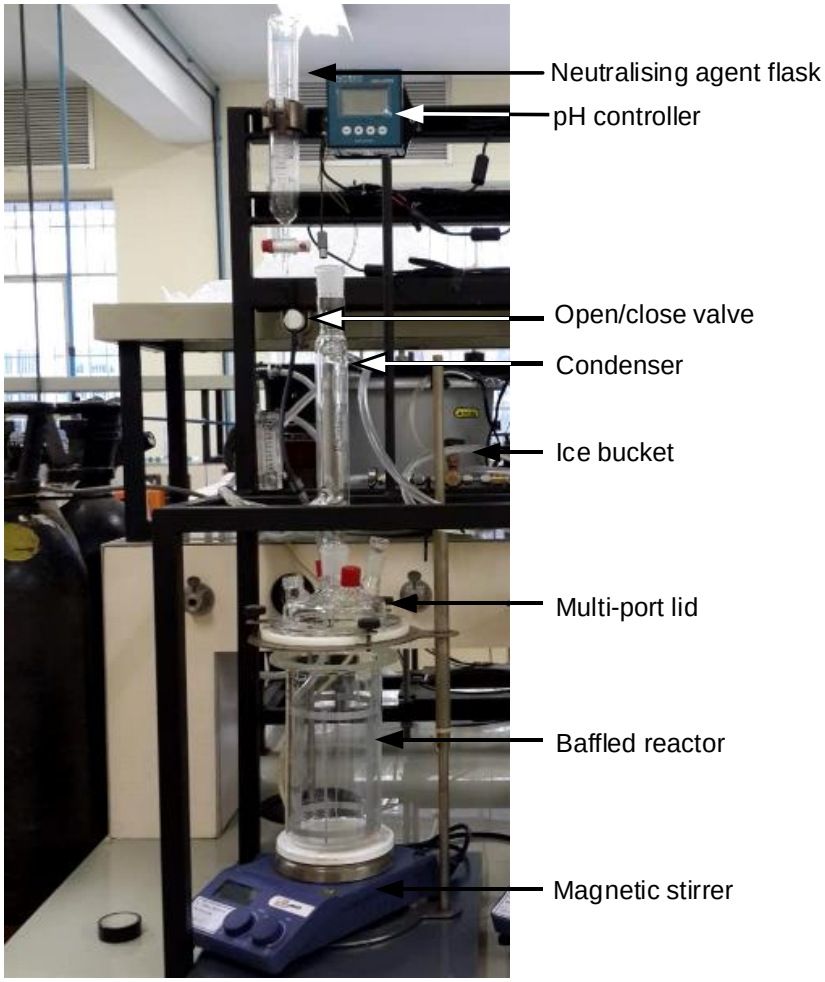

Figure 4-2: Experimental setup for synthetic experiments.

4.3. Experimental design

The synthetic experiments' method is described. The experimental method was developed from that of to that of other researchers' work, notably Dutrizac's (1996). The pH probes were 2-point calibrated with fresh buffer solution. The synthetic solution and the stirring pellet were added to the glass vessel and the vessel enclosed. The desired rotation speed and temperature were set on the magnetic stirrer. The ice bucket pump was started. The required neutralising agent solution and seed material were measured off. When the desired temperature had been reached, the zero-time sample was taken and afterward the seed material added followed by the addition of neutralising agent.

4.5 mℓ samples were taken, inline-filtered using a 0.22 µm syringe filter, cooled and lastly diluted with 0.1 M H_2SO_4 (1 mℓ H_2SO_4 per 3 mℓ sample) to prevent further reactions from taking place. During each sample taken, the pH was also recorded. The solution was filtered after each experiment and the solids were kept. The solids were water washed and dried.

The industry experimental method is similar in most aspects. Except that in-line filtration was done via a Buchner funnel with 0.45 µm membrane filters and the immediate dilution with H_2SO_4 was not done during the industry experimental. The pH was recorded before and after an experiment during the industry experimental.

Neutralisation, where applied, was done via the rapid addition of the required amount of caustic soda solution to reach the desired starting pH. The neutralising agent flask was used, which allowed consistent addition of base between experiments. The amount of caustic soda was determined experimentally by titrating the synthetic solution with caustic soda, as given in Appendix C.1.2.

4.4. Research design and methodology

The construction of EpH diagrams of the industry and synthesized solutions allowed identification of solid compounds that are likely to form under industry conditions. The EpH diagrams also shed light on the literature investigated, since the probable reactions and complexes could be clearly defined.

Overall five experimental phases were conducted and are defined as the 1) Industry, 2) Preparatory, 3) Screening, 4) OPM and 5) Seeding experiments. The Preparatory, Screening, OPM and Seeding experiments were performed with synthetic nickel sulphate solution.

4.4.1. Industry experimental

The Industry experiments consisted of experimental work with nickel sulphate solution and sludge samples obtained from WPL BMR and are divided into two phases: phase 1 and phase 2.

Phase 1 experiments' industry solutions were obtained whilst the plant was operational. A sample was taken during morning shift, filtered with 0.45 µm filters and was directly heated up to the desired temperature for the commencement of the experiment. Run specifications for phase 1 are given in Table 4-4. Each sample had a different composition and initial pH. Samples were unaltered, except for the addition of H_2SO_4 to Run I 5 and I 7, to lower their pH to 1.9.

Table 4-4: Industry experimental phase 1 runs.

Run	Temperature [°C]	Composition	Initial pH	End pH
I 1	75	Comp_1	2.73	2.68
I 2	95		2.73	2.66
I 3	75	Comp_2	2.65	2.61
I 4	95		2.65	2.45
I 5	95		1.88	1.63
I 6	95	Comp_3	3.01	2.26
I 7	95	Comp_3	1.85	1.55

Run specifications for phase 2 are given in Table 4-5.

Table 4-5: Industry experimental phase 2 runs.

Run	Temperature [°C]	Composition	Initial pH	End pH
I 8	90	Comp_4	1.98	1.80
I 9	90		2.04	1.96

The Industry experimental phase 2 used a 20 ℓ, 21-day aged industry nickel sulphate solution. The sample was taken from holding tank 700-TK-020 while the plant was not in operation. The solution aged at summer ambient temperature without agitation. The bulk industry sample contained sludge when filtered. 66.05 g of sludge was obtained.

4.50 g holding tank sludge was repulped in distilled water at 70 °C for 10 min; at a dilute liquid to solid ratio: 33:1. The bulk of the aged solid dissolved readily. Thereafter the insoluble filter cake was acid digested in aqua regia for ICP analysis.

4.4.2. Preparatory experimental

The Preparatory experiments collectively refer to the experiments conducted to establish the experimental method and give an early indication of the behaviour of various metal ions. It consists of various verification experiments and three liquid phase experiments. The synthesis method was refined and NaOH titration curves were constructed for accurate base addition to reach the desired pH. The Preparatory experimental analysis also contains visual observation data.

A one-factor approach was taken to initiate synthetic experimental work. One experiment, at pH 2.5 with no peroxide (Run P 1), was compared with two other experiments, Run P 2 at pH 2.5 with peroxide addition and Run P 3 at pH 3.5 with peroxide addition. 10 mℓ, 30 volume%

peroxide (200 % excess) was slowly added at the zero times of Run P 2 and Run P 3. Table 4-6 lists the preparatory runs. Temperature was fixed at 85 °C and the total metals concentration was 100 g/ℓ.

Table 4-6: Preparatory experimental runs.

Run number	$pH_{initial}$	$pH_{after\ peroxide\ addition}$	Peroxide addition	Run time (min)
P 1	2.49	2.49	No	480
P 2	2.49	2.15	200 % excess	360
P 3	3.68	2.31	200 % excess	360

Although the Preparatory experimental provides insight into the behaviour of the system, its results served an experimental development role. Peroxide addition also yielded uncontrollable results. The results are provided in Appendix C. The Screening experimental was developed to overcome the limitations of the Preparatory experimental runs.

4.4.3. Screening experimental

The Screening experimental utilized the D-Optimal design of experiment computational method to establish the effect of five factors: a) initial pH, b) iron valence state, c) total metal concentration, d) reaction temperature and e) the addition of goethite seed material, as summarised in Table 4-7. Table 4-8 lists the experiments conducted.

The Screening experimental served both a screening and comparative role. The pH was chosen based on the variability of plant solution reported, as well as the work of van Schalkwyk (2011). van Schalkwyk (2011) observed a leaching plateau at pH 4.0 in oxidative leaching tests.

Ferrous and ferric salts were interchanged, in order to simulate both conditions and the behaviour of other precious metals therewith. Preliminary work also tested the usage of molecular oxygen, but the fine tuning of a dedicated iron removal process would have diverted the attention from the OPM behaviour. It was out of scope and not desired by industry.

The total metals concentration was scaled from industry data in order to simulate 1) an unconcentrated solution typically produced by the first stage leach and 2) a concentrated solution as typically produced by the boil-off circuit in 700-TK-090. The total metals content were scaled down in order to synthetize synthetic solution at room temperature. See Appendix B 1 for details.

The temperature range of 70 °C to 90 °C is also scaled from industry conditions. The boil-off circuit and evaporator operate at 90 °C. The first stage leach solution in the holding tanks' temperature range from 70 °C to 90 °C.

The utilisation of seed material had the goal to serve as growth and possibly adsorption sites. The dosage amount of 10 g/ℓ, with a seed to iron in solution ratio of 2:1, was sufficient to pick up an effect in literature studies (Dutrizac, 1996; Hove *et al.,* 2009).

Table 4-7: Screening experimental matrix.

		Levels	
		-1	**+1**
A	**pH**	2.5	4.0
B	**Iron valence state**	2+	3+
C	**Total metal concentration**	65 g/ℓ	95 g/ℓ
D	**Temperature**	70 °C	90 °C
E	**Seeding**	None	Goethite seeding

Table 4-8: Summary of D-Optimal and Seeding experimental runs conducted.

New	**pH**	**Iron valence state**	**[Metals] [g/ℓ]**	**Tempe-rature [°C]**	**Seeding**	**Experimental**	**Solid characteri-sation**
1	4.0	2+	65	70	Goethite	D-Opt + Seeding	BET & PSD
2	2.5	3+	95	90	Goethite	D-Opt	XRD, BET & PSD
3	2.5	2+	95	90	None	D-Opt	-
4	4.0	2+	65	70	None	D-Opt + Seeding	SEM
5	2.5	2+	65	70	Goethite	D-Opt + Seeding	BET & PSD
6	2.5	2+	65	90	None	D-Opt	
7	2.5	3+	65	90	none	D-Opt	
8	4.0	3+	65	90	Goethite	D-Opt	BET & PSD
9	4.0	2+	95	90	None	D-Opt	XRD
10	4.0	3+	95	90	Goethite	D-Opt	XRD & SEM
11	4.0	3+	95	90	none	D-Opt	XRD
12	2.5	3+	65	70	Goethite	D-Opt	BET & PSD
13	2.5	3+	65	90	None	D-Opt	
14	2.5	2+	65	70	None	D-Opt + Seeding	
15	4.0	2+	65	70	None	D-Opt + Seeding	
16	2.5	2+	65	70	50 g/ℓ	Seeding	
17	4.0	2+	65	70	50 g/ℓ	Seeding	
18	2.5	3+	65	90	None	D-Opt	
19	2.5	3+	65	90	None	D-Opt	

The interpretation of the statistical analysis led to the development of two additional experimental phases, the OPM and the Seeding experiments.

4.4.4. D-Optimal design motivation

D-Optimal design of experiment method utilises computer algorithms with the optimality criterion of maximising the determinant of the Fischer information matrix X'X (Croarkin & Tobias, 2012). D-Optimal designs are robust in the sense that the experimenter can define the type of model, from first order to cubic, and the objectives, such as screening or comparative (Croarkin & Tobias, 2012). The optimal-class of experimental designs generally require less experimental runs to estimate parameters to the same precision as that of a classical design method, since a given objective is optimised.

The ability to specify the model of interest by manipulating the choice of model points from a candidate list was the main attractive feature of the D-Optimal design (Montgomery, 2001; Croarkin & Tobias, 2012). The D-Optimal method was initially chosen to construct a model with more than two levels for certain variables. For instance, more levels of pH (intermediate pH intervals) and seeding (including hematite seeding) were planned. The D-optimal model could be augmented robustly, due to its computational backbone. The inability to detect iridium, as the reader will note in the results section, was the primary setback that prevented such augmentation to be done on the model presented in this work. Also, hematite seed material had very low BET surface areas and given the performance of goethite seeds experiments with hematite was also abandoned.

The D-Optimal method might improve the observation of minor effects by shifting the focus from the interactions of unlikely effects. The specified likely and unlikely significant effects are tabulated in Table 4-9. The likely significant effects were modelled and model points, with the likely insignificant effects mentioned included within the error calculation. All third level interactions and higher were excluded. The resulting design constructed was very similar to a Res(IV) fractional factorial design, but with added lack-of-fit runs.

Table 4-9: Likely significant effects.

Likely significant effects	Likely insignificant effects
A - pH	BC
B - Valence	BD
C - [Metals]	BE
D - Temp	CD
E - Seeding	CE
AB	DE
AC	
AD	All three factor and higher effects
AE	
BD	
BE	

4.4.5. Other precious metals experimental

The Screening experiments' statistical analysis led to ambiguous results of other precious metals behaviour and spectral interferences caused difficulty interpreting iridium content over time. The OPM experimental aimed to fundamentally understand the behaviour of OPMs in a synthetic solution only consisting of ferrous, ferric or copper with the OPMs. The OPM experimental runs are given in Table 4-10.

Table 4-10: OPM experimental runs.

Run	Initial pH	Iron valence state	Total metal concentration [g/ℓ]	Temperature [°C]	Seeding
OPM 1	2.5	2+	2.5	90	none
OPM 2	4.0	2+	2.5	90	none
OPM 3	2.5	3+	2.5	90	none
OPM 4	4.0	3+	2.5	90	none
OPM 5	4.0	Cu (no Fe)	2.5	90	none

4.4.6. Seeding experimental

The Seeding experimental consists of two steps. Seed material was fundamentally characterised via particle size distribution (PSD) and surface area analysis via nitrogen adsorption according the Brunauer–Emmett–Teller (BET) theory was done of samples originating from the screening and OPM experimental. Hematite seed was also evaluated to be used in further experiments. Table 4-11 presents the PSD and BET samples, with reference to the liquid experiments the solids originated from.

Table 4-11: Particle size and surface area characterisation experiments.

Sample name	Liquid experiment
PSD 1	Reference goethite
PSD 2	Reference hematite
PSD 3 / SEM 5	OPM #4: Fe(III) & pH 4.0
PSD 4	#2: 2.5, 3+, 95 g/ℓ, 90 °C
PSD 5	#12: 2.5, 3+, 65 g/ℓ, 70 °C
PSD 6 / SEM 4	#8: 4.0, 3+, 65 g/ℓ, 90 °C
PSD 7	#5: 2.5, 2+, 65 g/ℓ, 70 °C
PSD 8	#1: 4.0, 2+, 65 g/ℓ, 70 °C

The goethite seeding quantity employed in the Screening experimental was fixed. Synthetic experiments were conducted with substantially more seed material in order to improve the observation of the effect of goethite seed. Screening experimental runs were combined with new experiments that utilised 50 g/ℓ seed to create the seeding experimental matrix, the design matrix is presented in Table 4-12 and the experimental design's runs are given in Table 4-13.

The Seeding experimental was conducted with ferrous iron, where its effect is expected to be utilised if successful.

Table 4-12: Seeding experimental matrix.

		Levels		
		-1	**+1**	**+2**
A	**Initial pH**	2.5	4.0	
E	**Seeding quantity**	None	10 g/ℓ	50 g/ℓ

Table 4-13: Seeding experimental runs.

Run number	pH	Iron valence state	[Metals] [g/ℓ]	Temperature [°C]	Seeding quantity
14	2.5	2+	65	70	0
4	4.0	2+	65	70	0
15	4.0	2+	65	70	0
5	2.5	2+	65	70	10 g/ℓ
1	4.0	2+	65	70	10 g/ℓ
16	2.5	2+	65	70	50 g/ℓ
17	4.0	2+	65	70	50 g/ℓ

4.4.7. Solid characterisation

Solid characterisation was conducted via scanning electron microscopy (SEM) and powder X-ray diffraction (XRD), with samples presented in Table 4-14, with reference to the liquid experiments

the solids originated from. SEM is considered the primary method yet was chronologically done after XRD analysis. Combining of XRD and SEM results provides the reader with a summarised account of solid characterisation.

Table 4-14: Solid characterisation samples.

Sample name	Analysis technique	pH	Iron valence state	Liquid experiment
Iron and OPM solution				
S 1	SEM	2.5	2+	OPM 1
S 2	SEM	4	2+	OPM 2
S 3	XRD	2.5	3+	OPM 3
S 4	SEM + XRD	4	3+	OPM 4
Nickel sulphate solution				
S 5	SEM + XRD	4	3+	#11
Seeded nickel sulphate				
S 6	XRD	Reference goethite		
S 7	XRD	2.5	3+	#2
S 8	SEM + XRD	4	3+	#10

4.5. Analysis techniques

4.5.1. Solution elemental composition

The synthetic solutions were analysed via an inductively coupled plasma - optical emission spectrometry (ICP-OES) for the elements: nickel, cobalt, iron, copper, arsenic, sodium, ruthenium, rhodium and iridium. Samples were diluted with 0.1 M H_2SO_4 to prevent precipitation and was analysed at the Stellenbosch University - Process Engineering Analytical lab.

Solution samples were analysed via a Thermo-Fischer iCAP 6000 series ICP-OES. The analysis method developed entailed using two dilutions. Base metals and arsenic were analysed via the radial view (side-on view) configuration, while OPMs and arsenic with a separate dilution with the axial view (end-on view) configuration. The axial view configuration allows a longer viewing path and resultantly a 5 to 10-fold improvement of the limit of detection, yet might increase spectral and matrix induced interferences (Hou & Jones, 2000). There were no anomalies in the comparison of radial and axial view spectral peaks generated by Thermo-Fischer's Qtegra software for PGMs and arsenic.

For example the spectral peaks for As 189.042 in both radial and axial configurations are presented in Figure 4-3. Different dilution factors caused the different absolute intensities measured.

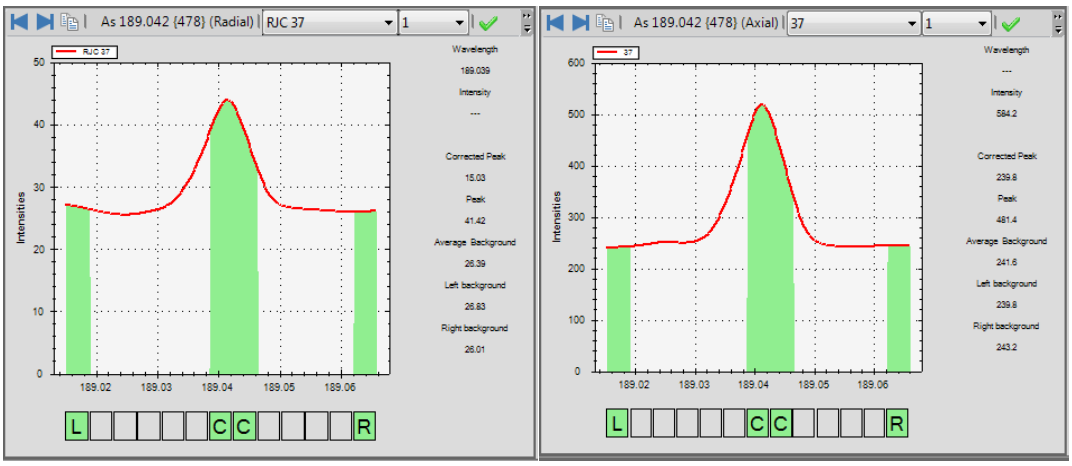

Figure 4-3: Spectral peaks for As 189.042, generated by Thermo-Fischer Qtegra software. Left analysed with radial view and right with axial view.

Industry solution analysis was done by Western Platinum Assay Lab (Phase 1) and at the Base Metal Refinery Lab on Spectro ICP-OES equipment (Phase 2).

4.5.2. XRD characterisation

The precipitate, already in a finely powdered form, were analysed using a Bruker AXS D8 Advance diffractometer. This instrument utilizes Cu-Kα radiation with a Positive Sensitive Vantec-1 detector. The detected peaks were normalized and matched to the International Centre for Diffraction Data (ICDD) powder detection file database of 1998. Cornell and Schwertmann (2003)'s powder XRD data were also considered during analysis, but was essentially covered in the database used. Data evaluation was done with Bruker's EVA software.

The step time, step size and counting times were varied in order to yield good statistics. The amorphous samples required significantly longer measuring times. A tube voltage of 40 kV and current of 40 mA were applied. Data analysis was done at iThemba LABS.

4.5.3. Acid digestion

The precipitate products formed by each experimental run could be dissolved in strong acids or reductants (Cornell & Schwertmann, 2003). Industry sludge and solids from synthetic solutions were successfully dissolved in aqua regia. Industry sludge dissolved readily in less than an hour. Synthetic solution solids were left in aqua regia for two days. A small fraction of fine white insoluble solids were detected with synthetic solids. The dissolved solution was analysed via ICP-OES.

Residues remained when attempting the digestion of commercial goethite. These residues were centrifuged out.

4.5.4. Particle size distribution

Particle size distribution analysis was done by screening agglomerate samples with a pass size of 106 µm, prior to analysis with a Saturn DigiSizer 5200. This step was done after inconsistent results were obtained from the unscreened samples. The refraction index of 2.268 for goethite and 1.715 for jarosite was used. A flowrate of 12 ℓ/min with 60 s circulation time and 60 s ultrasonic time at 60 % intensity was employed. A laser strength of 1.88 eV was used. Samples were pulped prior analysis and analysis was conducted with and without ultrasonic.

4.5.5. BET Surface area

Brunauer-Emmett-Teller theory (BET) surface area analysis with nitrogen gas was performed with a Micromeritics 3Flex 1.02 at the Stellenbosch University - Process engineering analytical lab.

Crystal lattice level transformation might occur during BET surface area work at elevated outgassing temperatures (Cornell & Schwertmann, 2003): Heating of a microporous ferrihydrite sample in air at 100 °C reduced the reported surface area from 235 m^2/g to 218 m^2/g. Further outgassing at 150 °C reduced the surface area to 178 m^2/g. Dihydroxylation of the ferric oxyhydroxides may occur, leading to the formation of slit-shaped micropores.

An outgassing temperature of 90 °C overnight, followed by 50 °C overnight, was initially employed to prevent crystal lattice transformation discussed above. At low outgassing temperature uncharacteristically low surface areas (< 10 m^2/g) were reported, which indicates that outgassing at low temperature might not have removed all adsorbed gas.

Thereafter the standard outgassing temperature of 250 °C was utilised. With reference goethite (PSD 1) a BET surface area of 131.01 m^2/g was reported after 6 h outgassing at 250 °C. The same sample was then outgassed for an additional 17 h at 250 °C that resulted in a BET surface area of 131.07 m^2/g. The BET surface area values between 6 h and 23 h total were in excellent agreement, suggesting accurate and reproducible values reported. Type II sorption isotherms were observed, as defined in ISO 9277:2010. The remaining samples were outgassed at 250 °C for 17 h. Table 4-15 lists two other repeated tests' results.

Table 4-15: BET surface area repeatability.

Sample name	BET surface area [m^2/g]	Micropore volume [m^2/g]	External surface area [m^2/g]
PSD 1.1	131.01	66.94	64.07
PSD 1.2	131.07	65.51	65.56
PSD 4.1	100.17	44.02	56.16
PSD 4.2	101.07	44.59	56.48
PSD 7.1	122.2	68.52	53.68
PSD 7.2	130.15	76.98	53.17

4.5.6. SEM Characterisation

Minerals were analysed by quantitative energy-dispersive X-ray spectroscopy (EDS) using a Zeiss MERLIN Field Emission Gun - Scanning Electron Microscope (SEM). Nickel, cobalt, iron, copper, sulphur, oxygen, chloride, ruthenium, rhodium, iridium and arsenic were determined via EDS using an Oxford Instruments® XMax 20 mm^2 detector and Oxford INCA software. Beam conditions during the quantitative analyses on the MERLIN FEG SEM were 20 kV and 16 nA, with a working distance of 9 mm. Mineral counting time was 15 s live-time for EDS. A cobalt standard was used for standardisation and verification of the analyses. The system is designed to perform high-resolution imaging concurrently with quantitative analysis, with errors ranging from ± 0.6 wt.% to 0.1 wt.% on the major elements using EDS.

Back-scattered electron detector images (SEM-BSE) were utilised to qualitatively define different precipitate phases. Secondary electron detector images (SEM-SE) provided surface morphology analysis and visual observation of the precipitates. Composition maps were drawn but were largely ineffective due to the predominance of iron and little deviations seen in samples. The maps could be used to identify different phases. Composition data presented are averaged from at least three corresponding data points. A sample spectrum for a data point is given in Figure 4-4.

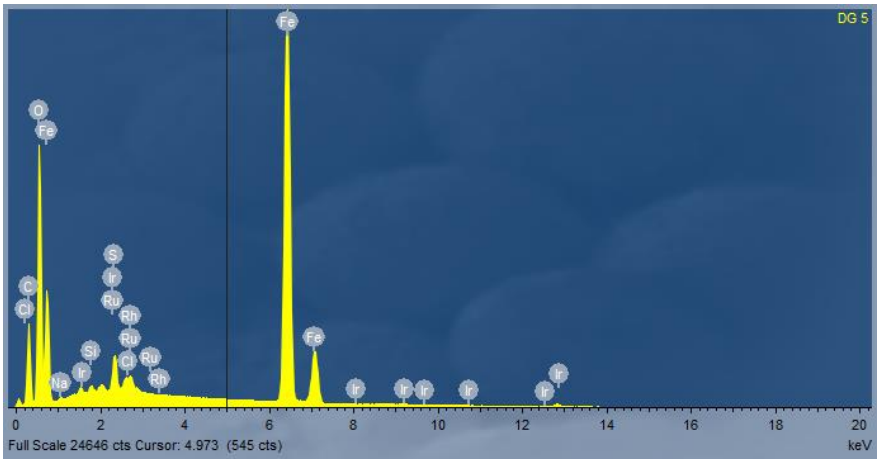

Figure 4-4: EDS spectrum for sample data point.

CHAPTER 5 - RESULTS AND DISCUSSION

5.1. Industry experimental

5.1.1. Phase 1 experimental

The first batch of industry experiments aimed to establish the behaviour of other precious metals over time in the holding tanks. Varying the temperature (75 °C – 95 °C), the pH range (1.9 – 3.0), and compositions were investigated.

Sludge formation was observed in all experiments. An exponential increase of sludge formation was observed as the pH was increased, as expected because pH is a function of the natural log of hydronium ion concentration. At pH 3.0, significantly more sludge formed compared to pH 2.7 and pH 1.9, regardless of the different solution compositions. For instance Run I 7 was acidified to pH 1.9, and had the same composition of Run I 6, which was left unaltered at pH 3.0. During Run I 7 almost no precipitate formed, while 1.51 g precipitate formed in Run I 6. Table 5-1 provides the pH and corresponding weight precipitated per pH group.

Table 5-1: Correlation between pH and the weight precipitated per 500 mℓ solution.

	Run	pH	Average sludge weight [g]
Low	I 5 & I 7	1.87	0.02
Medium	I 1 – I 4	2.69	0.11
High	I 6	3.01	1.51

During liquid phase investigation throughout this work, the term *precipitated* is attributed to an observed loss of the particular metal from solution, since effective solid liquid separation was applied prior to analysis. If the metal is not detected via ICP, it must be present in the solid phase. Therefore precipitation refers collectively to the possible chemical precipitation, entrainment and adsorption. The naming convention: “Run number: Composition; Temperature; pH” was used for this section.

The ruthenium and iridium content in solution is provided in Figure 5-1. The ruthenium and iridium remained constant over time. The 2 ppm ruthenium that precipitated in Run I 2 is likely not significant. Varying pH values of the industry solution had no effect on high temperature ruthenium and iridium precipitation. Temperature had no significant effect between runs of the same composition, as seen between Run I 3 and I 4 for instance.

Many industry variables affected the other precious metals concentration in the liquid solution. No correlation between the solution pH and the initial OPM concentration can be made. When the industry solution is left unaltered, no other precious metals would precipitate. It is predicted that no appreciable OPM precipitation could occur in holding tanks during normal operation. Variation, as observed in Run I 6, is likely due to dilution errors during experimental analysis.

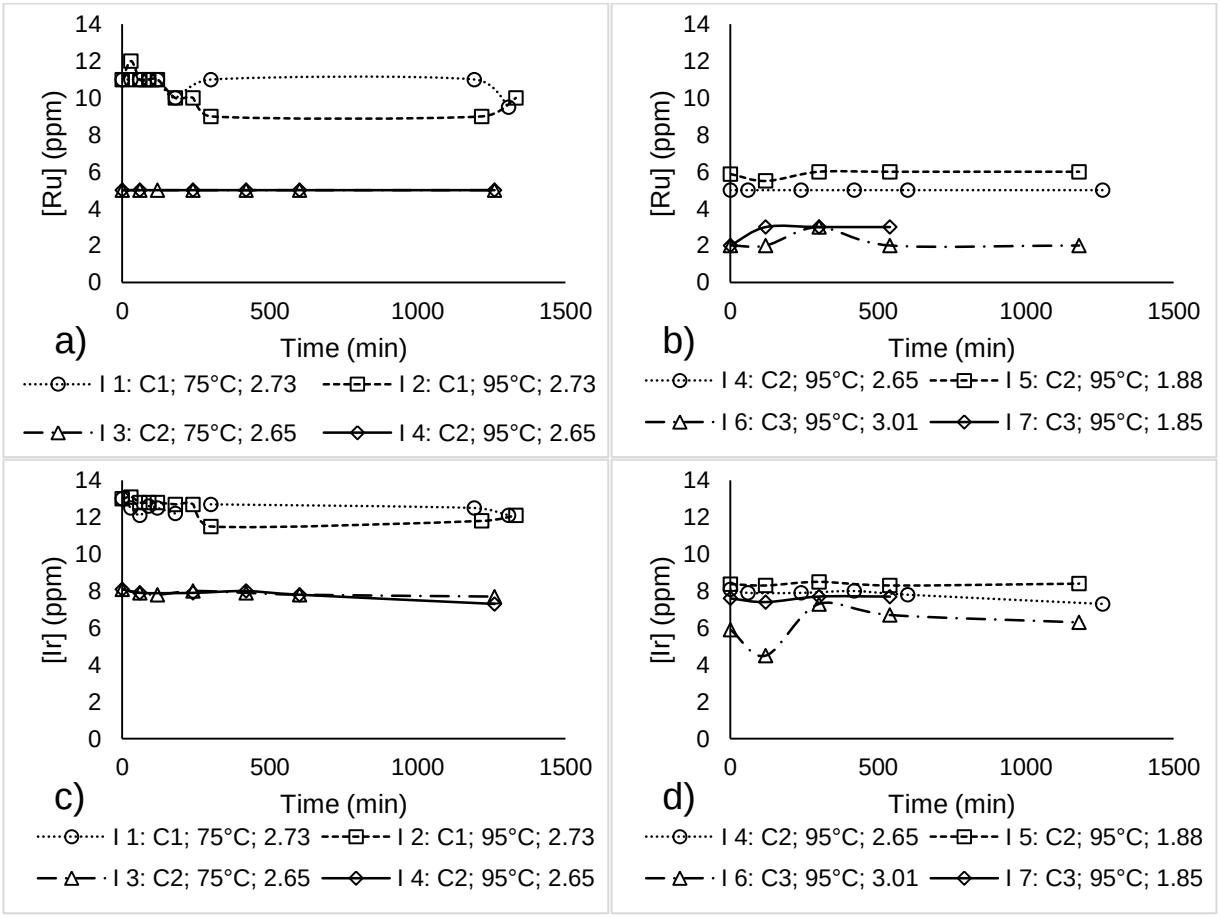

Figure 5-1: Ru (a) and b)) and Ir (c) and d)) content over time for Industry experimental phase 1. Run I 1-4 at pH 2.7, Run I 5 and I 7 at pH 1.9 and I 6 at pH 3.0.

The arsenic content over time for phase 1 is provided in Figure 5-2. Gradual arsenic precipitation occurs over the 20 h duration. The arsenic precipitation was more pronounced at 95 °C. compared to 75 °C. Experiments conducted at pH 1.9, had relatively lower arsenic precipitation, which suggests that arsenic loss is inhibited at the lower pH.

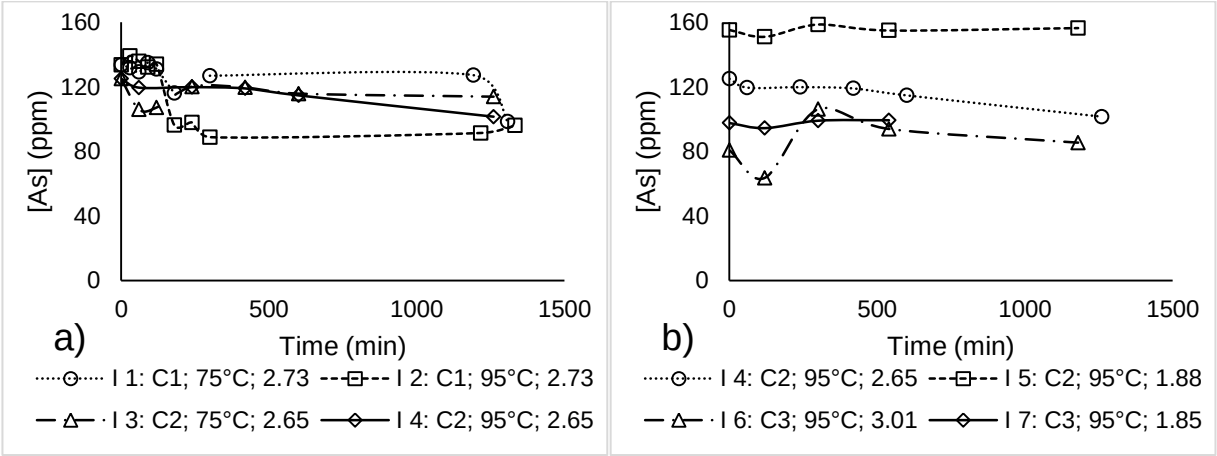

Figure 5-2: As content over time for Industry experimental phase 1.

It is concluded that other precious metals precipitation could not occur in unaltered industry nickel sulphate solution at elevated temperature between the range pH 1.9 to pH 3.0 over 20 h.

5.1.2. Phase 2 experiments

Phase 2 experiments were conducted with a 21-day aged industry bulk sample as given in Table 5-2. The elemental characterisation of the solid sludge as well as the effect of neutralisation was investigated.

The bulk solution contained an appreciable amount of iron and the total metals content of 121 g/ℓ was reported, which is higher than the normal operational total metals of 100 g/ℓ (refer to Table 2-1). The holding tanks aren't agitated and it is speculated that the higher total metals observed might be due to gradual gravity settling over the extended standing time.

The composition of the bulk industry sample is provided in Table 5-2. Notably, ruthenium content is significantly higher than normal industry operations. The large portion of iron is also detected. Spectral interferences prevented iridium analysis.

Table 5-2: Metal concentration of the 21-day aged industry solution of phase 2.

	Ni g/ℓ	Co mg/ℓ	Fe mg/ℓ	Cu mg/ℓ	Pt mg/ℓ	Pd mg/ℓ	Rh mg/ℓ	Ru mg/ℓ	Au mg/ℓ
Comp_4	121	860	2340	890	2.1	< 0.3	< 0.9	61.7	0.8

Two liquid experiments were conducted identically to the phase 1 experiments, summarised in Table 5-3. Run I 8's solution was left unaltered, while 10 mℓ, 0.05 M NaOH was added to Run I 9 at zero time.

Table 5-3: Industry experimental phase 2 runs.

Run	Temperature [°C]	Composition	Start pH -	End pH -
I 8	90	Comp_4	1.98	1.80
I 9	90		2.04	1.96

Similar to phase 1 experiments, no ruthenium precipitation is observed in Run I 8. The addition of 10 mℓ, 0.05 M NaOH resulted in 3 % iron precipitation in Run I 9, compared to 1 % iron precipitation in Run I 8. 8 % (5 ppm) ruthenium precipitation occurred in Run I 9, compared to 0 % ruthenium precipitation in Run I 8. No copper removal was observed and the ORP remained constant over the course of the experiment.

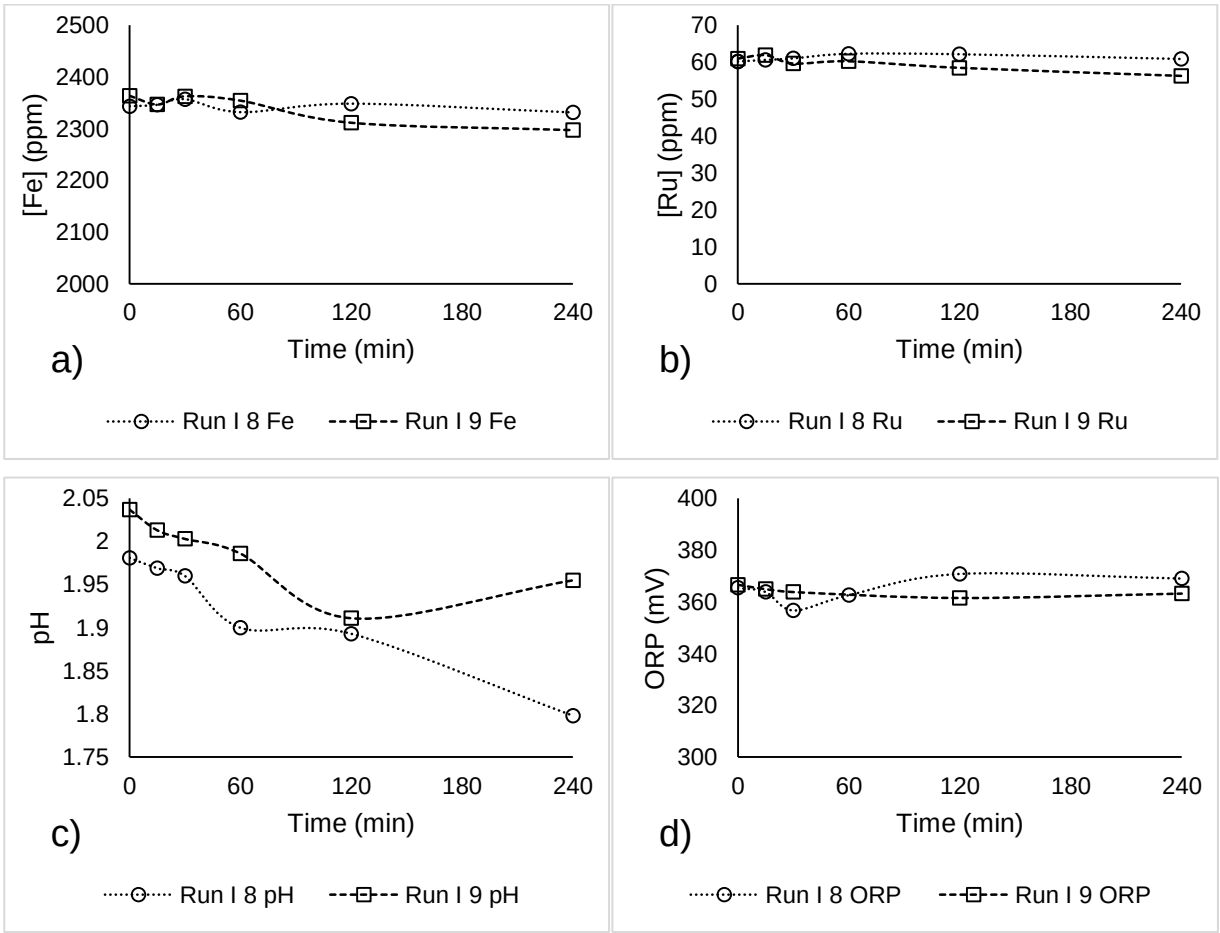

Figure 5-3: Fe, Ru, pH and ORP over time for Runs I 8 and I 9.

The addition of a little bit of NaOH led to iron and ruthenium precipitation over 240 min, even at pH values where phase 1 experiments did not indicate any gradual precipitation over 20 h.

5.1.3. Holding tank sludge analysis

Table 5-4 lists the metal mass obtained from water leaching and subsequent acid digestion of sludge filtered from the 21-day aged sample. Figure 5-4 graphically presents the elemental composition data. The iridium spectra could be observed at low nickel content and software interference correction was applied. Copper and cobalt were below detection limits.

The aged solid consisted of 89 % nickel, 10 % iron and 1 % other precious metals. The largest portion of the nickel was easily removable with the water leach. If nickel is present as hydrated $NiSO_4$ in the water leach solution, the stoichiometric calculation of sulphate and crystalized water would account for 4.36 g of the original sample. XRD data, to be discussed, also suggest the nickel is present as hydrated $NiSO_4$. A small fraction of iron was also leached. A portion of the iron was possibly loosely entrained, maybe as intermediate iron hydrolysis complexes. Half of the initial iridium was also leached, suggesting loose entrainment of iridium. A longer water leach or diluted acid leach might further remove nickel, but pose a risk to dissolve iridium too.

The acid digested sludge primarily consisted of iron, followed by nickel and other precious metals. Ruthenium, followed by iridium and rhodium was the most significant OPM in the sludge. Ruthenium did not appreciably dissolve with the water leach, suggesting a stable inclusion into the iron sludge.

Table 5-4: Actual metal weight in the 4.5 g solid sample via acid digestion and subsequent ICP analysis.

	Ni	Fe	Pt	Rh	Ru	Ir
	mg	mg	mg	mg	mg	mg
Water leach	971.3	5.2	0.14	0.16	0.03	1.37
Aqua regia	25	104.3	0.84	1.12	9.9	1.16

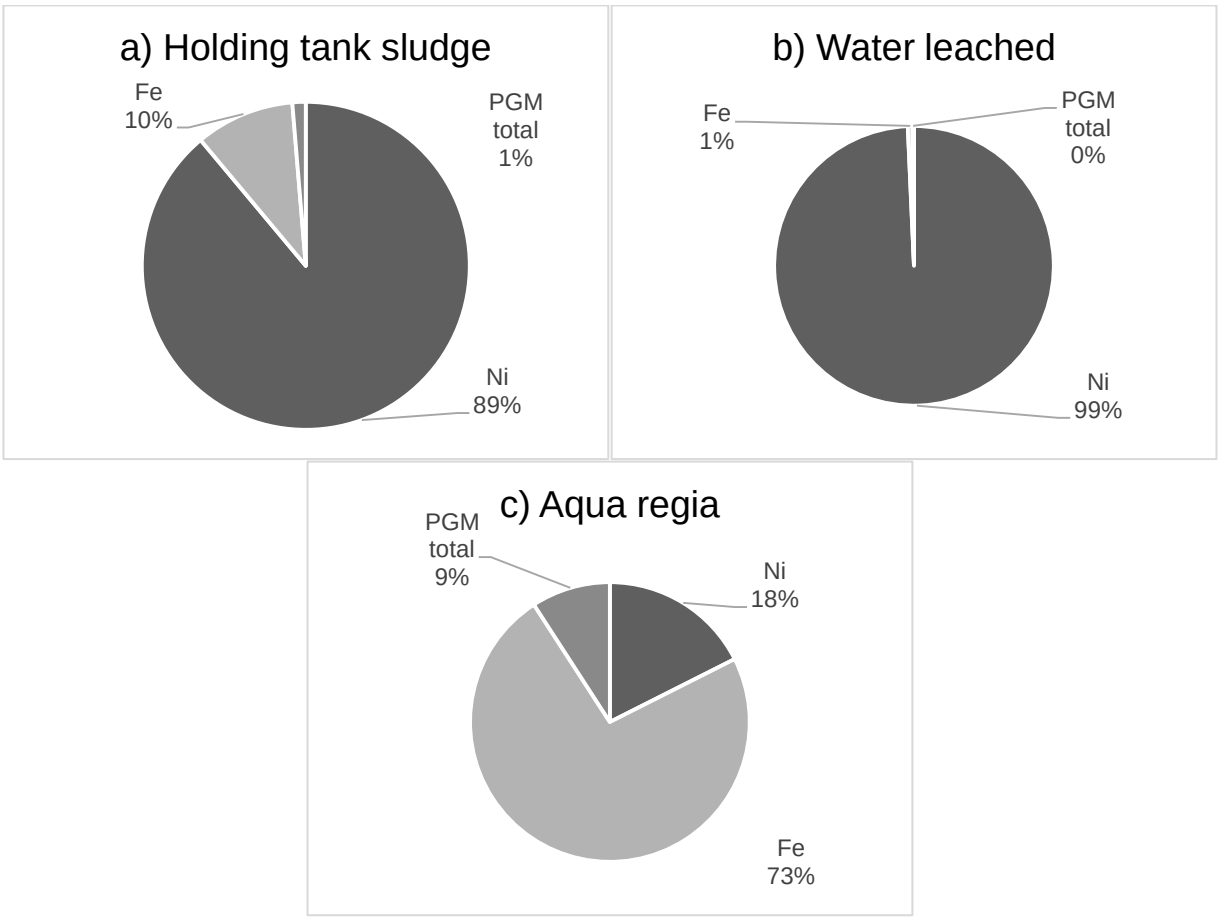

Figure 5-4: Elemental composition (wt.%) of aged holding tank sludge as a function of analysed metals with a) the overall sludge, b) the water leached portion and c) the remaining sludge digested with aqua regia.

Limited industry contact time and security constrains prevented the more thorough analysis of solid sludge.

5.2. Screening experimental

The data interpretation in the Screening experimental makes use of the following convention. The iron valence state and pH were identified as the two most prominent factors during iron precipitation, the largest impurity and the part of the reaction pathway speculated to scavenge OPMs. The data was therefore arranged in the following four quadrants: a) Fe(II) & pH 2.5, b) Fe(II) & pH 4.0, c) Fe(III) & pH 2.5 and d) Fe(III) & pH 4.0, as illustrated in Figure 5-5.

a) Fe^{2+}, pH = 2.5	b) Fe^{2+}, pH = 4.0
c) Fe^{3+}, pH = 2.5	d) Fe^{3+}, pH = 4.0

Figure 5-5: Data interpretation convention for synthetic experiments.

Throughout this section, reference to the other variables is made via shorthand in the legends of graphs. The convention "run number: total metal concentration, seeding, temperature" is used. For instance "#3: 95, N, 90" in the legend would refer to Run 3 at 95 g/ℓ total metals, N = no seeding or G = goethite seeding and temperature = 90 °C.

Error bars were generated from four repeatability runs, to be used throughout this section. The standard error at the particular time interval is plotted as error bars on the graphs, as shown on Figure 5-6. The errors were larger in the first few minutes of experiments, particularly for ferric experimental runs. Calculations are provided in Appendix B.2.

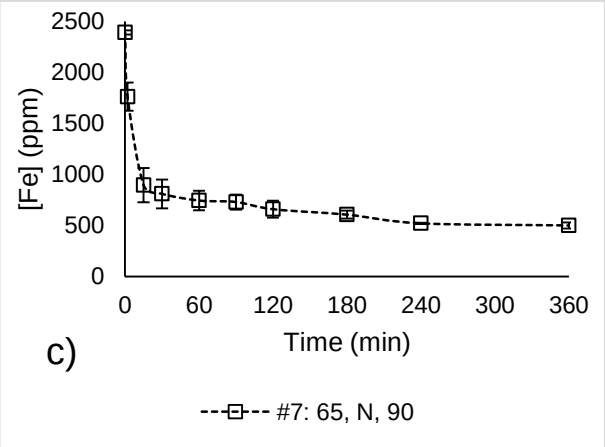

Figure 5-6: Example error bars

5.2.1. Iron precipitation

The iron concentration in solution is plotted as a function of time in Figure 5-7 for the Screening experiments. The four quadrants of iron behaved in characteristic manners. Essentially no

precipitation occurs in a) Fe(II) & pH 2.5, while complete and rapid iron precipitation occurs in d) Fe(III) & pH 4.0. Slight gradual precipitation is noted in b) Fe(II) & pH 4.0. Rapid hydrolysis occurs within the first 30 min in ferric experiments. The bulk of the iron loss occurs in the first 30 min. In c) Fe(III) & pH 2.5 rapid precipitation within the first minutes of the experiment is observed accounting to 58 % precipitation on average in 30 min followed by gradual precipitation to 73 % precipitation on average at 360 min. Error bars are plotted in a manner to prevent cluttering of graphs.

A significant amount of iron precipitation occurred during the heating up phase in Fe(III) runs, as can be observed with the relatively lower initial iron content reported in quadrant c) and d). Repeatability was a problem with ferric experiments in quadrant c), hence the four lack-of fit runs in the D-Optimal design done in this quadrant.

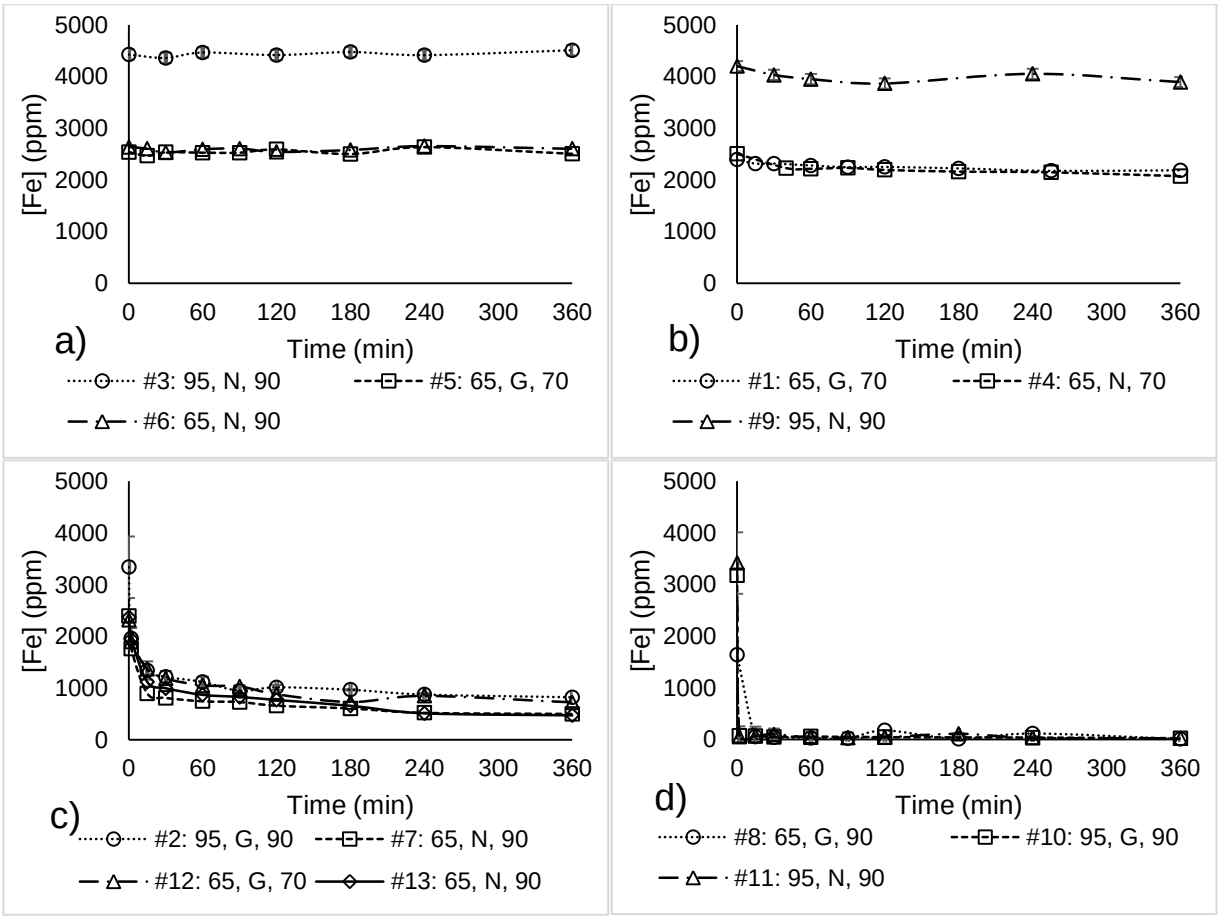

Figure 5-7: Fe over time during D-Optimal experiments at a) Fe(II) & pH 2.5, b) Fe(II) & pH 4.0, c) Fe(III) & pH 2.5 and d) Fe(III) & pH 4.0.

0.0 % - 1.2 %, mere 30 ppm, iron precipitation occurs in Run 3, Run 5 and Run 6 in a) Fe(II) & pH 2.5. 0.07 g solids (> 2.5 µm) were obtained via filtration after 6 h from Run 5. Run 3 was run for 24 h in order to obtain more solids.

The experimental data was analysed via the D-Optimal statistical design. Analysis of the factors total metals concentration, temperature and seeding was done via statistical analysis. Firstly seeding would be discussed, followed by the total metals concentration. Temperature was statistically insignificant. The iron content in ppm was converted to percent iron precipitated for statistical analysis. Anova statistics, residual analysis and calculations are provided in Appendix E.

The initial effects of variables can be communicated with results at the 30 min and 360 min intervals. The Pareto charts at 30 min and 360 min are given in Figure 5-8 and Figure 5-9, respectively, refer to the Anova analyses presented in Appendix D for the models, residual analyses and commentary on models. Orange bars denote positive effects to iron precipitation, while blue bars denote negative effects. At 30 min, factors pH (A), valence (B), total metals concentration (C), seeding (E), pH-total metals interaction (AC) and valence-seeding interaction (BE) were significant. Fewer effects were significant at 360 min, with only pH (A), valence (B), pH-valence interaction (AB) and pH-metal concentration interaction (AC). The large effects of valence and pH shrouded the effects of the other variables during iron analysis.

The iron valence state and pH were the two most significant effects throughout.

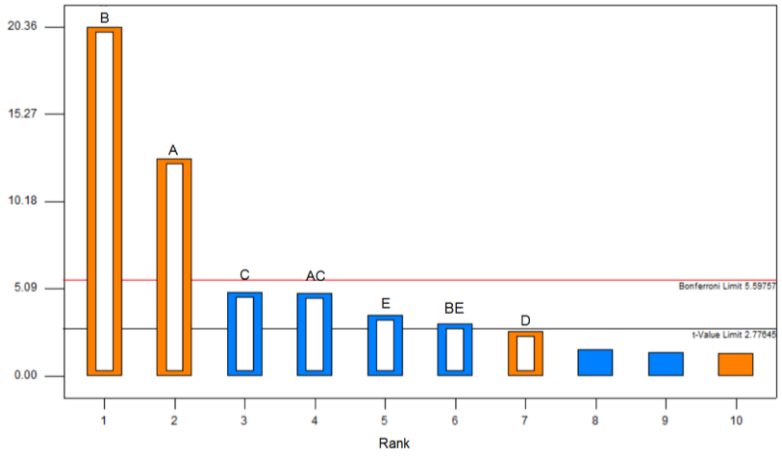

Figure 5-8: Pareto chart of Fe precipitated (%) at 30 min.

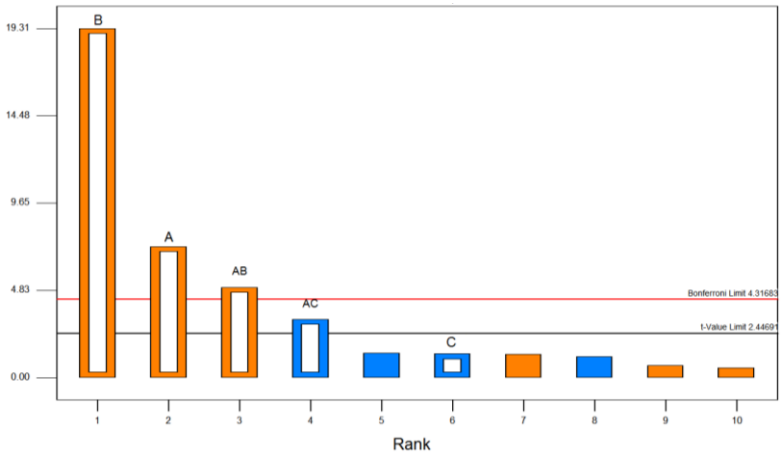

Figure 5-9: Pareto chart of Fe precipitated (%) at 360 min.

Negative contributions of seeding and the interaction of seeding with valence (BE) are noted at 30 min. The positive interactions would imply that seeding provides a precipitation surface for growth during iron precipitation, while the negative interaction implies that seed presence retards iron precipitation.

The lack of a noticeable effect of seeding at 360 min (also noted between 60 min to 240 min) suggests that either the seeding amount added in experiments was insufficient, that it has no effect over time or that it retards iron precipitation. Seeding is intended to aid gradual precipitation of iron via the presence of a growth surface. The growth surface would speed up precipitation if nucleation is the rate limiting step.

Interaction graphs of seeding with valence (BE) suggest that the amount of iron precipitated is lower in the presence of seed at Fe(III) & pH 2.5. Due to the fast precipitation at pH 4, and the fact that essentially no iron precipitated with ferrous experiments, the effect of seeding cannot be quantified at these mentioned conditions. No BE interaction graphs are given, at pH 2.5 and pH 4.0, in Figure 5-10. The Seeding experimental, discussed in Section 5.4., further investigates seeding behaviour in ferrous experiments.

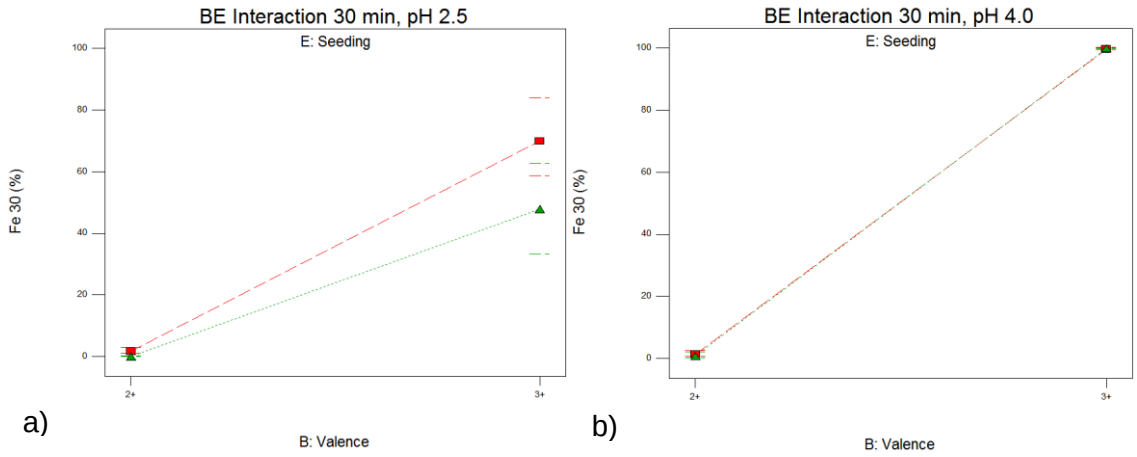

Figure 5-10: Interaction graphs for seeding with valence (BE) at ■ – no seed and ▲ – goethite seed. a) pH 2.5 and b) pH 4.0.

Seeding's behaviour in quadrant c) Fe(III) & pH 2.5, where seeding would theoretically have the most noticeable effect, further questions seeding's efficacy. Comparison between the experimental runs with and without seeding is given in Figure 5-11. 69 % iron precipitation in the seeded experiment, as opposed to 79 % - 80 % in unseeded runs, was observed. The presence of goethite seed might decrease the contact of NaOH and iron ions in solution, decreasing the quantity to iron hydrolysed and subsequently precipitated. The experiments (in Figure 5-11) were conducted at comparable conditions, since temperature's effect on iron precipitation was insignificant.

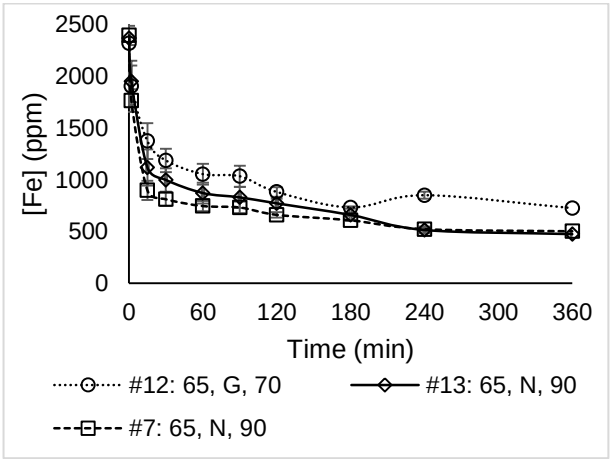

Figure 5-11: Seeding comparison between experimental runs in quadrant c) Fe(III) & pH 2.5 with goethite seeding.

The interaction of total metals concentration and pH (AC) had a negative influence on iron precipitation. Figure 5-12 provides the effect of metals concentration at 30 min and 360 min at Fe(II) & pH 4.0 and Fe(III) & pH 2.5 via its interaction with pH (AC). Contrastingly, lower iron

precipitation was observed from low metals concentration solutions at Fe(II) & pH 4.0. This observation can be ascribed to the fact that the same amount of neutralising agent was added in both 65 g/ℓ and 95 g/ℓ solutions to neutralise the solution to the desired pH. The same amount of ferrous (in ppm) would theoretically precipitate, but the calculation method yield a relatively lower percentage in concentrated solution for the same amount of iron precipitated.

Ferric runs at pH 2.5 indicated higher iron precipitation (in ppm) at higher metals concentration. For instance: With Fe(III) & pH 2.5: 68.4 % (1710 ppm) iron precipitated at 65 g/ℓ and 71.4 % (2550 ppm) iron precipitated at 95 g/ℓ at 30 min. The 65 g/ℓ total iron precipitation at 360 min increased to 74.8% (1870 ppm). At 95 g/ℓ, the total iron precipitation at 360 min increased to 86.1 % (3075 ppm).

The residual ferric content (ppm) between 95 g/ℓ and 65 g/ℓ at pH 2.5 is essentially the same, suggesting that the residual iron achieved is the solubility limit. Steady state was achieved at 240 min.

The interaction of metals concentration and pH (AC) is a significant term at both 30 min and 360 min. Figure 5-12 provides AC's effect at 30 min and 360 min with Fe(II) & pH 4.0 (left) and Fe(III) & pH 2.5 (right).

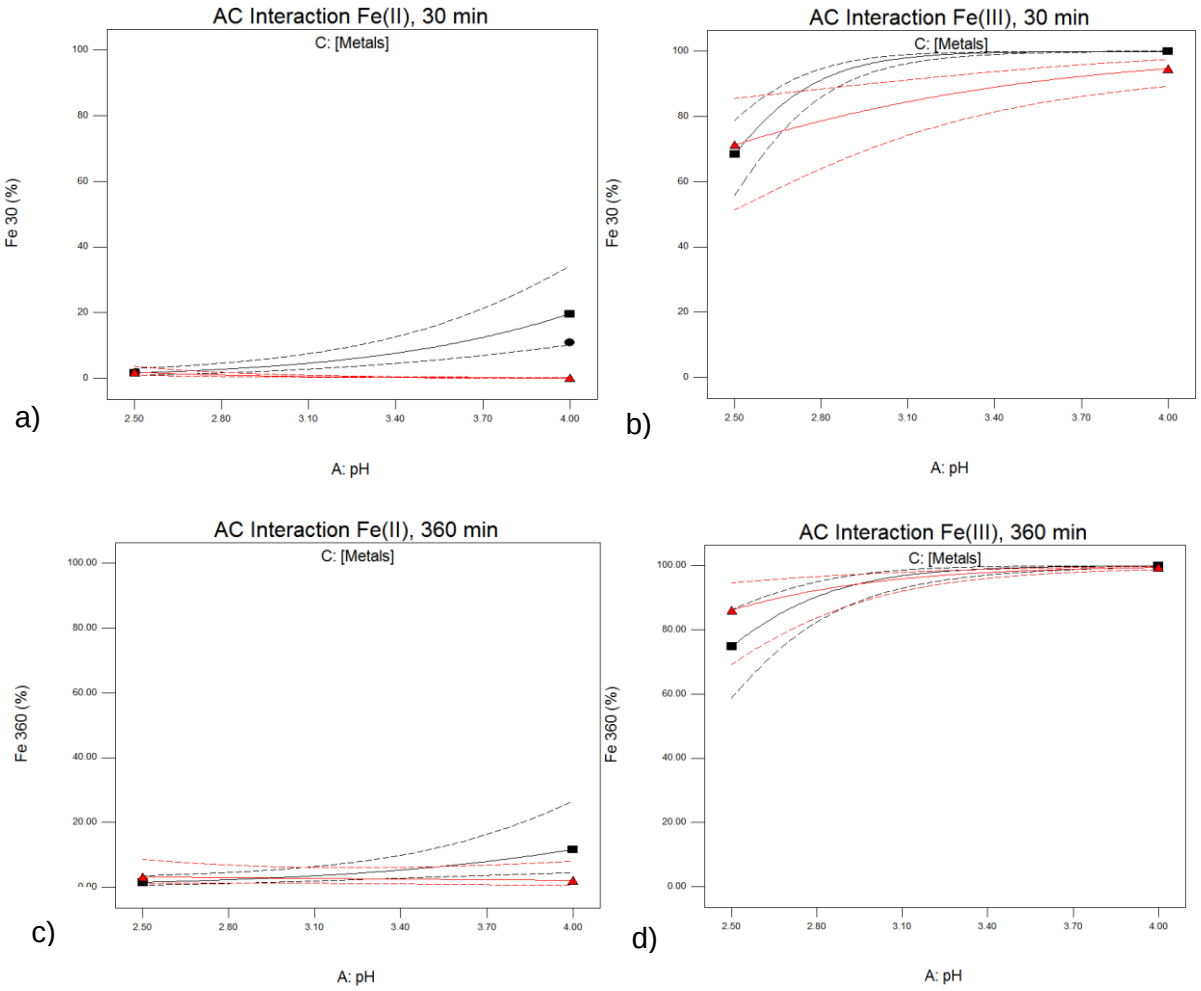

Figure 5-12: Interaction graphs for AC: metals concentration over pH with ■ – 65 g/ℓ and ▲ – 95 g/ℓ total metals. Fe(II) is presented left and Fe(III) is presented right. D: Average (not significant) and E: no seeding. 95 % confidence intervals are given with dash lines.

The higher total metals concentration may also make hydrolysis of other metals, specifically nickel present in high quantities, more likely. Yet no such observations were deductible from the experimental data. The ionic strength difference induced by the different total metals concentrations did not have a noticeable effect on iron precipitation, which would be the element where it would be most easily observable.

It is deducted that no major difference would occur between the unconcentrated filtrate and the intermediate solutions.

5.2.2. Arsenic precipitation

Gradual arsenic precipitation is observed in ferrous experiments, yet to a much larger extent than observed in the industry experimental. Rapid and complete arsenic precipitation was observed in all ferric runs. The high Fe:As ratio would favour the co-precipitation of arsenic. The only

exception was observed in Run 13, yet Run 7 and Run 13 are repeated runs where other elements, notably iron and OPMs, correlated well. The arsenic over time is given in Figure 5-13.

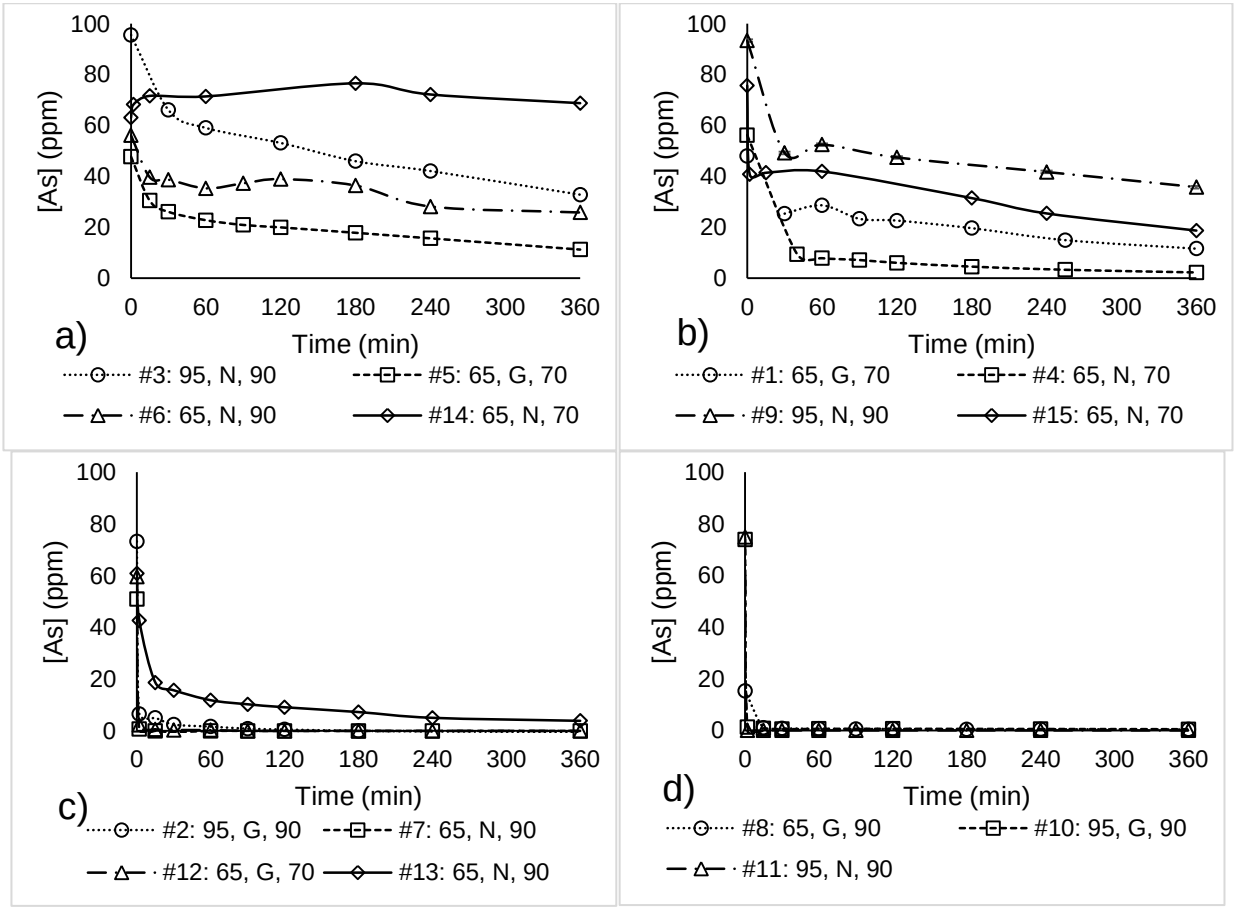

Figure 5-13: As over time during D-Optimal experiments at a) Fe(II) & pH 2.5, b) Fe(II) & pH 4.0, c) Fe(III) & pH 2.5 and d) Fe(III) pH = 4.0.

pH had no significant effect on arsenic precipitation. Figure 5-14 compares arsenic runs in the ferrous quadrant over pH. Similar arsenic behaviour is observed between Run 3 (pH 2.5) and 9 (pH 4.0) and Run 5 (pH 2.5) and Run 1 (pH 4.0). The insignificance of pH can be attributed to the predominance of one arsenic species over the pH range investigated: arsenic acid ($H_2AsO_4^-$) as revealed during the thermodynamic investigation (refer to Figure 3-2). The arsenic precipitation overall reactions are presented in Section 2.5. Arsenic precipitation is acid forming and requires neutralising agent for co-precipitation. The significant removal of arsenic in synthetic work, which was not observed during the industry experimental phase 1, is likely due to the addition of neutralising agent in synthetic work.

The observed pH independence also strongly suggest that arsenic precipitation is not influenced by iron precipitation at the high Fe:As. Thermodynamic modelling at the solution speculated the predominant precipitation product of $Co_3(AsO_4)_2$ at current conditions (Refer to Figure 3-5). The

cobalt results reported did not show any significant deviation. If the stoichiometry is obeyed, 98 ppm would react in a 65 g/ℓ experiment. No noticeable cobalt precipitation is observed in Figure 5-16, to be discussed.

A lower temperature would possibly not increase arsenic scavenging, since industry phase 1 implied the opposite – a slightly increased arsenic precipitation was observed at 95 °C, compared to 75 °C.

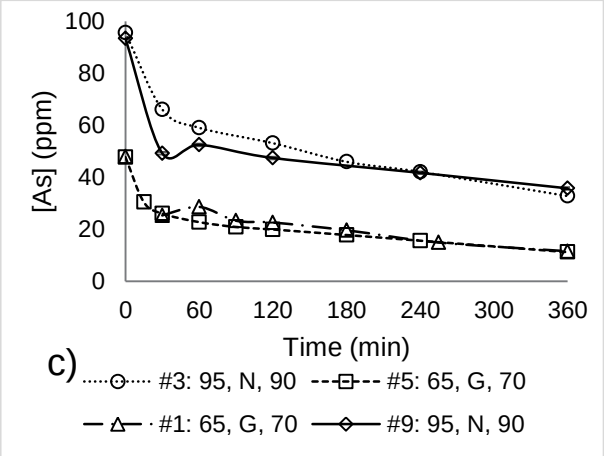

Figure 5-14: Fe(II) quadrant As comparison, with Run 3 and Run 9 at 90 °C & 95 g/ℓ total metals and Run 5 and Run 1 at 70 °C & 65 g/ℓ total metals.

The prevailing conditions of iron precipitation did not apply for arsenic precipitation. Only pH (A), iron valence (B) and total metals concentration (C) were significant during Anova analysis at 30 min. The discussion thereof does not add insight to above observations.

Arsenic precipitation would occur more readily than ferrous precipitation during the neutralisation of nickel sulphate solution.

5.2.3. Base metal precipitation

No noticeable entrainment of nickel or cobalt was observed. Graphs are given for nickel in Figure 5-15 and cobalt in Figure 5-16. Nickel and cobalt content remained constant in solution for the quadrants a) Fe(II) & pH 2.5, b) Fe(II) & pH 4.0 and c) Fe(III) & pH 2.5, within the measured experimental error. Base metal analysis of the Preparatory experimental base metals also didn't indicate any nickel or cobalt precipitation. The Preparatory experiments contained 100 g/ℓ nickel in synthetic solution. Gradual nickel entrainment onto the iron precipitate is not quantifiable within the experimental error since no gradual decrease of nickel in solution is observed.

Unintentional nickel and cobalt losses were controlled accordingly:

Local high-pH spots may form during rapid neutralising agent addition, especially when neutralising to pH 4.0 and when using a strong base. These local spots were visually observable as white spots on the liquid surface when the base and synthetic solution come into contact. Minimisation of the effect was achieved by diluting the NaOH. The dilution was optimised to ensure that experiments' total metals concentrations were not over diluted.

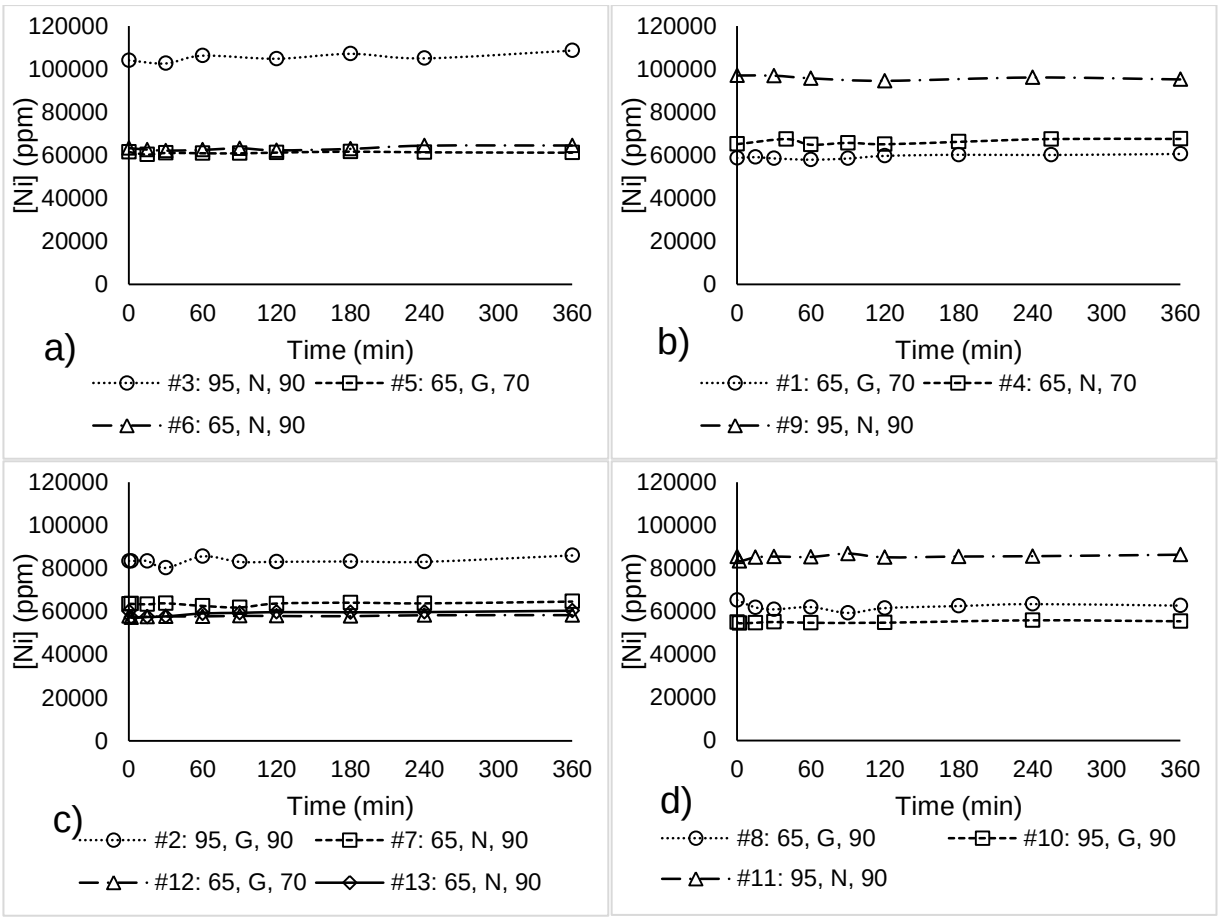

Figure 5-15: Ni over time during D-Optimal experiments at a) Fe(II) & pH 2.5, b) Fe(II) & pH 4.0, c) Fe(III) & pH 2.5 and d) Fe(III) & pH 4.0.

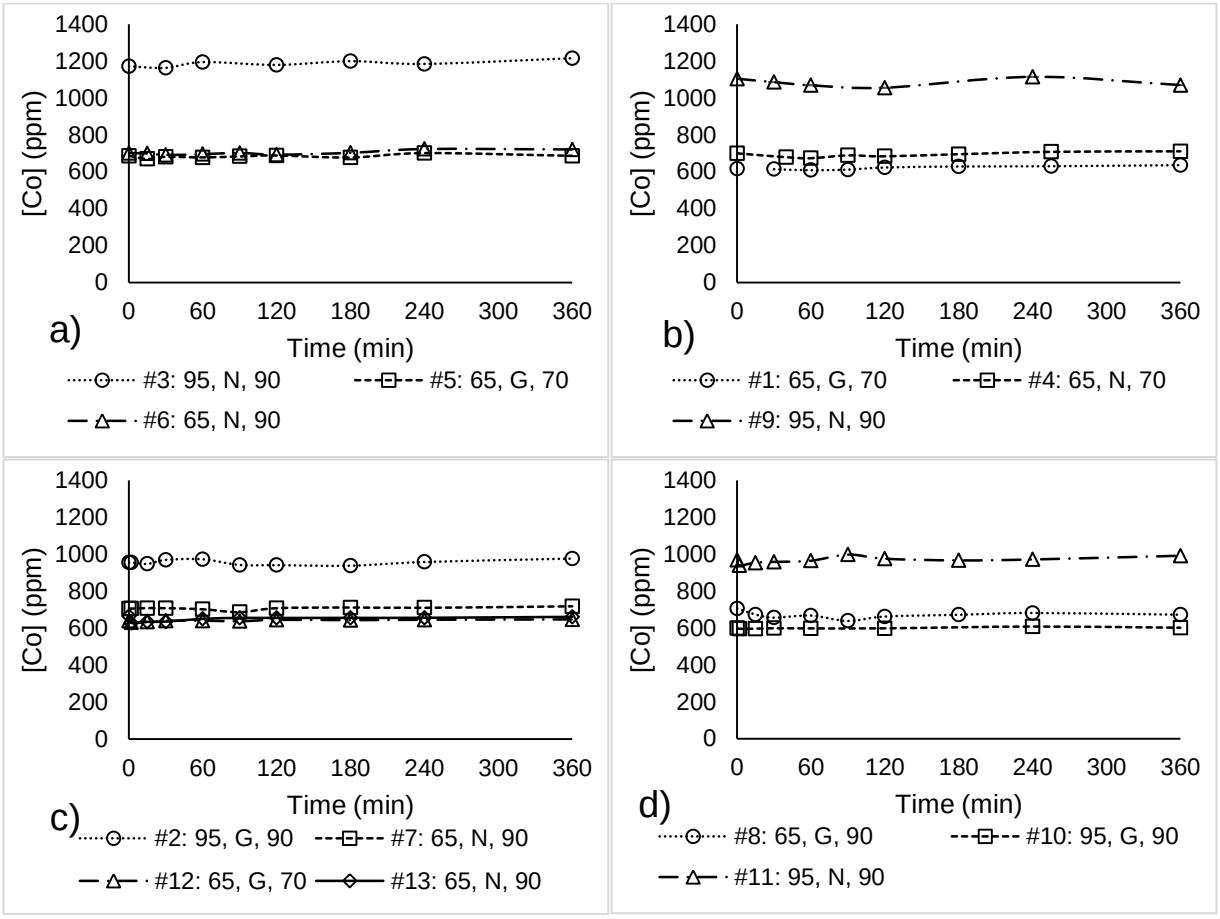

Figure 5-16: Co over time during D-Optimal experiments at a) Fe(II) & pH 2.5, b) Fe(II) & pH 4.0, c) Fe(III) & pH 2.5 and d) Fe(III) & pH 4.0.

The copper over time is presented in Figure 5-17. No gradual copper losses are observed at pH 2.5. A slight initial decrease of copper in solution is implied in pH 4.0 quadrants. Slight declines are observed, but fall within the experimental limit. Anomalies occurred in quadrant d): In Run 8, 36 % of the initial copper precipitated. Fluctuating copper content was also observed in Run 11, which stabilized to the initial value over time. An outlier in Run 1 (t = 180 min) is noted.

No noticeable copper entrainment was observed.

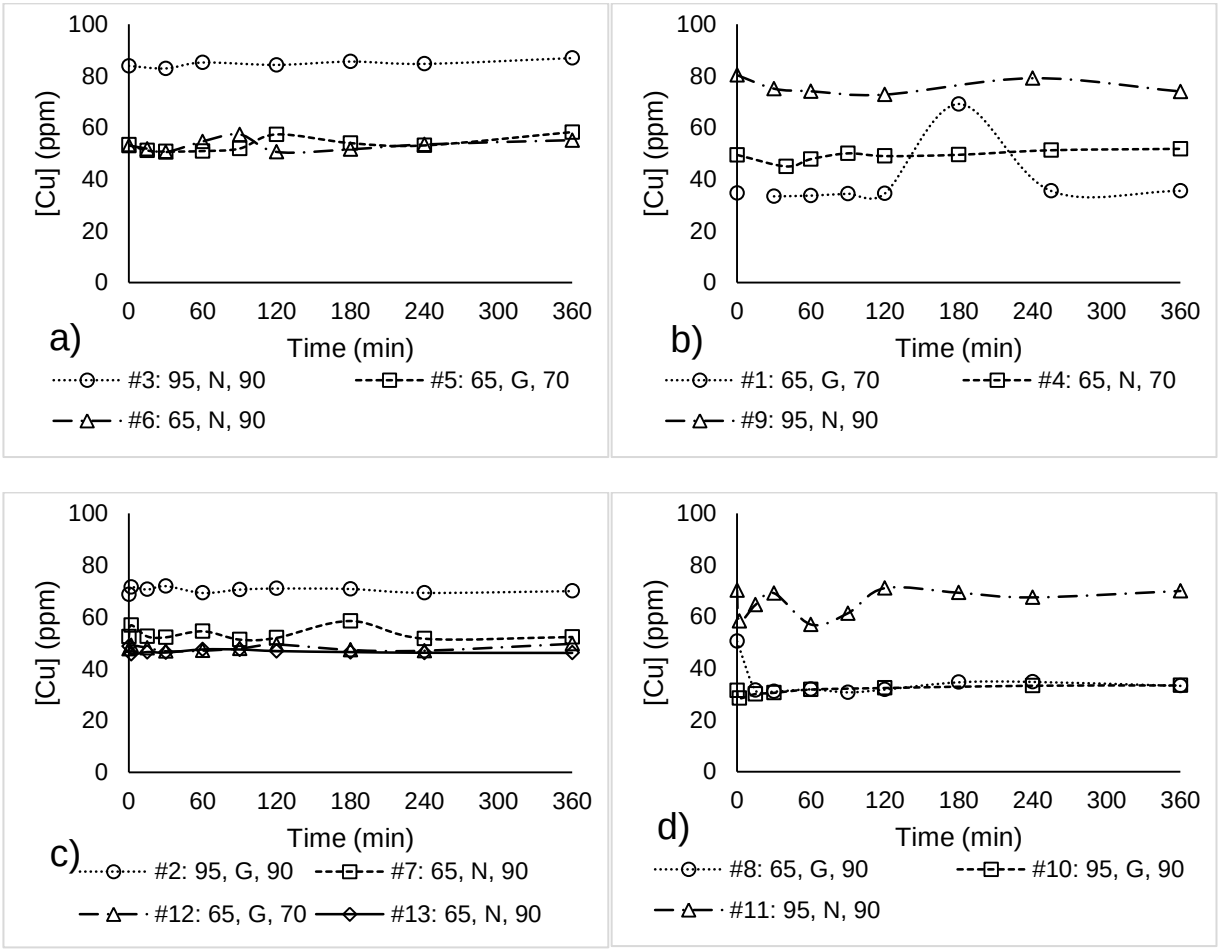

Figure 5-17: Cu over time during D-Optimal experiments at a) Fe(II) & pH 2.5, b) Fe(II) & pH 4.0, c) Fe(III) & pH 2.5 and d) Fe(III) & pH 4.0.

The anomalies in quadrant d) warranted further investigation. An additional experiment, with 50 ppm copper in sulphuric acid solution, was synthesized according to the standard method developed. This experiment was run at pH 4.0, T = 90 °C and with no seeding. Figure 5-18 presents the copper and pH over time. The synthetic solution's initial pH is also indicated. We observe 40 % copper precipitation as the neutralising agent was added between t = 0 min and 2 min, which correlates well with Run 8's 36 % loss.

This loss can therefore be attributed to the addition of neutralising agent to the system. Complete copper precipitation would not occur.

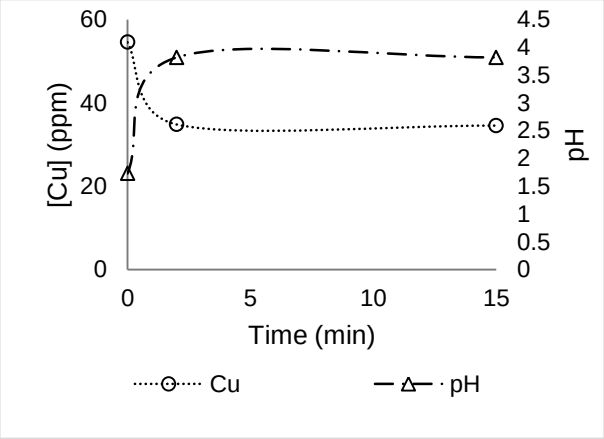

Figure 5-18: Cu-only experiment. [Cu] = 50 ppm.

5.2.4. Other precious metals precipitation

Ruthenium and rhodium concentration over time is given in Figure 5-19 and Figure 5-20, respectively. Partial to complete ruthenium and rhodium precipitation occurs at pH 2.5. Complete ruthenium and rhodium precipitation occurs at pH 4.0, regardless of the iron valence state present.

Overall, ruthenium precipitation was more complete than rhodium precipitation at pH 2.5. 70 % ruthenium precipitation occurred at pH 2.5 and 49 % rhodium precipitation occurred at pH 2.5, when taking the average. OPM precipitation in ferrous solution amounted 65 % ruthenium and 40 % rhodium and in ferric solution increased to 75 % ruthenium and 60 % rhodium.

Theoretically, if cation substitution is the mechanism of precipitation, 100 % of the investigated other precious metals can be structurally incorporated into goethite precipitate, yet a significant portion of OPM precipitation was observed in ferrous experimental runs.

Conflicting results are observed in runs at pH 2.5 with the synthetized nickel sulphate solution. Complete ruthenium precipitation was observed in Run 5 and Run 6, that cannot be described based on the variability of factors. Mass transport of NaOH in the solution might have been a limitation. It is believed that the rate of precipitation in both ferrous and ferric runs at pH 2.5 was mainly affected by the competition of eligible precipitating ions for the hydroxide ion.

Relatively more complete ruthenium and rhodium precipitation is noted at Fe(II) & pH 2.5 at lower OPM concentrations when compared to arsenic precipitation at these same conditions (refer to Figure 5-13).

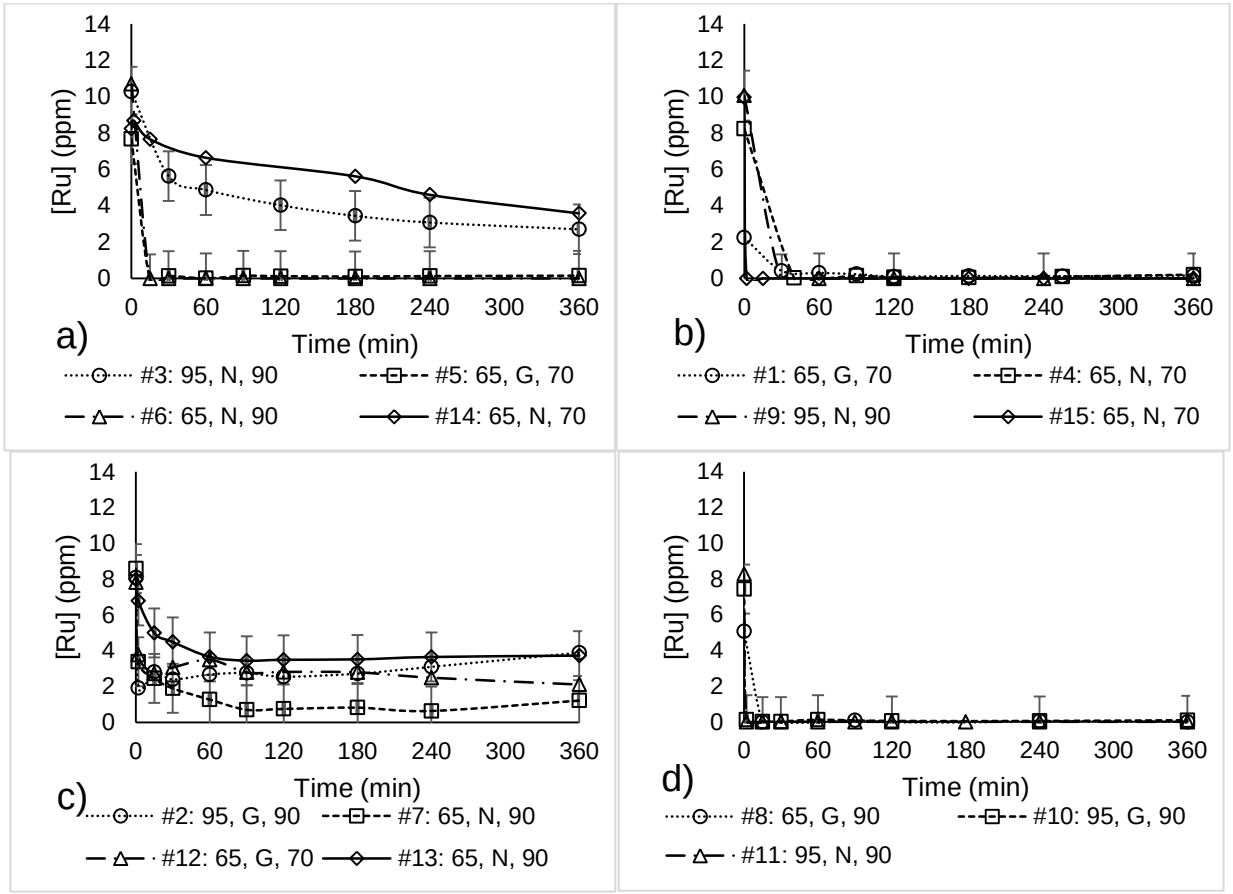

Figure 5-19: Ru over time during D-Optimal experiments at a) Fe(II) & pH 2.5, b) Fe(II) & pH 4.0, c) Fe(III) & pH 2.5 and d) Fe(III) & pH 4.0.

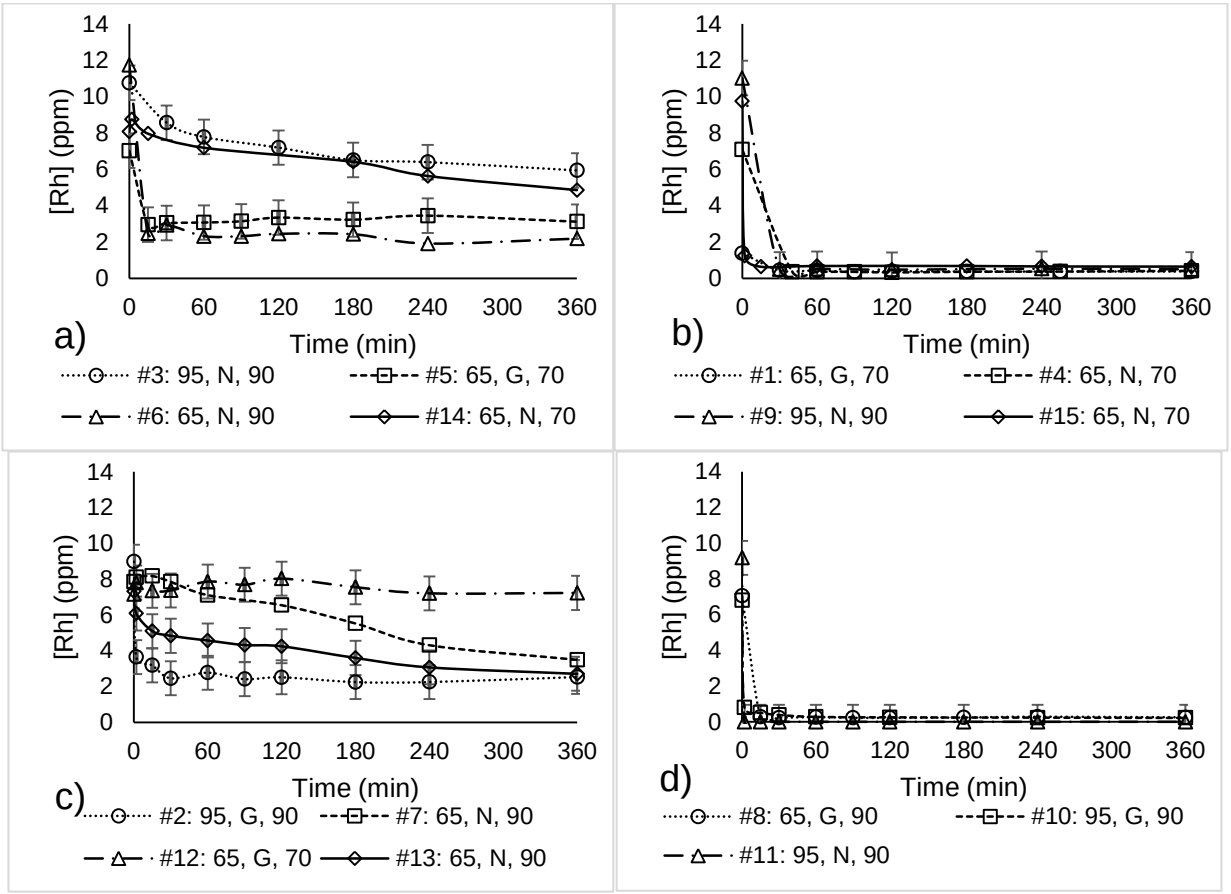

Figure 5-20: Rh over time during D-Optimal experiments at a) Fe(II) & pH 2.5, b) Fe(II) & pH 4.0, c) Fe(III) & pH 2.5 and d) Fe(III) & pH 4.0.

Factors pH (A) and temperature (D) were significant during D-Optimal analysis. An increase of temperature led to increased ruthenium and rhodium precipitation. Figure 5-21 is presented for the behaviour of ruthenium and rhodium with temperature at 30 min, as derived from statistical analysis. The Anova analysis is provided in Appendix D. A 32 % increase in ruthenium precipitation and a 36 % increase in rhodium precipitation when the solution temperature is increased from 70 °C to 90 °C.

During the industry experimental, temperature had no effect over the range of 75 °C to 95 °C in the absence of NaOH. The effect of temperature is coupled to the addition of NaOH.

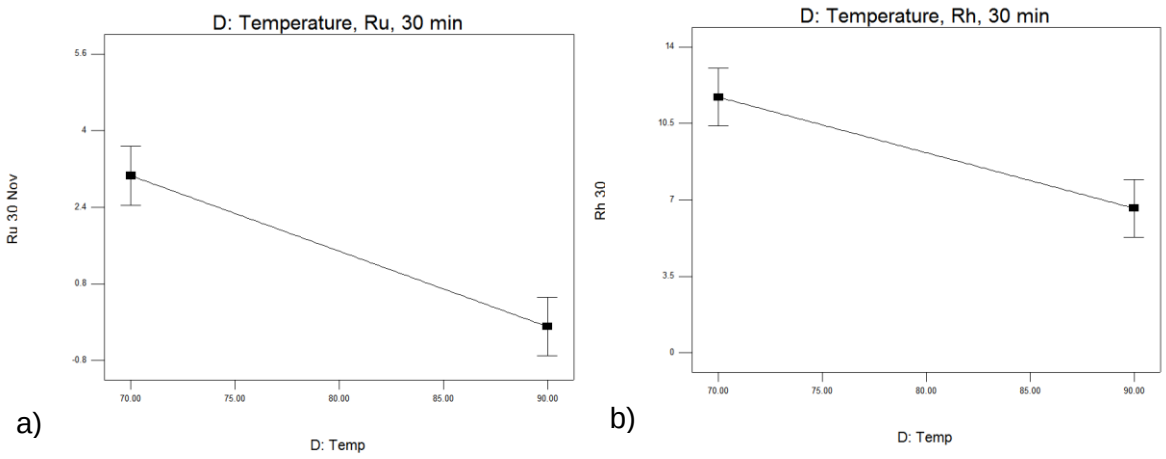

Figure 5-21: a) Ru and b) Rh content at 30 min and the effect of temperature thereon. Ferrous, no seeding and remaining factors averaged.

Statistical analysis predicted that ruthenium and rhodium precipitated more readily at lower total metals content at 30 min. The effect was minor (2 ppm difference) and inconsistent when observing data individually and was discarded to not have significance.

Seeding did not have a significant effect. Spectral interferences on the iridium band during ICP analysis, caused by the presence nickel and copper in the system, prevented the analysis of iridium in solution during D-Optimal experiments.

Recall the gradual 8 % ruthenium precipitation observed over 240 min with the addition 20 mg NaOH that raised the pH from pH 1.98 to pH 2.01, from the industry experimental phase 2. It is likely the addition of NaOH to the synthetic solution that led to ruthenium and rhodium precipitation at pH 2.5 and pH 4.0.

5.3. Other precious metals experimental

Figure 5-22 presents the other precious metal concentration over time during OPM Runs 1 to 4. The rapid ferric precipitation did increase the rate of OPM precipitation, yet equal OPM precipitation was observed between ferrous and ferric runs over 240 min. The amount of iron precipitated did not influence the quantity of OPMs precipitated. Iron content and pH over time are provided in Figure 5-23.

Initial precipitation, followed by gradual dissolution of iridium, occurred at pH 2.5. In OPM Run 1, 13 % iridium precipitation was observed at 15 min and gradual dissolution led to only 7 % iridium precipitation at 240 min. Similarly in OPM Run 3, 30 % initial precipitation at 15 min dissolved to 15 % iridium precipitation at 240 min. The dissolution of iridium suggests that its precipitated state is not thermodynamically stable.

Dissolution might be caused by the acid-forming nature of hydrolysis reactions of other ions present. Continued iron precipitation in OPM Run 1 and OPM Run 3 might lead to the destabilisation of iridium. Notably, the acid generation observed in Figure 5-23 is likely caused by the aging of meta-stable solid precipitates (Schwertmann & Carlson, 2005).

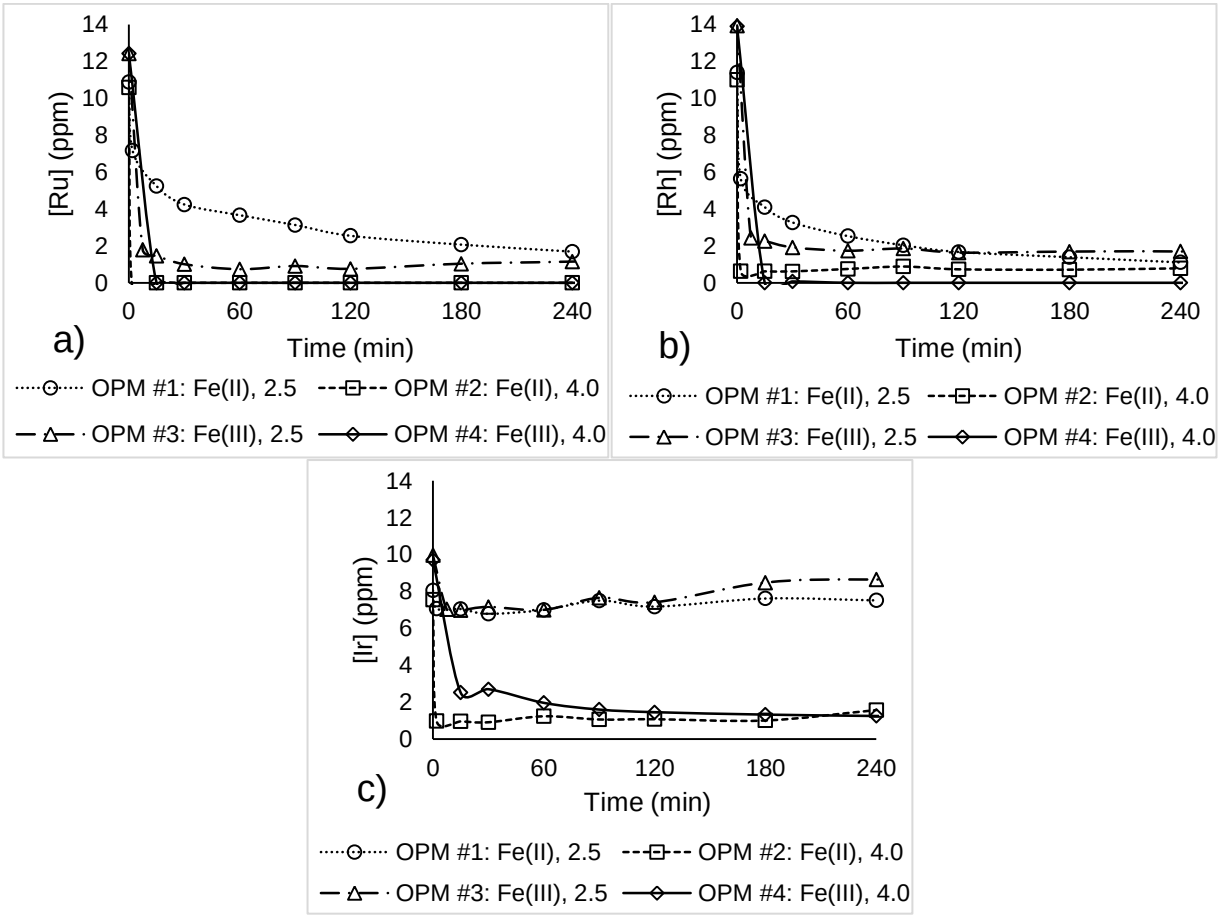

Figure 5-22: a) Ru, b) Rh and c) Ir over time in the OPM experimental.

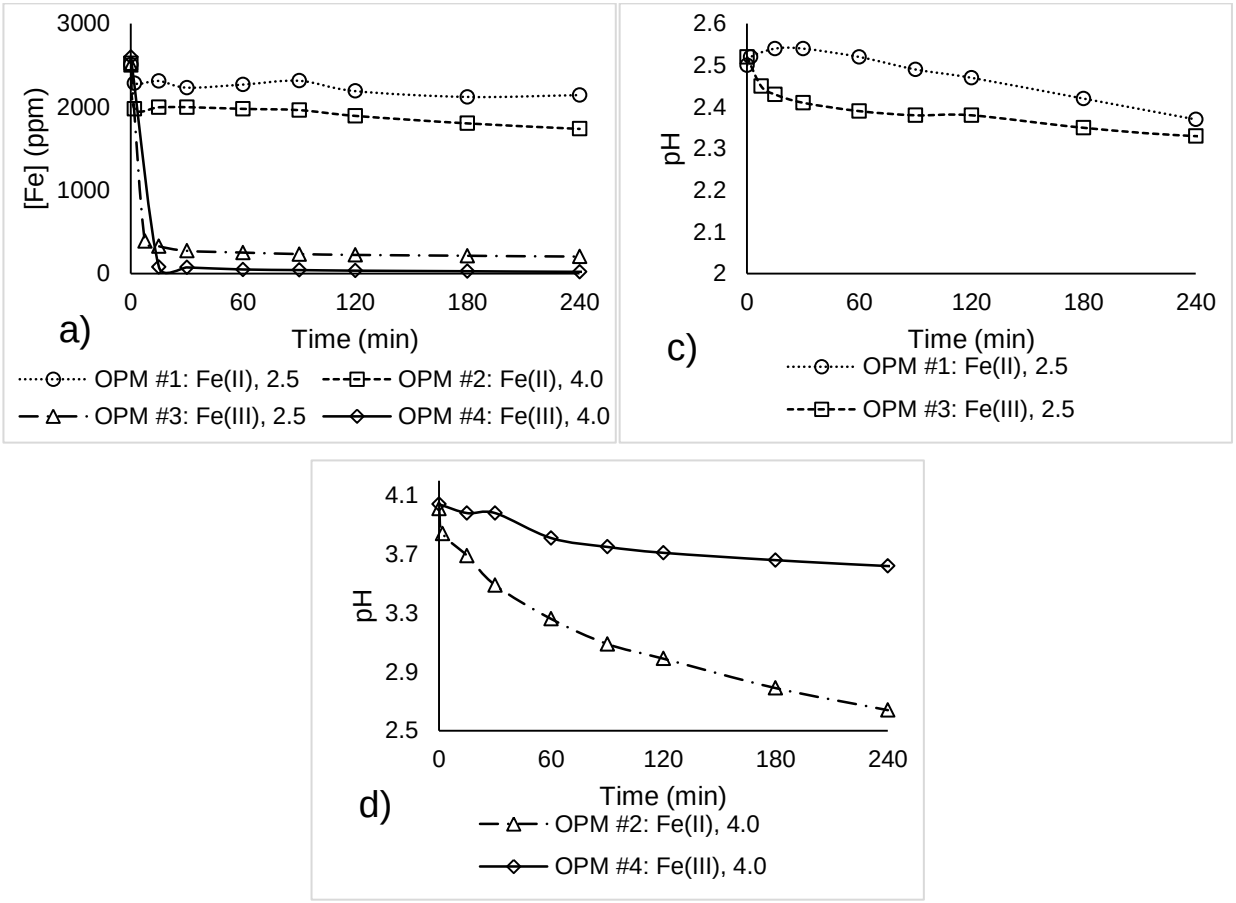

Figure 5-23: Fe and pH over time in the OPM experimental. a) Fe, b) pH 2.5 runs and c) pH 4.0 runs.

Ruthenium and rhodium precipitation rates were largely similar in ferrous and ferric experiments, except when in the complete absence of iron. OPM Run 5's solution consisted of only copper and other precious metals. OPM Run 5's data is presented in Figure 5-24. Immediate ruthenium precipitation is observed, while the rate of rhodium precipitation was more gradual. Complete rhodium precipitation was however achieved after 240 min.

Slight copper precipitation is noted during neutralisation, yet the loss is comparatively lower than the copper-only run's copper loss in Figure 5-18. The relatively lower copper precipitation in OPM Run 5 might be due competition with OPMs for hydroxide ions. Iridium spectral interferences, due to copper presence, prevented the analysis of iridium in OPM Run 5.

The rate of other precious metals precipitation is rapid in the presence of ferric precipitation. The rate of OPM precipitation is slower in the presence of ferrous, yet would result in the same amount of OPM precipitation from ferric runs over 240 min. In the complete absence of iron, effective ruthenium and rhodium precipitation was obtained, but the rate of rhodium precipitation decreased.

Comparison of other precious metals precipitation rates indicate that ruthenium precipitates more readily than rhodium, while iridium precipitation is the slowest. Redissolution of iridium is observed at pH 2.5, but at pH 4.0, almost all iridium precipitated.

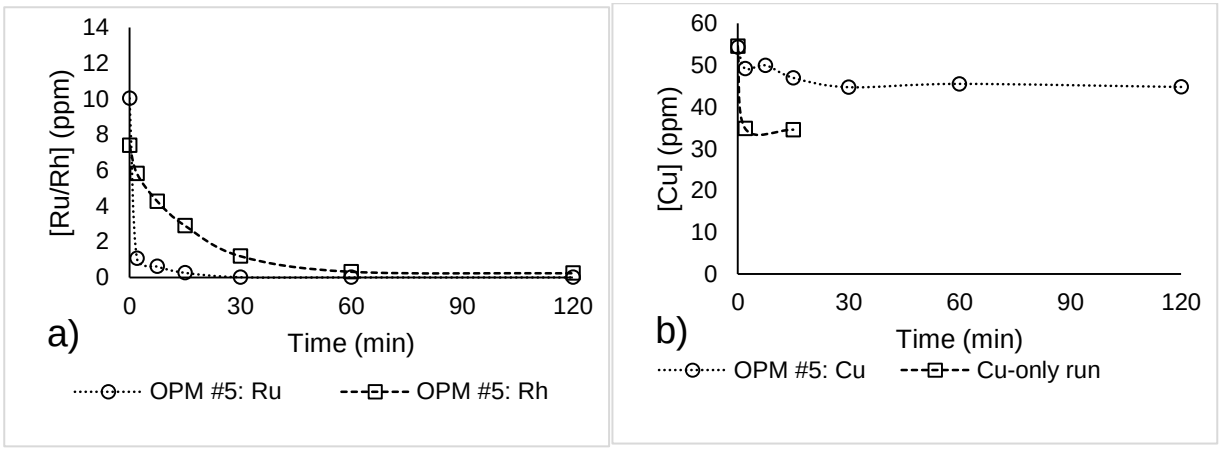

Figure 5-24: Cu-OPM Run 5 at pH 4.0 a) Ru and Rh over time and b) Cu over time, compared to the Cu-only run.

The hypothesis that other precious metals might be cation substituted into the iron lattice was rejected, based on the grounds that OPMs could precipitate in the absence of iron in solution.

Instead, the rapid rates of ruthenium and rhodium precipitation are comparable to the characteristic rate of simple monomolecular hydrolysis (Baes & Mesmer, 1976). It suggests that the hydrolysed complex was sufficiently insoluble to precipitate out. Polymolecular hydrolysis of PGMs would likely have a very slow rate, if present (Baes & Mesmer, 1976).

5.4. Seeding experimental

Section 5.4.1 discusses the particle size and surface area characterisation of goethite seed material. Section 5.4.2 onwards discusses the screening liquid experiments with increased goethite material.

5.4.1. Particle size and surface area characterisation

The particle size distributions (PSD) are provided collectively in Figure 5-25. The dry reference goethite sample, a), exhibits a monomodal PSD with a normally distributed curve at d_{50} = 1.3 µm. During repeated tests, an additional peak formed during ultrasound at 13 µm. The reason behind the gradual increase of this formation product is unknown but suspected to be an anomaly and was discarded.

It is evident that particle growth occurred during ferric precipitation reactions, Figure 5-25 b). Ferric precipitation particles have a negative skew distribution with d_{50} = 100.6 µm. The precipitation of goethite seed led to growth and agglomeration that didn't disperse during pulping or ultrasound. The actual grown particles in the ferric system were bigger than 100 µm, considering that 106 µm dry-sieving was implemented prior to particle size analysis to remove clumps.

The particles didn't grow in ferrous experiments, Figure 5-25 c), and no noticeable alteration can be observed. The consistency of goethite seed in ferrous experiments therefore acts as control experiments, advocating the growth observed in ferric precipitation reactions. The peak at 5.7 µm is most likely agglomeration. Agitation, at 600 rpm, was mild and did not cause particle breakage.

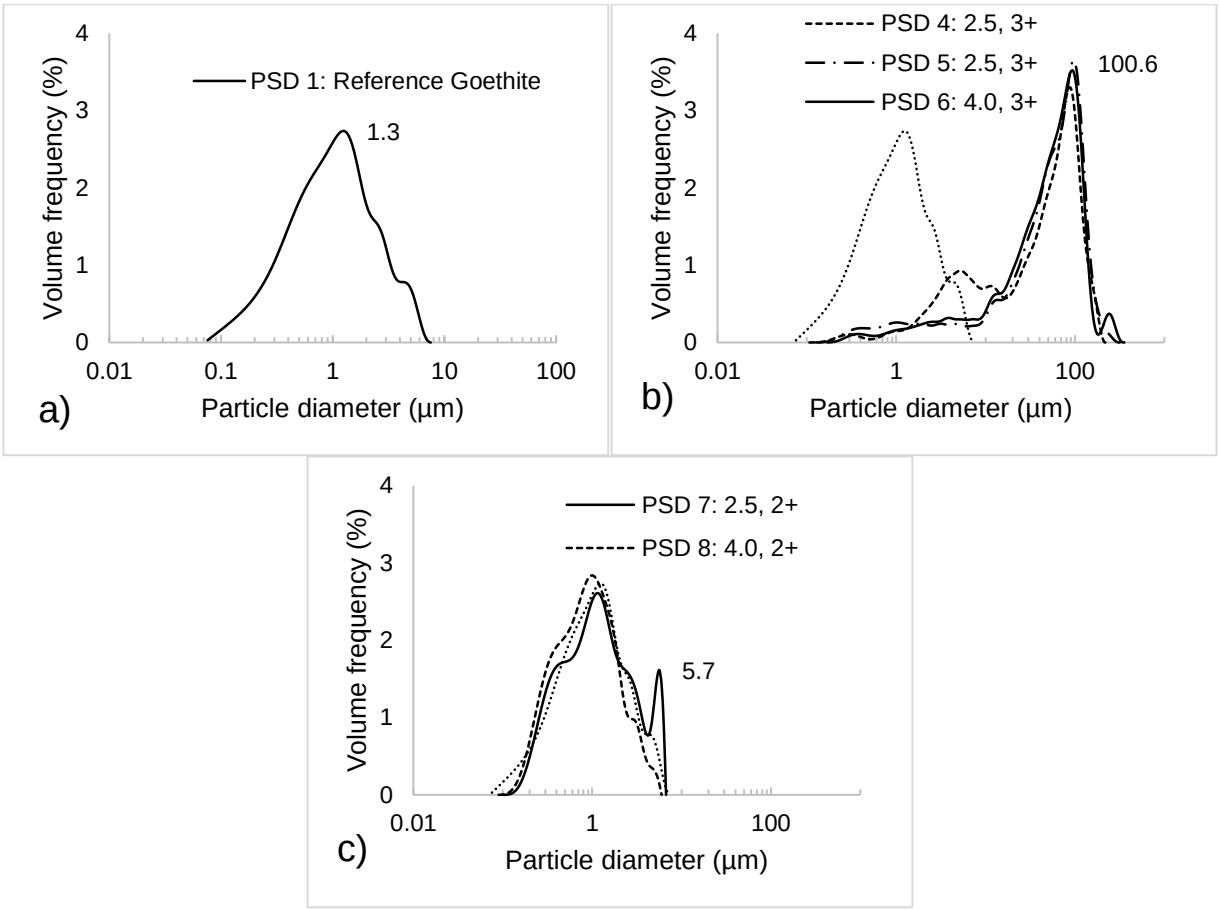

Figure 5-25: Particle size distribution for goethite seeded experiments with a) reference goethite, b) goethite seeded runs with Fe(III) and c) goethite seeded runs with Fe(II).

The particle size distribution for the iron precipitated without goethite seed is given in Figure 5-26. The particles that precipitated freely appear to be less fine in general. Note that this sample has not been sieved with a 106 µm sieve. About 48 % of the sample was bigger than 106 µm.

Even though the particle size is larger, its filterability was significantly worse than that of seeded experiments.

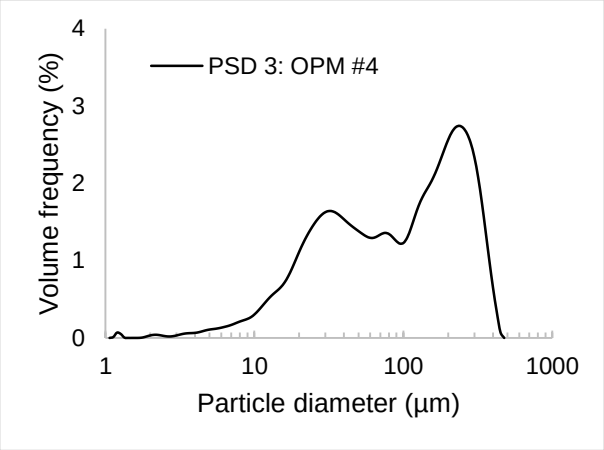

Figure 5-26: Particle size distribution for the Fe precipitated in OPM Run 4 with Fe(III) & pH 4.0.

The BET surface areas obtained is listed in Table 5-5. The reference goethite sample (PSD 1) had a BET surface area of 131.0 m^2/g. Goethite surface area is considered high in the range of 80 m^2/g to 150 m^2/g (Cornell & Schwertmann, 2003). The surface area is equally distributed between micropores and the external surface area. Micropores are molecular size pores sized less than 20 Å, mesopores range between 20 Å to 500 Å and macropores are larger than 500 Å (Rouquerol *et al.*, 1994).

Two methods of commercial hematite production exist (Cornell & Schwertmann, 2003). The surface area would be < 5 m^2/g when produced via calcination at 800 °C to 900 °C and can be up to 200 m^2/g, when produced via dehydroxylation of goethite below 600 °C. The reference hematite (PSD 2) had a very low surface area, indicated no porosity and it is therefore likely produced via calcination. The low surface area availability made hematite an unlikely agent for growth and adsorption. No liquid experiments were planned with hematite seed.

PSD 3, which precipitated from ferric-OPM solution, has a BET surface area of 215.8 m^2/g. PSD 3 is characterised as ferrihydrite in the SEM analysis section to follow. The expected surface areas of ferrihydrite compounds vary from 100 m^2/g to 700 m^2/g (Cornell & Schwertmann, 2003). Ferrihydrite forms fine agglomerated particles, which is expected to be microporous, yet PSD 3 indicates no porosity.

Table 5-5: BET surface area and deBoer t-plot results.

Sample name	Reference	Iron precipitation	BET surface area [m^2/g]	Micropore surface area [m^2/g]	External surface area [m^2/g]
PSD 1	Reference goethite	n/a	131.0	66.2	64.8
PSD 2	Reference hematite	n/a	6.3	0.0	6.3
PSD 3 (SEM 5)	OPM Run 4: Fe(III) & pH 4.0	100 %	215.8	0.0	216.6
PSD 4	#2: 2.5, 3+, 95 g/ℓ, 90°	75 %	100.6	44.3	56.3
PSD 5	#12: 2.5, 3+, 65 g/ℓ, 70°	69 %	82.0	43.9	38.1
PSD 6 (SEM 4)	#8: 4.0, 3+, 65 g/ℓ, 90°	100 %	156.5	64.0	92.6
PSD 7	#5: 2.5, 2+, 65 g/ℓ, 70°	1 %	126.2	72.8	53.4
PSD 8	#1: 4.0, 2+, 65 g/ℓ, 70°	9 %	136.1	87.1	49.0

The reference goethite contains an equal distribution of micropore surface area and external surface area, which can be considered two different active sites available for particle growth and adsorption. The number of active sites are fixed per seeded experiment. A decline in micropore surface area or external surface area suggests site level adsorption or growth occurring on the corresponding active sites.

The net BET surface area of ferrous experiments, PSD 7 and PSD 8, are roughly (± 5 m^2/g) the same as that of reference goethite, yet had increased micropore surface area and decreased external surface areas. The external surface area decrease implies growth and adsorption occurring on external surface area. The increased micropore surface area observed suggests the goethite particles undergo chemical weathering, leading to pore formation, in the acidic solution.

The total BET surface area declined in ferric experiments PSD 4 and PSD 5, due to a decrease of micropore surface area and external surface area of particles. PSD 6 had an increase BET surface area, with micropore surface area unchanged and an increased external surface area observed.

Figure 5-27 refers to the liquid experiment's iron content over time. pH 2.5 runs PSD 4 and PSD 5's iron content over time were very similar. The residual iron content is similar yet PSD 4 originates from concentrated solution (95 g/ℓ). Concentrated solutions were seeded with relatively more seed to maintain a 2:1 seed to Fe in solution ratio. More seed was present in PSD 4, but per active sites less had iron growth on active sites.

A decline in total surface area was caused by particle growth at pH 2.5. PSD 5's relatively lower external surface area and BET surface area was due to more growth sites occupied. Micropore surface area declined by a third, but not to the extent of freely precipitated iron (PSD 2) where no micropore surface area was recorded.

PSD 6's increase of BET surface area at pH 4.0 can be ascribed to the instantaneous iron precipitation that caused poor ordering of crystal structure and lead to a more amorphous surface area.

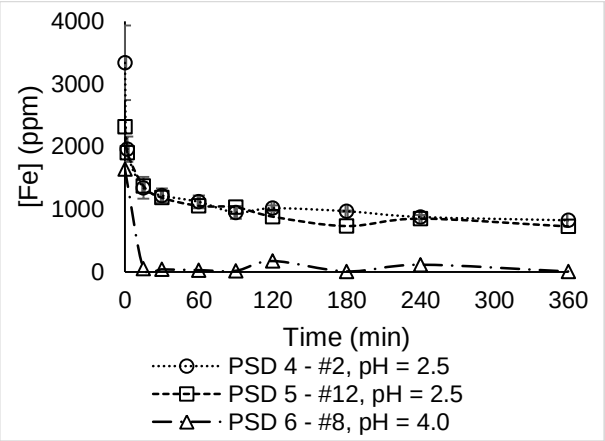

Figure 5-27: Fe content over time for PSD 4 to PSD 6.

5.4.2. Iron, arsenic, OPM and copper precipitation

Figure 5-28 presents the seeding experimental iron over time. All screening experiments were conducted with ferrous at 65 g/ℓ total metals and 70 °C. The total metals content at 50 g/ℓ goethite seed experiments were 20 % lower than that of 10 g/ℓ and unseeded experiments. 200 mℓ deionised water (RO water) was required to pulp and administer the 50 g/ℓ seed.

No gradual ferrous scavenging or increased iron precipitation over time were noted at pH 2.5 and pH 4.0 in the presence of 50 g/ℓ seed material. There is no substantial benefit to use goethite seeding if the purpose is to scavenge iron from solution.

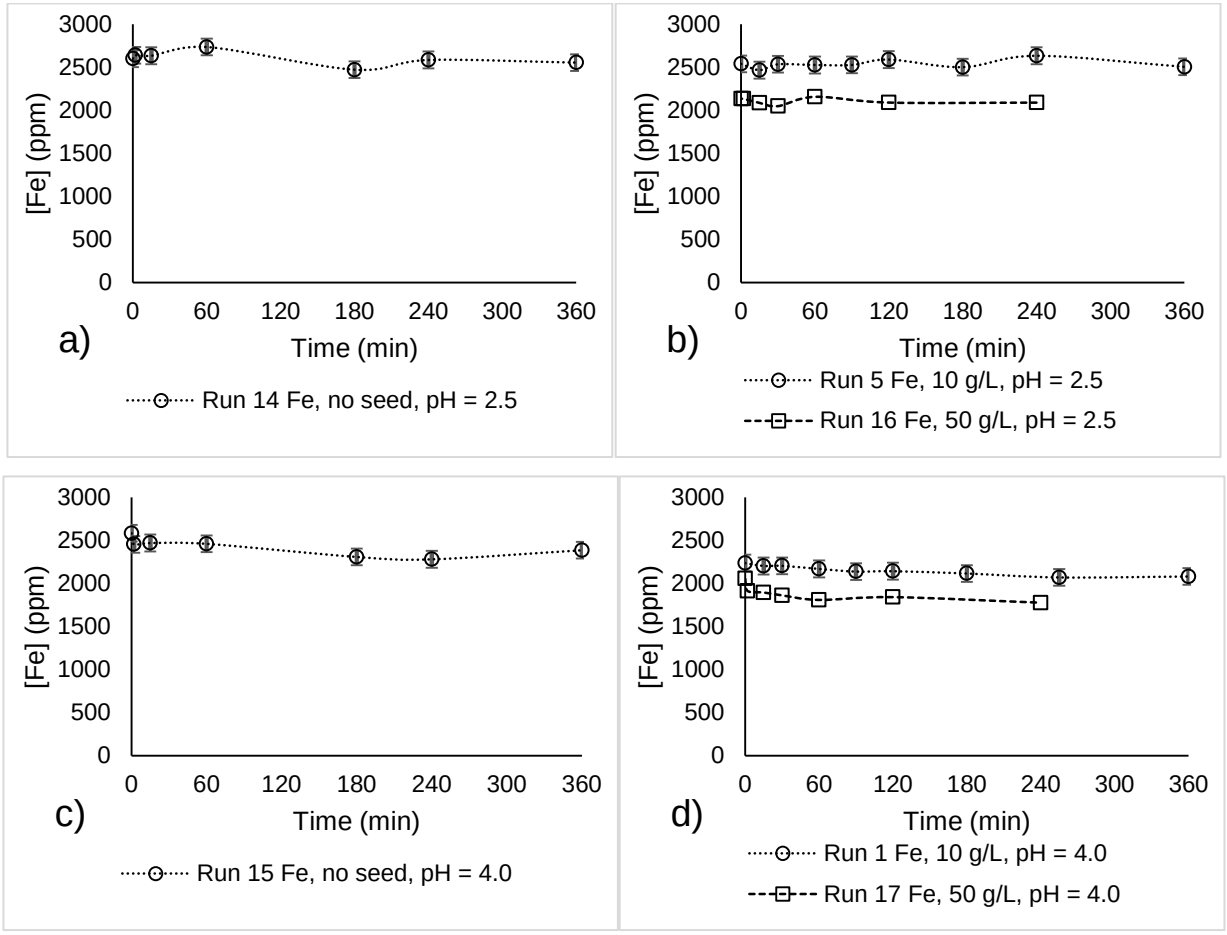

Figure 5-28: Seeding experimental Fe over time. a) and c) with no seed at pH 2.5 and pH 4.0. b) and d) with 10 gℓ and 50 g/ℓ seed at pH 2.5 and pH 4.0.

Arsenic over time in the Seeding experimental is presented in Figure 5-29. 50 g/ℓ seeding increased the scavenging of arsenic at pH 2.5. Arsenic appears to precipitate faster at pH 4.0 with 50 g/ℓ seed, but may be exaggerated due to the dilution induced by the addition of pulped seed material. Arsenic precipitation was not affected by pH in Screening experiments.

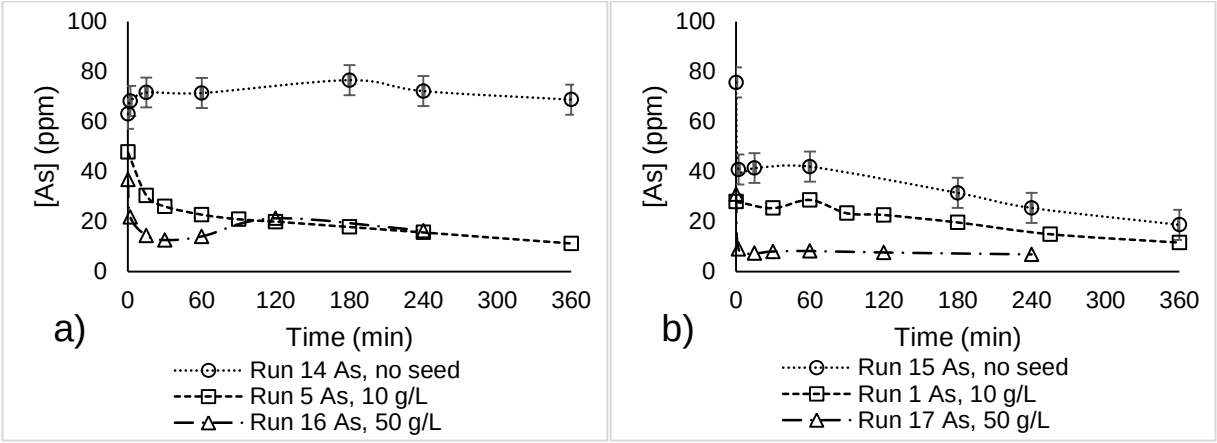

Figure 5-29: As over time in the Seeding experimental. a) pH 2.5 and b) pH 4.0.

Ruthenium and rhodium are presented over time in Figure 5-30. Run 16, with 50 g/ℓ seeding, did not cause any noticeable scavenging of ruthenium and rhodium content. Ruthenium and rhodium behaved similar in Run 5: no seed and Run 16: 50 g/ℓ seed. As with screening experiments, A pH of 4.0 led to complete ruthenium and rhodium precipitation. It is highly unlikely that the more unreactive iridium would behave differently. The presence of seed material did not aid the scavenging of OPMs.

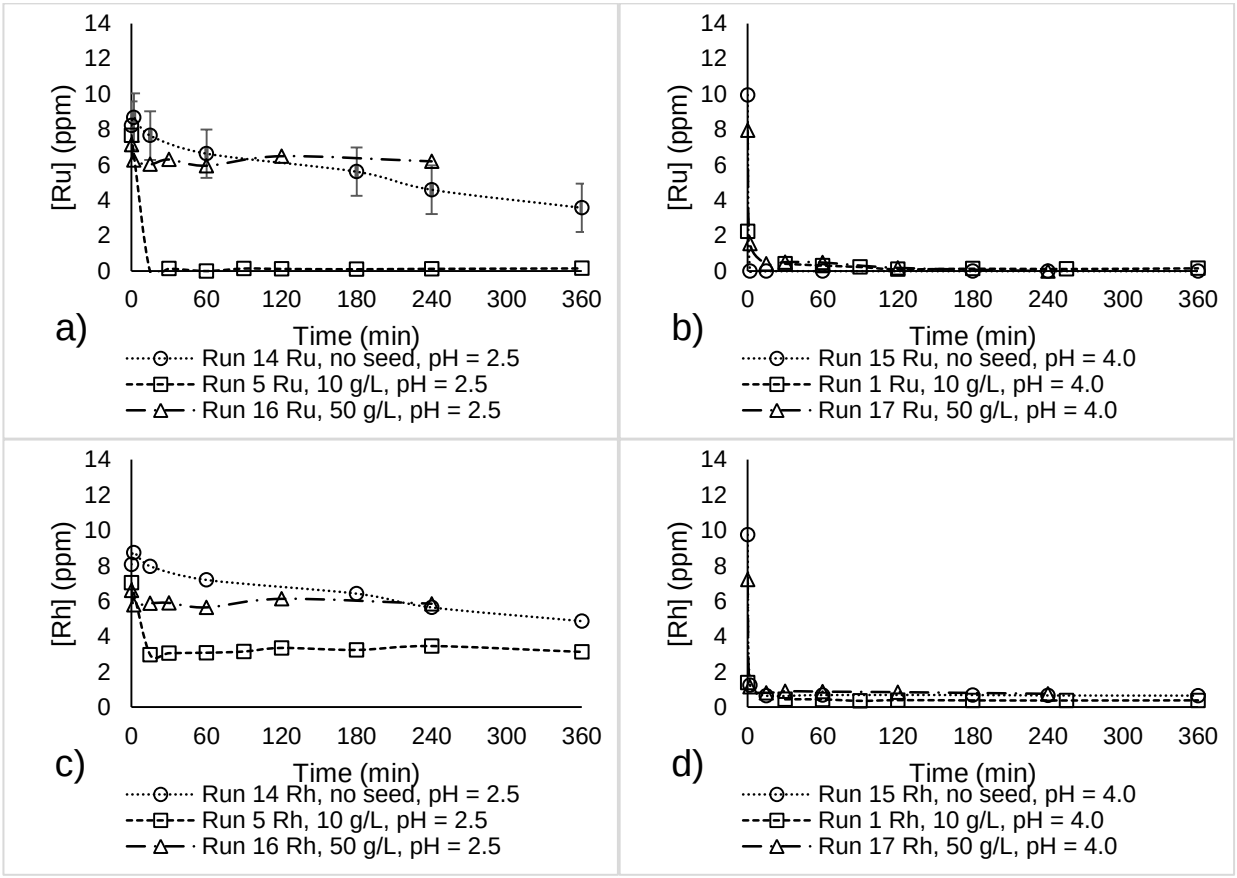

Figure 5-30: Ru and Rh over time in the Seeding experimental. With a) Ru at pH 2.5, b) Ru at pH 4.0, c) Rh at pH 2.5 and d) Rh at pH 4.0.

During no seeding and 10 g/ℓ seeding no appreciable copper collection occurred. Noticeable copper collection occurred in Run 17: pH 4.0 & 50 g/ℓ seeding. The copper content dropped after addition of neutralising agent from 48 ppm to 16 ppm. The 66 % copper precipitation observed is lower than observed in the copper-only experiment (40 %) in Figure 5-18. The copper over time for Run 16 and Run 17 are given in Figure 5-31.

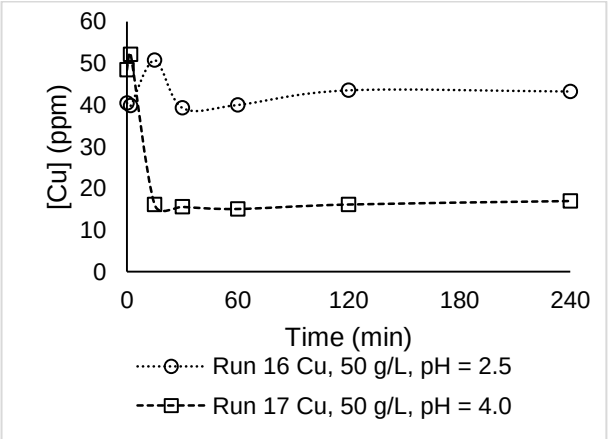

Figure 5-31: Cu in 50 g/ℓ seeded experiments.

5.5. Solid characterisation

5.5.1. Other precious metals experimental solids

Figure 5-32 presents the bulk composition of Sample 1's via back-scatter imaging (BSE). Sample 1 presents OPM Run 1's solid, precipitated from ferrous-OPM solution at pH 2.5. Three distinct iron oxide phases were observed, named the bulk, brittle and dense phases. Apart from the observation of different phases, solids were homogeneous in composition.

Energy dispersive X-ray spectroscopy mapping of samples areas (EDS) revealed the occurrence of individual iridium phases. The iridium phases were very dense and could be readily observed, defined as "Ir spots" in Figure 5-32. The image shown right has an iridium phase in the centre, which possibly acted as growth surface for the bulk iron oxide phase. This observation was consistent for iridium in all other samples. Additional SEM images are provided in Appendix A.5. Iridium was either present as independent particles, or was enveloped with the bulk iron oxide phase, as seen below.

Ruthenium and rhodium were only observed in low quantities as part of iron oxide phases. OPM-bearing iron oxide phases were observed with varying ruthenium and rhodium content.

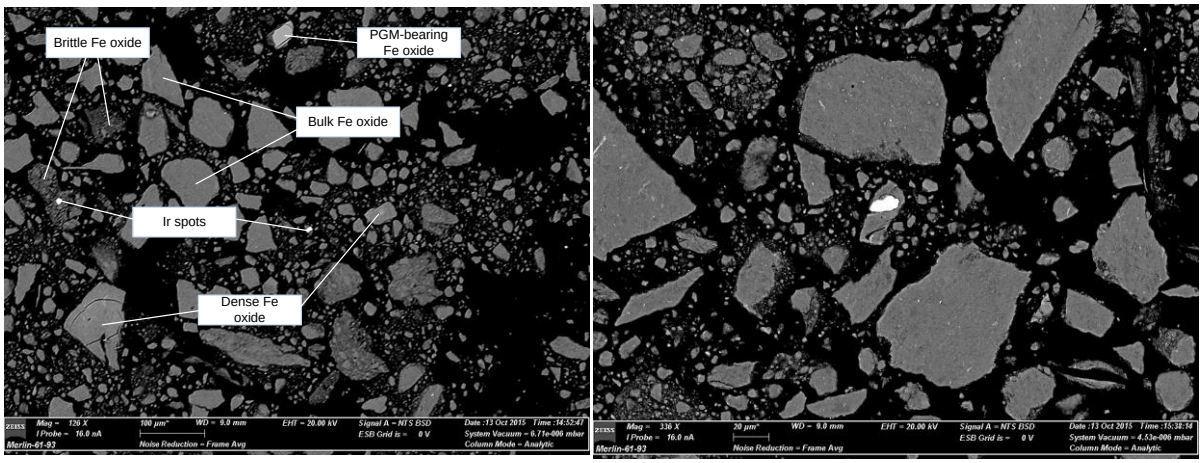

Figure 5-32: Bulk composition BSE image (left) and Magnified BSE image (right) of Sample 1: Fe(II) & pH 2.5.

Table 5-6 presents the elemental compositions of the defined phases. The bulk and brittle iron oxide phases are very similar. The Dense phase indicated the highest iron content and lowest incorporation of anionic impurities, i.e. sulphate and chloride. The Brittle phase is characterised by the lowest relative iron content and the presence of the most anionic impurities.

Table 5-6: Elemental composition (wt.%) of Sample 1 phases via EDS analysis. Fe(II) & pH 2.5.

	Fe	O	S	Cl	Ru	Rh	Ir
Bulk Fe oxide	54.9±0.4	40.4±0.1	3.7±0.1	0.5±0.1			
Brittle Fe oxide	53.4±0.7	40.7±0	4.1±0.1	1±0.2			
Dense Fe oxide	58.1±0.2	39.3±0.1	2.5±0.2				
Ir phase	2±0.5	13.1±0.1		23.3±1.8			60.5±2.9
OPM-bearing Fe oxide	44.6±1	48.7±0.4	3.1±0.7	0.5±0.3	0.7±0.2	2.4±0.2	

The three iron phases correspond stoichiometrically well with the structural formula of schwertmannite and ferrihydrite. Bingham et al. (1996) remarked that some of the sulphur content present in schwertmannite and ferrihydrite compounds may not be a structurally incorporated into the crystal lattice and can be adsorbed onto the iron oxide surface, yet no easy method exists to determine whether it is structurally incorporated or not. The Bulk and Brittle iron oxide phases are similar and can be considered the predominant phase in this sample.

The iridium phases observed are approximately 5 µm in size. The most abundant iridium phase consists of 60.5 % iridium, 23.3 % chloride and 11.6 % oxygen. The following stoichiometry can be deducted from the elemental data: $IrCl_{1.8}O_2$, considering the octahedral configuration of OPMs. Thermodynamic modelling suggested $IrCl_6^{3-}$ to be the predominant iridium ion at current conditions, and $IrCl_2(OH).3H_2O$ would be the speculative, electric charge balanced product.

The theoretical elemental weight distribution of possible minerals is given in Table 5-7. All sulphur content implies sulphate ions.

Table 5-7: Theoretical mineral elemental weight distribution (%) of expected minerals.

Name	Formula	Fe	O	S	H	Na	As
Magnetite	Fe_3O_4	72%	28%				
Hematite	Fe_2O_3	70%	30%				
Goethite	FeOOH	64%	36%		1%		
Ferrihydrite	$Fe_5HO_8.4H_2O$	58%	40%		2%		
Schwertmannite	$Fe_8O_8(OH)_6SO_4$	58%	37%	4%	1%		
Bernalite	$Fe(OH)_3$	52%	45%		3%		
Natrojarosite	$NaFe_3(OH)_6(SO_4)_2$.	33%	48%	13%	1%	5%	
Basic Ferric Sulphate	$Fe(SO_4)(OH)$	33%	47%	19%	1%		
Scorodite	$FeAsO_4.2H_2O$	24%	42%		2%		32%
Jarosite (H3O)	$(H_3O)Fe_3(OH)_6(SO_4)_2$	35%	50%	13%	2%		
Rhomboclase	$H_5FeO_2(SO_4)_2$.$2H_2O$	17%	60%	20%	3%		

Figure 5-33 provides a secondary electron (SE) image for Sample 1. Granular spheres are observed with a crystal size ranging between 50 – 100 nm in size. Compact aggregation of crystals are observed. The observed crystals have the structural qualities of both ferrihydrite and schwertmannite. It compares well with schwertmannite synthesized by Schwertmann and Carlson (2005) and ferrihydrite presented in Cornell and Schwertmann (2003). Homogeneous

nucleation likely leads to the small crystal structures observed. Crystals in the present sample are about a 100 times smaller than the crystals synthesized at 25 °C by Schwertmann and Carlson (2005). Distinction cannot be made on elemental composition alone. Natrojarosite can also form aggregated crystals, yet with more rigidity (Dutrizac & Chen, 2004).

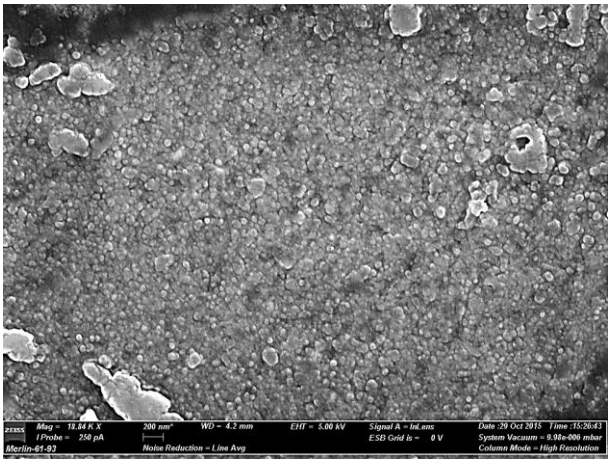

Figure 5-33: Magnified SE image of Sample 1: Fe(II) & pH 2.5.

Growth of iron oxide phase around foreign material was observed in Figure 5-34. The zirconium impurity possibly acted as a heterogeneous nucleation and growth site for the bulk iron oxide that surrounds it.

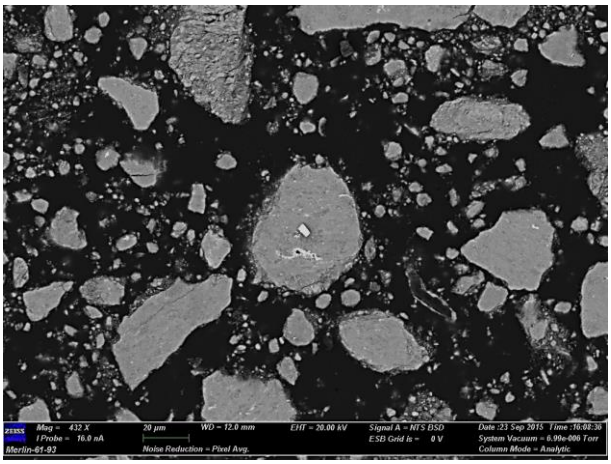

Figure 5-34: BSE image of a Zr impurity in precipitation Sample 1: Fe(II) & pH 2.5.

A highly heterogeneous iron precipitate was formed in Sample 2 from Fe(II) & pH 4.0, as given in Figure 5-35. Three distinctly different porous, micro-scale phases were observed. The elemental composition of defined phases is given in Table 5-8. Dense iron oxide phases, of 5 µm particle size, did not contain any sulphate or chloride ions. The 1 µm unit particle size medium-dense and dark bulk iron oxide phases contained the same quantity of sulphate and chloride ions. The bulk iron oxide phase indicated the consistent presence of OPMs.

The lowest density phase is an unusual location for other precious metals considering their high molecular weights. OPM precipitation was established to precipitate largely independent of iron precipitation during the OPM experimental. Its dispersed presence in the bulk iron phase indicates that initial ferric precipitation is faster and aggregation can capture the OPM solids during its precipitation.

It can be hypothesized that the bright iron phases are the initial nucleated iron oxides, on which the bulk iron oxides agglomerated to, considering the porous structure observed. All three phases are most likely ferrihydrite compounds.

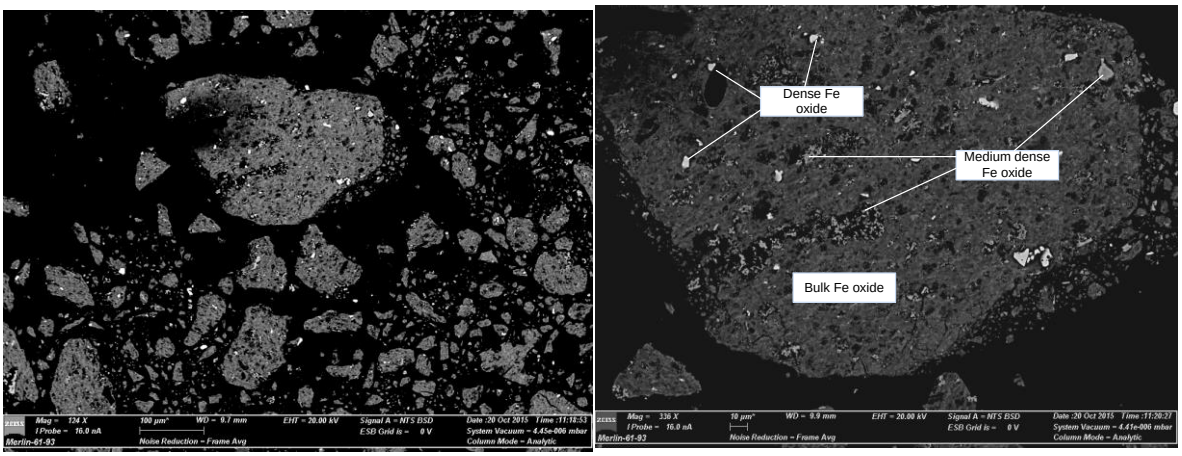

Figure 5-35: Bulk composition BSE image (left) and Magnified BSE image (right) of Sample 2: Fe(II) & pH 4.0.

Table 5-8: Elemental composition (wt.%) of Sample 2 phases: Fe(II) & pH 4.0.

	Fe	O	S	Cl	Ru	Rh	Ir
Dense Fe oxide	55.3±0.4	44.7±0.2					
Medium dense Fe oxide	56.2±0	38.2±0	1.9±0.1	0.3±0			
Bulk Fe oxide	55.1±0.4	37.8±0.2	1.9±0.1	0.3±0.1	1.5±0.2	1.4±0.2	1.2±0

The SE image of Sample 2 is given in Figure 5-36. Similar spherical aggregates are observed in Sample 2.

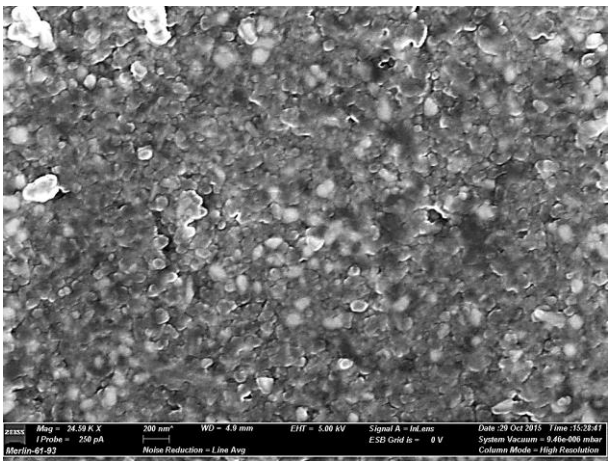

Figure 5-36: Magnified SE image of Sample 2: Fe(II) & pH 4.0.

Sample 3's diffractogram is presented in Figure 5-37. Sample 3 originates from ferric-OPM solution at pH 2.5. Conventional peak matching could not characterise the amorphous iron oxide. Sample 3 was compared to diffractograms reported by Yu *et al.* (2002), Cornell and Schwertmann (2003), Schwertmann and Carlson (2005), Das and Jim Hendry (2011) and Bazilevskaya *et al.* (2012). It is deducted that Sample 3 is a hybrid between poorly-crystalline goethite and schwertmannite, but may also contain some ferrihydrite. The matched parameters rhomboclase and jarosite is unlikely at conditions listed. Unfortunately limited SEM resources prevented SEM analysis of Sample 3.

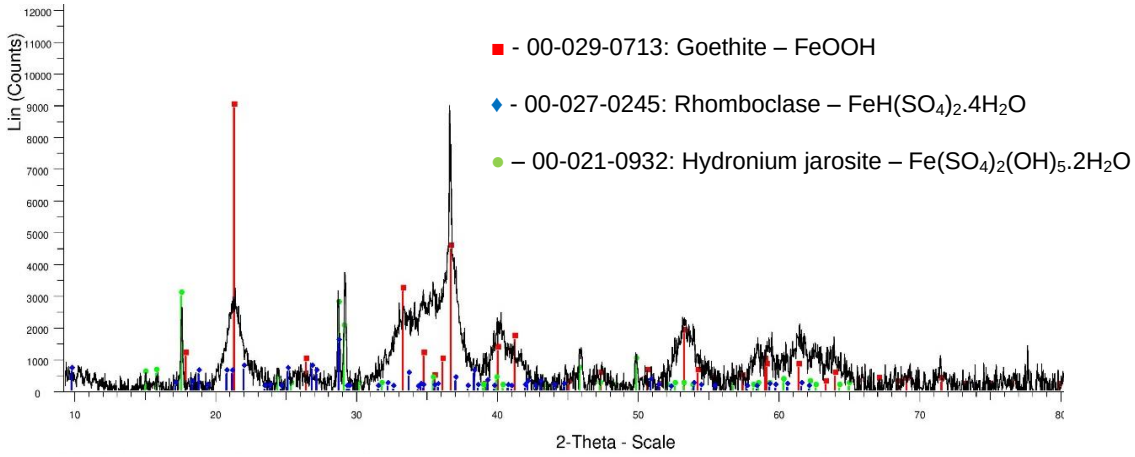

Figure 5-37: XRD Diffractogram of Sample 3: Fe(III)-OPM run at pH 2.5.

The diffractogram of Sample 4 is presented in Figure 5-38, originating from ferric-OPM solution at pH 4.0. Three amorphous peaks were observed, which roughly matched the amorphous areas observed in Sample 3. The peaks at 24°, 35.5° and 61° would match prominent peaks of schwertmannite.

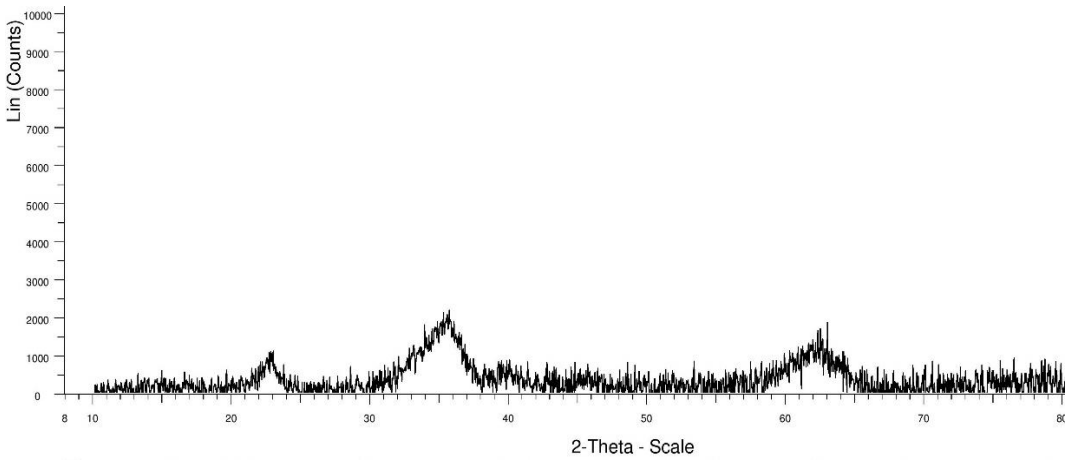

Figure 5-38: XRD Diffractogram of Sample 4: Fe(III)-OPM run at pH 4.0.

Figure 5-39 presents the BSE images of Sample 4. Sample 4 contained no fines, in contrast to Sample 1 and Sample 2 with ferrous solution. The absence of fines in ferric experiments agrees well with the particle size distribution work in Section 5.4.1.

Several phases were identified. Two homogeneous phases are observed, one of medium density (Bulk iron oxide) and the other of low density (Low density iron oxide). A heterogeneous phase is also present (Med density iron oxide) with small higher density phases interlocked (High density iron oxide).

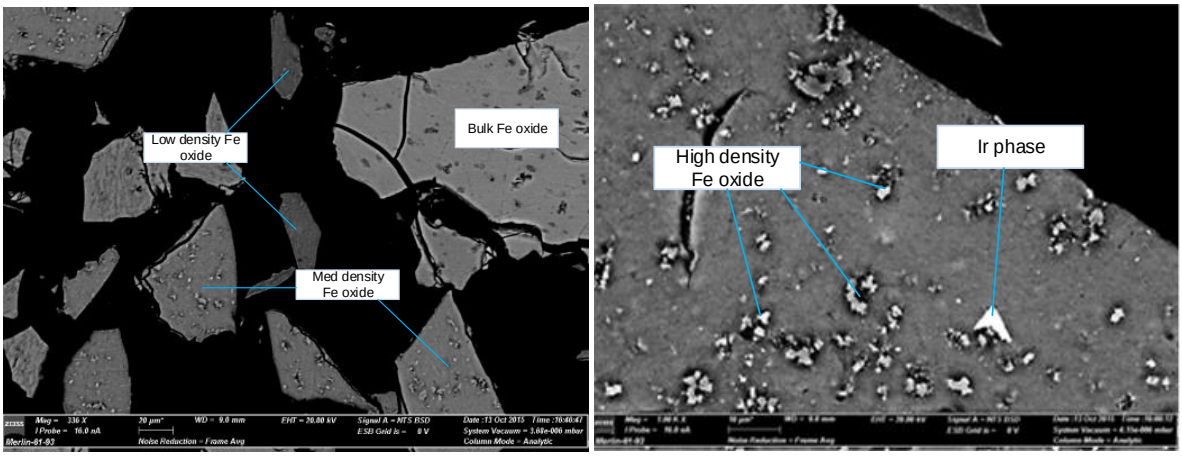

Figure 5-39: Bulk composition BSE image (left) and Magnified BSE image (right) of Sample 4: Fe(III) & pH 4.0.

Table 5-9 presents the elemental compositions of defined phases. In contrast to ferrous Samples 1 and 2, appreciably more sulphate is incorporated in the denser phases, with declining iron content as the density increases. Small amounts of sodium is structurally incorporated, which might imply the presence of minor jarosite amounts.

Table 5-9: Elemental composition (wt.%) of identified phases in SEM Sample 4. Fe(III) & pH 4.0.

	Fe	O	S	Cl	Ir	As	Na
Bulk Fe oxide	53.6±2.1	38.7±0.9	3±1			3.7±0.2	
Low density Fe oxide	51.3±1	40.5±0.5	4.5±0.6			3.1±0.2	0.3±0.2
Med density Fe oxide	47.5±0.5	43.1±0.3	6.3±0.3			3.1±0.1	
High density Fe oxide	37±2.5	47.6±1.3	9.2±1.4			2.6±0.3	1.8±0.2
Ir phase	4.5±0.4	2.5±0.4		12.2±2.3	80.7±2.3		
Ir phase 2	4.5±6.8	23.1±4.1		22.5±3.5	47.9±9.2		

An aggregated, relatively denser particle body is observed in Sample 4's SE image, given in Figure 5-40.

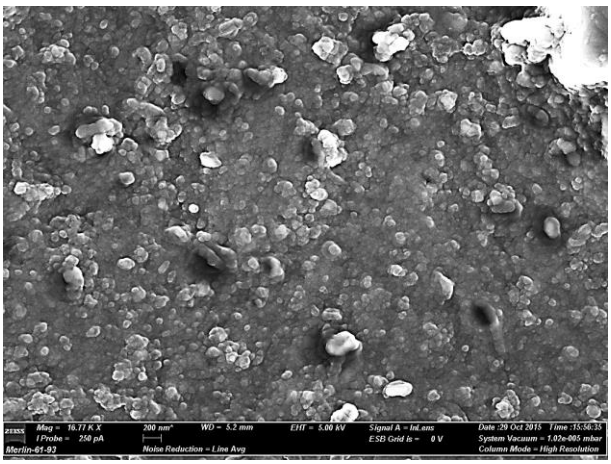

Figure 5-40: SE image for Sample 4: Fe(III) & pH 4.0.

5.5.2. Solids from nickel sulphate solution

Sample 5 originates from solution with ferrous at pH 4.0. Sample 5's XRD diffractogram is given in Figure 5-41. The diffractogram provided a well-crystalline fit to synthetic jarosite. Of the viable jarosite compounds, hydronium jarosite fitted data better than natrojarosite, even though natrojarosite is thermodynamically favoured (Dutrizac, 1996).

An unknown compound exhibited a very intense peak around 12° that could not be fitted to any compound in the database.

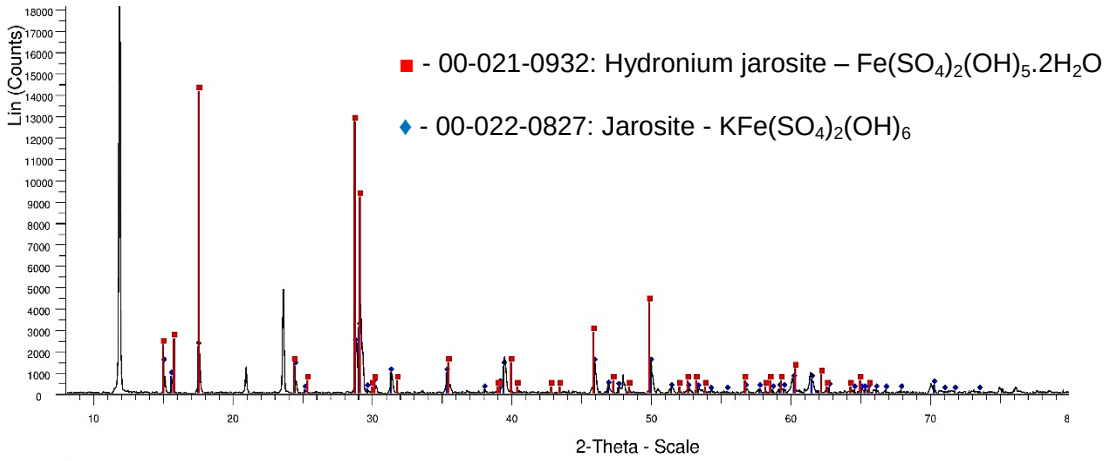

Figure 5-41: XRD Diffractogram for Sample 5: Fe(II) & pH 4.0.

Sample 5's BSE images are provided in Figure 5-42. The bulk phase in Sample 5 consisted of two intertwined, grain-like phases. Iridium phases were observed and other homogeneous iron oxides also formed. The grain-like particles were very brittle and would readily break during electron beam usage.

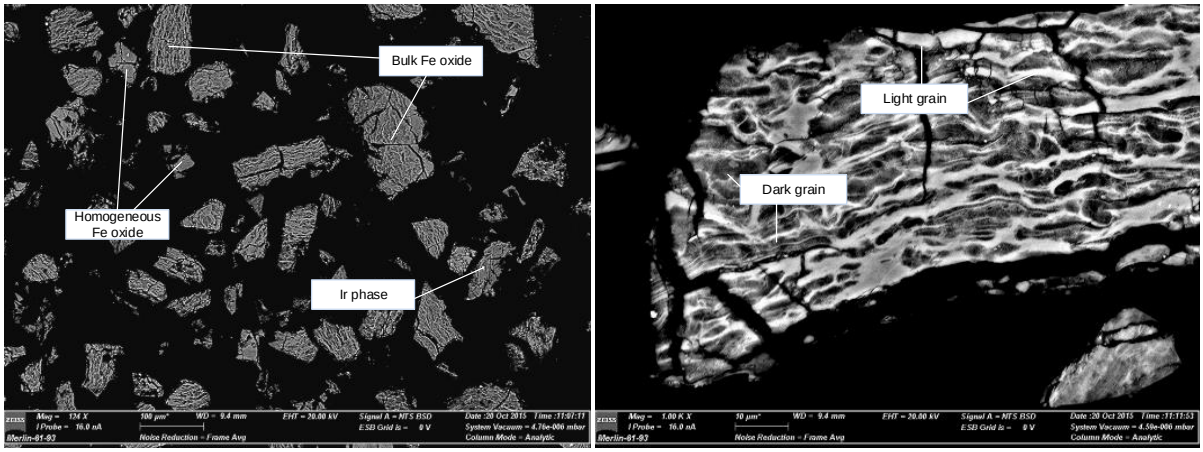

Figure 5-42: Bulk composition BSE image (left) and Magnified BSE image (right) of Sample 5: Fe(II) & pH 4.0.

Table 5-10 presents the elemental composition of different phases. When excluding other elements, the ratio of Fe:O is 55 %:44 %, and thus the predominant phases are predicted to be ferrihydrite. High and consistent OPM observations were obtained, likely due to the small amount of iron precipitation. The lighter grain contained relatively more arsenic and nickel, compared to the darker grain. OPMs ruthenium and rhodium were higher in the darker phase, similar to Sample 2.

Arsenic inclusion did not lead to varying Fe:O ratios and thus it did not necessarily impact the phase mineralogy apart from co-precipitation. No cobalt co-precipitation, as required for the hypothesized $Co_2(AO4)_3$, was observed.

Table 5-10: Elemental composition (wt.%) of identified phases in Sample 5: Fe(II) & pH 4.0.

	Fe	O	S	Cl	Ru	Rh	Ir	Ni	As
Darker grain	59.2±0.3	23.6±0.1	1.1±0.1		2±0.1	1.7±0		2.3±0.2	9.6±0.1
Lighter grain	58.6±0.4	24.1±0.2	1.4±0.1		1.4±0.4	0.4±0.4		2.6±0.1	10.8±0.2
Homo Fe-oxide	59.1±6.1	24.1±0.8	1.2±1		1.1±0.4	0.6±0.4		3.6±6.2	9.5±0.4
Ir phase	3.5±0.5	14±0.1		4.4±1.8			78±2.9		

In Figure 5-43, the darker grain appears to be more amorphous than the lighter, smooth grain. Amorphous inclusion of ruthenium is the most likely argument.

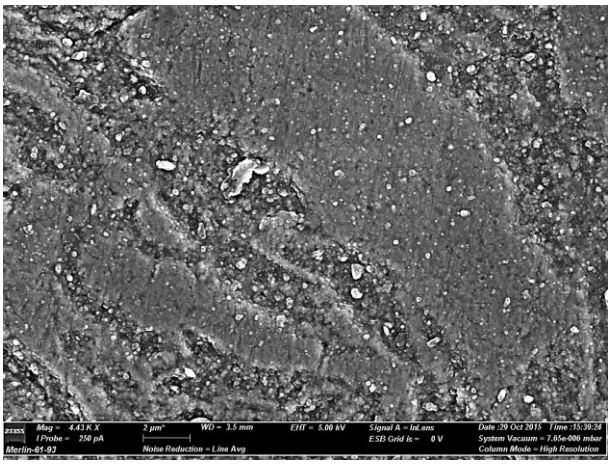

Figure 5-43: SE image of phase grains observed in Sample 5: Fe(II) & pH 4.0.

XRD and SEM data contradict each other. Sample 5 has too much elemental iron and not enough sulphate to be considered Jarosite elementally, yet the XRD peaks suggest it's a jarosite compound.

5.5.3. Solids from goethite seeded experiments

Considering the diffractogram of the reference material in Figure 5-44, it is undisputedly goethite.

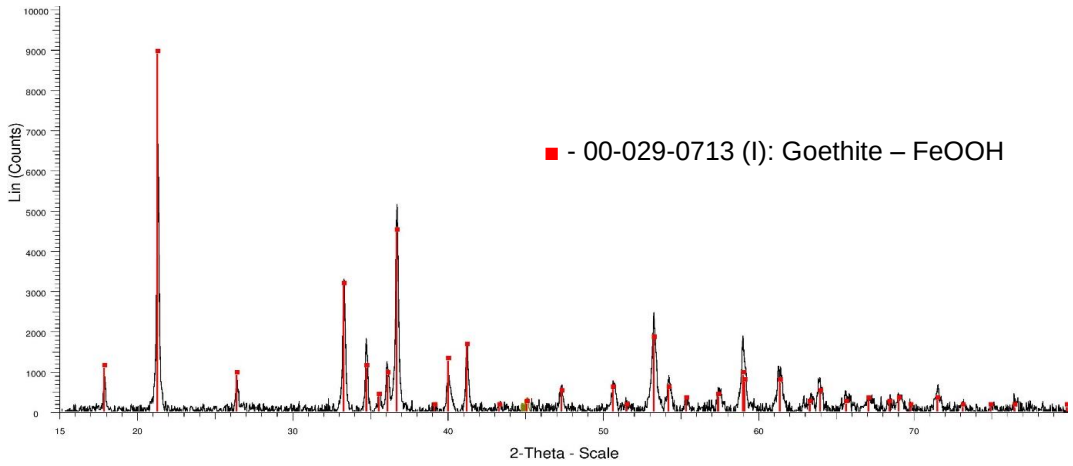

Figure 5-44: XRD Diffractogram of Sample 6: Reference goethite.

No broadening of peaks or the formation of other iron oxides are observed in the diffractograms of Sample 7 or Sample 8, presented in Figure 5-45 and Figure 5-46, respectively. Notably regersite, or nickel hexahydrate, is detected. Regersite presence suggests that nickel sulphate was scavenged from the 95 g/ℓ solution. No other minerals are observed.

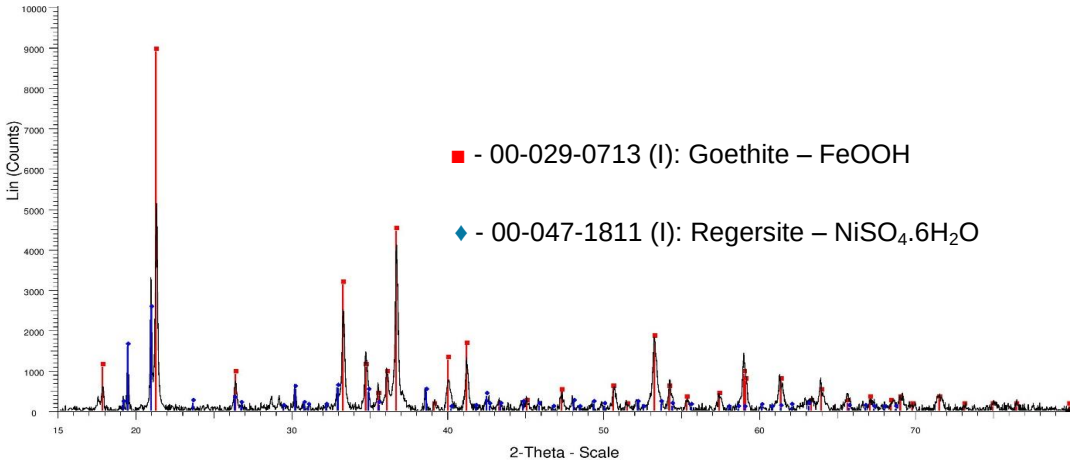

Figure 5-45: XRD Diffractogram of Sample 7: Seeded in Fe(III), pH 2.5 and 95 g/ℓ total metals.

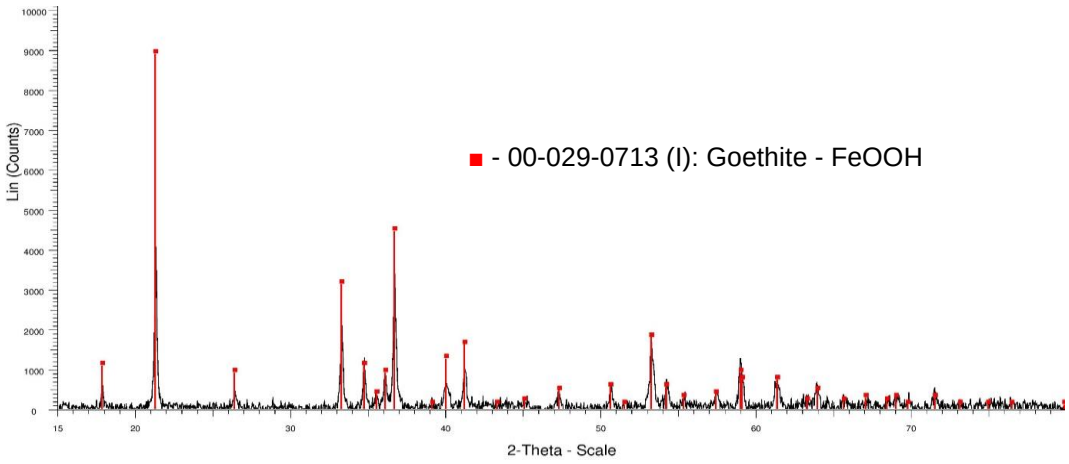

Figure 5-46: XRD Diffractogram of Sample 8: Seeded in Fe(III), pH 4.0 and 65 g/ℓ total metals.

Figure 5-47 presents the BSE images of seeding material. Evidence of growth on the seeding material is observed. The rims of the polished samples were scouted for different behaviour. The image right's boundary is thickly packed and contains a denser phase, which may be growth on the surface. The absence of particles with different density phases suggests growth. The seed phase's elemental composition was in perfect agreement with theoretic goethite, with 64 % iron and 36 % iron. Table 5-11 presents the elemental composition of the seed phase.

Higher density inclusions were observed at rims of certain material, such as in Figure 5-47 (right). The elemental composition of these phases indicate an iron oxide with contains stoichiometrically more oxygen. The higher density particles were only present in small quantities.

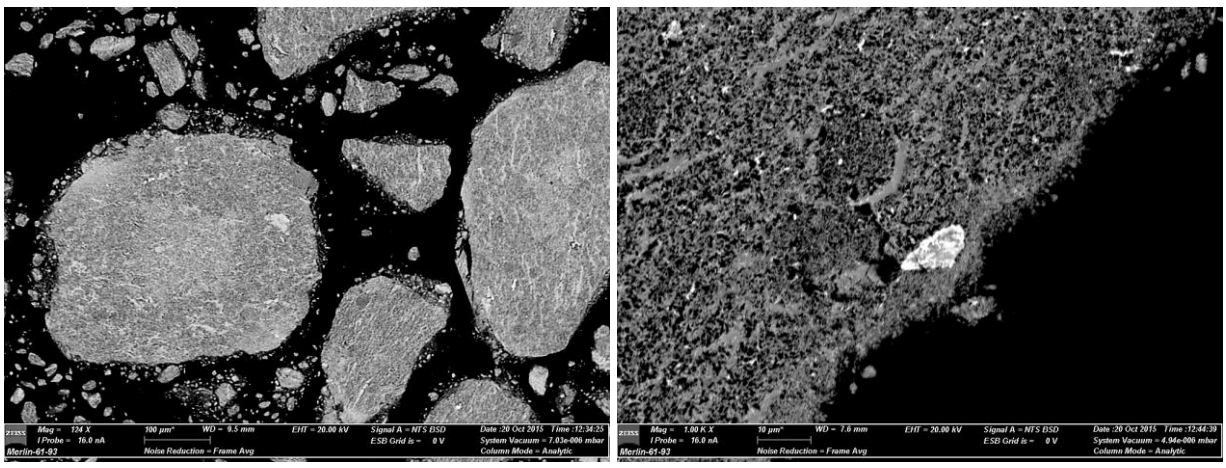

Figure 5-47: Bulk composition BSE image (left) and Magnified BSE image (right) of Sample 8: Seeded in Fe(III), pH 4.0 and 65 g/ℓ total metals.

Table 5-11: Elemental composition (wt.%) of identified phases in SEM Sample 8: Seeded in Fe(III), pH 4.0 and 65 g/ℓ total metals.

	Fe	O	S
Denser foreign Fe oxide	51.4±2.7	46.7±2.7	1.2±0.2
Goethite reference	64.7±0.5	35.1±0.1	0.2±0.1

Elongated, rod-like crystals are observed in Figure 5-48, which are in excellent agreement with SEM images of synthetic goethite crystals published (Kosmulski *et al.*, 2004).

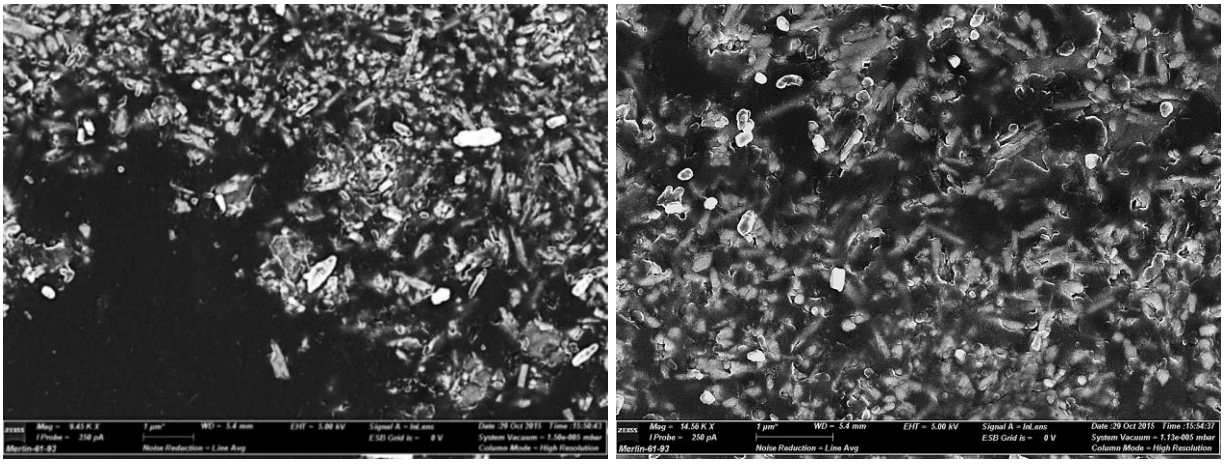

Figure 5-48: SE images for Sample 8: Seeded in Fe(III), pH 4.0 and 65 g/ℓ total metals.

The observation of the acicular rod crystals that are associated with goethite, the absence of spherical crystals, the uniform density observed with back-scatter images and the observed increase of overall particle size strongly suggest that seeding did induce the targeted growth of goethite in nickel sulphate solution with ferric.

CHAPTER 6 - CONCLUSION

6.1. Other precious metal behaviour

Other precious metals are observed in industry heat exchanger sludge. It was hypothesised that the observation of platinum group metals in heat exchanger sludge was the result of cation substitution during iron precipitation with OPM cations.

In order of rate, ruthenium > rhodium > iridium can potentially be precipitated from synthetic nickel sulphate solution. The ruthenium and rhodium precipitation was complete at pH 4.0. The rapid rate observed is believed to be caused by monomolecular hydrolysis. Iridium precipitation could only be characterised in the absence of nickel and copper. 79 % to 88 % iridium precipitation occurred at pH 4.0 and a residual iridium content of 1.4 ppm was observed. Partial precipitation occurred at pH 2.5, where other factors had significant impacts.

The iron valence state did have a significant effect on the results obtained in the Screening and OPM experimentals. It is concluded that the precipitation of OPMs occurred largely independent of the precipitation of iron. The OPM precipitation was induced by the rapid neutralisation of the synthetic solution. OPMs did not precipitate from unaltered industry solution in the range pH 1.9 to pH 3.0 over 20 h.

Temperature had a statistically significant effect on other precious metals precipitation at pH 2.5. Increased ruthenium precipitation and rhodium precipitation were observed at lower metals content (65 g/ℓ) and higher temperature (90 °C). The effect of total metals concentration was not significant.

Ruthenium precipitation and rhodium precipitation were increased by 32 % and 36 %, respectively, when precipitation temperature was increased from 70 °C to 90 °C.

During solid characterisation, ruthenium and rhodium were only observed in low quantities within iron oxide compounds. These iron compounds were distinguishable yet variable. Iridium had the tendency to precipitate without the inclusion of iron or other OPMs. The iridium precipitation product was complexed with chloride and oxygen in variable amounts. The iridium compound then served as a site of heterogeneous nucleation and growth of the bulk iron oxides.

The residual ruthenium and rhodium content in the concentrated metal solution (95 g/ℓ) is approximately 2 ppm higher than in the solution with the total metal concentration after 6 h. It is suggested that more competition for the hydroxide ion occurred at higher total metals concentration. Neutralisation as a means of OPM precipitation would be more efficient at low total metals concentration.

Goethite seeding had no impact on other precious metals precipitation. No improved capturing of OPMs during rapid neutralisation was observed. No gradual OPM scavenging was observed, not even in instances with 50 g/L seed.

Industry solution other precious metals precipitation via NaOH addition shows promise. Addition of 0.05 M NaOH to industry solution resulted in 8 % OPM precipitation.

6.2. Solid characterisation

A wide variety of iron precipitation products were observed in the study, which are all best described under the ferrihydrite and schwertmannite umbrella. Iron oxide phases of varying Fe:O:SO_4 content were detected via SEM-BSE and EDS. SEM-SE imaging revealed granular, spherical crystals, as commonly associated with ferrihydrite.

The iron oxide phases precipitated at pH 4.0 in fundamental iron-OPM experiments were investigated. The bulk iron oxide phase would contain small, euhedral iron oxide phases of higher density, typically characterised with relatively higher iron content and the absence of anionic impurities, chloride and sulphate. The bulk of the iron oxide compound likely grew onto these euhedral sites. The bulk iron oxide at pH 2.5 was more homogeneous in composition.

The iron oxide precipitated from synthetic solution with ferrous at pH 2.5 had grain-like boundaries between two iron oxide phases. Sulphate, nickel and arsenic are present in both phases but little compositional distinction can be made between the denser and darker phases. This sample was prone to breakage due to electron beam analysis, suggesting a relatively weaker lattice structure.

6.3. Effect of goethite seed

It was hypothesized that the addition of goethite seed material may act as a suitable growth site during the precipitation of iron from solution.

The goethite seed material employed were characterised via particle size distribution and surface area analysis via the BET method. Goethite seed had a normally distributed particle size with d_{50} = 1.3 µm. It had a BET surface area of 131.0 m^2/g, which was equally distributed between micropore surface area (66.2 m^2/g) and external surface area (64.8 m^2/g).

Significant particle growth occurred in ferric liquid experiments with a negative skew distribution with d_{50} = 100 µm. Ferrous experiments had an unchanged particle size distribution. SEM-BSE imaging and corresponding EMS analyses revealed large particles of uniform density and composition, often surrounded by clouds of smaller particles with the same composition.

Goethite acicular-shaped crystals are observed via SEM-SE imaging - no evidence of ferrihydrite formation (as spherical particles observed elsewhere in this work) was observed. Goethite seeding appeared to induce targeted precipitation as observed via the solid characterisation techniques.

The rate and extent of iron, arsenic and other precious metals precipitation were not influenced by the presence of seed material in solution. Some experiments suggested that goethite presence in solution may have inhibited iron precipitation. The rate of precipitation in ferrous experiments was likely dependent on the oxidation of ferrous to ferric alone.

Goethite seeding shows promise to be used in iron precipitation circuits, as a means to obtain a consistent iron precipitation product. Goethite seed does however not increase the rate of precipitation.

6.4. Recommendations

Verification via replication of current work with industry solution would establish whether the findings regarding other precious metals precipitation is valid on industrial level.

Fundamental characterisation of platinum group metal chemistry in sulphate media would greatly benefit the understanding of other precious metals behaviour in base metal operations. Iridium chemistry in sulphate media would essentially be the most important. The largest quantity of iridium losses are reported industrially, whilst its precipitation in this study appears to be the least during neutralisation.

Other methods of other precious metal synthesis may be required to adequately present the system. This study used soluble chloride salts, yet the industry solution would possibly contain less chloride than what was introduced with synthetic work. Further work that use OPM complexes that do not contain chloride may further help establish the fundamental behaviour of the OPMs. Soluble rhodium sulphate crystals are commercially available, for instance.

The crystallo-chemical nature of ruthenium, and rhodium particles can furthermore also be established with XRD and SEM analysis.

BIBLIOGRAPHY

Agatzini, S., Kontopoulos, A., Maraboutis, P. & Xenidis, A. 1986. Removal of iron-nickel-cobalt solutions by precipitation and solvent extraction techniques, in *International Symposium on Iron control in Hydrometallurgy*. Toronto: Ellis Horwood Limited: 353-373.

Allan, R.W., Haigh, C.J. & Hamdorf, C.J. 1970. *Patent No. AUS 424,095.*

André, J.A; Masson, N.J.A. 1973. The goethite process in re-treating zinc leaching residues, in *Light metals: A.I.M.E 102nd Annual meeting*. Chicago: Metallurgical Society of AIME.

Arslan, C. & Arslan, F. 2003. Thermochemical Review of Jarosite and Goethite Stability Regions at 25 and 95C. *Turkish Journal of Engineering and Environmental Sciences*, 27(1):45-52.

Au-Yueng, S.C.F. & Bolton, G.L. 1986. Iron control in processes developed at Sherrit-Gordon Mines, in *International Symposium on Iron control in Hydrometallurgy.* Toronto: Ellis Horwood Limited: 131-162.

Baes, C.F. & Mesmer, R.E. 1976. *The hydrolysis of cations.* New York: Wiley.

Bale, C.W., Chartrand, P., Decterov, S.A., Eriksson, G., Hack, K., Mahfoud, B., Melançon, J., Pelton, A.D. & Petersen, S. 2002. FactSage Thermochemical Software and Databases. *Calphad Journal, 26*(2):189-228.

Bazilevskaya, E., Archibald, D.D. & Martinez, C.E. 2012. Rate constants and mechanisms for the crystallization of Al nano-goethite under environmentally relevant conditions. *Geochimica et Cosmochimica Acta, 88*(1):167-182.

Bezuidenhout, G.A., Eksteen, J.J., Akdogan, G., Bradshaw, S.M. & De Villiers, J.P.R. 2013. Pyrometallurgical upgrading of OPM-rich leach residues from the Western Platinum base metals refinery through roasting. *Minerals Engineering*, 53(1):228-240.

Bingham, J.M., Schwertmann, U., Traina, S.J., WInland, R.L. & Woolf, M. 1996. Schwertmannite and the chemical modeling of iron in acid sulfate waters. *Geochim. Cosmochim. Acta*, 60:2111-2121.

Boldt, J.R., Queneau, P. & Mckinstry, H.E. 1967. *The winning of nickel: its geology, mining and extractive metallurgy*. London: Methuen.

Bryson, A.W. & Te Riele, W.A.M., 1987. Factors that effect the kinetics of nucleation and growth and the purity of goethite precipitates produced from sulphate solutions. In Dutrizac, J.E. & Monhemius, A.J., eds. *International Symposium on Iron Control in Hydrometallurgy* (pp. 377 – 390). Toronto, 1987. Ellis Horwood Limited.

Bryson, L.J., Hofirek, Z., Collins, M.J., Stiksma, J. & Berezowsky, R.M. 2008. New matte leaching developments at Anglo Platinum's Base metal refinery, in *Hydrometallurgy 2008, Proceedings of the Sixth International Symposium.* Phoenix: Society for Mining, Metallurgy and Exploration, Inc: 228-240.

Burkin, A.R. 2001. *Chemical Hydrometallurgy: Theory and principles*. London: Imperial College Press.

Carvalho-e-Silva, M.L, Ramos, A.Y, Tolentino, H.C.N., Enzweiler, J., Netto, S.M. & Alves, M.C.M. 2003. Incorporation of Ni into natural goethite. An investigation by X-ray absorption spectroscopy. *American Mineralogist, 88*(1):876-882.

Chang, J.C. & Garner, C.S. 1965. Kinetics of Aquation of Aquopentachloroiridate(III) and Chloride Anation of Diaquotetrachloroiridate(III) Anions. *Inorganic Chemistry*, 4(2)209-215.

Chang, Y., Zhai, X.L. & Fu, B. 2009. Removal of iron from acidic leach liquor of lateritic nickel ore by goethite precipitate. *Hydrometallurgy*, 101(1):84-87.

Colborn, R.P. & Nicol, M.J. 1973. An investigation into the kinetics and mechanism of the oxidation of iron (II) by oxygen in aqueous chloride solutions. *Journal of the south african institute of mining and metallurgy*, 281-289. Retrieved from http://www.saimm.co.za/Journal/v073n09p281.pdf

Connick, R.E. & Fine, D. 1960. Ruthenium(III) Chloride Complexes: $RuCl^{2+}$. *Journal of the American Chemical Society*, 82:4187-4191.

Cornell, R.M. & Schwertmann, U. 2003. *The Iron Oxides: Structure, Properties, Reactions, Occurences and Uses.* 2nd ed. Weinheim: Wiley.

Cramer, L.A. 2001. The Extractive Metallurgy of South African Ores. *The Journal of The Minerals, Metals & Materials Society*, 53(10):14-18.

Croarkin, C. & Tobias, P. 2012. *NIST/SEMATECH e-Handbook of Statistical Methods.* Retrieved from NIST: http://www.itl.nist.gov/div898/handbook/

Crundwell, F., Moats, M., Ramachandran, V., Robinson, T.G.& Davenport, W.G. 2011. *Extractive Metallurgy of Nickel, Cobalt and Platinum-Group Metals*. 1st ed. Amsterdam: Elsevier.

Das, S., Jim Hendry, M. & Essilfie-Dughan, J. 2011. Transformation of two-line ferrihydrite to goethite and hematite as a function of pH and temperature. *Environmental science and technology*, 45(1):268-275.

Davey, P.P. & Scott, T.R. 1976. Removal of iron from leach liquors by the "goethite" process. *Hydrometallurgy, 2*(1):25-33.

Dirksen, J.A. & Ring, T.A. 1991. Fundamentals of crystallization: kinetic effects on particle size distributions and morphology. *Chemical Engineering Science, 46*(10):2389-2427.

Dorfling, C. 2011. *Characterisation and dynamic modelling of the behaviour of platinum group metals in high pressure sulphuric acid/oxygen leaching systems*. Stellenbosch: Stellenbosch University [PhD Thesis].

Dreisinger, D.B. & Peters, E. 1989. The Oxidation of Ferrous Sulphate by molecular oxygen under zinc pressure-leach conditions. *Hydrometallurgy, 22*(1):101-119.

Droppert, D.J. 1996. *The ambient pressure precipitation of crystalline scorodite (FeAsO4.2H2O) from sulphate solutions*. Montreal: McGill University [M.Eng Thesis].

Dutrizac, J.E. 1980. The physical chemistry of iron precipitation, in *Lead-Zinc-Tin '80*. Las Vegas: Metallurgical Society of AIME: 532-564.

Dutrizac, J.E. 1982. Jarosite-type compounds and their application in the metallurgical industry, in *Hydrometallurgy research development and plant practice*. Warrendale: The Minerals, Metals & Materials Society: 531-553.

Dutrizac, J.E. 1987. An overview of iron precipitation in hydrometallurgy. *Crystallisation and Precipitation.* Saskatoon: Pergammon Press: 259-283.

Dutrizac, J.E. 1996. The effect of seeding on the rate of precipitation of ammonium jarosite and sodium jarosite. *Hydrometallurgy*, 42(3):293-312.

Dutrizac, J.E. & Chen, T.T. 2004. Factors affecting the incorporation of cobalt and nickel in jarosite-type compounds. *Canadian Metallurgical Quarterly*, 43(3):305-320.

Dutrizac, J.E. & Dinardo, O. 1983. The co-precipitation of copper and zinc with lead jarosite. *Hydrometallurgy*, 11(1):61-78.

Dutrizac, J.E. & Jambor, J.L. 1987. Behaviour of cesium and lithium during the precipitation of jarosite-type compounds. *Hydrometallurgy,* 17(2):251-265.

Dutrizac, J., & Jambor, J.L. 2007. Characterization of the iron arsenate–sulphate compounds precipitated at elevated temperatures. *Hydrometallurgy,* 86(3):147-163.

Eksteen, J.J., van Beek, B. & Bezuidenhout, G.A. 2011. Cracking a hard nut: An overview of Lonmin's operations directed at smelting of UG2-rich concentrate blends. *The Journal of The Southern African Institute of Mining and Metallurgy*, 111(1):681-690.

El-Awady, A.A., Bounsall, E.J. & Garner, C.S. 1967. Kinetics of aquation of cis- and trans-diaquotetrachloroiridate(III) anions and chloride anation of 1,2,6-triaquotrichloroiridium(III). *Inorganic Chemistry*, 6(1):79-86.

Elwell, D. & Scheel, H.J. 2011. *Crystal growth from high temperature solutions*. London: Academic Press.

Emett, M.T. & Khoe, G.H. 1994. Environmental Stability of Arsenic bearing hydrous iron oxide, in *EPD congress 1994*. Warrendale: The Minerals, Metals & Materials Society: 384-395.

Factsage, 2011 *Summary of databases* [Online]. Available: http://www.crct.polymtl.ca/fact/documentation/FSData.htm Date of access: 3 Apr 2014.

Faramanz, D.A., Ragnu, S., Ernest, B., Ziadin, S.S. & Amid, M. 2005. Modelling of ferric iron complexation and precipitation reactions, in *9th International Mine Water Congress* Oviedo: Springer: 481-488.

Fleming, C.A. 2009. *Basic Iron Sulphate - A potential killer for pressure oxidation processing of refractory gold concentrates if not handled appropriately*. Montreal: SGS Minerals Services.

Forrester, J.S. & Ayres, G.A. 1963. Rhodium (III) in Aqueous Solutions. *Journal of physical chemistry*, 63(11):1979.

Goldberg, R.N. & Hepler, L.G. 1968. Thermochemistry and oxidation potentials of the platinum group metals and their compounds. *Chemical Reviews*, 68(2):229-252.

Goldschmidt, V.M. 1937. The principles of distribution of chemical elements in minerals and rocks. *Journal of the Chemical Society, 1*(0):655-673.

Greenwood, N.N. & Earnshaw, A. 1995. *Chemistry of the Elements.* Oxford: Butterworth Heineman.

Grund, S.C., Hanusch, K. & Wolf, H.U. Arsenic and arsenic compounds, in B. Elvers (Ed.), *Ullman's encyclopedia of industrial chemistry*, 6th ed. New York: Wiley. Retrieved May 21, 2014, from http://onlinelibrary.wiley.com/book/10.1002/14356007

Grundl, T. & Delwiche, J. 1993. Kinetics of ferric oxyhydroxide precipitation. *Journal of Contaminant Hydrology, 14*(1):71-97.

Gupta, C.K. & Mukherjee, T.K. 1990. *Hydrometallurgy in exctration processes*. Boca Raton: CRC Press.

Habashi, F. 1999. *Textbook of hydrometallurgy*. 2nd ed. Quebec: Métallurgie Extractive Quebec.

Han, K.n, Narita, E. & Lawson, F. 1982. The coprecipitation behavior of Co (II) and Ni (II) with Fe (III), Cr (III) and Al (III) from aqueous ammoniacal solutions. *Hydrometallurgy*, 8(4):365-377.

Havlik, T. 2008. *Hydrometallurgy: Principles and applications*. Cambridge: Woodhead Publishing.

Helm, L. & Merbach, A. 2005. Inorganic and Bioinorganic Solvent Exchange Mechanisms. *Chemical Reviews, 105*(6):1923-1960.

Hove, M., van Hille, R.P. & Lewis, A.E. 2009. The effect of different types of seeds on the oxidation and precipitation of iron. *Hydrometallurgy, 97*(3-4), 180-184.

Hou, X. & Jones, B.T. 2000. Inductively Coupled Plasma/Optimal Emission Spectrometry, in R.A. Meyers (Ed.) *Encyclopedia of Analytical Chemistry*. Chichester: Wiley: 9468-9485.

Huffman, R.E. & Davidson, N. 1956. Kinetics of the ferrous iron-oxygen reaction in sulphuric acid solution. *Journal of the American Chemical Society, 78*(19):4836-4842.

Ivanov-Emin, B.N., Borzova, L.D., Egorov, A.M., & Malyugina, S.G. 1971. *Russian journal of inorganic chemistry*, 16:1474.

Jia, Y. & Demopoulos, G.P. 2008. Coprecipitation of arsenate with iron(III) in aqueous sulfate media: Effect of time, lime as base and co-ions on arsenic retention. *Water research*, 42(3):661-668.

Jiang, H., & Lawson, F. 2006. Reaction mechanism for the formation of ammonium jarosite. *Hydrometallurgy, 82*(3-4):195-198.

Jollie, D. 2008. *Platinum 2008.* Hertfordshire: Johnson Matthey Public Limited Company.

Jones, R.T. 1999. Platinum Smelting in South africa. *Journal of Science*, 95(1):525-534.

Kendall, M.R., Madden, A.S., Madden, M.E.E. & Hu, Q. 2013. Effects of arsenic incorporation on jarosite dissolution rates and reaction products. *Geochimica et Cosmochimica Acta*, 112(1):192 - 207.

Knight, R.S., & Sylva, R.N. 1975. Spectrophotometric investigation of iron(III) hydrolysis in light and heavy water at 25C. *Journal of Inorganic and Nuclear Chemistry, 37*(3):779-783.

Koretsky, M.D. 2004. *Engineering and chemical thermodynamics.* New York: Wiley.

Kosmulski, M., Durand-Vidal, S., Maczka, E. & Rosenholm, J.B. 2004. Morphology of synthetic goethite particles. *Journal of Colloid and Interface Science*, 271(2):261-269.

Lamya, R.M. 2007. *A fundamental evaluation of the atmospheric pre-leach section of the nickel-copper matte treatment process.* Stellenbosch: Stellenbosch University [PhD thesis].

Lascelles, K., Morgan, L.G., Nicholls, D. & Beyersmann, D. 2002. Nickel Compounds, in B. Elvers (Ed.), *Ullman's encyclopedia of industrial chemistry*, 6th ed. New York: Wiley. Retrieved May 21, 2014, from http://onlinelibrary.wiley.com/book/10.1002/14356007

Le Berre, J.F., Gauvin, R. & Demopoulos, G.P. 2008. A study of the crystallization kinetics of scorodite via the transformation of poorly crystalline ferric arsenate in weakly acidic solution. *Colloids and Surfaces A: Physicochemical and Engineering Aspects*, 315(1):117-129.

Lonmin Plc. 2013. *Annual Report and Accounts FY 2013*. London: Lonmin Plc.

Lottering, C., Eksteen, J.J. & Steenekamp, N. 2012. Precipitation of rhodium from a copper sulphate leach solution in the selenium/tellurium removal section of a base metal refinery. *The Journal of The Southern African Institute of Mining and Metallurgy, 112*:287-294.

Lowson, R.T. 1982. Aqueous Oxidation of Pyrite by Molecular Oxygen. *Chemical Reviews, 82*(5):461-493.

Mathews, C.T. & Robins, R.G. 1972. The oxidation of aqueous ferrous sulphate solutions by molecular oxygen. *Journal of the Australasian Insitute of Mining and Metallurgy, 242*:47-56.

Mazeina, L., Majizlan, J. & Navrotsky, A. 2006. Polymorphic transformations of iron oxides: A thermodynamic review, in *Goldschmidt conference 2006*. Melbourne: Geochemical Society: 406.

McKay, D.R. 1952. *A kinetic study of the oxidation of pyrite in aqueous suspension.* Vancouver: University of British Colombia [M.Sc Thesis].

Montgomery, D.G. 2001. *Design and Analysis of Experiments. 5th ed.* New York: Wiley.

Murphy, P.J., Posner, A.M. & Quirk, J.P. 1976. Characterization of partially neutralized ferric nitrate solutions. *Journal of Colloid and Interface Science, 56*(2):270-283.

Nell, J. 2004. Melting of platinum group metal. *The Journal of The Southern African Institute of Mining and Metallurgy*, 6(1):423-428.

Nicol, M.J. 2006. *Hydrometallurgy: Theory and Practice.* Perth: Murdock University.

Nielsen, A.E. 1964. *Kinetics of precipitation.* Oxford: Pergammon Press.

Nikishova, N.I., Retinyem, A.L. & Syseeva, V.V. 1974. Mechanisms of oxidation of iron (II) chloride and sulphate by oxygen. *Zhurnal Prikladnoi Khimii - Russian Journal of Applied Chemistry, 47*(10):2228-2232.

NIST. 2011. *Henry's Law data: Oxygen*. Retrieved June 11, 2014, from NIST Chemistry webbook: http://webbook.nist.gov/cgi/cbook.cgi?ID=C7782447&Units=SI&Mask=10#Solubility

Nogueira, C.A., Oliveira, P.C. & Pedrosa, F.M. 2009. Separation of cadmium, cobalt and nickel by solvent extraction using nickel salts of the extractants. *Solvent Extraction and Ion Exchange, 27*(2):295-311.

Olivier, M.C. 2011. *Developing a solvent extraction process for the separation of cobalt and iron from nickel sulfate solutions.* Stellenbosch: Stellenbosch University [M.Eng Thesis].

Paktunc, D., Dutrizac, J.E. & Gertsman, V. 2008. Synthesis and phase transformations involving scorodite, ferric arsenate and arsenical ferrihydrite: Implications for arsenic mobility. *Geochimica et Cosmochimica Acta*, 72(11):2649-2672.

Palmer, D.A. & Harris, G.M. 1975. Kinetics, mechanism, and stereochemistry of the aquation and chloride anation reactions of fac- and mer-trichlorotriaquorhodium(III) complexes in acidic aqueous solution. Complete reaction scheme for complex ions of the general formula [RhCln(OH2)6-n]3-n. *Inorganic Chemistry*, 14(6):1316-1321.

Pamplin, B.R. 1975. *Crystal Growth*. Oxford: Pergamon Press Ltd.

Pantuzzo, F.L., Ciminelli, V.S.T. & de Brito, W. 2008. New evidences for the role of precipitation and adsorption during Fe(III)-As(V) coprecipitation, in *Hydrometallurgy 2008, Proceedings of the Sixth International Symposium*. Phoenix: Society for Mining, Metallurgy and Exploration, Inc: 30-148.

Papassiopi, N., Vircikova, E., Nenov, V., Kontopoulos, A. & Molnar, L. 1996. Removal and fixation of arsenic in the form of ferric arsenates. Three parallel experimental studies. *Hydrometallurgy*, 41(2):243-253.

Plasket, R.P. & Dunn, G.M. 1986. Iron rejection and impurity removal from nickel leach liquor at Impala Platinum Limited, in *International Symposium on Iron control in Hydrometallurgy*. Toronto: Ellis Horwood Limited: 695-718.

Pletcher, D. & Urbina, R.I. 1997a. Electrodeposition of rhodium Part 1. Chloride Solutions. *Journal of Electoanalysis Chemistry*, 421(1-2):137-144.

Pletcher, D. & Urbina, R.I. 1997b. Electrodeposition of rhodium Part 2. Sulfate Solutions. *Journal of Electoanalysis Chemistry*, 421(1-2):145-151.

Pley, M. & Wickleder, M.S. 2005. Two crystalline modifications of RuO4. *Journal of Solid State Chemistry*, 178(10):3206-3209.

Poulsen, I.A. & Garner, C.S. 1962. A Thermodynamic and Kinetic Study of Hexachloro and Aquopentachloro Complexes of Iridium(III) in Aqueous Solutions. *Journal of the American chemical society*, 84(11):2032-2037.

Rao, C.R.M. & Reddi, G.S. 2000. Platinum group metals (OPM) occurrence, use and recent trends in their determination. *Trends in Analytical Chemistry*, 19(9):565-586.

Renner, H. 2002. Platinum Group Metals and Compounds, in B. Elvers (Ed.), *Ullman's encyclopedia of industrial chemistry*, 6th ed. New York: Wiley. Retrieved May 21, 2014, from http://onlinelibrary.wiley.com/book/10.1002/14356007

Riecke, H.G. 1960. *Oxidation of Fe2+ to Fe3+ with Oxygen in Autoclave*. Berlin: Berlin Technical University [PhD Thesis].

Robb, W. & Harris, G.M. 1965. Some Exchange and Substitution Reactions of Hexachlororhodium (III) and Pentachloroaquorhodium (III) in aqueous acid solutions. *Journal of the American Chemical Society*, 87(20):472–4476.

Rönnholm, M.R., Wärnå, J., Valtakari, D., Salmi, T. & Laine, E. 2001. Kinetics and mass transfer effects in the oxidation of ferrous sulfate over doped active carbon catalysts. *Catalysis Today, 66*(2):447–452.

Ronnholm, M.R., Wärnå, J., Salmi, T., Turunen, I. & Luoma, M. 1999. Kinetics of oxidation of ferrous sulfate with molecular oxygen. *Chemical Engineering Science*, 54(19):4223-4232.

Rose, A.L., & Waite, T.D. 2007. Reconciling kinetic and equilibrium observations of iron(III) solubility in aqueous solutions with a polymer-based model. *Geochimica et Cosmochimica Acta, 71*(23):5605-5619.

Rouquerol, J., Avnir, D., Fairbridge, C.W., Everett, D.H., Haynes, J.M., Pernicone, N., Ramsay, J.D.F., Sing, K.S.W. & Unger, K.K. 1994. Recommendations for the characterization of porous solids (Technical Report). *Pure and Applied Chemistry*, 66(8):1739-1758.

Schwertmann, U. & Carlson, L. 2005. The pH-dependent transformation of schwertmannite to goethite at 25°C. *Clay minerals*, 40(1):63-66.

Seidell, A. 1965. Solubilities of Inorganic and Metal Organic Compounds. *American Chemical Society, 2*:1219.

Seymour, R.J. & O'Farrelly, J.I. 2006. Platinum group metals, Compounds, in A. Seidel (Ed.), *Kirk-Othmer Encyclopedia of Chemical Technology,* 5th ed. New York: Wiley.

Shannon, R.D. 1976. Revised effective ionic radii and systematic studies of interatomic distances in halides and chalcogenides. *Acta Crystallographica, 32*(1):751-767.

Sigma-Aldrich. 2010. *Arsenic(III) Oxide Product Information.* St. Louis: Sigma Aldrich.

Silvermanm, M.A. & Levy, H.A. 1950. *Studies of the upper valence states of ruthenium in aqueous solutions.* Oak Ridge: Univeristy of Tennessee.

Singer, P.G. & Stumm, W. 1970. Acidic Mine Drainage: The Rate-Determining Step. *Science, 167*(3921): 1121-1123.

Singh, B., Sherman, D.M., Gilkes, R.J, Wells, M.A. & Mosselmans, J. 2002. Incorporation of Cr, Mn and Ni into goethite (α-FeOOH): mechanism from extended X-ray absorption fine structure spectroscopy. *Clay Minerals, 37*(1):639-649.

Sippola, H. 1992. Rautasulfaatin liukoisuuden mallitus rikkihappo-vesisysteemissa (English: Iron sulfate solubility modelling of the sulfuric acid - water systems). Helsinki: Helsinki University of Technology [M.Eng Thesis].

Steenekamp, N. & Dunn, G.M. 1999. Operations of and improvements to the Lonrho Platinum Base metal refinery, in *EPD Congress 1999.* Toronto: The Minerals, Metals & Materials Society: 365-378.

Stilwell, L.C. 2008. Platinum, electricity and the economy, in *The third international platinum conference 'Platinum in Transformation'*. Johannesburg: Southern African Institute of Mining and Metallurgy.

Takeno, N. 2005. *Atlas of Eh-pH diagrams*. Hong Kong: National Institute of Advanced Industrial Science and Technology.

Thyse, E.J. 2014. *Effect of iron endpoint during Peirce-Smith converting on matte mineralogy and downstream processing of base and platinum group metals.* Stellenbosch: Stellenbosch Univeristy [PhD thesis].

Thyse, E.J., Akdogan, G. & Eksteen, J.J. 2011. The effect of changes in iron-endpoint during Peirce–Smith converting on PGE-containing nickel converter matte mineralization. *Minerals Engineering*, 24(7):688-697.

Tozawa, K., Sasaki, K. & Umetsu, Y. 1983. The effect of the second dissociation of sulphuric acid on hydrometallurgical processes: the electrical conductivity of sulphuric acid-containing electrolytes and the hydrolysis of ferric sulphate solutions at elevated temperatures*, in Hydrometallurgy, Research, Development and Plant Practice.* Warrendale: Metallurgical Society of AIME: 375.

Turnbull, D. & Vonnegut, B. 1952. Nucleation Catalysis. *Industrial and Engineering Chemistry, 44*(6):1292-1297.

van der Woude, J., de Bruyn, P. & Pieters, J. 1984. Formation of colloidal dispersions from supersaturated iron(III) nitrate solutions. III. Development of goethite at room temperature. *Colloids and surfaces, 9*(2):173-188.

van Schalkwyk, R.F. 2011. *Leaching of Ni-Cu-Fe-S Peirce Smith converter matte: Effects of Fe-endpoint and leaching conditions on kinetics and mineralogy.* Stellenbosch: Stellenbosch University [M.Eng Thesis].

van Schalkwyk, R.F., Eksteen, J.J., & Akdogan, G. 2013. Leaching of Ni-Cu-Fe-S converter matte at varying iron endpoints; mineralogical changes and behaviour of Ir, Rh and Ru. *Hydrometallurgy,* 136:36-45.

Vermaak, C.F. & Hendriks, L.P. 1976. A review of the mineralogy of the Merensky Reef, with specific reference to new data on the precious metal mineralogy. *Economic Geology*, 71(7): 1244-1269.

Viljoen, K. 2003. *Ruthenium(III) Aqua-chloro complex chemistry: The interconvertion of the hexachlororuthenate(III) and Aquachlororuthenate(III) species.* Stellenbosch : University of Stellenbosch [M.Sc Thesis].

Walton, A.g. 1967. *The formation and properties of precipitates.* New York: Wiley.

Wang, K. 2012. *Impurity rejection in the nickel laterite leach system.* Perth: Curtin University [PhD Thesis].

Webster, N.A.S., Loan, M.J., Madsen, I.C., Knott, R.B. & Kimpton, J.A. 2011. An investigation of the mechanisms of goethite, hematite and magnetite-seeded $Al(OH)_3$ precipitation from synthetic Bayer liquor. *Hydrometallurgy, 102*(1-2):72-79.

Wills, B.A.& Napier-Munn, T. 2006. *Wills' Mineral Processing Technology*. 7th ed. New York: Elsevier.

Wright, M. 2007. *An Introduction to Aqueous Electrolyte Solutions.* New York: Wiley.

Yu, J., Park, M., & Kim, J. 2002. Solubilities of synthetic schwertmannite and ferrihydrite. *Geochemical Journal*, 36:119-132.

Zhu, Y. & Merkel, B.J. 2001. *The Dissolution and Solubility of Scorodite, FeAsO4·2H2O. Evaluation and Simulation with PHREEQC2*. Freiberg: TU Bergakedemie.

Zinck, J.M. 1993. *An Investigation into the hydrolytic precipitation of iron(III) from sulphate-bearing effluents.* Montreal: McGill University [M.Eng Thesis].

APPENDIX A: RAW DATA

A.1 Industry experimental data

	Run	pH	Comp	T [°C]
	I 1	2.73	Comp 2	75
Time [min]	Ru [ppm]	Ir [ppm]	As [ppm]	Pb [ppm]
0	11	13.0	133.6	2.6
30	11	12.5	131.8	2.5
60	11	12.1	129.1	2.4
90	11	12.6	135.0	2.6
120	11	12.5	130.9	2.6
180	10	12.2	116.0	2.5
300	11	12.7	126.9	2.6
1192	11	12.5	127.2	2.5
1308	9.5	12.1	98.4	1.9

	Run	pH	Comp	T [°C]
	I2	2.73	Comp 2	75
Time [min]	Ru [ppm]	Ir [ppm]	As [ppm]	Pb [ppm]
0	11	13.0	133.6	2.6
30	12	13.1	139.2	2.7
60	11	12.8	135.8	2.7
90	11	12.8	132.2	2.6
120	11	12.8	133.9	2.6
180	10	12.7	96.2	2.5
240	10	12.7	97.9	2.5
300	9	11.5	88.8	2.3
1217	9	11.8	91.4	0.0
1332	10	12.1	96.0	0.0

	Run	pH	Comp	T [°C]
	I 3	2.65	Comp 3	75
Time [min]	Ru [ppm]	Ir [ppm]	As [ppm]	Pb [ppm]
0	5	8.1	125.0	2.0
60	5	7.9	106.0	1.8
120	5	7.8	107.2	1.8
240	5	8.0	120.1	1.7
420	5	7.9	119.6	1.7
600	5	7.8	115.8	1.6
1260	5	7.7	113.9	1.7

	Run	pH	Comp	T [°C]
	I 4	2.65	Comp 3	95
Time [min]	Ru [ppm]	Ir [ppm]	As [ppm]	Pb [ppm]
0	5	8.1	125.0	2.0
60	5	7.9	119.5	1.7
240	5	7.9	119.8	1.6
420	5	8.0	119.0	1.7
600	5	7.8	114.7	1.7
1260	5	7.3	101.5	1.6

	Run	pH	Comp	T [°C]
	I 5	1.88	Comp 3	95
Time [min]	Ru [ppm]	Ir [ppm]	As [ppm]	Pb [ppm]
0	5.9	8.4	155.2	1.8
120	5.5	8.3	151.0	2.5
300	6	8.5	158.6	2.5
540	6	8.3	154.9	2.2
1180	6	8.4	156.4	0.0

	Run	pH	Comp	T [°C]
	I 6	3.01	Comp 4	95
Time [min]	Ru [ppm]	Ir [ppm]	As [ppm]	Pb [ppm]
0	2	5.9	80.7	1.4
120	2	4.5	63.6	1.2
300	3	7.3	106.1	1.5
540	2	6.7	93.9	1.5
1180	2	6.3	85.4	0.0

	Run	pH	Comp	T [°C]
	I 7	1.85	Comp 4	95
Time [min]	Ru [ppm]	Ir [ppm]	As [ppm]	Pb [ppm]
0	2	7.6	97.6	1.7
120	3	7.4	94.4	1.6
300	3	7.7	99.0	1.7
540	3	7.7	99.3	1.7
1180		sample lost		

	Run	pH	Comp	T [°C]			
	I 8	1.98	Comp 4	90			
Time [min]	Ni [g/ℓ]	Fe [ppm]	Co [ppm]	Cu [ppm]	Ru [ppm]	pH	ORP [mV]
0	121.29	2343	854	863	60.2	1.98	365
15	120.86	2338	857	872	60.6	1.97	364
30	121.35	2358	854	857	61.0	1.96	357
60	121.85	2343	850	919	62.3	1.90	363
120	121.36	2350	854	877	62.2	1.89	371
240	121.78	2341	851	874	60.9	1.80	369

	Run	pH	Comp	T [°C]			
	I 9	2.04	Comp 4	90			
Time [min]	Ni [g/ℓ]	Fe [ppm]	Co [ppm]	Cu [ppm]	Ru [ppm]	pH	ORP [mV]
0	121.96	2358	849	867	61.0	2.04	367
15	122.43	2350	846	848	61.9	2.01	365
30	121.70	2352	851	863	59.7	2.00	364
60	122.42	2358	846	798	60.3	1.99	336
120	122.65	2319	845	837	58.5	1.91	362
240	122.28	2298	847	857	56.3	1.96	363

A.2 Preparatory experimental data

Run	pH	Valence		T [°C]
P 1	2.5	2+		85
Time [min]	Ni [ppm]	Fe [ppm]	Co [ppm]	Cu [ppm]
2	75378	1978	566	74
45	78365	1928	545	74
105	78891	1866	541	71
153	78578	1869	544	71
240	77271	1910	553	75
360	78489	1840	544	72
480	77852	1818	549	72

Run	pH	Valence		T [°C]
P 2	2.5	2+ with peroxide		85
Time [min]	Ni [ppm]	Fe [ppm]	Co [ppm]	Cu [ppm]
2	88972	2270	633	40
10	90337	858	623	39
30	88919	629	633	41
70	89270	421	631	39
120	90252	1640	624	39
180	90422	1236	623	38
240	88938	928	633	39
360	90269	1556	624	40

Run	pH	Valence		T [°C]
P 3	3.7	2+ with peroxide		85
Time [min]	Ni [ppm]	Fe [ppm]	Co [ppm]	Cu [ppm]
2	89829	2083	614	36
10	89941	1320	613	39
30	89629	1203	615	38
70	89417	1027	617	38
120	87749	584	629	38
180	89370	515	617	37
240	88927	544	620	39
360	91466	212	638	39

A.3 Screening and Seeding experimental data

The following convention is used:

Run number | pH | Iron valence state | Total metals concentration | Temperature | Seeding

Values given are in ppm.

Run	pH	Valence	Total metals [g/ℓ]	T [°C]	Seed

	1	4	2+	65	70.0	Goethite	
Time [min]	Ni [ppm]	Fe [ppm]	Co [ppm]	Cu [ppm]	As [ppm]	Ru [ppm]	Rh [ppm]
0	58707	2395	616	35	48.0	2.24	1.39
30	58493	2317	614	33	25.4	0.42	0.44
60	57898	2279	609	34	28.7	0.31	0.44
90	58442	2246	612	34	23.3	0.23	0.36
120	59668	2251	623	34	22.6	0.10	0.40
180	60190	2223	629	69	19.7	0.14	0.38
255	60090	2175	630	35	15.0	0.12	0.38
360	60576	2187	636	35	11.6	0.16	0.39

	Run	pH	Valence	Total metals [g/ℓ]	T [°C]	Seed	
	2	2.5	3+	95	90	Goethite	
Time [min]	Ni [ppm]	Fe [ppm]	Co [ppm]	Cu [ppm]	As [ppm]	Ru [ppm]	Rh [ppm]
0	83495	3338	956	69	73.3	8.08	8.98
2	83470	1960	957	72	6.6	1.91	3.65
15	83449	1341	948	71	5.0	2.82	3.18
30	80265	1219	970	72	2.5	2.39	2.46
60	85637	1118	973	69	1.7	2.67	2.77
90	83073	948	943	71	0.9	2.76	2.41
120	83104	1016	942	71	0.5	2.55	2.51
180	83279	969	939	71	0.0	2.72	2.25
240	83108	876	959	69	0.0	3.10	2.25
360	86066	823	977	70	0.0	3.89	2.53

	Run	pH	Valence	Total metals [g/ℓ]	T [°C]	Seed	
	3	2.5	2+	95	90.0	None	
Time [min]	Ni [ppm]	Fe [ppm]	Co [ppm]	Cu [ppm]	As [ppm]	Ru [ppm]	Rh [ppm]
0	84414	3591	951	68	95.6	10.28	10.76
30	83259	3538	944	67	66.1	5.63	8.57
60	86189	3624	970	69	59.1	4.87	7.78
120	85041	3584	957	68	53.1	4.03	7.20
180	86887	3632	973	69	46.0	3.44	6.51
240	85181	3583	961	69	42.1	3.08	6.40
360	88105	3659	986	70	32.8	2.70	5.94

	Run	pH	Valence	Total metals [g/ℓ]	T [°C]	Seed

	4	4	2+	65	70.0	None	
Time [min]	Ni [ppm]	Fe [ppm]	Co [ppm]	Cu [ppm]	As [ppm]	Ru [ppm]	Rh [ppm]
0	65132	2506	700	49	56.3	8.24	7.10
40	67477	2229	679	45	9.4	0.03	0.37
60	64862	2215	674	48	7.9	0.00	0.36
90	65710	2232	689	50	7.2	0.15	0.37
120	65079	2194	684	49	6.0	0.06	0.33
180	66205	2161	695	49	4.6	0.04	0.37
255	67503	2147	708	51	3.3	0.10	0.38
360	67553	2072	711	52	2.3	0.21	0.42

Run	pH	Valence	Total metals [g/ℓ]	T [°C]	Seed
	5	2.5	2+	65	70	Goethite	
---	---	---	---	---	---	---	---
	5	2.5	2+	65	70	Goethite	
Time [min]	Ni [ppm]	Fe [ppm]	Co [ppm]	Cu [ppm]	As [ppm]	Ru [ppm]	Rh [ppm]
0	61452	2540	687	53	47.8	11.24	10.30
15	60263	2467	670	51	30.5	0.00	2.96
30	61035	2535	681	51	26.1	0.13	3.05
60	60887	2527	678	51	22.8	0.01	3.08
90	60855	2527	684	52	20.9	0.15	3.14
120	61201	2590	689	57	20.0	0.13	3.35
180	61649	2502	678	54	17.8	0.11	3.24
240	61340	2634	702	53	15.7	0.13	3.45
360	61157	2505	687	58	11.3	0.15	3.12

	Run	pH	Valence	Total metals [g/ℓ]	T [°C]	Seed	
	6	2.5	2+	65	90	None	
Time [min]	Ni [ppm]	Fe [ppm]	Co [ppm]	Cu [ppm]	As [ppm]	Ru [ppm]	Rh [ppm]
0	63269	2638	701	53	56.2	8.00	7.18
15	62595	2605	700	52	39.7	0.00	2.47
30	62104	2529	691	50	38.7	0.00	2.94
60	62479	2593	696	55	35.3	0.00	2.33
90	63194	2608	702	57	37.3	0.00	2.33
120	62247	2543	693	51	38.9	0.00	2.45
180	62927	2579	703	52	36.4	0.00	2.43
240	64425	2654	724	53	28.2	0.00	1.92
360	64508	2602	721	55	25.8	0.00	2.19

	Run	pH	Valence	Total metals [g/ℓ]	T [°C]	Seed	
	7	2.5	3+	65	90	None	
Time [min]	Ni [ppm]	Fe [ppm]	Co [ppm]	Cu [ppm]	As [ppm]	Ru [ppm]	Rh [ppm]
0	63535	2393	707	52	51.0	8.59	7.86
2	63609	1764	707	57	0.7	3.39	8.10
15	63375	896	709	52	0.0	2.45	8.17
30	63844	810	709	52	0.0	1.89	7.85
60	62658	745	703	55	0.0	1.27	7.11
90	61949	731	687	51	0.0	0.70	4.47
120	63752	660	709	52	0.0	0.75	6.54
180	64136	607	712	58	0.0	0.82	5.52
240	63837	522	711	52	0.0	0.63	4.31
360	64655	501	719	52	0.0	1.21	3.49

	Run	pH	Valence	Total metals [g/ℓ]	T [°C]	Seed	
	8	4	3+	65	90.0	Goethite	
Time [min]	Ni [ppm]	Fe [ppm]	Co [ppm]	Cu [ppm]	As [ppm]	Ru [ppm]	Rh [ppm]
0	65230	1640	706	50	15.3	5.07	7.06
15	61846	52	673	31	1.0	0.00	0.28
30	60923	40	656	31	0.8	0.00	0.23
60	61982	28	668	32	0.6	0.00	0.27
90	59272	18	638	31	0.5	0.08	0.22
120	61510	173	662	32	0.6	0.00	0.22
180	62474	8	672	35	0.4	0.00	0.24
240	63378	113	681	35	0.5	0.04	0.29
360	62659	6	672	33	0.4	0.00	0.25

	Run	pH	Valence	Total metals [g/ℓ]	T [°C]	Seed	
	9	4	2+	95	90.0	None	
Time [min]	Ni [ppm]	Fe [ppm]	Co [ppm]	Cu [ppm]	As [ppm]	Ru [ppm]	Rh [ppm]
0	86586	3751	986	72	93.4	10.06	11.03
30	86511	3600	969	67	49.3	0.00	0.50
60	85427	3527	954	66	52.5	0.00	0.52
120	84379	3451	942	65	47.5	0.00	0.48
240	85750	3618	995	71	41.7	0.00	0.54
360	84956	3475	955	66	35.8	0.00	0.50

	Run	pH	Valence	Total metals [g/ℓ]	T [°C]	Seed	
	10	4	3+	95	90.0	Goethite	
Time [min]	Ni [ppm]	Fe [ppm]	Co [ppm]	Cu [ppm]	As [ppm]	Ru [ppm]	Rh [ppm]
0	87181	3173	950	73	83.0	10.89	9.97
2	86343	68	945	65	1.9	0.26	1.84
15	86718	65	946	69	1.2	0.03	1.18
30	87302	47	949	71	0.9	0.04	0.88
60	86738	54	948	73	0.9	0.27	0.64
120	86796	43	949	75	0.9	0.11	0.58
240	88543	35	964	78	0.8	0.11	0.54
360	87827	23	954	78	0.7	0.20	0.50

	Run	pH	Valence	Total metals [g/ℓ]	T [°C]	Seed	
	11	4.0	3+	95	90	None	
Time [min]	Ni [ppm]	Fe [ppm]	Co [ppm]	Cu [ppm]	As [ppm]	Ru [ppm]	Rh [ppm]
0	85407	3415	969	70	75.0	8.27	9.18
2	83335	53	939	58	0.0	0.00	0.00
15	85097	69	954	65	0.0	0.00	0.00
30	85466	97	958	69	0.0	0.00	0.00
60	85304	37	965	57	0.0	0.00	0.00
90	86847	33	998	61	0.0	0.00	0.00
120	85137	41	976	71	0.0	0.00	0.00
180	85488	108	967	69	0.0	0.00	0.00
240	85645	30	972	67	0.0	0.00	0.00
360	86344	21	992	70	0.0	0.00	0.00

	Run	pH	Valence	Total metals [g/ℓ]	T [°C]	Seed	
	12	2.5	3+	65	70	Goethite	
Time [min]	Ni [ppm]	Fe [ppm]	Co [ppm]	Cu [ppm]	As [ppm]	Ru [ppm]	Rh [ppm]
0	57896	2318	641	48	59.6	7.82	7.16
2	57339	1901	633	49	2.4	3.77	7.81
15	57594	1372	635	48	0.6	2.72	7.35
30	57774	1185	641	47	0.4	3.06	7.37
60	57776	1053	641	47	0.3	3.49	7.86
90	58030	1033	638	48	0.0	2.79	7.69
120	57967	881	646	49	0.0	2.81	8.03
180	57892	732	644	47	0.0	2.79	7.55
240	58320	850	646	47	0.0	2.49	7.21
360	58370	725	648	50	0.0	2.11	7.23

	Run	pH	Valence	Total metals [g/ℓ]	T [°C]	Seed	
	13	2.5	3+	65	90.0	None	
Time [min]	Ni [ppm]	Fe [ppm]	Co [ppm]	Cu [ppm]	As [ppm]	Ru [ppm]	Rh [ppm]
0	60183	2366	665	49	60.9	7.99	7.31
2	57263	1948	629	46	42.7	6.79	6.08
15	57537	1117	635	47	18.7	4.99	5.10
30	57787	997	636	46	15.7	4.49	4.83
60	59149	871	651	48	11.9	3.66	4.57
90	59412	829	656	47	10.3	3.44	4.32
120	59786	771	656	47	9.1	3.49	4.25
180	59692	659	657	46	7.3	3.52	3.60
300	59787	514	657	46	5.1	3.65	3.07
360	60430	474	662	46	3.9	3.73	2.71

	Run	pH	Valence	Total metals [g/ℓ]	T [°C]	Seed	
	14	2.5	2+	65	70.0	None	
Time [min]	Ni [ppm]	Fe [ppm]	Co [ppm]	Cu [ppm]	As [ppm]	Ru [ppm]	Rh [ppm]
0	60511	2535	667	47	63.1	8.23	8.07
2	61280	2594	671	55	68.3	8.68	8.74
15	62267	2587	678	52	71.7	7.66	7.97
60	63750	2687	697	54	71.4	6.64	7.19
180	58780	2426	640	45	76.6	5.62	6.41
240	60655	2513	655	48	72.2	4.60	5.64
360	60657	2482	659	45	68.8	3.58	4.86

	Run	pH	Valence	Total metals [g/ℓ]	T [°C]	Seed	
	15	4	2+	65	70.0	None	
Time [min]	Ni [ppm]	Fe [ppm]	Co [ppm]	Cu [ppm]	As [ppm]	Ru [ppm]	Rh [ppm]
0	71463	2946	782	53	75.7	9.96	9.75
2	71280	2799	779	52	40.9	0.00	1.25
15	71265	2816	780	54	41.4	0.00	0.64
60	71194	2806	776	56	42.0	0.00	0.69
180	69561	2632	760	52	31.5	0.00	0.69
240	70300	2601	765	51	25.5	0.00	0.66
360	73794	2721	807	61	18.7	0.00	0.65

	Run	pH	Valence	Total metals [g/ℓ]	T [°C]	Seed	
	16	2.5	2+	65	70.0	Goet 100 g/ℓ	
Time [min]	Ni [ppm]	Fe [ppm]	Co [ppm]	Cu [ppm]	As [ppm]	Ru [ppm]	Rh [ppm]
-1	53091	2180	581	41	51.2	6.99	6.38
0	51418	2135	559	40	36.9	7.15	6.60
2	53662	2134	580	40	21.9	6.27	5.79
15	51589	2087	560	51	14.5	6.04	5.87
30	50970	2049	557	39	12.6	6.31	5.89
60	53279	2157	579	45	14.1	5.96	5.64
120	51326	2090	559	44	21.3	6.50	6.12
240	52076	2090	566	43	16.4	6.20	5.85

Run	pH	Valence	Total metals [g/ℓ]	T [°C]	Seed	
17	4	2+	65	70.0	Goet 100 g/ℓ	
Time [min]	Ni [ppm]	Fe [ppm]	Co [ppm]	Cu [ppm]	As [ppm]	Ru [ppm]	Rh [ppm]
-1	52998	2531	578	48	57.7	8.04	7.14
0	53167	2056	582	52	30.9	7.95	7.22
2	51983	1913	566	16	9.0	1.56	1.15
15	52797	1895	569	16	7.4	0.42	0.81
30	51465	1862	558	15	8.1	0.51	0.90
60	50805	1809	548	16	8.2	0.49	0.88
120	52224	1841	568	17	7.7	0.19	0.85
240	52665	1777	570	18	6.9	0.00	0.76

Run	Valence	Total metals [g/ℓ]	T [°C]	Seed
18	3+	65	90.0	None
Time [min]	Ni [ppm]	Fe [ppm]	Co [ppm]	Cu [ppm]
0	63480	2385	721	71
2	64638	2379	741	70
15	64912	1724	744	70
30	64799	1569	742	71
60	65551	1570	751	68
90	66623	1348	764	69
120	68151	1338	776	73
180	66146	1205	757	75
240	67426	1088	775	70

Run	Valence	Total metals [g/ℓ]	T [°C]	Seed
19	3+	65	90.0	None
Time [min]	Ni [ppm]	Fe [ppm]	Co [ppm]	Cu [ppm]
0	67936	2361	775	72
2	68288	2304	780	73
15	72186	2012	827	74
30	70222	1737	800	83
60	72519	1637	831	74
90	68272	1480	776	69
120	67613	1387	770	70
180	71807	1359	821	72
240	70867	1330	808	70

A.4 OPM experimental data

Time [min]	Run OPM 1 Fe [ppm]	pH 2.5 Ir [ppm]	Valence 2+ Ru [ppm]	Rh [ppm]
0	2505	8.05	10.88	11.40
2	2285	7.07	7.17	5.64
15	2312	7.05	5.24	4.10
30	2232	6.79	4.25	3.27
60	2268	7.00	3.67	2.53
90	2314	7.50	3.14	2.04
120	2190	7.18	2.55	1.67
180	2120	7.62	2.07	1.39
240	2142	7.52	1.69	1.11

Time [min]	Run OPM 2 Fe [ppm]	pH 2.5 Ir [ppm]	Valence 2+ Ru [ppm]	Rh [ppm]
0	2522	7.55	10.60	11.01
2	1978	0.97	0.00	0.63
15	1996	0.95	0.00	0.62
30	1998	0.91	0.00	0.62
60	1977	1.23	0.00	0.75
90	1962	1.06	0.00	0.88
120	1893	1.07	0.00	0.73
180	1803	1.00	0.00	0.71
240	1737	1.57	0.00	0.79

Time [min]	Run OPM 3 Fe [ppm]	pH 2.5 Ir [ppm]	Valence 3+ Ru [ppm]	Rh [ppm]	As [ppm]
0	2502	9.97	12.44	13.94	86.2
7.5	390	7.03	1.79	2.43	4.5
15	328	6.98	1.47	2.27	3.0
30	273	7.16	1.01	1.92	2.2
60	252	7.00	0.74	1.74	1.1
90	234	7.65	0.91	1.86	0.2
120	224	7.41	0.76	1.64	0.3
180	214	8.48	1.04	1.69	0.2
240	204	8.65	1.15	1.70	0.2
360	194	8.48	1.42	1.54	1.2

Time [min]	Run OPM 4 Fe [ppm]	pH 4 Ir [ppm]	Valence 3+ Ru [ppm]	Rh [ppm]	As [ppm]
0	2598	9.70	12.42	13.91	81.1
15	81	2.52	0.00	0.00	2.4
30	74	2.70	0.00	0.07	1.3
60	50	1.96	0.00	0.00	0.9
90	43	1.60	0.00	0.00	0.3
120	36	1.45	0.00	0.00	0.3
180	29	1.32	0.00	0.00	0.3
240	22	1.25	0.00	0.00	0.3
360	15	1.09	0.00	0.00	1.3

Time [min]	Run OPM 5 Ru [ppm]	pH 4 Rh [ppm]	Cu [ppm]
0	10.03	7.40	54.30
2	1.07	5.82	49.16
7.5	0.61	4.26	49.95
15	0.26	2.90	46.98
30	0.01	1.19	44.73
60	0.00	0.32	45.52
120	0.00	0.23	44.78

A.5 Other SEM images

A.5.1 Sample 1

SE images:

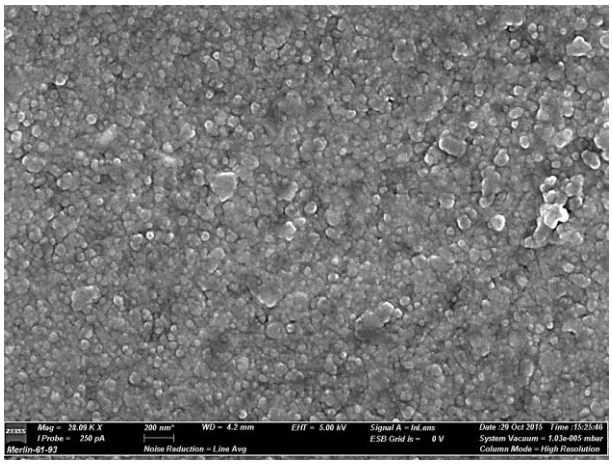

Figure A-0-1: Additional SE image of Sample 1.

BSE images:

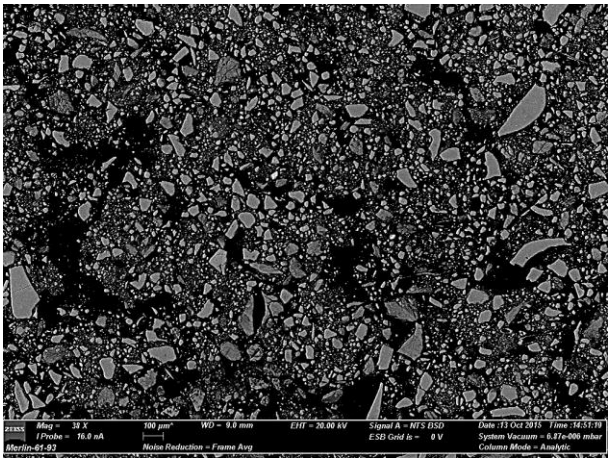

Figure A-0-2: Bulk view (BSE) of Sample 1.

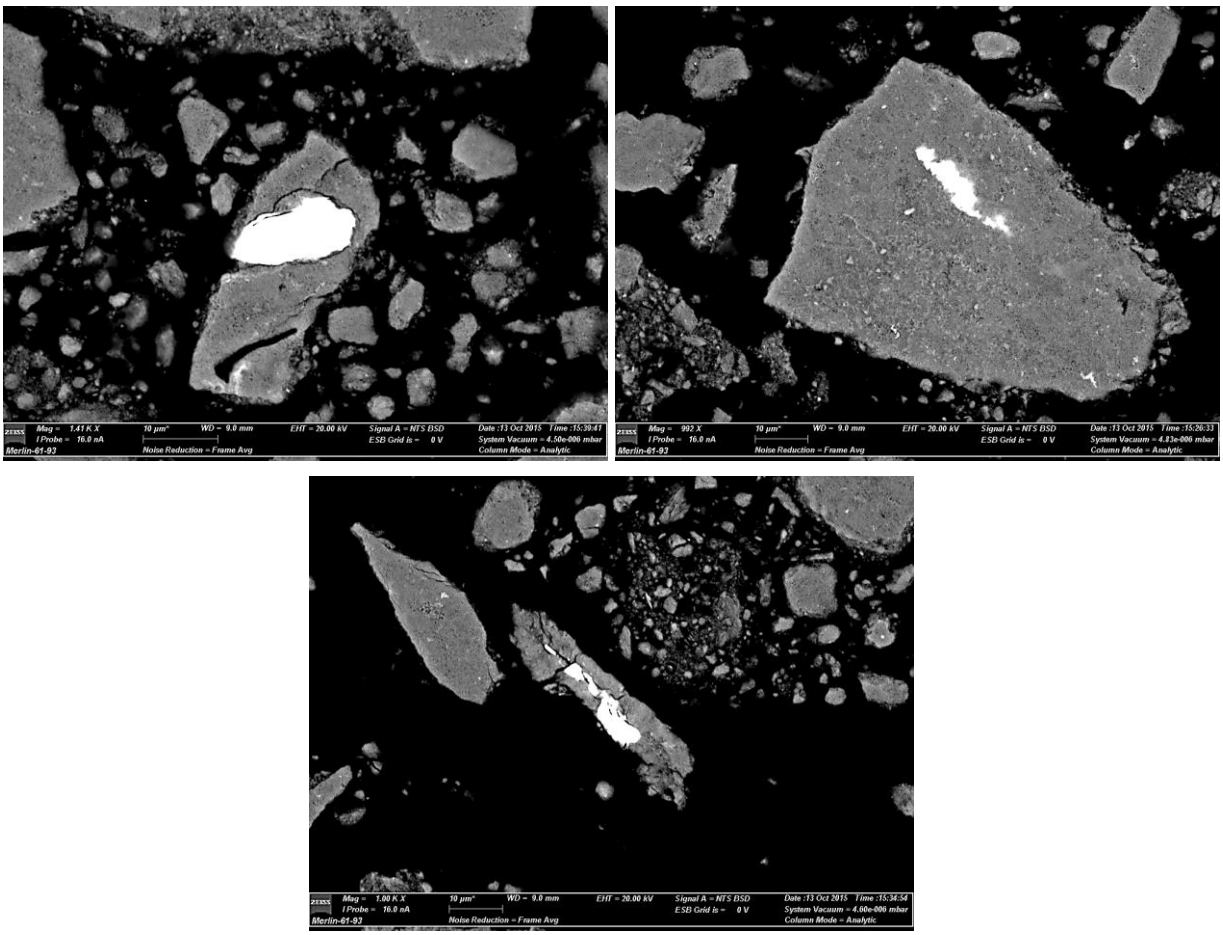

Figure A-0-3: Magnified BSE images of iridium phases (bright) in Sample 1.

A.5.2 Sample 2

SE images:

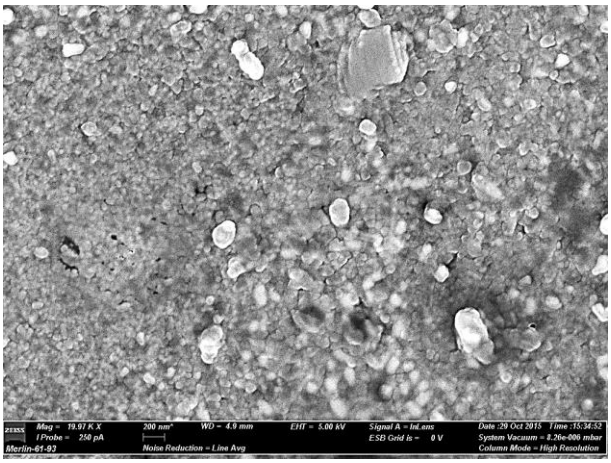

Figure A-0-4: Additional SE image of Sample 2.

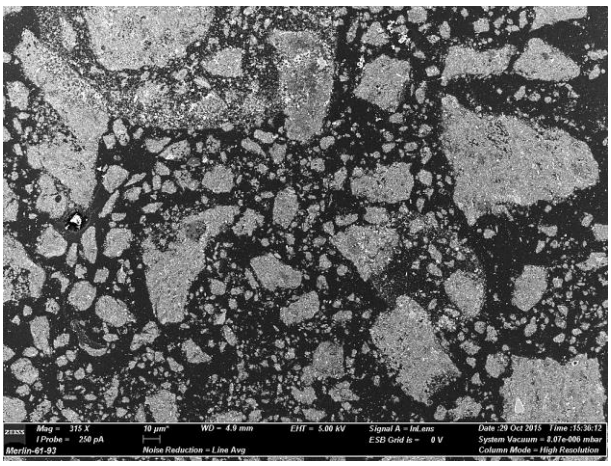

Figure A-0-5: Bulk SE image of Sample 2.

BSE images:

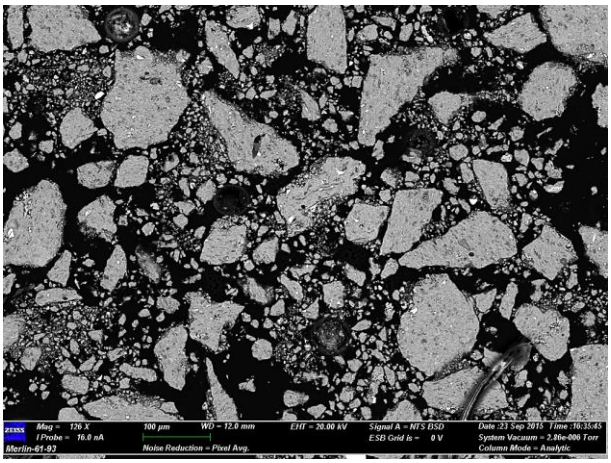

Figure A-0-6: High brightness image of Sample 2.

A.5.3 Sample 4

SE images:

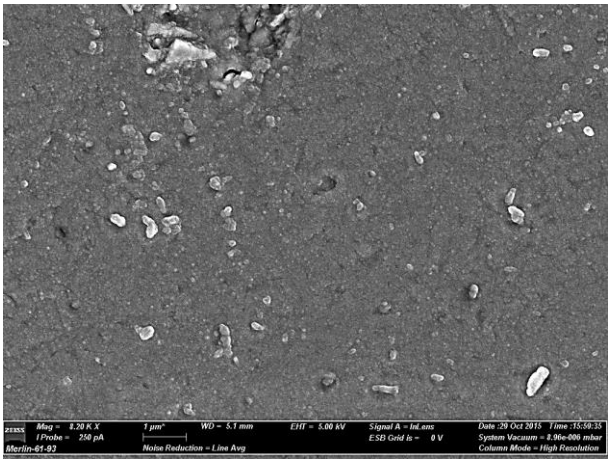

Figure A-0-7: Bulk SE image of Sample 4.

BSE images:

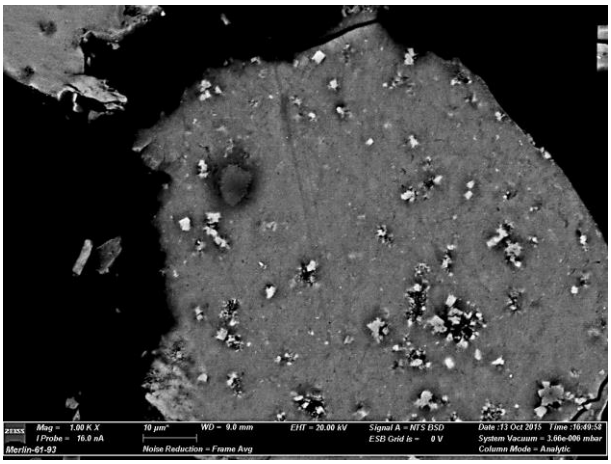

Figure A-0-8: Additional heterogeneous phase BSE image of Sample 4.

The dark spot observed above was induced by the electron beam.

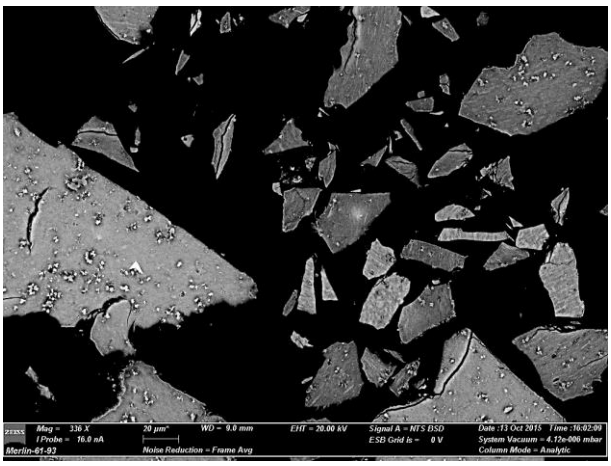

Figure A-0-9: Additional BSE image indicating various phases in Sample 4.

A.5.4 Sample 5

SE images:

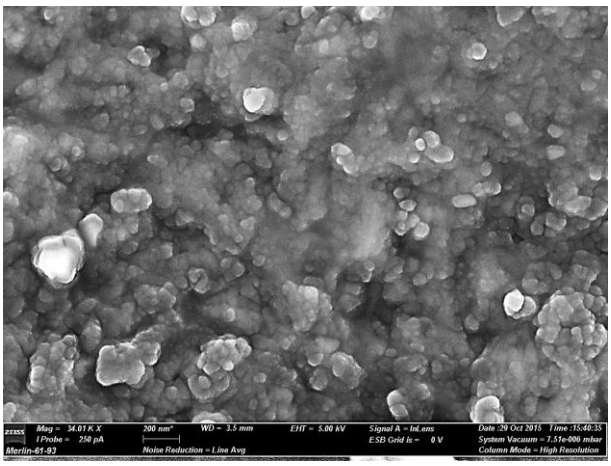

Figure A-0-10: SE image within the dark grain of Sample 5.

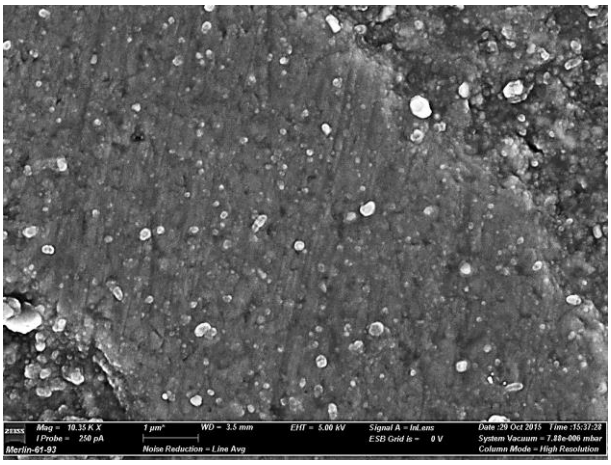

Figure A-0-11: SE image of the lighter grain of Sample 5.

BSE images:

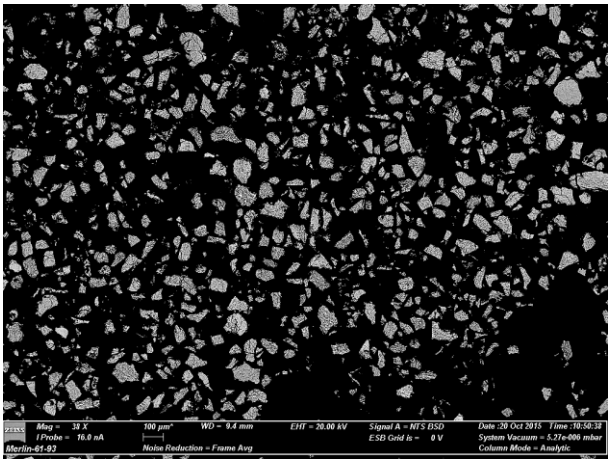

Figure A-0-12: Bulk view of Sample 5 (BSE).

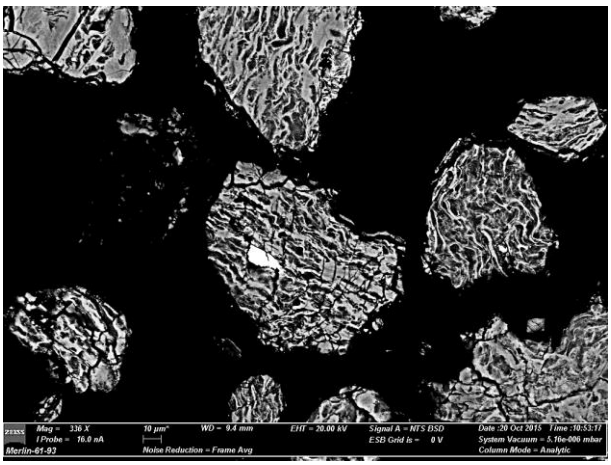

Figure A-0-13: BSE image of iridium phase within Sample 5.

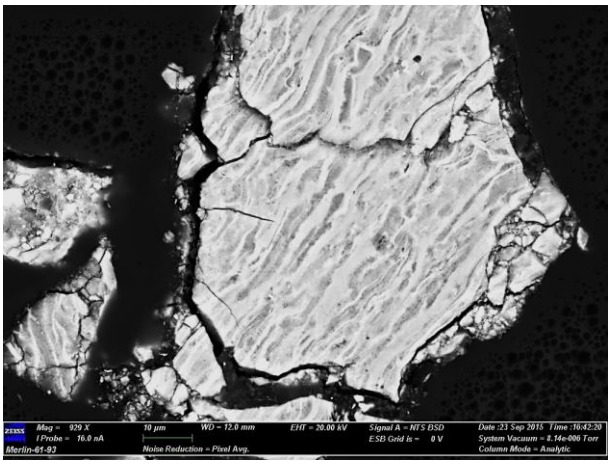

Figure A-0-14: High brightness BSE image of Sample 5.

A.5.5 Sample 8

SE images:

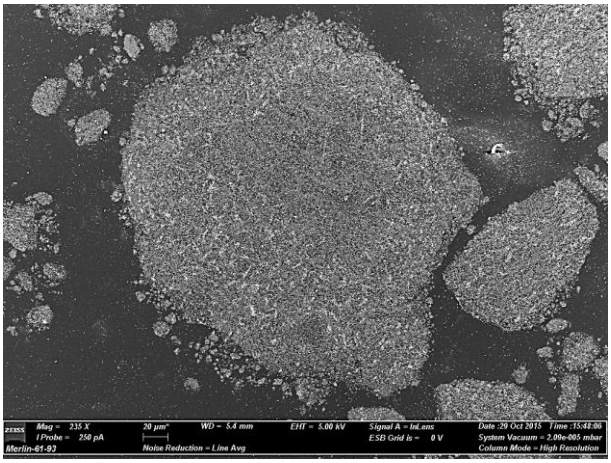

Figure A-0-15: SE image of bulk goethite seeded Sample 8.

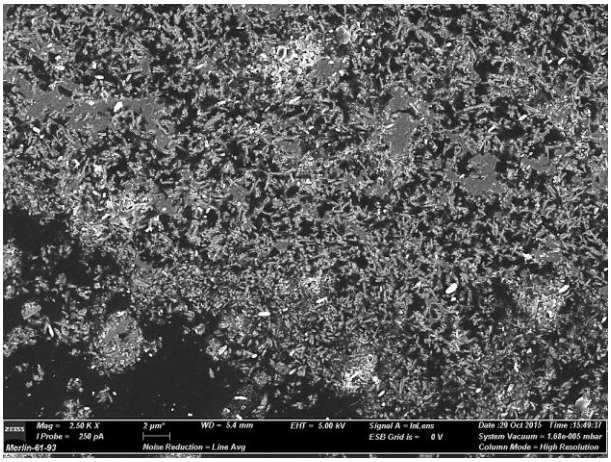

Figure A-0-16: Zoomed-out image of goethite rods observed in Sample 8.

BSE images:

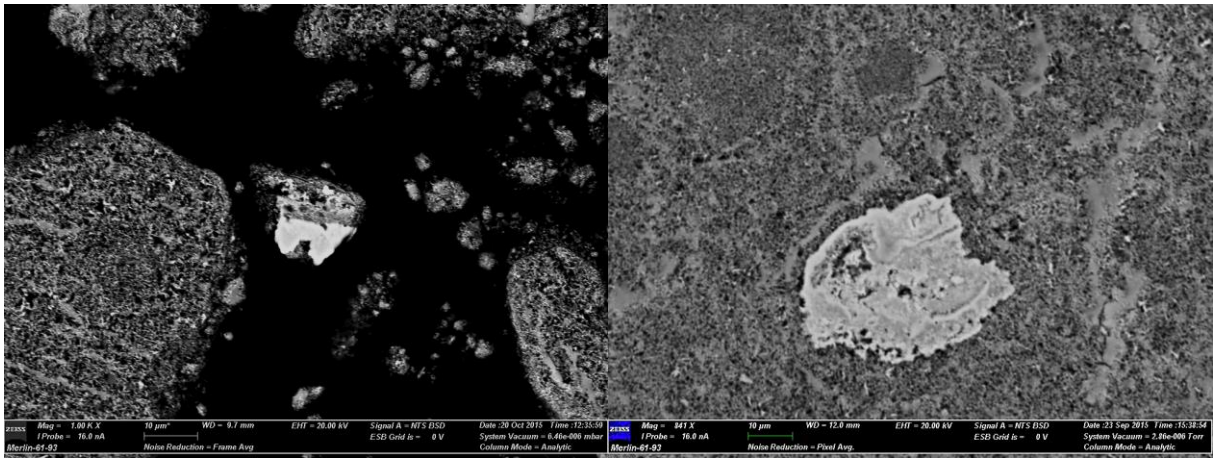

Figure A-0-17: Additional BSE images of iron oxides with variable Fe:O ratio's to the goethite seed material in Sample 8.

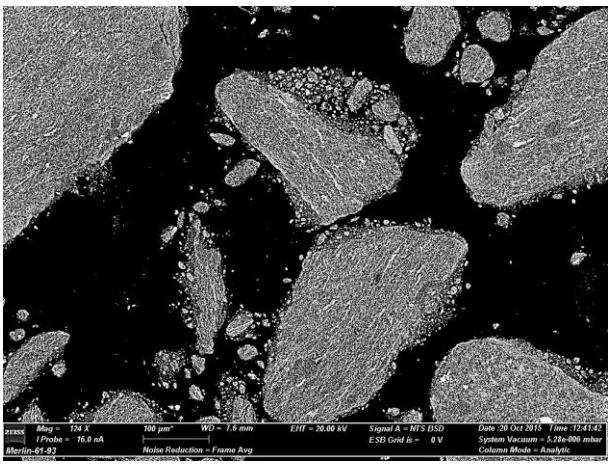

Figure A-0-18: Additional BSE image of bulk goethite seed particles in Sample 8.

APPENDIX B: EXPERIMENTAL METHOD

B.1 Nickel reduction in synthetic solutions

The nickel sulphate solution is being evaporated at the plant, boiling off excess water. The two states of concentration was simulated by using total metals concentration as a variable. The unconcentrated solution contains 100 g metals/ℓ and the second, concentrated solution would contain between 150 g metals/ℓ to 170 g metals/ℓ.

The solubility of $NiSO_4.6H_2O$ crystals are between 694 g crystals/kg H_2O at 25 °C, which is equal to 153 g Ni/kg H_2O. The solubility of nickel sulphate increases to 734 g/kg H_2O at 95 °C (Seidell, 1965).

The concentrated solution could theoretically be synthesized at 25 °C. In practice, a small fraction of insolubles were observed, which could've potentially interfered with the experiments. The decision was taken to reduce the total metals content in order to achieve synthesis at room temperature.

Olivier's (2011) work investigated the same nickel sulphate solution. A summary of the collected plant data, Olivier's (2011) synthetic solution and a proposed solution for this work is given in Table B-0-1.

Table B-0-1: Summary of nickel sulphate plant stream, Olivier's (2011) synthetic solution and the proposed synthetic solution for this work:

	[Ni] [g/ℓ]	**[Fe]** [g/ℓ]	**[Co]** [g/ℓ]
Plant data	100	2.5	0.65
Olivier (2011)	83.3	3.3	1.07
Proposed solution	62.5	2.5	0.65

The lowered nickel content also enabled more sensitive detection of the trace elements of interest and was also more comparable to the work of Olivier (2011). The lower nickel content also allowed synthesis and storage of concentrated nickel solution at room temperature.

B 2 Experimental error calculation

Four lack-of-fit experiments were conducted during the Screening experimental in order to measure the repeatability.

The mean ($\bar{x}$) and standard deviation (s) were calculated. Thereafter the standard error was calculated by dividing the standard deviation with the square root of the number of samples (N).

$$standard\ error\ (SE) = \frac{s}{\sqrt{N}}$$

The t critical value for a 90 % confidence interval was obtained.

$$t = \frac{\bar{x}-\mu}{SE}$$

Thereafter the confidence interval can be calculated.

$$Confidence\ interval\ (CI) = \bar{x} \pm (SE \times t)$$

The standard error was calculated at each time interval for each metal, and is presented graphically for the base metals in Figure B-0-1 and for OPMs in Figure B-0-2. The base metals nickel, cobalt and copper remain consistent throughout the experiment. The readings reported at 15 min and 30 min vary somewhat at random places, such as the 15 min and 30 min marks for nickel and at 180 min for copper, but are overall consistent with each other.

A descending cone-shaped decrease in the error magnitude is observed for iron over time. It is evident that the reaction was faster in the one instance. The large error bars of these species undoubtedly relate to the fast ferric experiment hydrolysis observed throughout the experiments. It can be caused by faster manual addition of neutralising agent or small time discrepancies between the experiments.

The actual, time-specific standard error bars were assigned to all ferric experiments. The ferrous runs' iron graphs were assigned with the average standard errors, which is in any case an overestimation of the error for these ferrous experiments.

The time error would not surpass 2 min. This considers the variable time when adding neutralising agent via the manual valve, the seed addition and the taking of the first sample. The estimated vertical error bar is less than the circle's (or shape's) diameter used in graphs and therefore wasn't added to graphs.

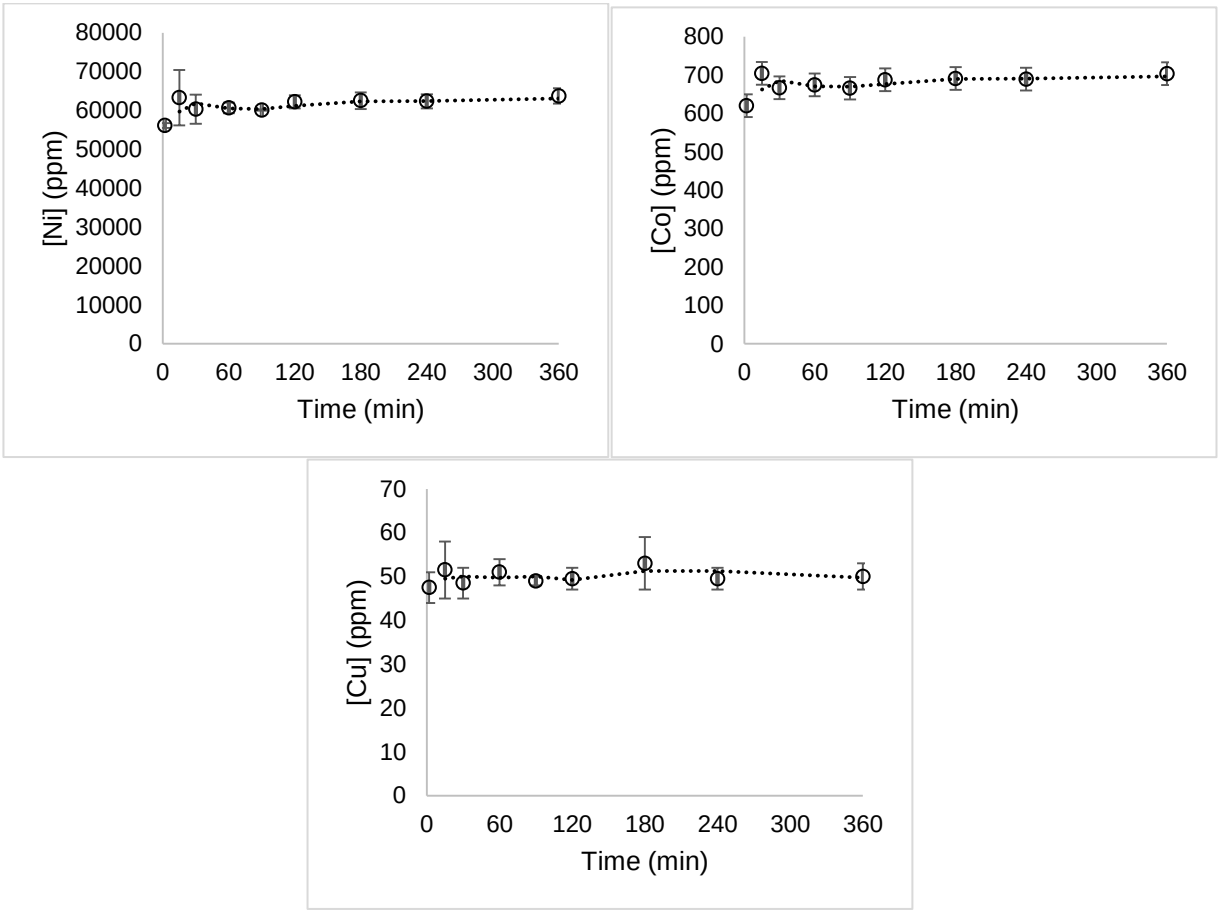

Figure B-0-1: Base metal error bars generated.

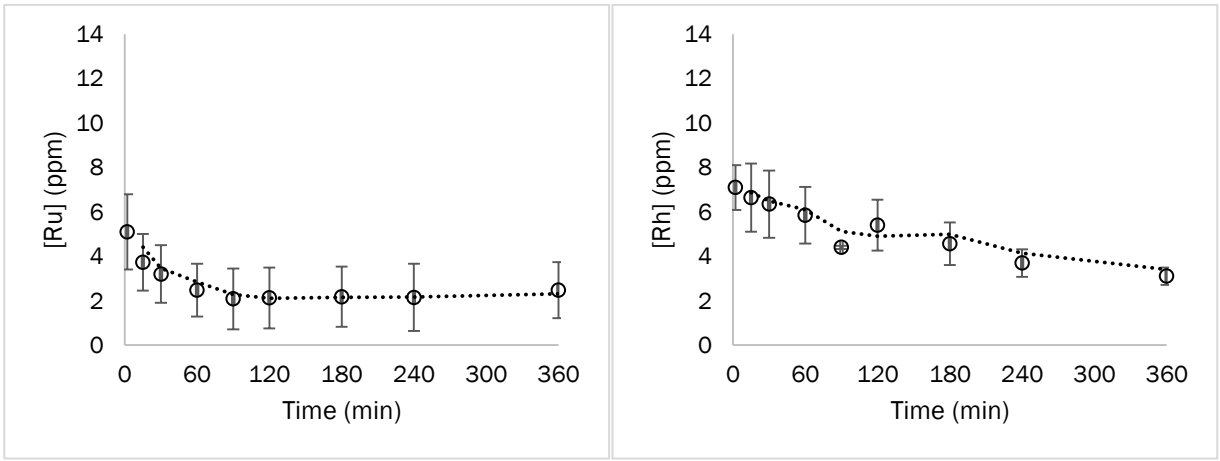

Figure B-0-2: Ruthenium and rhodium error bars generated.

Run 18 and 19's initial pH was 2.3, instead of 2.5, in order to establish variability of iron content at lower pH and to observe how sensitive the system is to pH alteration. Figure E-0-2 provides the repeatability between the controlled experiments. Table B-0-2 and Table B-0-3 provides the calculated errors.

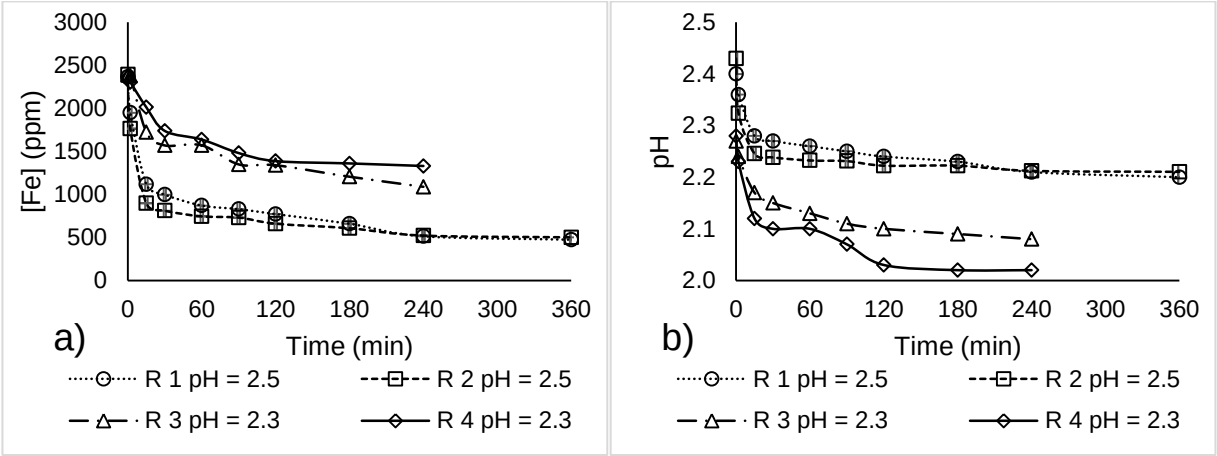

Figure B-0-3: Iron and pH over time for repeatability test work.

Table B-0-2: Iron R 1 and R 2 repeatability at Fe(III) & pH 2.5.

Iron: R 1 and R 2 repeatability				
x (mean)	s (stdev.s)	standard error	CI (90 %)	Error
2380	19	10	21	2%
1856	131	65	139	15%
1007	156	78	167	33%
904	132	66	141	31%
808	89	44	95	23%
780	69	35	74	19%
715	79	39	84	23%
633	37	18	39	12%
518	6	3	6	2%
487	19	14	29	12%

Table B-0-3: Iron R 3 and R 4 repeatability at Fe(III) & pH 2.3.

Time	x (mean)	s (stdev.s)	standard error	CI (90 %)	Error
0	2374	16.84	8.42	17.95	1.5%
2	2342	52.58	26.29	56.05	5%
15	1869	203.41	101.70	216.82	23%
30	1653	119.05	59.53	126.90	15%
60	1604	47.50	23.75	50.63	6%
90	1415	93.35	46.67	99.50	14%
120	1363	34.09	17.04	36.33	5%
180	1283	109.10	54.55	116.29	18%
240	1209	170.93	85.46	182.20	30%

The average standard errors (over time) are given in Table B-0-4.

Table B-0-4: Standard error between duplicate runs.

	Standard error [ppm]
Ni	2286
Co	29.5
Cu	3.5
As	7.4
Ru	1.37
Rh	0.95

B 3 ICP data analysis and interference

The spectral lines used to ICP-OES analysis are given in Table B-0-5. Instances with multiple lines per element were averaged.

Table B-0-5: Spectral lines used for ICP-OES analysis.

Element	Spectral lines used		
Ni	Ni 221.647 {452} (Radial)		
Co	Co 228.616 {447} (Radial)	Co 237.862 {142} (Radial)	Co 238.892 {141} (Radial)
Cu	Cu 324.754 {104} (Radial)	Cu 327.396 {103} (Radial)	
Fe	Fe 238.204 {141} (Radial)	Fe 259.940 {130} (Radial)	
Na	Na 589.592 {57} (Radial)	Na 818.326 {41} (Radial)	
As	As 189.042 {478} (Radial)	As 189.042 {478} (Axial)	
Ir	Ir 224.268 {450} (Axial)		
Ru	Ru 266.161 {126} (Axial)		
Rh	Rh 343.489 {98} (Axial)	Rh 369.236 {91} (Axial)	

B 4 Synthesis method and accuracy

The synthetic solutions were made up by measuring the amount of metal salt on a scale with an accuracy rating of ± 0.00005 g. The humanly possible accuracy of the weighted metal salts accounted to a ± 0.0005 g deviation from the calculated metal salt required. The required

amount of metal salt was calculated with the supplier's purity and molecular weight specifications. Sample calculations are given below:

$$\%\ metal\ in\ salt = \frac{molecular\ weight\ of\ metal}{total\ molecular\ weight} \times purity\ [wt\%]$$

$$salt\ required\ [g] = \frac{metal\ required\ [g]}{\%\ metal\ in\ salt}$$

Impurity content was considered and initially calculated with the amounts of salts added and didn't attribute to a noticeable increase in any particular metal over its specified limits. Analytical grade reagents were used.

During experiments neutralisation with NaOH was applied in order to get the synthetic solution to the desired pH. The addition of neutralising agent slightly diluted the synthetic solution. Initially the exact volumetric amount of NaOH solution added was recorded and the ICP readings were adjusted according to the following calculation:

$$[M]_{volume\_corrected} = [M]_{raw\_ICP\_reading} \times \frac{500\ ml}{(500+x)ml}$$

However, this calculation could not account for the actual volume difference caused by the addition of neutralisation and was therefore discarded.

APPENDIX C: ADDITIONAL EXPERIMENTAL WORK

C.1 Preparatory experimental

C.1.1 Iron behaviour during peroxide oxidation

Gradual iron precipitation occurred in Run P 1. Over the course of the 8 h run, 160 ppm (8 %) iron precipitated. The solution pH also gradually decreased from initial pH 2.49 to pH 2.43. The solution Eh = 354 + 200 mV falls within the FeOOH thermodynamic stability area in constructed EpH diagrams (refer to Figure 3-1). Gradual oxidation as a result of solution chemistry will occur. Precipitate was observed on glassware at the liquid-air interface after experiments, which suggests that air oxidation of metals occurred. The hydrolysis of iron is acid forming and leads to the gradual decrease in pH observed. The iron in solution and the corresponding pH are provided for Run P 1 – Run P 3 in Figure C-0-1.

Run P 2 and Run P 3 were subjected to peroxide addition, which visually had an erratic bubbling effect when added at t = 0 min. Peroxide addition neutralising led to the rapid oxidation of ferrous and spontaneous precipitation was noted. A sudden drop in iron content over time and pH was noted. The pH followed the trend of the iron in solution for all three experiments.

Oscillating iron content was observed in Run P 2. 81 % iron precipitation occurred rapidly, which was followed by partial iron dissolution from 60 min onwards. Visually, aggressive fizzing was observed when slowly adding peroxide. The excess oxidation might have over-oxidised iron and other ions to yield unstable products, which dissociated again given time to reach equilibrium.

Run P 3, at pH 3.6 did not exert oscillating iron content over time, instead gradual iron precipitation was noted that lead to 90 % iron loss at t = 360 min. The pH dropped from pH 3.6 to pH 2.3 within the first two minutes of the experiment.

No induction period was required for the precipitation of iron, which strongly suggest that the iron was supersaturated enough to nucleate immediately after neutralisation and oxidation. No solids were visually observed on the epoxy coated pH probe, the Pt-100 temperature probe or the baffles of the reactor, suggesting that these foreign surfaces did not significantly aid nucleation or growth.

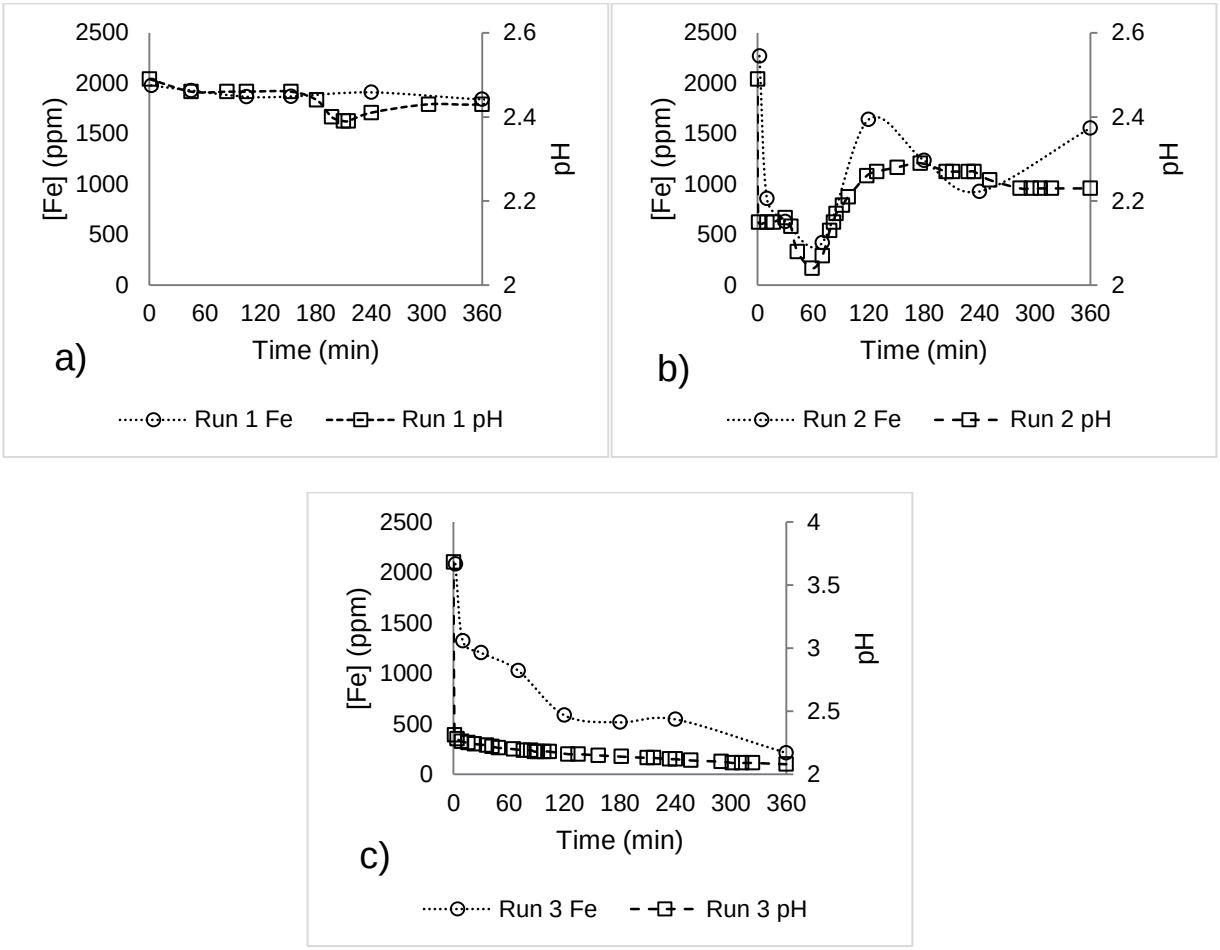

Figure C-0-1: Fe in solution and pH over time for Preparatory experimental runs, a) Run P 1: pH 2.5, no peroxide, b) Run P 2: pH 2.5, with peroxide and c) Run P 3: pH 3.6, with peroxide.

The filter cakes obtained are given in Figure C-0-2 for Run P 2 and Run P 3. Apart from the higher quantity of precipitate of Run P3, a distinct colour difference between the two samples is observed.

Figure C-0-2: Filter cakes of Run P 3 at pH 3.7 (Left) and Run P 2 at pH 2.5 (Right).

Base metals nickel, cobalt and copper did not precipitate in the Preparatory experimental. The experimental data is provided in Appendix A. Notably, peroxide addition did not influence the concentration of the base metals. Comprehensive base metal behaviour analysis is done in the Screening experimental.

C.1.2 Neutralisation of synthetic solution

An equivalence point, i.e. a rapid rise in pH, was observed in the Preparatory experimental runs when the pH was increased above pH 3. Uncontrolled pH overshooting was possible when manual addition of NaOH was done. Potentiometric titration, by titrating the synthetic solution slowly with NaOH and recording the resulting pH, was done. The potentiometric titration data was used to accurately calculate the required amount of NaOH.

The equivalence point occurs at approximately pH 4.5; with the rapid pH rise starting at pH 3.3. The system behaved as if weak acid-base interaction occurred in the high metal content solution. A control experiment indicated that significantly less NaOH was required in the absence of metal ions. A typical neutralisation curve, as generated by potentiometric titration, is given in Figure C-0-3.

It is believed that the equivalence point is caused due to the complexation of nickel in the solution. The equivalence point occurred near the 0.5 stoichiometric mole ratio of $[OH^-]/[Ni^{2+}]$. A supporting EpH diagram of nickel is also given in Figure C-0-3 and lists a dimer: $Ni_2(OH)^{3+}$ as the predominant ion in solution. The mole ratio equivalence at 0.5 agrees well with the proposed complexation of a nickel dimer.

A neutralisation strategy was developed. Only a fraction of the NaOH shown in Figure C-0-3 was required when applying rapid NaOH neutralisation. 8.9 mℓ, 2 M NaOH was used for the neutralisation to pH 2.5 and 45.5 mℓ, 2 M NaOH was used for the neutralisation to pH 4.0 from the initial pH of 1.7. The last few drops would simply be added slower, to prevent an overshoot in experiments neutralised to pH 4.0. The iron valence state did not influence the end pH significantly, but concentrated runs tended to require slightly less NaOH. Ferrous and ferric runs required an identical quantity of NaOH to neutralise the solutions to the respective pHs.

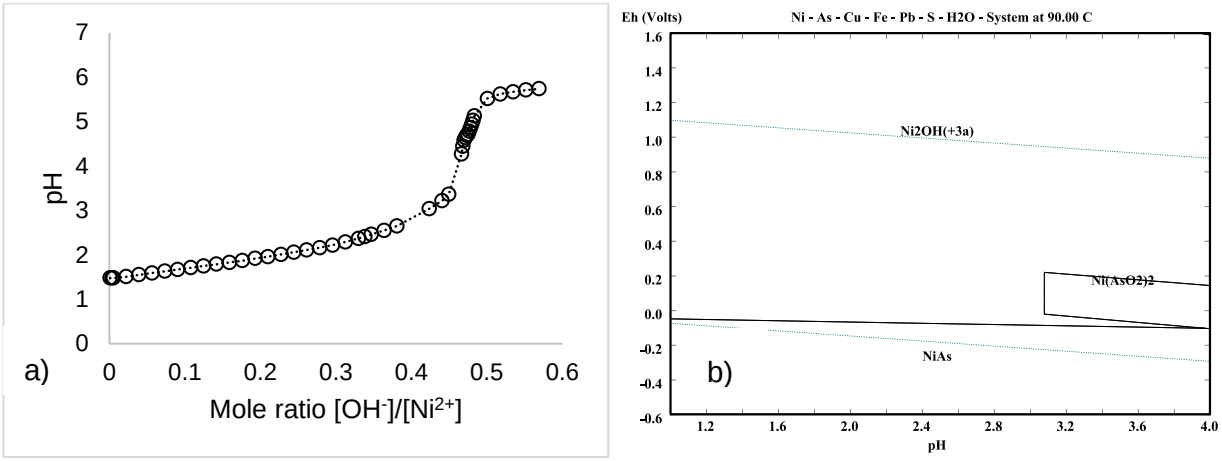

Figure C-0-3: a) Neutralisation curve for 65 g/ℓ nickel sulphate solution with Fe(II) at 90 °C. b) EpH diagram at 90 °C for nickel sulphate solution.

APPENDIX D: ANOVA ANALYSIS

The percentage of metal that precipitated was calculated from the respective metal in solution over time data (ppm) according to the following calculation.

$$M(\%) = \frac{M_{initial} - M_t}{M_{initial}}$$

with M depicting the metal concentration in ppm.

The percentage data was transformed to accommodate for the finite range of the coded data, i.e. from 0 % to 100 % precipitated. This method is recommended by the statistical software used, for yield and finite range data.

$$y' = \ln\left(\frac{y - y_{min}}{y_{max} - y}\right)$$

Both a half-normal plots and Pareto charts were collectively used in order to determine the significant effects and to include into the statistical model. Table E-0-1 presents the aliasing of the D-Optimal design.

Table E-0-1: D-Optimal design alias calculation.

[Intercept] = Intercept + 0.167 * BD + 0.167 * BE + CD - 0.667 * CE - 0.667 * DE
[Block 1] = Block 1 - 0.333 * BD - 0.333 * BE - 0.667 * CE - 0.667 * DE
[Block 2] = Block 2 + 0.333 * BD + 0.333 * BE + 0.667 * CE + 0.667 * DE
[A] = A + BC + 0.643 * BD - 0.214 * BE + 0.429 * CE + 0.429 * DE
[B] = B + 0.643 * BD - 0.214 * BE + 0.429 * CE + 0.429 * DE
[C] = C + AD - 2 * BC - 1.64 * BD + 0.214 * BE + CD - 2.43 * CE - 1.43 * DE
[D] = D - AD + 2 * BC + 1.33 * BD + 0.333 * BE - CD + 2.67 * CE + 1.67 * DE
[E] = E + BC + 0.548 * BD + 0.262 * BE + 0.81 * CE + 0.81 * DE
[AB] = AB + BC + 0.595 * BD + 0.0238 * BE + 0.619 * CE + 0.619 * DE
[AC] = AC + AD - BC - 0.786 * BD - 0.0714 * BE - 0.857 * CE - 0.857 * DE
[AE] = AE - BC - 0.738 * BD - 0.31 * BE - 1.05 * CE - 1.05 * DE

Iron at 30 min

Table E-0-2 provides the Anova table reduced for the model of iron precipitated at 30 min. A large model F-value of 151.32 suggests that there is a 0.01 % chance that this F-value occurs

due to noise. Model terms A, B, C, E, AC and BE are all significant, with all excluded terms being insignificant.

Table E-0-2: Anova table for Fe precipitated (%) at 30 min.	Sum of Squares	df	Mean Square	F Value	p-value Prob > F
Block	0.03	1.00	0.03		
Model	154.59	7.00	22.08	151.32	0.0001
A-pH	23.46	1.00	23.46	160.73	0.0002
B-Valence	60.50	1.00	60.50	414.57	< 0.0001
C-[Metals]	3.46	1.00	3.46	23.71	0.0082
D-Temp	0.98	1.00	0.98	6.70	0.0608
E-Seeding	1.85	1.00	1.85	12.65	0.0237
AC	3.38	1.00	3.38	23.16	0.0086
BE	1.34	1.00	1.34	9.21	0.0386
Residual	0.58	4.00	0.15		
Lack of Fit	0.37	3.00	0.12	0.58	0.7204
Pure Error	0.21	1.00	0.21		
Cor Total	155.20	12.00			

A normal plot of residuals and the residuals versus predicted plot are given in Figure E-0-1. The residuals follow a normal distribution with no obvious patterns. A random scatter within the error margins in the residuals versus predicted plot is observed. The data is normally distributed and independent which suggests that the model fitted to the data is adequate.

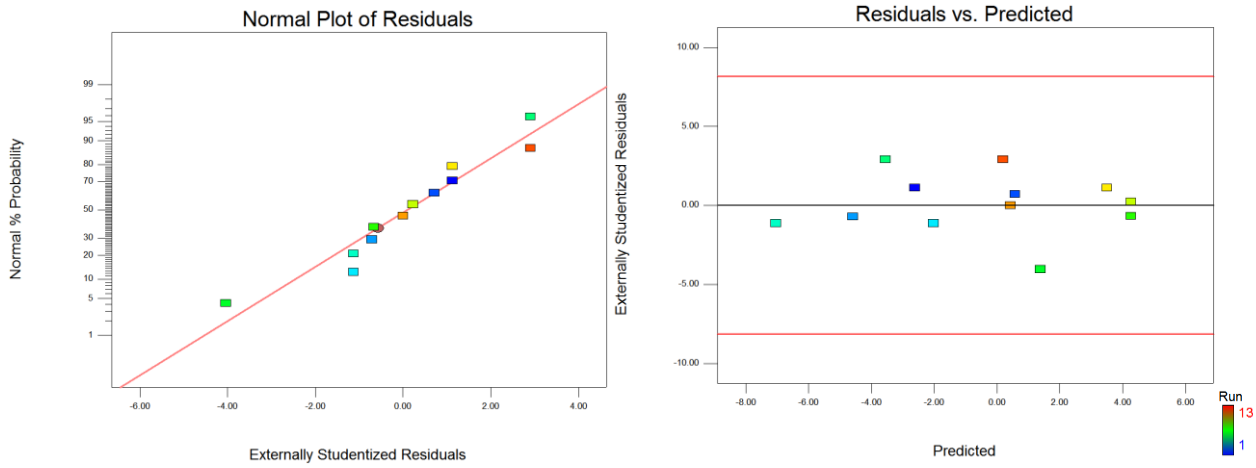

Figure E-0-1: Normal plot of residuals and residuals vs predicted plot for Fe at 30 min (%).

Iron at 60 min

The Pareto chart with model effects highlighted is given in Figure E-0-2. Table E-0-3 provides the Anova table reduced for the model of iron precipitated at 60 min. A large model F-value of 128.83 suggests that there is a 0.01 % chance that this F-value occurs due to noise. Model terms A and B were significant with p-values below 0.05.

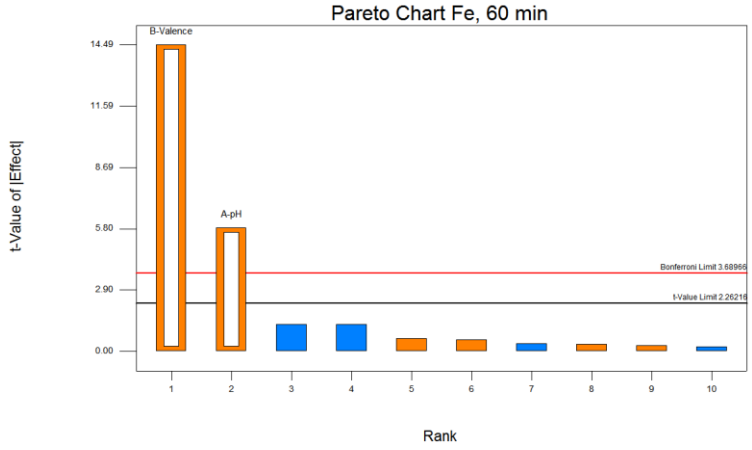

Figure E-0-2: Pareto chart of Fe precipitated (%) at 60 min with significant factors highlighted.

Table E-0-3: Anova table for Fe precipitated (%) at 60 min.

	Sum of Squares	df	Mean Square	F Value	p-value Prob > F
Block	0.06	1	0.06		
Model	168.20	2	84.10	128.83	2.38E-07
A-pH	22.26	1	22.26	34.09	2.47E-04
B-Valence	137.04	1	137.04	209.93	1.52E-07
Residual	5.88	9	0.65		
Lack of Fit	5.87	8	0.73	77.63	0.09
Pure Error	0.01	1	0.01		
Cor Total	174.13	12			

A normal plot of residuals and the residuals versus predicted plot are given in Figure E-0-3. The residuals follow a normal distribution with no obvious patterns. A random scatter within the error margins in the residuals versus predicted plot is observed. The data is normally distributed and independent which suggest that the model fitted to the data is adequate.

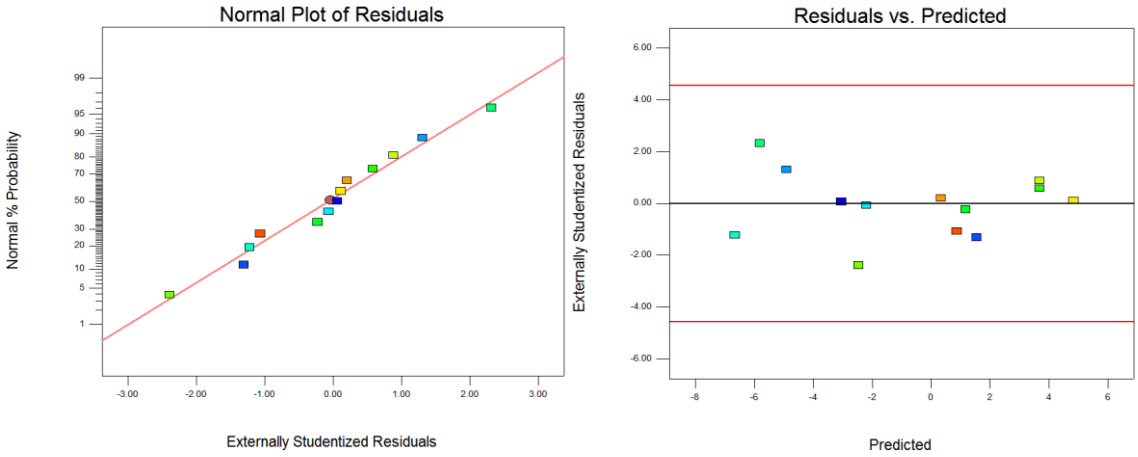

Figure E-0-3: Normal plot of residuals and residuals vs predicted plot for Fe at 60 min (%).

Iron at 120 min

The Pareto chart with model effects highlighted is given in Figure E-0-4. Table E-0-4 provides the Anova table reduced for the model of iron precipitated at 120 min. A large model F-value of 158.03 suggests that there is a 0.01 % chance that this F-value occurs due to noise. Model terms A and B were significant with p-values below 0.05.

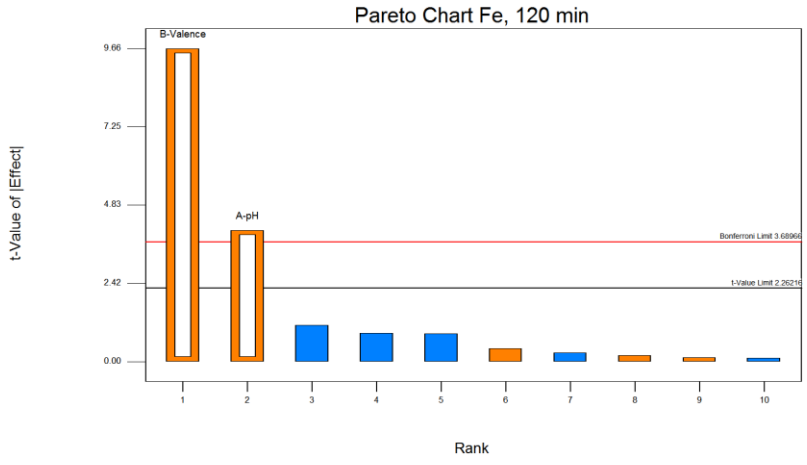

Figure E-0-4: Pareto chart of Fe precipitated (%) at 120 min, with significant factors highlighted.

Table E-0-4: Anova table for Fe precipitated (%) at 120 min.

	Sum of Squares	df	Mean Square	F Value	p-value Prob > F
Block	0.12	1	0.12		
Model	140.38	2	70.19	58.03	7.19E-06
A-pH	19.85	1	19.85	16.42	2.88E-03
B-Valence	112.91	1	112.91	93.36	4.76E-06
Residual	10.89	9	1.21		
Lack of Fit	8.26	8	1.03	0.39	0.85
Pure Error	2.62	1	2.62		

Cor Total	151.39	12

A normal plot of residuals and the residuals versus predicted plot are given in Figure E-0-5. The residuals follow a normal distribution with no obvious patterns. A random scatter within the error margins in the residuals versus predicted plot is observed. The data is normally distributed and independent, suggesting that the model fitted to the data is adequate.

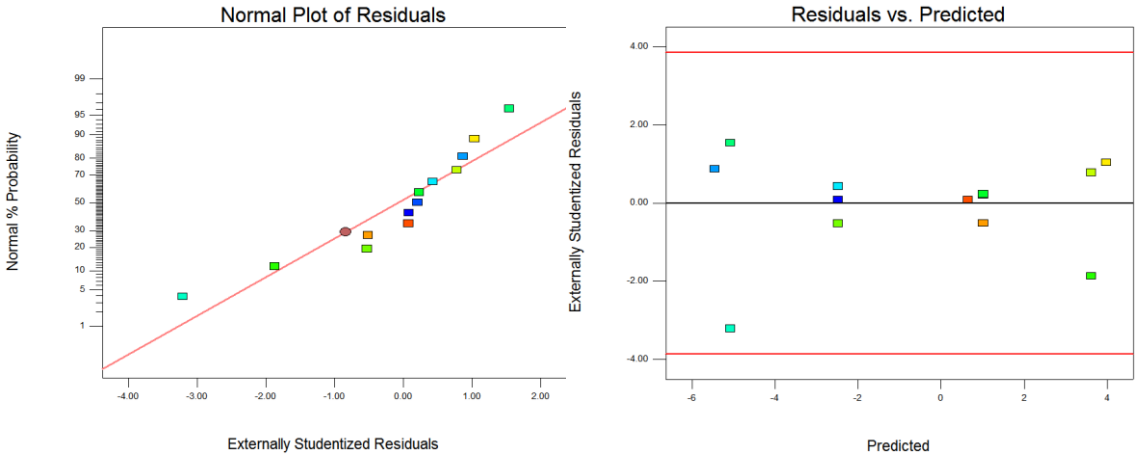

Figure E-0-5: Normal plot of residuals and residuals vs predicted plot for Fe at 120 min (%).

Iron at 240 min

The Pareto chart with model effects highlighted is given in Figure E-0-6. Table E-0-5 provides the Anova table reduced for the model of iron precipitated at 240 minutes. A large model F-value of 48.16 suggests that there is a 0.01 % chance that this F-value occurs due to noise. Model terms A and B were significant with p-values below 0.05.

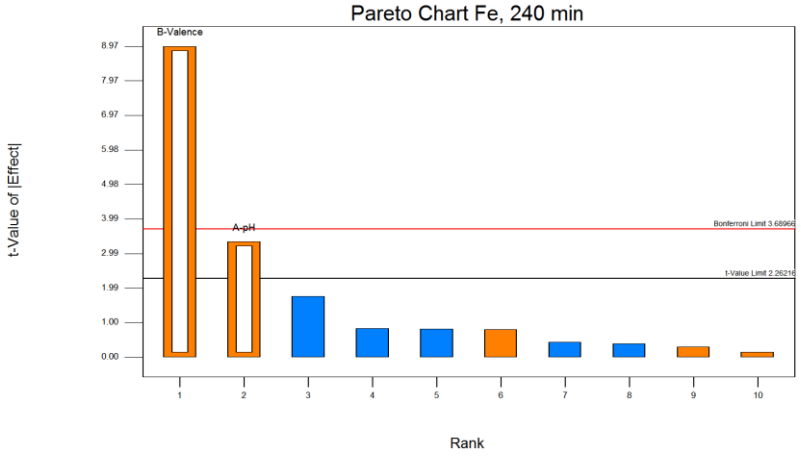

Figure E-0-6: Pareto chart of Fe precipitated (%) at 240 min with significant factors highlighted.

Table E-0-5: Anova table for Fe precipitated (%) at 240 min.

	Sum of Squares	df	Mean Square	F Value	p-value Prob > F
Block	0.05	1	0.05		
Model	153.19	2	76.59	48.16	1.56E-05
A-pH	17.62	1	17.62	11.08	8.82E-03
B-Valence	127.88	1	127.88	80.41	8.80E-06
Residual	14.31	9	1.59		
Lack of Fit	12.25	8	1.53	0.74	0.72
Pure Error	2.06	1	2.06		
Cor Total	167.55	12			

A normal plot of residuals and the residuals versus predicted plot are given in Figure E-0-7. The residuals follow a normal distribution with no obvious patterns. A random scatter within the error margins in the residuals versus predicted plot is observed. The data is normally distributed and independent which suggest that the model fitted to the data is adequate.

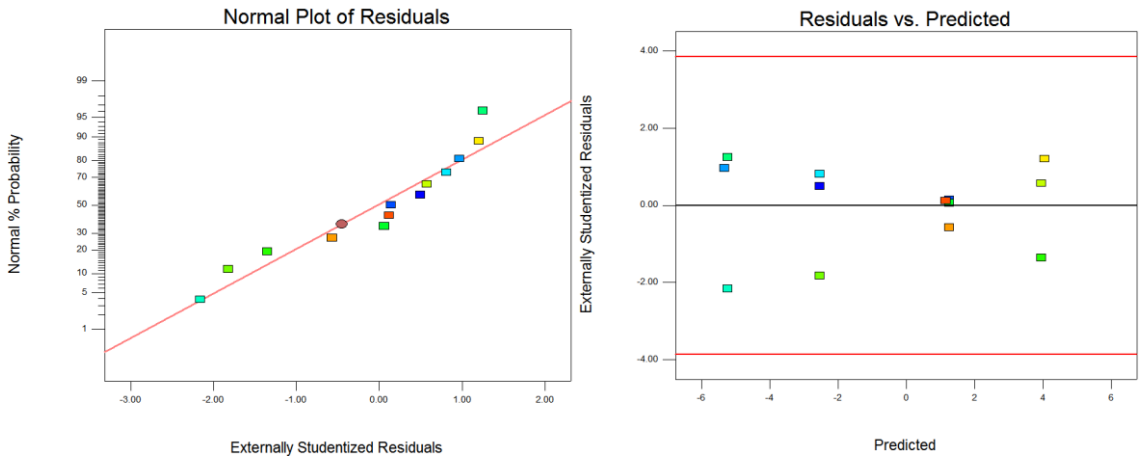

Figure E-0-7: Normal plot of residuals and residuals vs predicted plot for Fe at 240 min (%).

Iron at 360 min

Table E-0-6 provides the Anova table reduced for the model of iron precipitated at 360 min. A large model F-value of 114.19 suggests that there is a 0.01 % chance that this F-value occurs due to noise. Model terms A, B and AC are significant with p-values below 0.05. Model term C is insignificant, (p-value > 0.05) but is added to support the hierarchy.

Table E-0-6: Anova table for Fe precipitated (%) at 360 min.

	Sum of Squares	df	Mean Square	F Value	p-value Prob > F
Block	1.13	1	1.13		
Model	166.15	5	33.23	114.19	7.30E-06
A-pH	15.26	1	15.26	52.44	3.52E-04
B-Valence	108.46	1	108.46	372.70	1.25E-06
C-[Metals]	0.50	1	0.50	1.72	0.238

AB	7.26	1	7.26	24.94	0.002
AC	3.00	1	3.00	10.31	0.018
Residual	1.75	6	0.29		
Lack of Fit	1.28	5	0.26	0.54	0.767
Pure Error	0.47	1	0.47		
Cor Total	169.03	12			

A normal plot of residuals and the residuals versus predicted plot are given in Figure E-0-8. The residuals follow a normal distribution with no obvious patterns. A random scatter within the error margins in the residuals versus predicted plot is observed. The data is normally distributed and independent which suggest that the model fitted to the data is adequate.

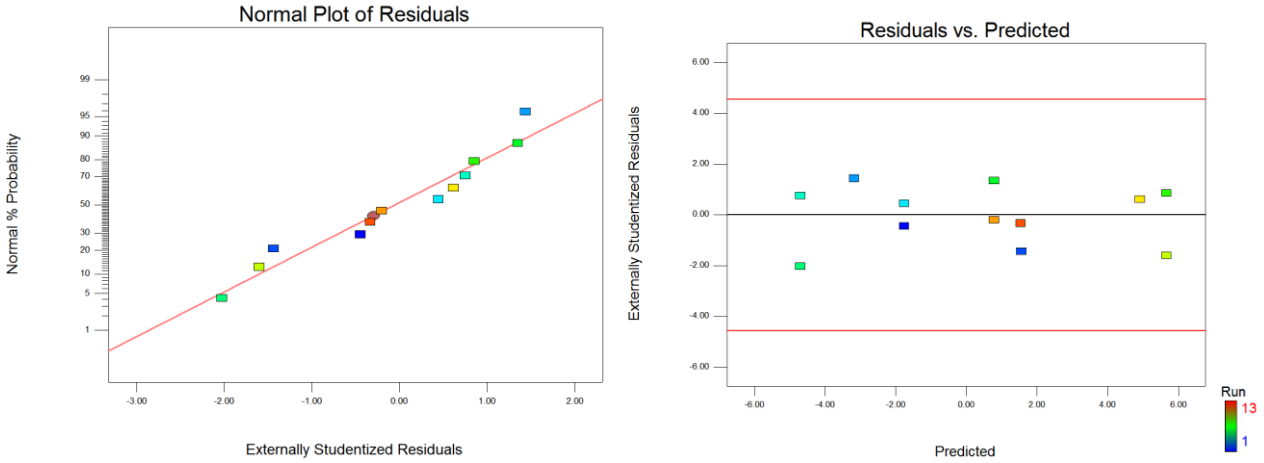

Figure E-0-8: Normal plot of residuals and residuals vs predicted plot for Fe at 360 min.

As at 30 min

Anova analysis for arsenic at 30 min is presented in Table E-0-7. The Model F-value of 16.90 implies the model is significant. There is only a 0.08 % change that this model is due to process noise.

Table E-0-7: Anova analysis for As precipitation at 30 min.

	Sum of Squares	**df**	**Mean Square**	**F Value**	**p-value Prob > F**
Block	433.84	1.00	433.84		
Model	4028.11	3.00	1342.70	16.90	0.0008
A-pH	641.75	1.00	641.75	8.08	0.0218
B-Valence	2507.11	1.00	2507.11	31.55	0.0005
C-[Metals]	603.99	1.00	603.99	7.60	0.0248
Residual	635.71	8.00	79.46		
Lack of Fit	635.63	7.00	90.80	1135.05	0.0229
Pure Error	0.08	1.00	0.08		
Cor Total	5097.66	12.00			

OPMs at 30 min

Anova analysis for ruthenium and rhodium at 30 min is presented in Table E-0-8 and Table E-0-9. Residual analysis was also done. Other time intervals did not yield additional information.

Table E-0-8: Anova analysis for Ru precipitation at 30 min.

Source	Sum of Squares	df	Mean Square	F Value	p-value Prob > F
Block	0.25	1	0.25		
Model	45.32	4	11.33	42.95	< 0.0001
A-pH	41.41	1	41.41	157.0	< 0.0001
B-Valence	8.30	1	8.30	31.47	0.0008
C-[Metals]	5.71	1	5.71	21.66	0.0023
D-Temp	3.84	1	3.84	14.54	0.0066
Residual	1.85	7	0.26		
Lack of Fit	1.84	6	0.31	170.82	0.0585
Pure Error	0.00	1	0.002		
Cor Total	47.42	12			

Table E-0-9: Anova analysis for Rh precipitation at 30 min.

Source	Sum of Squares	df	Mean Square	F Value	p-value Prob > F
Block	0.10	1	0.10		
Model	38.34	4	9.59	14.88	0.0016
A-pH	33.98	1	33.98	52.76	0.0002
B-Valence	5.44	1	5.44	8.44	0.0862
C-[Metals]	7.52	1	7.52	11.67	0.0112
D-Temp	2.56	1	2.56	3.98	0.0228
Residual	4.51	7	0.64		
Lack of Fit	4.51	6	0.75		
Pure Error	0.00	1	0.00		
Cor Total	42.95	12			

APPENDIX E: PUBLICATIONS BASED ON THIS THESIS

Presentations at national symposia and workshops:

Coetzee R., Dorfling, C., Snyders, C.A. & Bradshaw, S.M. 2014. Platinum group metals behaviour during impurity precipitation from nickel sulphate leach liquors. *Mineral Processing 2014*, Western Cape Branch of SAIMM, Cape Town, South Africa, 7 – 8 August 2014.

Coetzee R., Dorfling, C., Snyders, C.A. & Bradshaw, S.M. 2015. Iridium, ruthenium and rhodium behaviour during iron precipitation from nickel sulphate leach solutions. *Mineral Processing 2015*, Western Cape Branch of SAIMM, Cape Town, South Africa, 6 – 7 August 2015.